AN EXPERIMENTAL INVESTIGATION STUDYING THE INFLUENCE OF DIMPLES ON A FILM COOLED TURBINE BLADE LEADING EDGE

THESIS

Paul G. Frisinger, Captain, USAF

AFIT/GAE/ENY/09-M10

DEPARTMENT OF THE AIR FORCE

AIR UNIVERSITY

AIR FORCE INSTITUTE OF TECHNOLOGY

Wright-Patterson Air Force Base, Ohio

The views expressed in this thesis are those of the author and do not reflect the official policy or position of the United States Air Force, Department of Defense, or the United States Government.

AFIT/GAE/ENY/09-M10

AN EXPERIMENTAL INVESTIGATION STUDYING THE INFLUENCE OF DIMPLES ON A FILM COOLED TURBINE BLADE LEADING EDGE

THESIS

Presented to the Faculty

Department of Aeronautics and Astronautics

Graduate School of Engineering and Management

Air Force Institute of Technology

Air University

Air Education and Training Command

In Partial Fulfillment of the Requirements for the

Degree of Master of Science in Aeronautical Engineering

Paul G. Frisinger, BSAE

Captain, USAF

March 2009

AFIT/GAE/ENY/09-M10

AN EXPERIMENTAL INVESTIGATION STUDYING THE INFLUENCE OF DIMPLES ON A FILM COOLED TURBINE BLADE LEADING EDGE

Paul G. Frisinger, BSAE

Captain, USAF

Approved:

_____//signed//_____	_19 Mar 09_
Paul King	Date
_____//signed//_____	_19 Mar 09_
Mark Reeder	Date
_____//signed//_____	_18 Mar 09_
Marcus Polanka	Date

AFIT/GAE/ENY/09-M10

Abstract

An investigation was conducted to examine the effect of a row of cylindrical surface dimples in reducing the heat load on a turbine blade leading edge model. The models consisted of a foam cylindrical leading edge with a flat afterbody fabricated from Plexiglass. A single coolant hole was located 21.5° from the leading edge, angled 20° to the surface and 90° from the streamwise direction. The leading edge diameter to hole diameter ratio was *D*/*d* = 18.7. A row of seven dimples was placed upstream of one of the coolant holes. Infrared thermography techniques were used to determine the adiabatic effectiveness, η, and heat transfer coefficient, *h*, distributions so that the net heat flux reduction, Δq_r, could be calculated. Freestream conditions consisted of Reynolds numbers of 60,000 and 30,000 at both low turbulence and high turbulence. At Re = 60k, the dimples proved to increase the area averaged η by an average of 0.007, while the dimpled cases performed equally, if not slightly poorer, than a smooth surface at the lower Reynolds number. The heat transfer coefficient was not greatly affected by the presence of the dimples beyond an x/d location of 0.5. Because the heat transfer coefficient remained relatively unchanged while η increased at Re = 60k, the area averaged net heat flux reduction was increased slightly, by an average of 0.02, for the cases with dimples at those freestream conditions. At Re = 30k, the dimpled and non-dimpled cases exhibited virtually identical net heat flux reduction values. The two maximum net heat flux reductions occurred at Re = 60k, M = 0.25 at low turbulence and Re = 60k, M = 0.5 at high turbulence. These two net heat flux reductions were increased by an area averaged Δq_r of 0.025. Although, the dimpled cases provided slight improvement to the adiabatic effectiveness for some cases, any advantage was generally less than the uncertainty, indicating that the dimples' effect was negligible.

To my wife and our three wonderful boys

Acknowledgements

I would like to thank Captain James Rutledge for his mentorship and assistance with this experiment. I would also like to thank Dr. Paul King for his optimism and confidence in my abilities during my time here. This experiment would not have been possible without the hard work provided by Jan LeValley, Daniel Ryan, and Jason "Turk" Vangel of the AFIT model shop. I would also like to thank Dr. Richard Rivir and the Air Force Research Laboratory, Propulsion Directorate, Research Cell 21 for the use of their equipment and facilities. Finally, I would like to thank my family, whose endless support made this work possible.

Paul G. Frisinger

Table of Contents

List of Figures

Page

List of Tables

Nomenclature

Symbol	Description
A	Area, (m^2)
a	Speed of sound (m/s^2)
C	Sutherland's constant, (120 ^oK); Resistance constant, (0.02631258)
C_p	Specific heat at constant pressure, $\left(\frac{kJ}{kg*K}\right)$
$\left(\frac{dT}{dx}\right)$	Temperature gradient, $\left(\frac{^\circ K}{m}\right)$
d	Diameter, (m)
D	Characteristic dimension, diameter, (m)
f	Frequency of vortex shedding, (1/s)
F	Thrust, (N)
$F/\dot{m}$	Specific thrust, $\left(\frac{N}{kg/s}\right)$
Fr	Frössling number, $\left(\frac{Nu_D}{\sqrt{Re_D}}\right)$
FLIR	Forward Looking Infrared
h	Height, (m)
h	Heat transfer coefficient, $\left(\frac{W}{m^2K}\right)$
I	Current, (Amps)
IR	Infrared
k	Thermal conductivity, $\left(\frac{W}{m*K}\right)$
L	Length, (m)
$\dot{m}$	Mass flow, (kg/s)
M	Blowing ratio, $\left(\frac{\rho_c U_c}{\rho_\infty U_\infty}\right)$
Ma	Mach number, $\left(\frac{U}{a}\right)$
Nu_D	Nusselt number, $\left(\frac{hD}{k_f}\right)$

P	Pressure, (Pa)
ΔP	Difference in pressure, (Pa)
Pr	Prandtl number, $\left(\frac{C_p \mu}{k} = \frac{\nu}{\alpha}\right)$
R	Recovery factor
R	Universal gas constant, (287 $\frac{J}{kg*K}$)
$R(T)$	Temperature dependent resistance, (Ω)
Re_x	Reynolds number whose characteristic dimension is a length
Re_D	Reynolds number whose characteristic dimension is a diameter
Δq_r	Heat load reduction
$q", \dot{q}$	Heat flux, $\left(\frac{W}{m^2}\right)$
$q"_{ref}$	Reference heat flux assuming evenly distributed current, $\left(\frac{W}{m^2}\right)$
q_{ratio}	Ratio of heat fluxes used to correct flux distribution
St	Strouhal number, $\left(\frac{f L_c}{U_\infty}\right)$
t	Thickness, (m)
T	Temperature, (^{o}K)
T_o	Reference temperature for use in Sutherland's Law, (291.15 ^{o}K)
ΔT	Difference in temperature, (^{o}K)
TSFC	Thrust specific fuel consumption, $\left(\frac{kg}{N*s}\right)$
U	Velocity, (m/s)

Greek Symbols

α	Absorptivity; Thermal diffusivity, $\left(\frac{m^2}{s}\right)$
δ	Uncertainty
ϵ	Emissivity
Λ/d	Relative integral length scale

λ	Nondimensionalized surface temperature, $\left(\frac{T_\infty - T_s}{T_\infty - T_c}\right)$
μ	Dynamic viscosity, $\left(\frac{kg}{m*s}\right)$
μ_o	Reference viscosity for use in Sutherland's Law, (18.27e-6 Pa*s)
η	Adiabatic Effectiveness, $\left(\frac{T_\infty - T_{aw}}{T_\infty - T_c}\right)$
ϕ	Overall effectiveness, $\left(\frac{T_\infty - T_s}{T_\infty - T_c}\right)$
ρ	Density, $\left(\frac{kg}{m^3}\right)$
σ	Stefan-Boltzmann constant, (5.67e-8 $\frac{W}{m^2K^4}$)
ν	Kinematic viscosity, $\left(\frac{N*s}{m^2}\right)$

Subscripts

∞	Freestream
aw	Adiabatic Wall
c	Coolant, coolant hole
$cond$	Conduction
d	Dimples
f	Film cooling
m	Model
n	Without dimples
o	Without film cooling
rad	Radiation
s	Surface
w	Wall
$\bar{x}$	Spanwise average of x
$\bar{\bar{x}}$	Area average of x

AN EXPERIMENTAL INVESTIGATION STUDYING THE INFLUENCE OF DIMPLES ON A FILM-COOLED TURBINE BLADE LEADING EDGE

CHAPTER 1. INTRODUCTION

The Romans were very likely the creators of the first turbomachine around 70 B.C. with their paddle-type water wheel for grinding grain.[1] More than two millennia later, the same concept powers the vast majority of aircraft today as gas turbine engines. These gas turbine engines have many advantages over other power plants including higher thrust-to-weight ratios, low lubricating oil consumption due to the absence of rubbing parts, and high reliability.[2] On-going studies continue to be conducted in an effort to determine ways of increasing the performance and efficiency of the modern gas turbine engine.

Due to advances in compressor design and overall efficiency, the limiting parameter becomes the turbine rotor inlet temperature. Both thermal efficiency and power output increase with increasing turbine rotor inlet temperature as illustrated in Figure 1.1. For example, to double the power output of modern turbine engines, the turbine rotor inlet temperature must be increased from 2600F to 3600F.[3] Two additional parameters are improved as the turbine rotor inlet temperature is increased: specific thrust ($F/\dot{m}$) and thrust specific fuel consumption (TSFC).[4] As the specific thrust is increased, the cross-sectional area of the engine decreases resulting in a smaller, therefore lighter, power plant. An increase in TSFC indicates enhanced fuel efficiency, boosting the aircraft's range.

A seemingly easy solution to increase performance is to raise the temperature entering the turbine. For obvious reasons, the temperature must be limited by the allowable temperature of the turbine blade materials to prevent thermal fatigue and material failure. However, advanced gas turbine engines operate at rotor inlet temperatures much higher than the allowable metal temperatures of the turbine blade materials, because the blade is cooled .[5] Gas turbine engines have been able to operate at higher and higher temperatures as both materials and cooling techniques are enhanced.

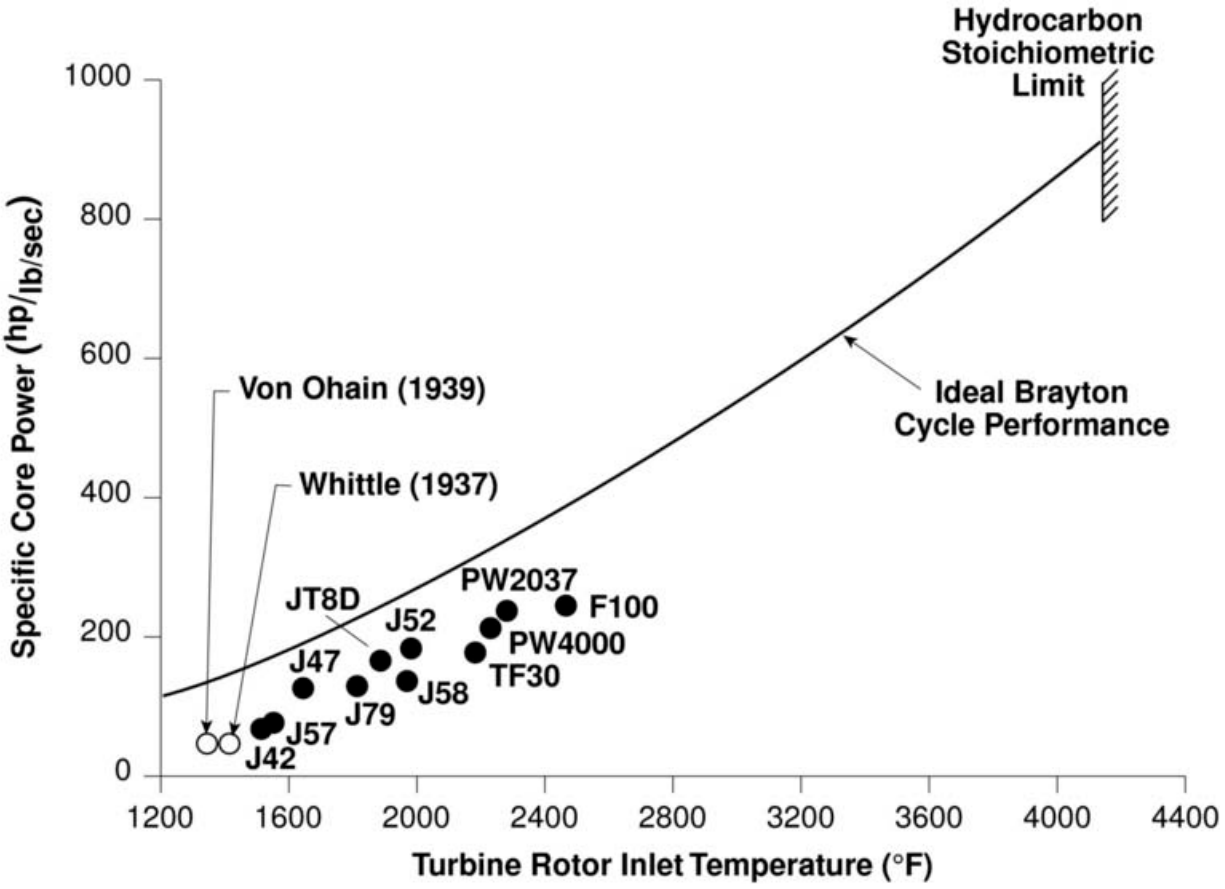

Fig 1.1 Specific core power as a function of turbine rotor inlet temperature.[6]

1.1 HEAT TRANSFER IN TURBINES

Due to the high temperatures involved in a gas turbine engine, it is important to understand how heat is transferred from one body to another. Heat is transferred either by conduction, convection, radiation, or a combination of the three.

Conduction describes the transport of energy through a medium due to a temperature gradient. The physical mechanism governing conduction is the random molecular activity of atomic particles as they interact and exchange energy. Conduction occurs in turbine blades at surfaces exposed to fluid, as well as, within the turbine blade material. Heat conduction is quantified by Fourier's law and can be expressed as,

$$q" = k(\frac{dT}{dx}) \quad 1.1$$

where $q"$ is the heat flux, or heat rate per unit area, k is the thermal conductivity of the medium, and $\frac{dT}{dx}$ is the temperature gradient.

Convection is a heat transfer method that transfers energy between a surface and a fluid moving over the surface. The energy is transferred by advection due to the bulk fluid motion, as well as, the random motion of fluid particles similar to conduction. Convection is a very effective way to transfer heat away from a body. Unfortunately, the opposite is also true; as in the case of an extremely high temperature fuel-air mixture flow over a turbine blade. Convective heat transfer can be quantified by Newton's law of cooling and is quantified by,

$$q" = h(T_\infty - T_w) \quad 1.2$$

where $q"$ is the convective heat flux, h is the heat transfer coefficient, T_∞ is the temperature of the freestream fluid, and T_w is the temperature at the surface. The heat transfer coefficient is difficult to determine and is often the goal of convection heat transfer experiments.

Radiation, the final method of heat transfer, defines energy that is emitted by matter at a temperature above absolute zero. While conduction and convection require a medium to transport the energy, radiation does not. This form of heat transfer can be successfully accomplished in a total vacuum. While energy can be emitted, it can also be absorbed from other bodies. The net rate of heat transfer due to radiation can be expressed as,

$$q" = \epsilon\sigma {T_s}^4 - \alpha\sigma {T_w}^4 \quad 1.3$$

where $q"$ is the heat flux due to radiation, ϵ is the emissivity of the surface, α is the absorptivity of the surface, σ is the Stefan-Boltzmann constant (5.67e-8 $\frac{W}{m^2K^4}$), T_s is the temperature of the surroundings, and T_w is the temperature at the wall. The aforementioned equation accounts for the difference between the thermal energy released due to radiation emission and that which is gained due to

radiation absorption.[7] Radiation heat transfer is usually much smaller than the heat transferred due to conduction or convection in turbines and can be neglected for many cases.

1.1.1 Boundary Layer Theory

A boundary layer is a layer of fluid near a bounding surface that is distinguishable due to flow characteristics caused by friction. Boundary layers are fundamental to the understanding of convective heat transfer, therefore a critical concept in turbine blade cooling.

As the flow of a fluid encounters a body, the particles in contact with the surface will assume zero velocity. These zero velocity particles will impede the motion of adjacent particles. Shear stresses acting in planes parallel to the surface are the cause of the retardation of fluid motion. The previous layer will hinder each subsequent layer of particles until a sufficient distance away from the surface is reached where the effect becomes negligible. The distance where the velocity reaches 99% of the freestream flow velocity is called the boundary layer thickness. As the flow moves downstream along the surface, the boundary layer grows. It is important to note that because the velocity of fluid particles is zero at the surface of a body, all heat is transferred by means of conduction.

When the freestream and surface temperatures differ, another type of boundary layer forms called a thermal boundary layer. The fluid particles in contact with the surface will equilibrate to match the surface temperature. These particles will then exchange energy to adjacent particles. As each previous layer of particles exchanges energy to subsequent layers, a temperature gradient develops in the flow. Moving away from the surface, it is evident that the temperature will eventually reach that of the freestream. Similar to the concept of a velocity boundary layer, the thermal boundary layer is defined where the difference in local temperature and surface temperature reaches 99% of the difference in freestream temperature and surface temperature.

1.1.2 Dimensionless Parameters

A dimensionless parameter is a unit-less value that describes a particular physical system. Such a number is generally defined as the product or ratio of quantities, which have units, in a way that the units cancel. Dimensionless parameters are often used to reduce the number of variables involved. In the fields of fluid mechanics and heat transfer, several dimensionless parameters reveal a large amount of information regarding the flow.

Of these, the Reynolds number, Re_D, is arguably the most significant. The Reynolds number is a ratio of the inertial forces to the viscous forces and is quantified by:

$$Re_D = \frac{\rho U D}{\mu} \tag{1.4}$$

where ρ is the density of the fluid, U is the freestream velocity of the fluid, D is the characteristic dimension (in our case, the diameter of the leading edge), and μ is the viscosity of the fluid. The Reynolds number determines the presence of laminar or turbulent flow. At low Reynolds numbers the viscous forces dominate, thereby dampening any disturbances, resulting in laminar flow. At higher Reynolds numbers, the inertial forces become more dominant relative to viscous forces and the small disturbances may be amplified to a point where transition to turbulent flow occurs.

Another important unit-less parameter is the Mach number. The Mach number is a ratio of the fluid velocity to the local speed of sound as illustrated below:

$$Ma = \frac{U}{a} \tag{1.5}$$

where a is the local speed of sound. Many fluid properties can be determined almost exclusively by the Mach number.

The Prandtl number is an important parameter which is defined as the ratio of momentum diffusivity to thermal diffusivity and is quantified in the following manner:

$$Pr = \frac{C_p \mu}{k} = \frac{\nu}{\alpha} \quad (1.6)$$

where C_p is the specific heat at constant pressure, μ is the viscosity, and k is the thermal conductivity. The Prandtl number is also equally defined by ν and α which represent the kinematic viscosity and thermal diffusivity, respectively. The Prandtl number defines the relative thicknesses of the velocity and thermal boundary layers. A fluid whose Prandtl number is less than one represents a case where the thermal boundary layer is larger than the velocity boundary layer. If the Prandtl number was greater than one, the opposite is true. A value of one implies that both boundary layers are of equal size.

Another dimensionless parameter of particular interest in heat transfer applications is the Nusselt number which is defined as the ratio of convective heat transfer to conductive heat transfer at the surface of a boundary as shown below:

$$Nu_D = \frac{hD}{k_f} \quad (1.7)$$

where h is the heat transfer coefficient, D is the characteristic dimension, and k_f is the thermal conductivity of the fluid. The Nusselt number is used to nondimensionalize the heat transfer coefficient.

The adiabatic effectiveness is a dimensionless parameter that describes the performance of film cooling. Film cooling will be discussed in greater detail in Chapter 2. The adiabatic effectiveness is defined as:

$$\eta = \frac{T_\infty - T_{aw}}{T_\infty - T_c} \quad (1.8)$$

where T_{aw} is the resulting local temperature of a non-conductive wall exposed to a freestream flow and T_c is the temperature of the coolant. The maximum value for η is one, indicating perfect cooling. The adiabatic effectiveness is also defined as the nondimensional adiabatic wall temperature.

The recovery temperature, $T_{recovery}$, is the resulting temperature due to aerodynamic heating and is defined as,

$$T_{recovery} = T_\infty \left\{1 + r\frac{\gamma - 1}{2} Ma_\infty^2\right\} \quad 1.9$$

where T_∞ is the freestream temperature, Ma_∞ is the Mach number of the freestream, γ is the ratio of specific heats of the gas, and r is the recovery factor. The recovery factor was found to be equal to $\sqrt{Pr}$ for laminar flows and $Pr^{1/3}$ for turbulent flows.[8] The Mach number for this experiment was less than 0.3, and therefore is characterized as incompressible flow. At these low speeds $T_{recovery}$ is approximately equal to T_∞.

Another important dimensionless parameter used in this experiment was the Frössling number illustrated below. The Frössling number is used to nondimensionalize the heat transfer coefficient.

$$Fr = \frac{Nu_D}{\sqrt{Re_D}} \quad 1.10$$

1.2 COOLING TECHNIQUES

Cooling techniques employ a coolant fluid, usually bled from upstage compressor air, to reduce the temperature experienced by components within the turbine engine. Numerous methods involving the coolant fluid have been studied and are currently being used in modern turbine engines. Two distinct categories of turbine blade cooling exist: internal cooling and external cooling. Advanced aircraft use a combination of the two to provide adequate cooling.

Internal cooling techniques utilize the coolant fluid inside the turbine blade and heat is transferred by means of convection. Jet impingement, rib-tabulated, and pin fin cooling comprise internal cooling techniques used today. Jet impingement cooling consists of a high mass flow coolant fluid impinging the internal surface of the blade and is most often employed at the leading edge where the most heat transfer is needed. Many turbine blades have internal serpentine channels whose walls are rib-roughened to promote heat transfer and extract the heat from the blade and into the coolant fluid. Another internal cooling technique is pin-fin cooling where pins, located inside the turbine blade, are exposed to the coolant flow. The pins effectively increase the internal surface area of the blade to

promote convective heat transfer. While internal cooling techniques have their benefits, the investigation at hand deals exclusively with film cooling.

Film cooling is an external cooling technique that uses a coolant fluid at discrete locations along a surface exposed to high temperatures to protect the area of injection, as well as downstream.[9] Although film cooling has been studied for over 50 years, much is still not understood due to the complex flow through a turbine and the many variables involved such as gas properties and injection hole locations, shapes, sizes and quantity. Film cooling employs a coolant fluid that acts as a thermal barrier protecting the material surface from the hot gases of the freestream flow. Modern aircraft use upwards of 20% of high pressure compressor bleed air to provide the coolant fluid. While the coolant fluid allows a higher temperature at the inlet of the turbine, bleeding the compressor air also generates losses.

1.3 DIMPLES

Dimples are concave surface indentations that have long been known to effectively initiate laminar-turbulent boundary transition. The purpose of employing dimples is to alter the flow downstream by causing local flow separation and generating elevated levels of turbulence intensity. With the increase in turbulence, the flow reattaches to the surface downstream with a higher momentum enabling the flow to overcome adverse pressure gradients.[10] Multiple longitudinal vortices are the mechanism driving the increase in downstream turbulence resulting in a flow that can be maintained stably in the near wall region for extended distances. Numerous variables affect the vortex characteristics including dimple geometry (spherical or cylindrical shape, single row, array, asymmetrical, etc.), Reynolds number, dimple height to diameter ratio, and dimple depth to pre-dimple boundary layer.

1.3.1 Flow Through a Dimple

To more completely understand the effect of dimples, a discussion of the flow structure within the dimple itself is necessary. With the use of smoke lines, it was observed that fluid was drawn from above the dimple and converged on the downstream rim of the dimple. Pairs of recirculation zones also existed within the dimple. Fluid in the central region of the dimple traveled upward and out of the dimple forming the pair of stream-wise counter-rotating vortices that stretched downstream. Fluid is supplied from the sides of the dimple to replace the ejected fluid and the process repeats at a certain vortex shedding frequency dependent on the many variables mentioned previously.[11]

1.3.2 Boundary Layers and Dimples

The aerodynamic effects of the spherical dimples on a golf ball have been studied extensively. It has been observed that dimples proved to effectively transition the boundary layer from laminar to turbulent flow without the viscous losses associated with other roughness triggers. Another observation showed that shallower dimples (h/D ~0.1) reduced the critical Reynolds number corresponding to a rapid decrease in the drag coefficient for cylindrical models.[12] This is consistent with other findings revealing that dimples are the best passive approach as vortex generators to promote boundary layer adhesion while avoiding viscous losses on the low pressure side of a turbine blade.[13, 14]

The shape of the dimple, whether spherical or cylindrical, can also play an important role in the characteristics of the flow downstream. The aerodynamic effects of cylindrical dimples were first studied in 1953. Applying this early work, other studies suggested that cylindrical dimples exhibited more viscous losses than spherical dimples.[15] Cylindrical dimples were also shown to have a longer separation region within the dimple than spherical dimples.[16]

Much research has been conducted to determine which variables can be used to predict the flow characteristics within and downstream of a dimple. The minimum value for the drag coefficient was observed to correspond to a maximum value of the Strouhal number ($St = \frac{fL_c}{U_\infty}$), where f is the

frequency of vortex shedding.[17] Ensuring boundary layer attachment downstream of the dimple was found to be highly dependent on the frequency of vortex shedding.[18] The effect of the depth to diameter ratio on flow dynamics within and downstream of a dimple is another parameter previously studied. It was concluded that the ratio proved to be an effective parameter to aid in predicting vortex production. Values of *h/D* from 0.1 to 0.5 were shown to be the most effective range.[19]

1.3.3 Heat Transfer and Dimples

The possibility of a change in heat transfer characteristics due to the vortex's produced by dimples has prompted further research. The twin vortex structures produced within the dimple are most prominent on the downstream rim of the dimple, as well as, the flat surface immediately downstream of the dimple.[20] An increase in heat transfer coefficient, h, was observed with concave spherical dimples due to the mixing caused by boundary layer separation and reattachment.[21]

The effect of a single dimple was examined in a rectangular cooling channel for Re_x = 10,000 and Re_x = 40,000. A region of recirculation was observed in the upstream half of the dimple causing a lower heat transfer rate than that of the downstream half where the flow reattached. The twin vortices generated within the dimple increased mixing and thus, the heat transfer immediately downstream of the dimple. It was concluded that overall heat transfer was increased 2-2.5 times when compared to a non-dimpled surface.[22]

Another experiment focusing on flow and heat transfer characteristics within spherical and cylindrical dimples on a flat plate was conducted in 1983. Dimple depth to diameter ratios ranged from 0.2-1.0 while the Re_x was held constant at 110,000. A region of low pressure was observed on the leading edge of the dimple cavity and a high static pressure region on the trailing edge. It was concluded that although dimples increase overall heat transfer when compared to a smooth surface, a minimum increase was observed around an *h/D* value of 0.2.[23]

1.4 OBJECTIVE OF CURRENT RESEARCH

The vortices produced within and downstream of the dimple create regions of high shear and low pressure bringing high-energy fluid down to the low-energy fluid near the surface thereby inhibiting boundary layer separation. This mechanism may also be beneficial for preventing lift-off of the coolant and increasing the useful cooling length of the film on a film cooled surface. The enhanced mixing due to the turbulent re-attachment is also expected to increase the heat transfer coefficient, a detrimental effect.

The objective of this effort involves investigating the use of dimples to entrain and mix primarily the coolant flow to determine if the use of dimples with film cooling can reduce the heat load experienced by the turbine blade and thereby improve the adiabatic film effectiveness and extend the effective length of the film cooling while maintaining the heat transfer coefficient at sufficiently low levels.

CHAPTER 2. EXPERIMENTAL THEORY AND PROCEDURE

Cooling the turbine blades is essential to realize an increase in thermal efficiency of a gas turbine engine; however, further comprehension of the flow within the engine must be acquired to achieve any benefit. The flow within gas turbine engines is extremely complex, consisting of highly unsteady, turbulent, three-dimensional flow. Failure to optimize cooling designs will result in considerable losses generated from bleeding the compressor with little, if any, cooling in the turbine.

2.1 EXTERNAL AND OVERALL TURBINE COOLING

Film cooling is the method of cooling the external surface of the turbine blade providing thermal protection from the hot freestream gas mixture within the turbine. A very complex interaction of the hot freestream and coolant flows exists at and downstream of the cooling hole. Consideration must be given to this interaction in an effort to maximize the effectiveness of the film cooling. If the design is not optimized, the presence of cooling holes and a secondary flow at a temperature different than the freestream could adversely affect the viscous boundary layer resulting in a decrease in thermal efficiency.

Newton's Law of Cooling is used to define the heat load of a turbine blade as the heat transfer between the hot freestream flow and the surface of the blade. Equation 1.2 is repeated here to illustrate the heat transferred without film cooling,

$$q''_o = h_o(T_\infty - T_w) \tag{1.2a}$$

where the subscript *o* is used to define properties in the absence of film cooling. Similarly, the rate of heat transfer between the freestream flow and the turbine blade in the presence of film cooling is shown below,

$$q''_f = h_f(T_f - T_w) \tag{2.1}$$

where the subscript *f* defines those properties when film cooling is used. When film cooling is present, the heat transfer coefficient is expected to increase due to the mixing in the boundary layer with the

freestream flow. Without a temperature difference between the surface and the flow in contact with the surface, zero convective heat transfer would exist. Although the cases with and without film cooling both exhibit a temperature difference, the driving force for the film cooling case is $(T_f - T_w)$ as shown in Figure 2.1. The potential exists for a smaller temperature difference resulting in a decrease in heat transferred to the turbine blade, as long as the heat transfer coefficient is kept to reasonably low levels.

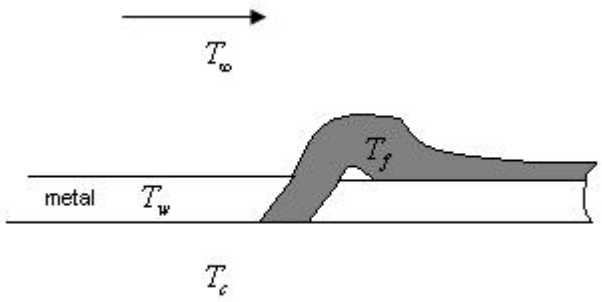

Fig 2.1 Film cooling plume illustration[24]

When the coolant's component of velocity normal to the surface is increased, the coolant is more likely to leave the surface, a phenomenon called lift off. Lift off is extremely undesirable because when the coolant leaves the surface, it no longer performs its purpose of cooling the blade.

The heat load ratio with film cooling to that without film cooling was given by,

$$\frac{\dot{q}_f}{\dot{q}_o} = \frac{h_f}{h_o}\left(\frac{T_f - T_w}{T_\infty - T_w}\right) = \frac{h_f}{h_o}\left\{1 - \eta\left(\frac{T_\infty - T_c}{T_\infty - T_w}\right)\right\} = \frac{h_f}{h_o}\{1 - \eta\phi^{-1}\} \qquad 2.2$$

where a ratio of heat loads less than 1.0 corresponds to the film cooling reducing the heat load experienced by the turbine blade.[3] The term $\frac{T_\infty - T_c}{T_\infty - T_w}$ is a nondimensional form of the actual wall temperature, and is approximately 5/3 for modern turbine cooling systems.[25] Values for h_o and $\frac{T_\infty - T_c}{T_\infty - T_w}$ are assumed to be constant, while values for h_f and η are allowed to vary depending on the particular cooling scheme employed. The smaller the value of the heat load ratio, the better cooling scheme.

In a similar manner, the heat loads for the cases with and without dimples can be compared to ascertain the dimples' effect on the heat transferred. The adiabatic effectiveness, η, and the heat

transfer coefficients are needed to obtain the heat load on the surface. The heat loads for the cases with and without dimples will be compared using the net heat flux reduction equations below:

$$\Delta q_{rd} = 1 - \frac{q_d}{q_o} = 1 - \frac{h_d\left(T_{aw_d} - T_w\right)}{h_o\left(T_{aw_o} - T_w\right)} = 1 - \frac{h_d(\eta_d - \phi)}{h_o(-\phi)} = 1 - \frac{h_d}{h_o}\left(1 - \frac{\eta_d}{\phi}\right) \quad 2.3$$

$$\Delta q_{rn} = 1 - \frac{q_n}{q_o} = 1 - \frac{h_n\left(T_{aw_n} - T_w\right)}{h_o\left(T_{aw_o} - T_w\right)} = 1 - \frac{h_n(\eta_n - \phi)}{h_o(-\phi)} = 1 - \frac{h_n}{h_o}\left(1 - \frac{\eta_n}{\phi}\right) \quad 2.4$$

where the subscript *d* indicates properties with dimples, the subscript *n* indicates properties without dimples, the subscript *o* indicates properties without dimples or film cooling, and ϕ is the overall effectiveness defined as $\frac{T_\infty - T_s}{T_\infty - T_c}$. The value of ϕ was assumed to be 0.6 to represent a value typical for an actual turbine blade.[26] The assumption of constant ϕ , and therefore a constant surface temperature is adequate for the small region on the leading edge of an actual turbine blade. The net heat flux reduction must be greater than zero for any benefit to be realized.

Two distinct experiments are normally conducted to obtain values for the heat transfer coefficient, h, and the adiabatic effectiveness, η. With the freestream and coolant temperatures known, the adiabatic effectiveness is calculated using the measured temperature at the wall. An additional experiment is required to determine the heat transfer coefficient using Newton's Law of Cooling. The use of dimples is expected to improve the adiabatic effectiveness, as well as increasing the heat transfer coefficient. Because finding the net heat flux reduction requires both variables, it is important to determine whether the improvement in η compensates for the increase in h. If h is significantly increased, a negative heat flux reduction indicating an increase in heat load, is possible.

2.1.1 Actual and Modeled Leading Edge Turbine Cooling

Apart from cooling hole geometry and configuration, the fluid properties of the freestream and coolant air greatly influence the film cooling's effectiveness. The coolant-to-freestream pressure ratio (P_c/P_∞) and temperature ratio (T_c/T_∞) have been found to be two of the more significant parameters. Typical values for P_c/P_∞ range from 1.02 to 1.10, while T_c/T_∞ values range from 0.5 to 0.85. The blowing ratio, another important parameter used in film cooling, is defined as the ratio of the coolant mass flow rate to the freestream mass flow rate and is shown below,

$$M = \frac{\rho_c U_c}{\rho_\infty U_\infty} \qquad 2.5$$

where the subscript *c* corresponds to the coolant flow properties. The previously mentioned values for coolant-to-freestream pressure ratio and temperature ratio correspond to blowing ratio and density ratio (ρ_c/ρ_∞) values from 0.5 to 2.0 and 2.0 to 1.5, respectively. Even though, the experiment's pressure, temperature and density ratios differ from those in an actual film cooled turbine, the nondimensional values of blowing ratio and adiabatic effectiveness represent typical values.

The leading edges of actual turbine blades possess an elliptical shape, somewhat different than the semi-cylindrical leading edge used in this experiment. However, the adiabatic effectiveness on the cylindrical leading edge was determined to be virtually identical to the elliptical leading edge.[27] This result is further supported as most experiments found in literature use cylindrical leading edges. Another difference in the model being used is the flat-afterbody yielding a sudden change in curvature, a trait absent in actual turbine blades. Data obtained in the aforementioned area would be extremely unreliable; therefore, emphasis will be placed primarily on the circular section.

2.2 EXPERIMENT SETUP

The experiment was conducted at the Air Force Research Laboratory's low speed, open loop wind tunnel located at Wright-Patterson Air Force Base. The wind tunnel has a test section measuring 21.89 cm x 30.48 cm. The tunnel's freestream flow is provided by filtered air within the laboratory that

is passed to a centrifugal blower located just outside the facility, driving the flow back inside towards the test section. A heater and chiller allow the freestream temperature to be regulated prior to entering a 76.2 cm diameter settling chamber just upstream of the test section. The coolant, used to produce the film cooling, was supplied from compressed air passed through a filter, pressure regulator, heater/chiller, and finally an Omega brand Rotometer, which measures the volumetric flow rate. A diagram of the test facility is shown in Figure 2.2.

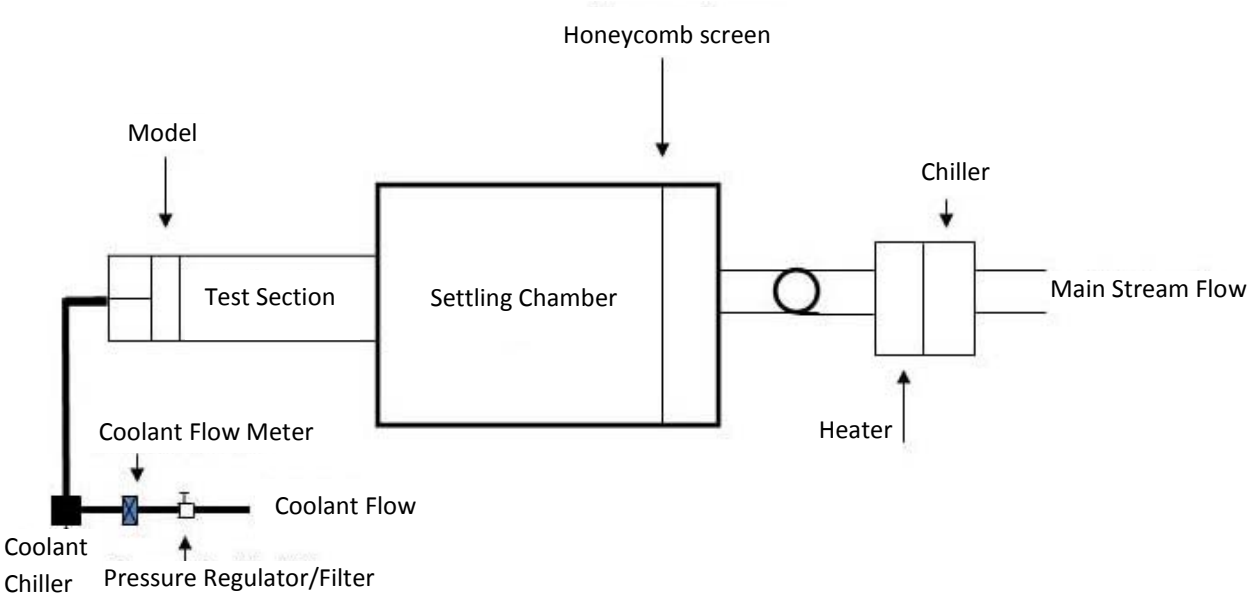

Fig 2.2 Schematic of test facility[24]

A FLIR ThermoCAM SC3000 camera was used to acquire the necessary thermal data. The camera has a 20° x 15° field of view at 0.3 m from the model test area producing a pixel array of size 320 x 240. The FLIR camera takes 3 to 5 pixels to recognize a temperature difference between two objects in the camera field of view. The intermediary pixels are averages of the surrounding pixels. In addition to the image, a 320 x 240 array was created for each image containing the temperature values corresponding to each pixel for use in MATLAB.

2.2.1 The Leading Edge Models

The leading edge models were constructed of FR-7106 Last-a-Foam, a high-density (6 lb/ft^3) polyurethane foam, produced by General Plastics Manufacturing Company. The foam material was chosen due to its low thermal conductivity (0.03 $\frac{W}{m\,K}$) to better represent an adiabatic wall by reducing the heat conducted through the model. The models were fabricated to replicate previous leading edge model geometry.[24, 28, 29] The turbine blade leading edge region was modeled by a half cylinder of diameter 8.89 cm, height of 36.4 cm, and thickness of 1.92 cm. One coolant hole of dimension D_m/D_c= 18.7 was positioned 21.5° around from the stagnation line. The hole had length to diameter ratio of L_c/D_c = 11.69, and was angled 20° to the surface and 90° from the streamwise direction. The models were mounted on Plexiglass frames, representing the flat-afterbody, designed to fit the height of the wind tunnel's test section. To better represent a black body, all the models' leading edges were painted a flat black.

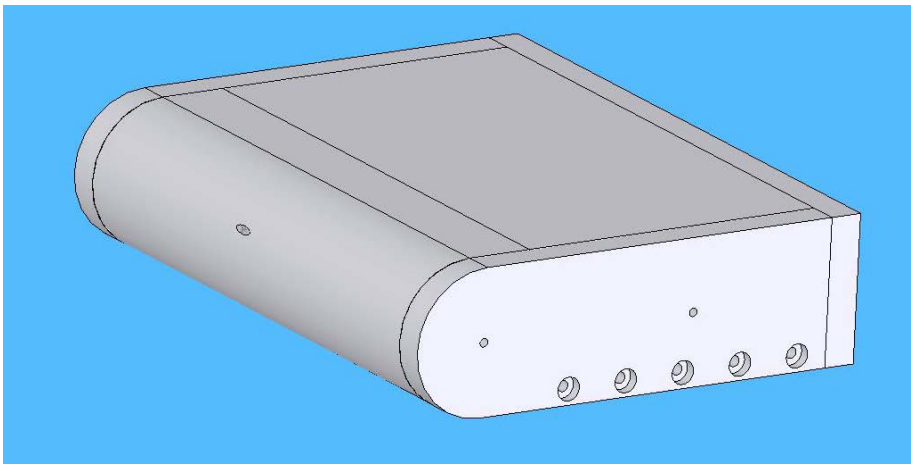

Fig 2.3 Representation of leading edge model

Coolant flow was supplied through an adapter to the rear of the frame and into a plenum that enveloped the cooling hole entrance inside the model. A diagram illustrating the plenum and thermocouple location within the plenum can be seen in Figure 2.4. Undesired temperature deviation

due to settling of the cooling fluid within the frame was prevented by guiding the fluid directly to the plenum using a 3/8” outside diameter hose.

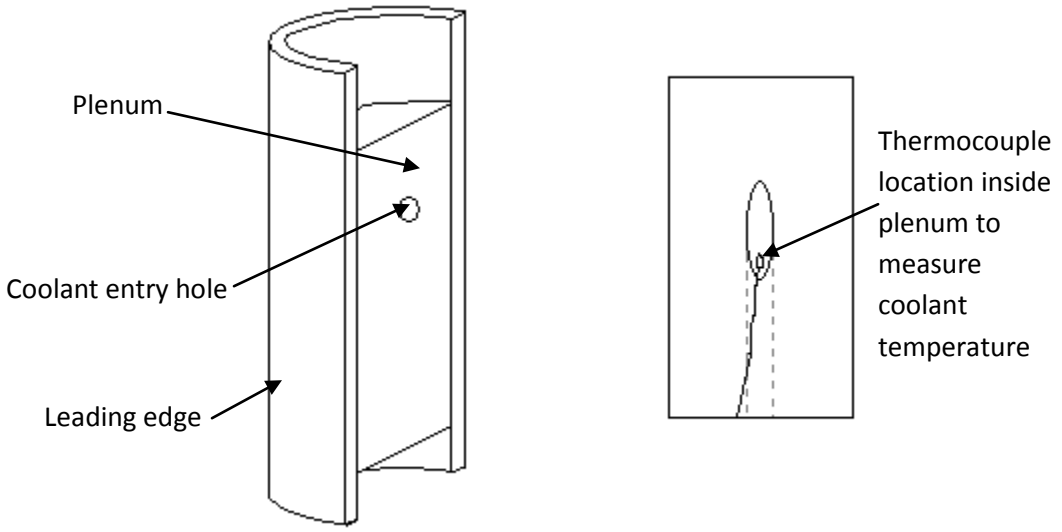

Fig 2.4 Diagram illustrating plenum and coolant thermocouple location

2.2.2 The Dimple Pattern

Cylindrical dimples were chosen for the experiment due to their ease of fabrication. Upstream dimples were chosen because a previous experiment concluded that upstream dimples provided better adiabatic performance than downstream dimples.[24] Choosing only upstream dimples also reduces the parameter space and total number of experiments to a more reasonable level given time constraints.

The dimple geometry was chosen to replicate previous experiments, shown in Figure 2.5, as closely as possible.[24] Slight variations from the aforementioned experiments in dimple diameter and dimple depth are present because a 0.381 cm flat drill bit could not be located. The 0.381 cm drill mentioned was most likely a typographical error as it is not a standard dimension. Instead, a 0.391 cm flat drill bit was used to create a row of seven dimples spaced 1.5 D_d apart. The dimples are 0.782 mm deep resulting in a height to diameter ratio (h/D) of 0.2. The row of dimples was placed 1.5 D_c upstream from the coolant hole. Although, the design called for the centerlines of the center dimple and coolant hole to align, the row of dimples was inadvertently fabricated 0.2 cm off of the centerline in the

spanwise direction. It was deemed that this minor error would not adversely affect the results of the experiments.

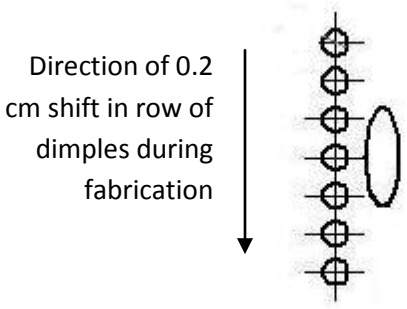

Figure 2.5 Dimple arrangement[24]

2.2.3 Instrumentation

Bare type J thermocouples were used at various locations on the model to provide a more accurate measurement of the temperature. Locations included at the coolant hole entrance within the plenum, on the inside surface of the model to account for conduction, inside the Rotometer for determining density of the coolant, and one exposed to the freestream. Additionally, two thermocouples were attached to the surface of the model within the view of the IR Camera. With the position of the thermocouples noted, a comparison of the measurements from both the camera and thermocouples were used to provide a temperature calibration. A second order polynomial curve fit was used to obtain temperature measurements that were more accurate than the camera could provide. The uncertainties associated with the experiment will be discussed in greater detail in Section 2.8. An example of one of the calibration curves along with its corresponding equation can be seen in Figure 2.6. The equation has many more significant digits than necessary because the numbers were used in this form by Excel for use in the curve fit. Temperature calibrations were conducted for each

experiment at various expected temperatures during experimentation to account for any changes in the accuracy of the IR Camera.

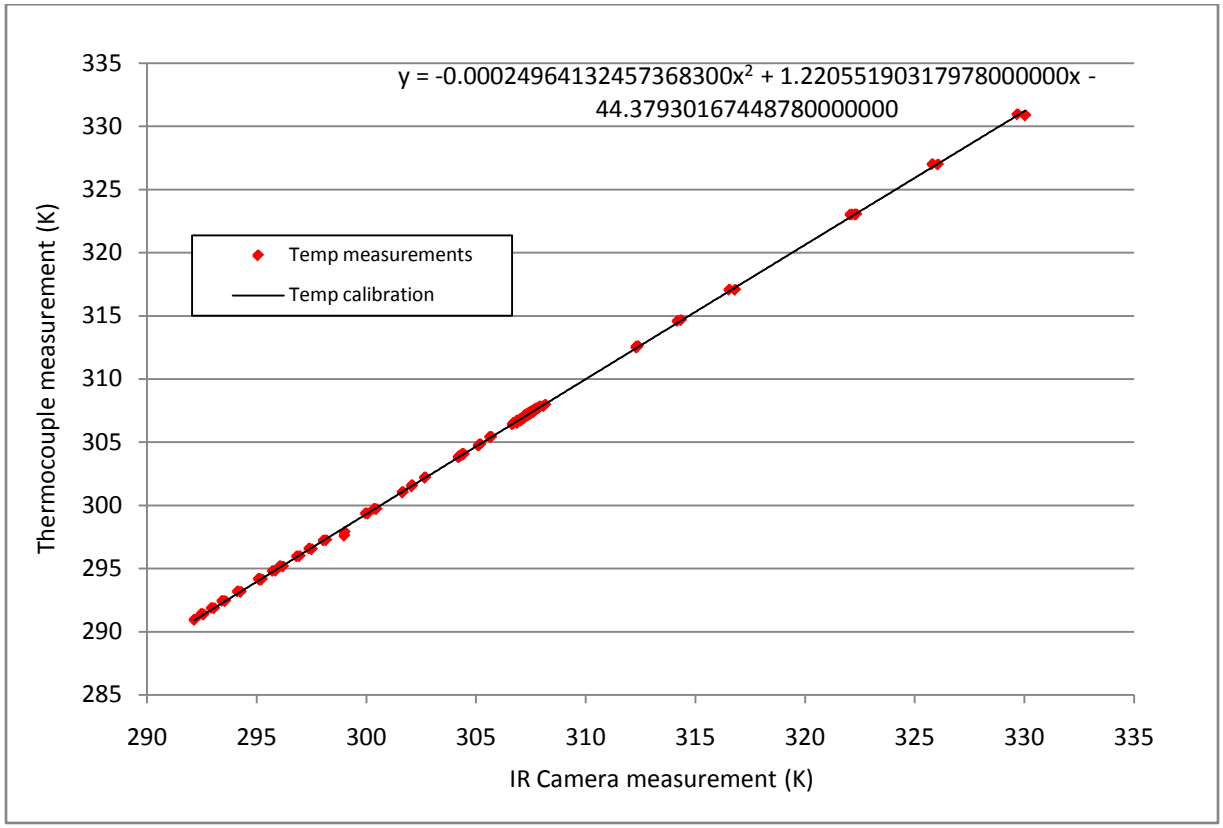

Fig 2.6 Example of temperature calibration curve

A pitot-static tube, connected to an Omega PCL-1B handheld pressure transducer, was used during the experiment to calculate the freestream gage pressure. The static pressure was found to be 98.358 kPa at the approximate elevation of 820 ft using the 1976 standard atmosphere tables. The freestream velocity was found using Bernoulli's equation as seen in Equation 2.6.

$$\Delta P = \frac{1}{2}\rho U^2 \tag{2.6}$$

where ΔP is the pressure difference or gage pressure, ρ is the density of the air, and U is the freestream velocity. The density was calculated using the Perfect Gas Law as illustrated in Equation 2.7.

$$\rho = \frac{P}{RT} \tag{2.7}$$

where P is the pressure, R is the universal gas constant (287 $\frac{J}{kg*K}$), and T is the temperature measured in degrees Kelvin. The Reynolds number was determined using Equation 1.4 which has been repeated below.

$$Re_D = \frac{\rho U D}{\mu} \quad 1.4$$

The values for ρ, U, and D are all known; however, μ is a function of temperature and was calculated using Sutherland's Law as shown in Equation 2.8.

$$\mu = \mu_o \frac{T_o + C}{T + C}\left(\frac{T}{T_o}\right)^{\frac{3}{2}} \quad 2.8$$

where T_o is a reference temperature of 291.15 K, μ_o is a reference viscosity in Pa s at reference T_o, C is Sutherland's constant (120 K), and T is the temperature measured by the freestream thermocouple. The Reynolds number throughout the experiments was maintained within 2% of the desired value.

The volumetric flow rate of the coolant was measured by the Rotometer which was essentially a vertical, slightly tapered, hollow cylinder with graduated lines from 0 to 100. The setting was determined by the location of a glass ball floater along the height of the apparatus. The uncertainty reading the meter was $\pm$ 0.5 resulting in a blowing ratio uncertainty of $\pm$ 0.04 at Re = 30k and $\pm$ 0.02 at Re = 60k. A complex correlation provided by the Rotometer manufacturer, Omega Engineering, Inc., was used to calculate the desired setting for a particular blowing ratio.

A Labview program was employed to collect the aforementioned data and display actual Reynolds number, actual blowing ratio, as well as the thermocouple temperatures values. When prompted, the Labview program triggered a second computer to capture the image corresponding to the values just obtained.

2.3 X/D CALIBRATION

Because the images obtained by the IR Camera are two-dimensional, the actual location along the curved three-dimensional model had to be determined. To accomplish this, masking tape, with

metal strips spaced 1.0 cm apart, was adhered to the model. The image captured with the metal strips, shown in Figure 2.7, was used to ascertain the pixel location of each metal strip. A second order polynomial curve fit, shown in Figure 2.8, was used to determine the x/d location as a function of pixel location. The coefficients of the curve fit were applied in a MATLAB script file to generate the actual location along the model. The location corresponding to x/d = 0 is the center of the coolant hole. This calibration was accomplished each time a model was installed in the wind tunnel.

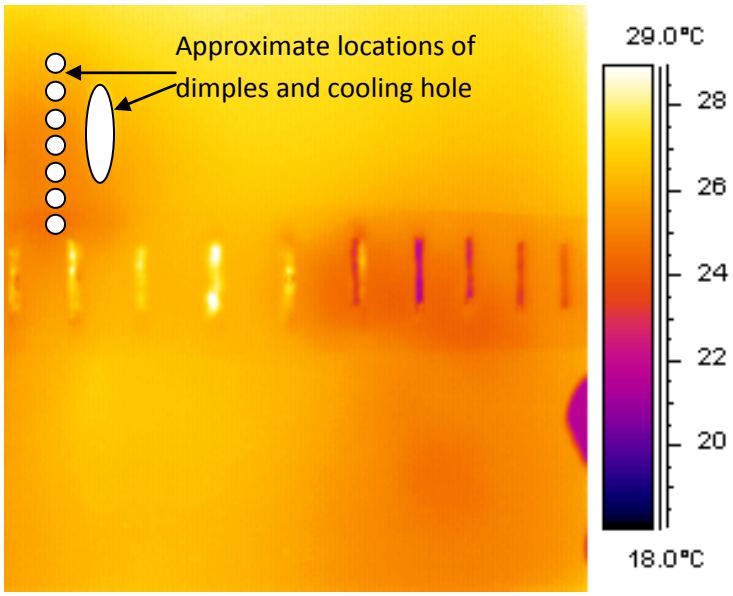

Fig 2.7 IR Camera image showing metal strips for x/d calibration

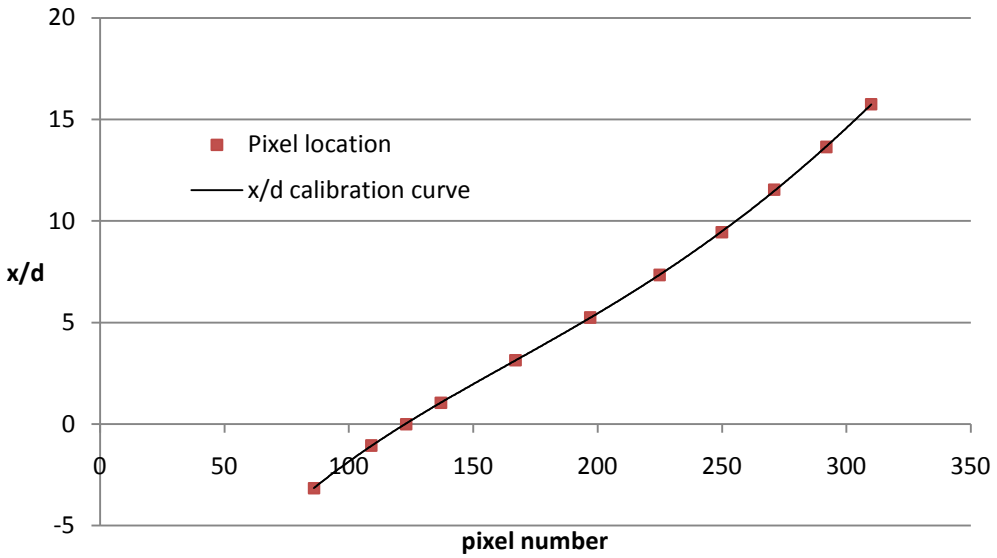

Fig 2.8 Example of x/d calibration curve

Similar to the x/d calibration, another calibration was accomplished to determine y/d location as a function of pixel location; however, because there was no curvature in the y-direction, a linear curve fit was sufficient. In the y/d calibration case, the metal strips were oriented in the vertical direction.

2.4 EXPERIMENTAL PARAMETERS

Experiments were performed at two freestream Reynolds numbers of Re_D = 60,000 and 30,000, held within 2% of the target Reynolds number. A turbulence grid was also employed to observe the effects at an elevated level of freestream turbulence. The turbulence intensity and length scales for the different freestream conditions were found by the use of a hot-wire anemometer and are shown in Table 1. Six blowing ratios, consisting of 0.25, 0.5, 0.75, 1.0, 1.25, and 1.5 were tested for each freestream condition.

Table 1 Freestream Conditions

Re_D	Turbulence Condition	Turbulence (%)	Λ / d
30000	Low	0.693	13.20
30000	High	4.670	7.66
60000	Low	0.672	24.20
60000	High	4.530	7.54

2.5 CALCULATION OF ADIABATIC EFFECTIVENESS

The adiabatic effectiveness, defined by Equation 1.8 and repeated below, was discussed briefly in Chapter 1. Only three temperature measurements were needed to calculate the value for η.

$$\eta = \frac{T_\infty - T_{aw}}{T_\infty - T_c} \tag{1.8}$$

The temperatures for the freestream, T_∞, and the coolant, T_c, were obtained by the thermocouples. The adiabatic wall temperature, T_{aw}, was derived from the IR camera data. An adiabatic effectiveness value was calculated for each pixel in the image using Equation 1.8. However, a correction was needed to account for the small amount of conduction occurring through the foam.

2.5.1 Conduction Correction

Although the foam material of the leading edge was chosen to adequately represent an adiabatic surface, some conduction inevitably occurred through the foam. If left unchanged, a non-zero adiabatic effectiveness would result where no film cooling was present. To account for this small amount of heat transfer, a conduction correction was used.[30]

Because the coolant hole was drilled 20^o to the surface, a relatively large amount of heat would be transferred through the foam where the material is thin. The circled region in Fig 2.9 corresponds to an area where observable conduction is occurring.

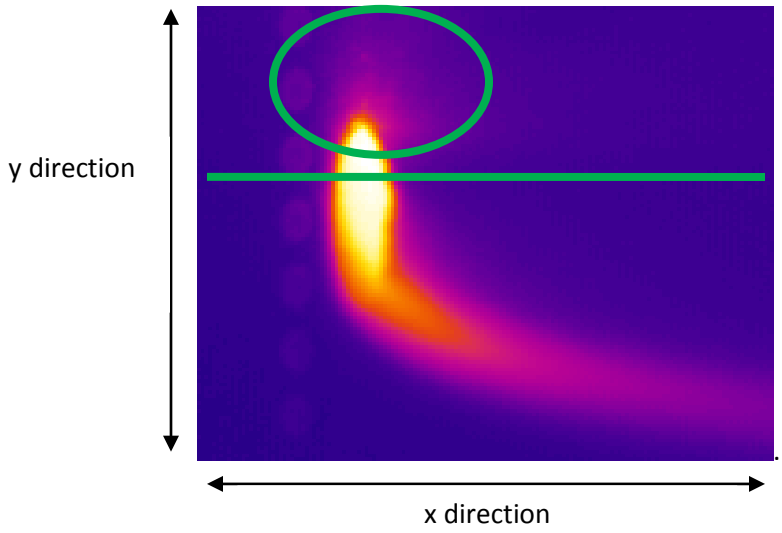

Fig 2.9 Image illustrating conduction through the foam

To correct for the conduction, a blowing ratio of approximately 2.0 was chosen to ensure the coolant was ejected with enough momentum to prevent coolant from flowing over the region where conduction was taking place. It was observed that the blowing ratio had minimal effect on the amount of conduction transferred through the foam because the temperature difference between the inside and outside surfaces was relatively unaffected by the mass flow emitted from the coolant hole. A y-location was chosen, illustrated by the green line in Figure 2.9, to aid in the acquisition of η_o, or the measured value of η where no film cooling is present. Above the line, the measured value of η_o was calculated for each pixel and applied to all test condition images. For determination of η_o below the line, the value was found at a y-location located towards the bottom of each image, and therefore far from the coolant plume. The value of η_o at each x-location was applied to all y values below the green line for that particular x-location and was typically around 0.04. The adiabatic effectiveness was corrected using Equation 2.9 below.

$$\eta_{corrected} = \frac{1}{1-\eta_o}(\eta_{measured} - \eta_o) \qquad 2.9$$

The conduction correction ensures that the adiabatic effectiveness will equal 1.0 when perfect film cooling is occurring and 0.0 when no film cooling is occurring.

2.6 CALCULATION OF HEAT TRANSFER COEFFICIENT

As mentioned previously, usually two experiments are conducted to acquire both the adiabatic effectiveness and the heat transfer coefficient. For determination of the heat transfer coefficient, a known current was supplied through a heat flux plate attached to the surface of a second model. Obviously, the heat flux plate had to be minimally invasive to adequately integrate data from both experiments. During this experiment, the freestream and coolant temperatures were kept as close as possible. Therefore, any temperature gradients present were identified to be caused by the heat transfer coefficient alone.

2.6.1 Heat flux plate design

The heat flux plate used in this experiment was fabricated from 0.0508 mm thick stainless steel shim stock and had dimensions 13.97 cm x 24.77 cm. A water jet was employed to cut holes in the heat flux plate to match the location of the dimples and coolant hole on the surface of the model. Room Temperature Vulcanizing (RTV) silicone sealant was used to attach the heat flux plate to the surface of the model while carefully aligning the holes to accommodate both the dimples and the coolant hole. The current was directed uniformly through the heat flux plate by using copper bus bars, formed to match the curvature of the model, located on opposite sides of the plate. A silver conductive epoxy was used to attach the bus bars, as soldering directly to the heat flux plate would have damaged the foam underneath. The design and assembly of the model leading edge can be seen in Figure 2.10.

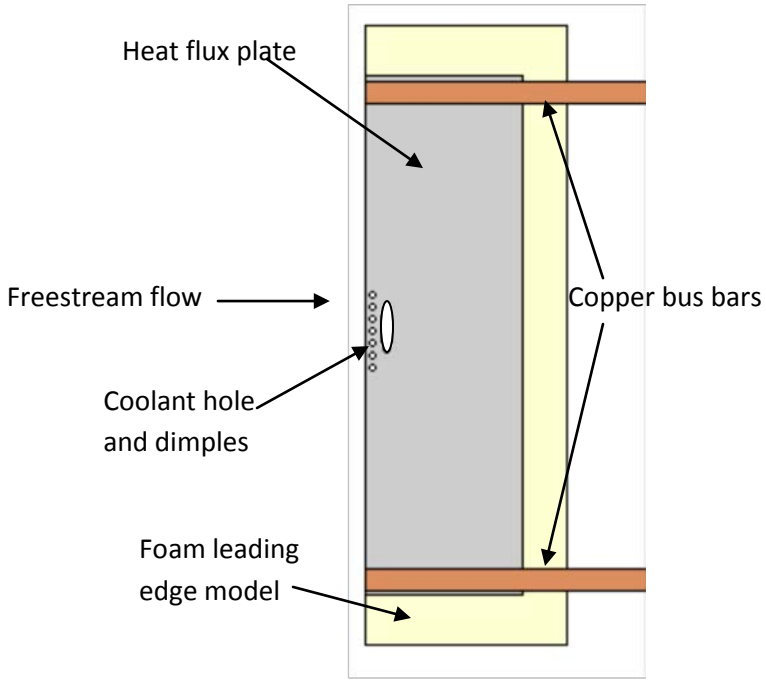

Fig 2.10 Heat flux plate design and implementation

2.6.2 Procedure for calculating heat transfer coefficient

The current distribution, and therefore the heat flux distribution was influenced by the presence of the holes in the heat flux plate. To account for the holes' influence on the current distribution, they were covered with Kapton tape to prevent the aerodynamic effects associated with the dimples from interfering with the temperature distribution on the surface of the heat flux plate. The image obtained from this one test provided a reference heat flux that was transformed into a ratio for the entire image and is explained in the following pages. To acquire the average heat flux across the plate a y-location near the bus bars, and far from the holes, was assumed to exhibit relatively evenly distributed current, therefore constant heat flux. The heat flux, attributed to ohmic heating, was calculated by using Equation 2.10 shown below,

$$q''_{ref} = \frac{I^2 R(T)}{A} \qquad 2.10$$

where I is the current supplied through the heat flux plate, $R(T)$ is the temperature dependent resistance of the heat flux plate expressed in Equation 2.10 below, and A is the area of the heat flux plate between the bus bars.

$$R(T) = C * \{(9.96x10^4)T_s + 0.67166\}, where\ C = 0.02631258 \quad 2.11$$

T_s is the surface temperature in degrees Kelvin measured by the IR camera. The resistance is given in Ohms. Equation 2.11 was derived by a curve fit of data found in standard material specification documents.

A value for the heat transfer coefficient was found for every x/d location. However, the heat transfer due to conduction and radiation must be removed from the total heat flux found using Equation 2.10 leaving only the convective heat transfer. The values for the heat transferred by both conduction and radiation were found using the following equations:

$$q''_{rad} = \sigma\varepsilon(T_s^4 - T_\infty^4) \quad 2.12$$

$$q''_{cond} = \frac{k}{\frac{D}{2} ln \frac{D}{D-2t}} * 0.86(T_s - T_c) \quad 2.13$$

where the net radiation transfer is found using an equation similar to Equation 1.3. A difference in equations exists because the leading edge is assumed to exhibit absorptivity,α, equal to emissivity, ε. Because the model was painted a flat black, ε was assumed to be approximately 0.95. The conduction equation above differs from Equation 1.1 because of the curvature of the model. Equation 1.1 was derived assuming one-dimensional heat transfer. In the conduction equation, k is the thermal conductivity of the foam material (0.03 $\frac{W}{m\,K}$), D is the diameter of the leading edge (8.89 cm), and t is the thickness of the leading edge (1.92 cm). The temperature difference, ($T_s - T_c$), utilizes the coolant temperature as opposed to the inside surface temperature in determining the conduction because they were approximately equal. The heat transfer coefficient far from the holes was found using a relation

derived from Newton's Law of Cooling explained in Chapter 1 (see Equation 1.2). The resulting equation, accounting for the heat transferred due to conduction and radiation, is shown below.

$$h = \frac{\overset{"}{q}_{ref} - q_{cond} - q_{rad}}{T_s - T_\infty} \tag{2.14}$$

Because the dimples and coolant hole were covered with Kapton tape, the heat transfer coefficient should be dependent on its x/d location only. Although the heat flux is not uniform due to the presence of the dimples any elevated values of the heat flux would also result in a larger surface temperature at that location. To account for this, a ratio was derived by algebraic manipulation of Equation 2.13. The ratio was found by applying the h found from Equation 2.14 to every location in the image and is quantified below.

$$q_{ratio} = \frac{\overset{"}{q}_{measured}}{\overset{"}{q}_{ref}} = \frac{h(T_s - T_\infty) + q_{cond} + q_{rad}}{\overset{"}{q}_{ref}} \tag{2.15}$$

The values of q_{ratio} are arranged in an array that correct the heat flux at a particular location to match the heat transfer coefficient at the corresponding x/d location found from Equation 2.14. The q_{ratio} array was multiplied to the $\overset{"}{q}_{ref}$ constant for each test condition to account for the uneven current distribution attributable to the holes in the heat flux plate.

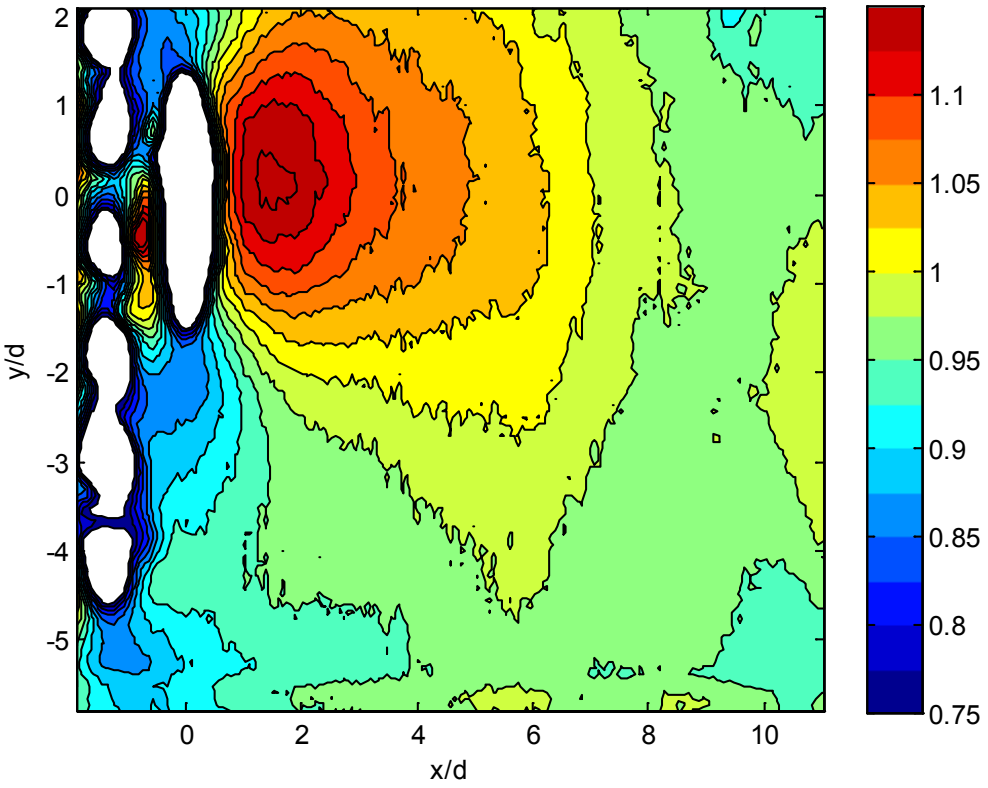

Figure 2.11 Contour plot of q_{ratio} values on the surface of the heat flux plate

In a similar manner, the heat transfer coefficient for the test data was found by:

$$h = \frac{q''_{ref} * q_{ratio} - q_{cond} - q_{rad}}{(T_\infty - T_c)(\eta - \lambda)} \qquad 2.16$$

where λ is the nondimensionalized surface temperature and can be expressed as:

$$\lambda = \frac{T_\infty - T_s}{T_\infty - T_c} \qquad 2.17$$

Because both η and q_{ratio} were needed to calculate the above relation, the values for these arrays were interpolated to correspond with final values for x/d and y/d to complement the x/d and y/d values found from the heat flux experiment images.

2.7 DATA WITHOUT DIMPLES

The initial design called for a model with two coolant holes; one without dimples and one with the upstream dimples so the data could be compared. During preliminary testing, it was concluded that

the blowing ratios at the two holes differed due to unknown aerodynamic effects within the plenum that enveloped the coolant fluid. The models were modified by plugging the coolant hole without dimples with clay. Upon hardening, the clay was sanded to match the curvature of the model.

The results obtained from these experiments would be of little value if there was no comparison to that of models without dimples. A previous investigation acquired data without dimples under identical freestream conditions and blowing ratios.[30] Even though the models were designed identically, the data comparison proved inconclusive and showed evidence of uncertainties associated with experimenting with different models. The differences associated with the two unique heat flux plates were a major concern.

Using the same model to acquire data, both with and without dimples, would prove to be the best solution. To adequately represent a model without dimples, the existing dimples were covered with Kapton tape that extended beyond the stagnation point to mitigate any affects arising from the flow encountering a small step. The resulting models were used to obtain data without dimples. In an effort to alleviate any uncertainties that may have been present, the tape was then removed to acquire data with dimples. The experiment was conducted for both the adiabatic effectiveness and the heat flux models.

2.8 UNCERTAINTY

The measurement devices used in this experiment to collect various temperatures included the FLIR ThermoCAM SC3000 and the type J thermocouples. The IR camera has an accuracy of $\pm$ 1% for a given temperature range or $\pm$ 1 ^{o}K, whichever is greater. Because the temperature ranges in this experiment were on the order of 20 ^{o}K, the resulting accuracy was $\pm$ 1 ^{o}K. The type J thermocouples uncertainty was conservatively estimated to be $\pm$0.2 ^{o}K based on data from type J thermocouple specification sheets.

The data collected from both the IR camera and thermocouples were used to calibrate the values measured by the camera via the method described in section 2.2.3. The values measured by the IR camera were adjusted using the quadratic equation provided from the second order polynomial curve fit. Uncertainty in the calibration is given by Equation 2.16 below,

$$\delta = 1.96 * \sqrt{\sum_{i=1}^{N} \frac{(T_{measured} - T_{calculated})_i^2}{N - (m+1)}} \qquad 2.17$$

where N is the number of data points taken, m is the order of polynomial used in the curve fit, and the 1.96 constant is used to provide the 95% confidence interval.

The uncertainty found for the adiabatic effectiveness collection of data was found to be ±0.2 ^{o}K, while that of the heat flux experiment was ±0.8 ^{o}K. A higher value of uncertainty for the heat flux test was most likely due to the surface thermocouples slightly protruding into the flow causing an undesired increase in *h*, therefore an elevated temperature gradient at the thermocouple weld. The heat flux plate prevented the thermocouples from being embedded into the foam to preserve the contour of the leading edge. Although, the uncertainty is relatively high, it's still less than 4% of the average temperature difference during the course of experiments.

The uncertainties inherently associated with each element in the equations for determining the adiabatic effectiveness, the heat transfer coefficient, and the net heat flux reduction combined to increase the uncertainties of the desired parameters. Conservative estimates for the uncertainty were determined to be $\pm$0.005 for η, $\pm$0.01 for Fr, and $\pm$0.01 for Δq_r.

2.9 REPEATABILITY

For each freestream condition, a blowing ratio of 0.75 was tested twice to analyze the repeatability of the experiment. The maximum variability in η of $\pm$0.006 was found at Re = 30k with low freestream turbulence. The three other freestream conditions tested all exhibited errors less than 0.05 in η. The Rotometer's setting proved to be a fairly accurate measure of the coolant's flow rate. Typical

results comparing the first and second tests for both spanwise averaged η and spanwise averaged Fr are shown below in Figures 2.12 and 2.13. The remaining results look very similar to the ones below indicating that the experiment is extremely repeatable.

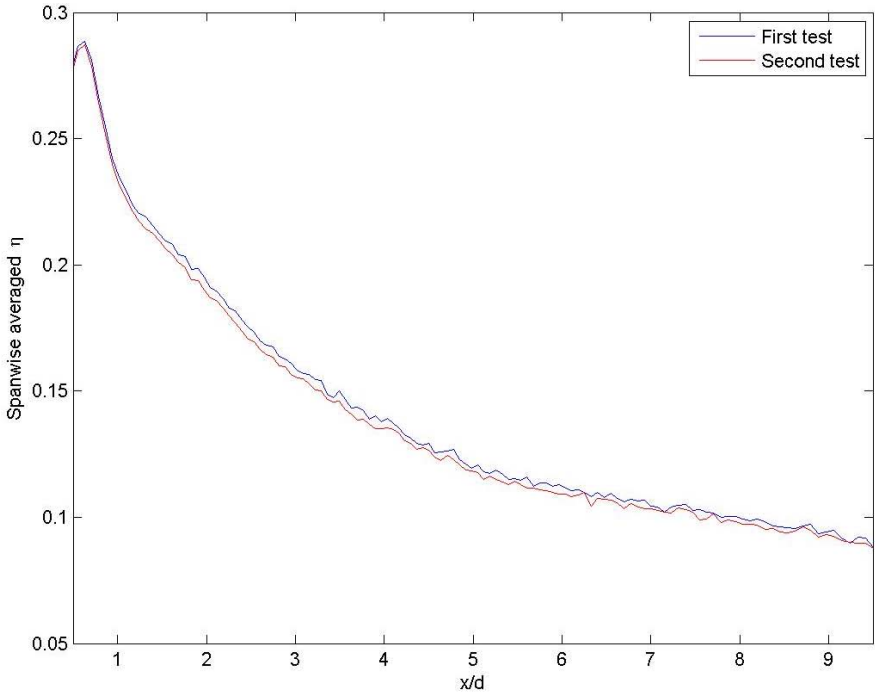

Fig 2.12 Repeatability test showing spanwise averaged η

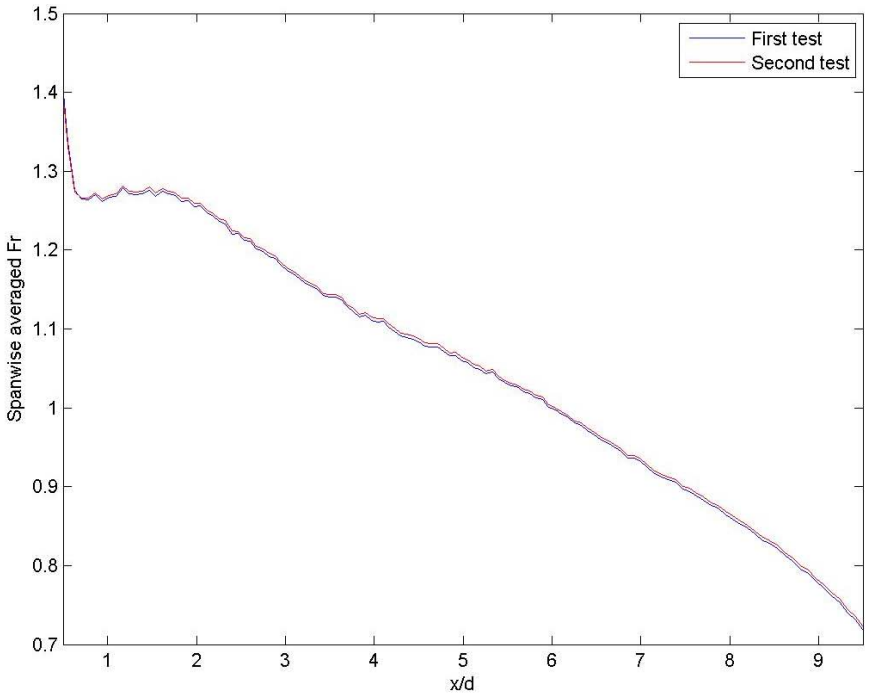

Fig 2.13 Repeatability test showing spanwise averaged *Fr*

CHAPTER 3. EXPERIMENTAL RESULTS

To determine the dimples' effect on the overall heat load, both the adiabatic effectiveness, η, and the heat transfer coefficient, h, must be calculated. These values were calculated using the methods described in Chapter 2. Contour plots were created from the data to aid in comparing the results. In addition to the contour plots, both spanwise averaged and area averaged values were obtained to more easily discern differences in the images.

The contour plots presented data from x/d = -0.5 to x/d = 9.5, while the y/d values ranged from -5 to 2. When a row of cooling holes is employed, the spacing between the holes is called the pitch. The y/d values were chosen to represent an artificial pitch for the experiment and were consistent for all images. On an actual turbine blade, the averaged adiabatic effectiveness over a distance of ± 1 pitch would yield identical results for each cooling hole in a row of cooling holes. The center of the cooling hole is located at x/d = 0 and y/d = 0.

Although the contour plots provide a clear picture of the flow, they are very difficult to compare to one another. Spanwise averaged parameters are values that are averaged over one pitch and provide insight how the parameter changes with x/d location. The spanwise averaged parameters are plotted starting at an x/d location of 0.5, which corresponds to the downstream edge of the coolant hole, to remove the extraneous information inside the coolant hole. These values are designated by a single bar above the parameter (e.g. $\bar{\eta}$, $\overline{Fr}$, $\overline{\Delta q_r}$). Area averaged parameters go one step further by assigning each image a single value. The single value does not provide information about eccentricities within the flow, but it is extremely valuable for easily comparing images. Area averaged values were calculated with y/d values from -2 to 5 and x/d values from 0.5 to 9.5. The area averaged values are designated by a double bar above the parameter (e.g. $\bar{\bar{\eta}}$, $\overline{\overline{Fr}}$, $\overline{\overline{\Delta q_r}}$).

3.1 DIMPLES' EFFECT ON ADIABATIC EFFECTIVENESS

The adiabatic effectiveness contour plots, located in Appendix A, were used to calculate both the spanwise averaged adiabatic effectiveness, $\bar{\eta}$, and area averaged adiabatic effectiveness, $\bar{\bar{\eta}}$. Note that some of these contour plots exhibit a region above the coolant hole where nonzero adiabatic effectiveness exists (see Figure A.33 and A.34). This phenomenon is most likely caused because the conduction correction under-correcting at that location for those cases. The values are small enough that they do not greatly affect either the spanwise or area averaged η. Another region exists in the bottom left of the images where the adiabatic effectiveness appears to be higher. Conduction through the clay covering the bottom unused coolant hole is the most likely cause. Representative contour plots of η, presenting data with and without dimples, are shown in Figures 3.1 and 3.2. The cooling hole has been covered because data in the cooling hole is unreliable, as well as unnecessary.

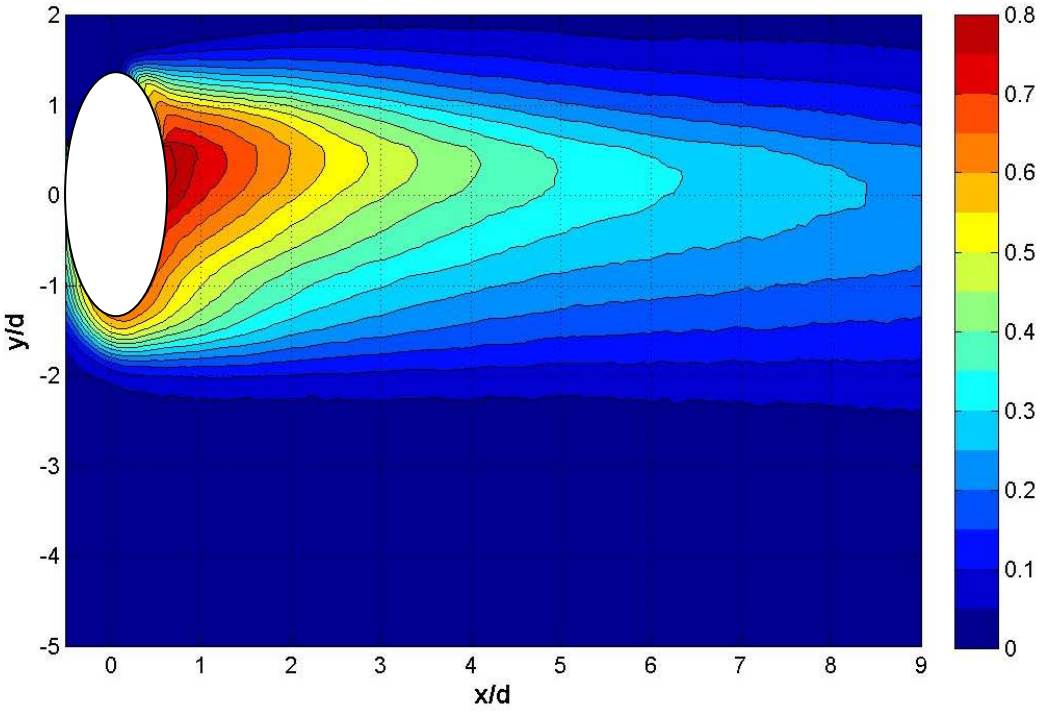

Fig 3.1 Contour of η without dimples at Re = 60k and high turbulence for M = 0.25

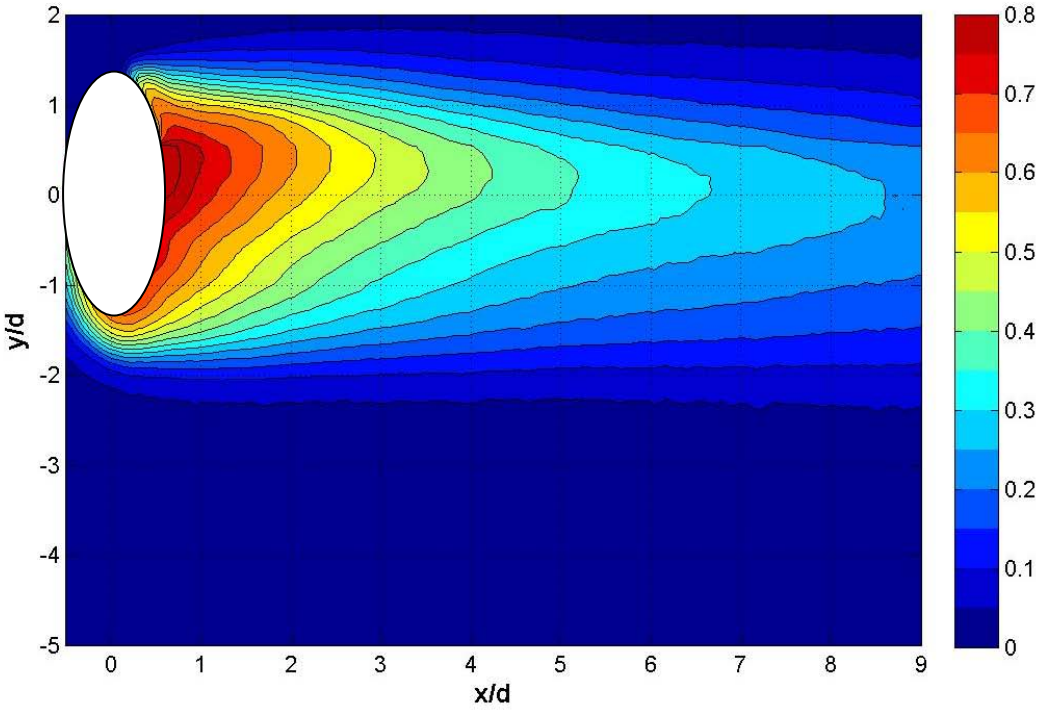

Fig 3.2 Contour of η with dimples at Re = 60k and high turbulence for M = 0.25

A MATLAB program was used to average all spanwise values of η at each streamwise location. The values for $\bar{\eta}$ can be found for all conditions in Appendix B, however an example of one of the plots is shown in Figure 3.3, corresponding to the data obtained from Figures 3.1 and 3.2 above. Values for the cases with and without dimples can be easily compared via these plots. The example shown in Figure 3.3 shows the case with dimples has a higher spanwise averaged adiabatic effectiveness compared to the case without dimples.

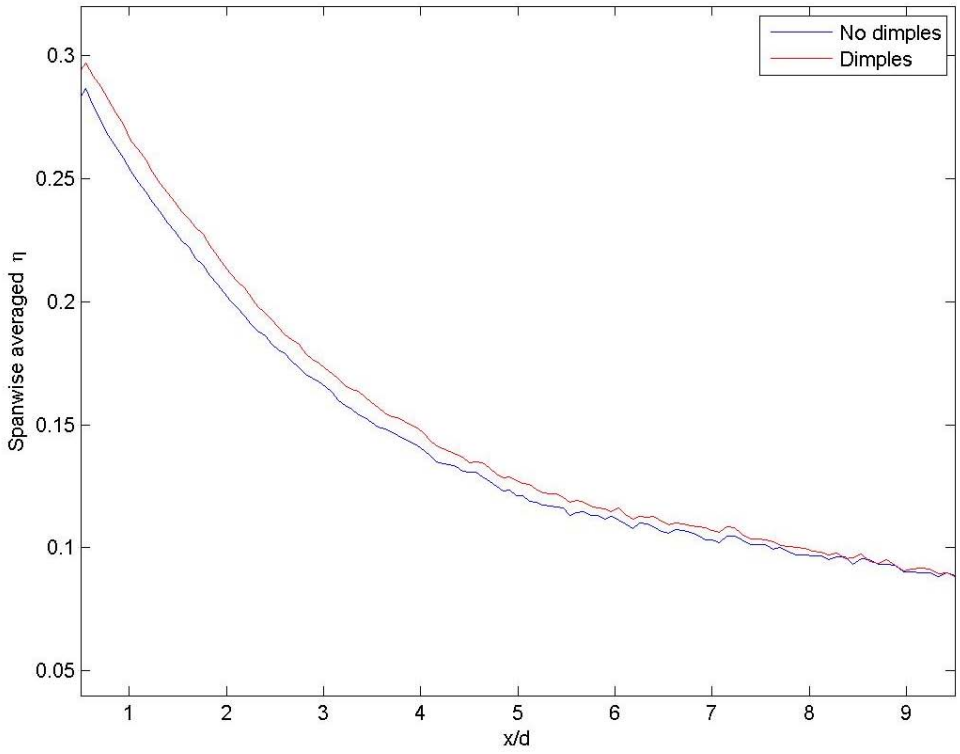

Fig 3.3 Spanwise averaged η at Re = 60k and high turbulence for M = 0.25

The area averaged adiabatic effectiveness values can be found in Table 2. The values of $\bar{\bar{\eta}}$ are also plotted in Figures 3.3-3.6 to provide more visually interpretive results. Although these figures show the adiabatic effectiveness' dependence on the blowing ratio, they can easily be used to interpret the dependence on both the Reynolds number and the turbulence intensity.

Table 2 Area averaged adiabatic effectiveness

Freestream Condition	Case	M = 0.25	M = 0.5	M = 0.75	M = 1.0	M = 1.25	M = 1.5
Re = 60k, high Tu	No dimples	0.135	0.140	0.130	0.120	0.110	0.100
	Dimples	0.140	0.145	0.135	0.120	0.110	0.100
	Difference	0.005	0.005	0.005	0.000	0.000	0.000
Re = 30k, high Tu	No dimples	0.125	0.150	0.125	0.110	0.100	0.090
	Dimples	0.120	0.145	0.125	0.110	0.095	0.090
	Difference	-0.005	-0.005	0.000	0.000	-0.005	0.000
Re = 30k, low Tu	No dimples	0.145	0.170	0.135	0.115	0.100	0.090
	Dimples	0.155	0.165	0.135	0.120	0.105	0.090
	Difference	0.010	-0.005	0.000	0.005	0.005	0.000
Re = 60k, low Tu	No dimples	0.165	0.150	0.135	0.120	0.105	0.095
	Dimples	0.185	0.155	0.140	0.125	0.110	0.095
	Difference	0.020	0.005	0.005	0.005	0.005	0.000

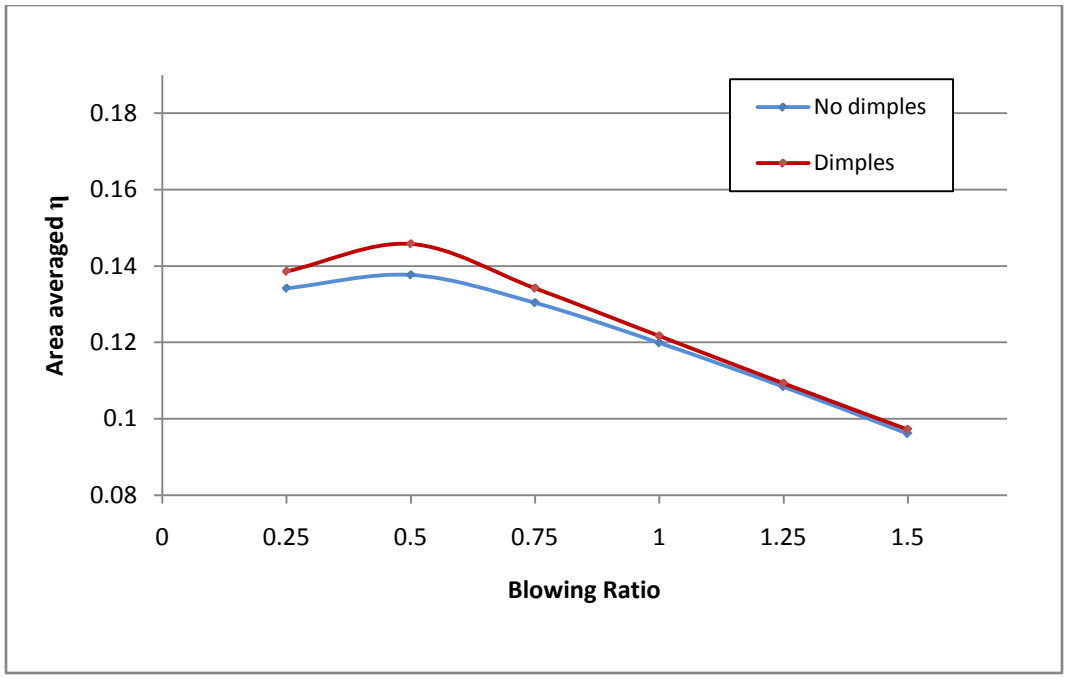

Fig 3.4 Area averaged η at Re = 60k and high Turbulence

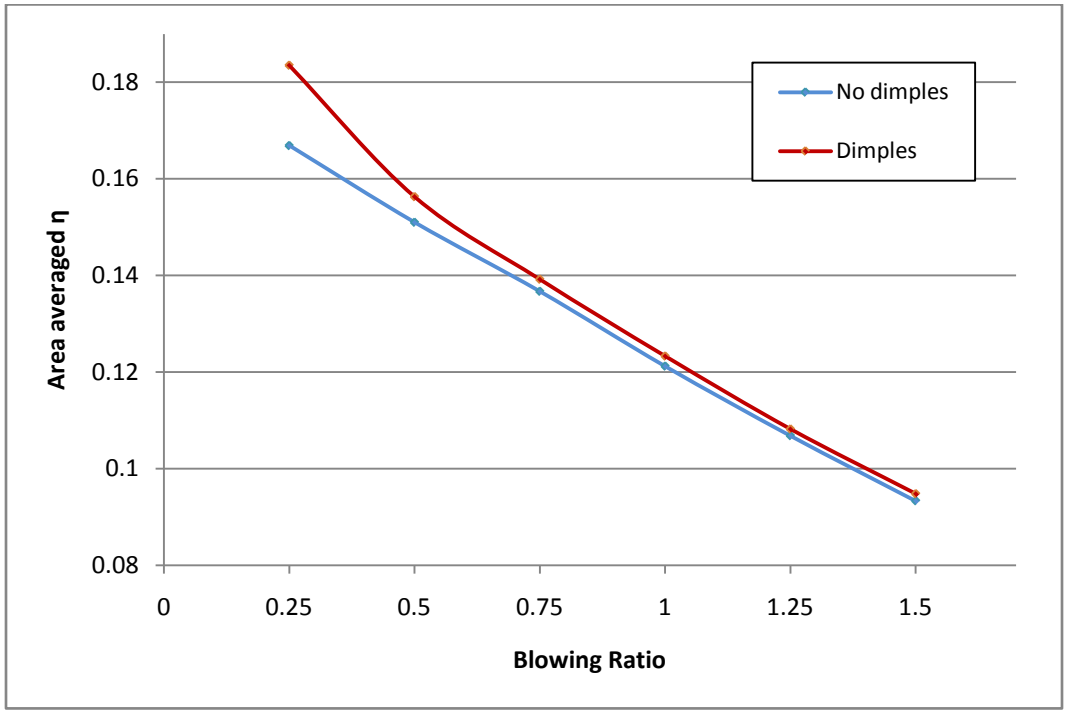

Fig 3.5 Area averaged η at Re = 60k and low Turbulence

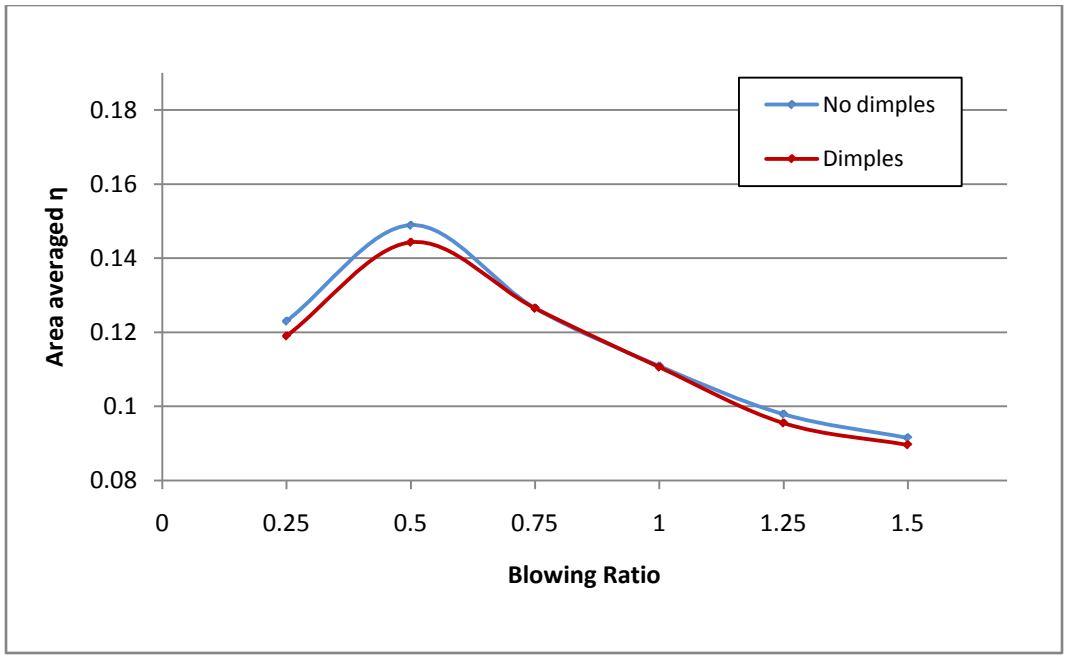

Fig 3.6 Area averaged η at Re = 30k and high Turbulence

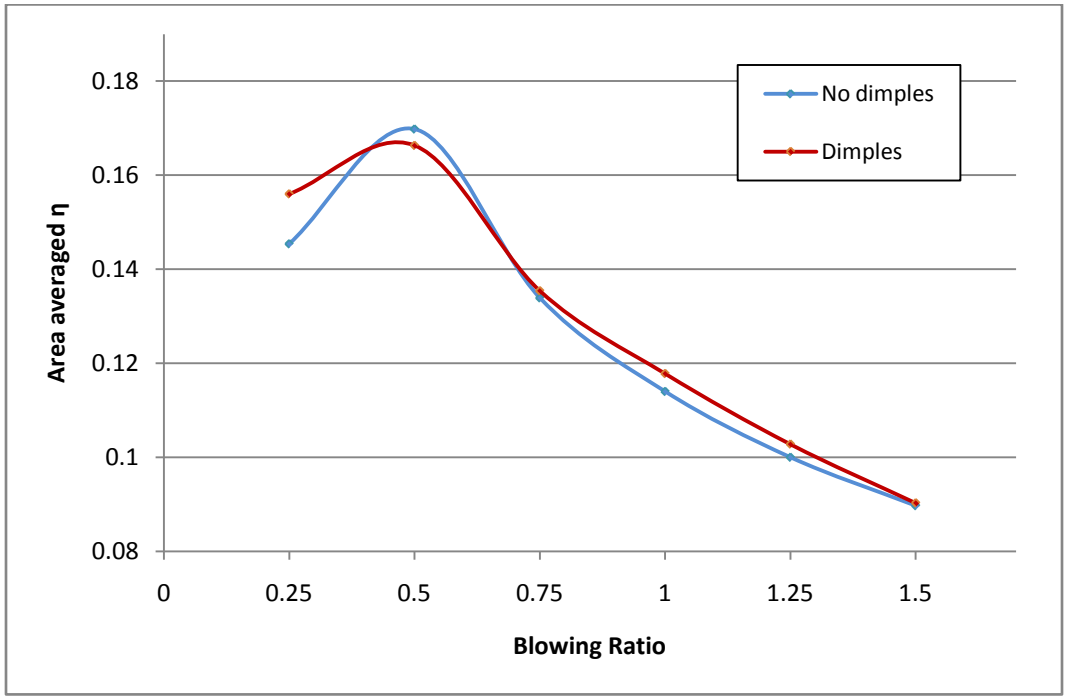

Fig 3.7 Area averaged η at Re = 30k and low Turbulence

3.1.1 The Effect of Blowing Ratio on η

An obvious result arising from Figures 3.4-3.7 is that a higher adiabatic effectiveness is achieved as the blowing ratio is reduced. Three of the four freestream conditions shows a peak at a blowing ratio of M = 0.5, with the lone exception occurring at Re = 60k and low turbulence producing a maximum at M = 0.25. Because only intervals of M = 0.25 were observed, it is possible that the real maximum could exist at a blowing ratio around the observed maximum.

The fact that the higher blowing ratios generate lower values for the adiabatic effectiveness seems sensible. At the higher blowing ratios, a larger component of velocity normal to the surface exists causing lift off of the coolant. When lift off occurs, the coolant is no longer close to the surface and the blade's temperature increases, yielding lower values for η.

3.1.2 The Effect of Reynolds number on η

At the higher Reynolds number (60,000), the cases with dimples performed consistently better, although less than the uncertainty present. For the three lower blowing ratios the average difference in $\bar{\bar{\eta}}$ was 0.007 indicating that on average each pixel was approximately 0.007 higher for the case with dimples. The rows labeled 'Difference' in Table 2 can be used to determine the average change in η for each pixel. The cases for the three higher blowing ratios showed much smaller differences. It can be concluded that the dimples' effect on η at these higher blowing ratios is negligible, most likely due to the dimples' inability to entrain the coolant that is no longer in contact with the surface.

The cases with Re = 30k yielded much more vague results. At first glance it would appear that η is at its maximum at M = 0.5; however, for this particular Reynolds number the case without dimples outperforms the case with dimples by $\Delta\,\bar{\bar{\eta}}$ of approximately 0.004. However, the differences are less than the estimated uncertainty thus any perceived advantage would be negligible.

As the Reynolds number is decreased from 60,000 to 30,000, the adiabatic effectiveness slightly decreases at the four higher blowing ratios (M = 0.75, M = 1.0, M = 1.25, and M = 1.5). This may result

from the dimples generating weaker vortices at a lower Reynolds number. The ability to entrain the coolant film may be inhibited yielding a slightly smaller adiabatic effectiveness. At the lowest blowing ratio, M = 0.25, the adiabatic effectiveness decreases more significantly than the previously mentioned cases. Conversely, a blowing ratio of M = 0.5 produces an increase in the adiabatic effectiveness at the lower Reynolds number.

3.1.3 The Effect of Turbulence on η

Elevating the level of turbulence, at the four higher blowing ratios, results in a slight decrease in the adiabatic effectiveness. At the lowest blowing ratios of M = 0.25 and M = 0.5, the increase in turbulence causes a significant decrease in $\Delta \bar{\bar{\eta}}$ by approximately 0.02 on average. These lower blowing ratios have the least amount of lift off due to less momentum normal to the surface. The increased turbulence causes increased mixing with the warmer freestream, increasing the temperature of the film yielding lower values for adiabatic effectiveness. At the higher blowing ratios the change is smaller because less coolant film is in contact with the surface; therefore less mixing with the freestream occurs due to lift off.

3.2 DIMPLES' EFFECT ON FRÖSSLING NUMBER

The heat transfer coefficient is presented as the dimensionless Frössling number described by Equation 1.10. An increase in *Fr* indicates an increase in *h*. The Frössling number contour plots are located in Appendix C, while the spanwise averaged Frössling number plots are located in Appendix D.

An example of a contour plot used in determining both the spanwise averaged and area averaged Frössling number can be seen in Figure 3.8 below. The elevated values immediately downstream of the coolant hole are caused by the mixing between the freestream and the coolant emitted from the hole. On a smooth surface, the heat transfer coefficient is only a function of its x/d location. For this case, the contour lines would be vertical lines. Evidence of the vertical contours can be seen toward the bottom of the image where they exist below y/d = -4.

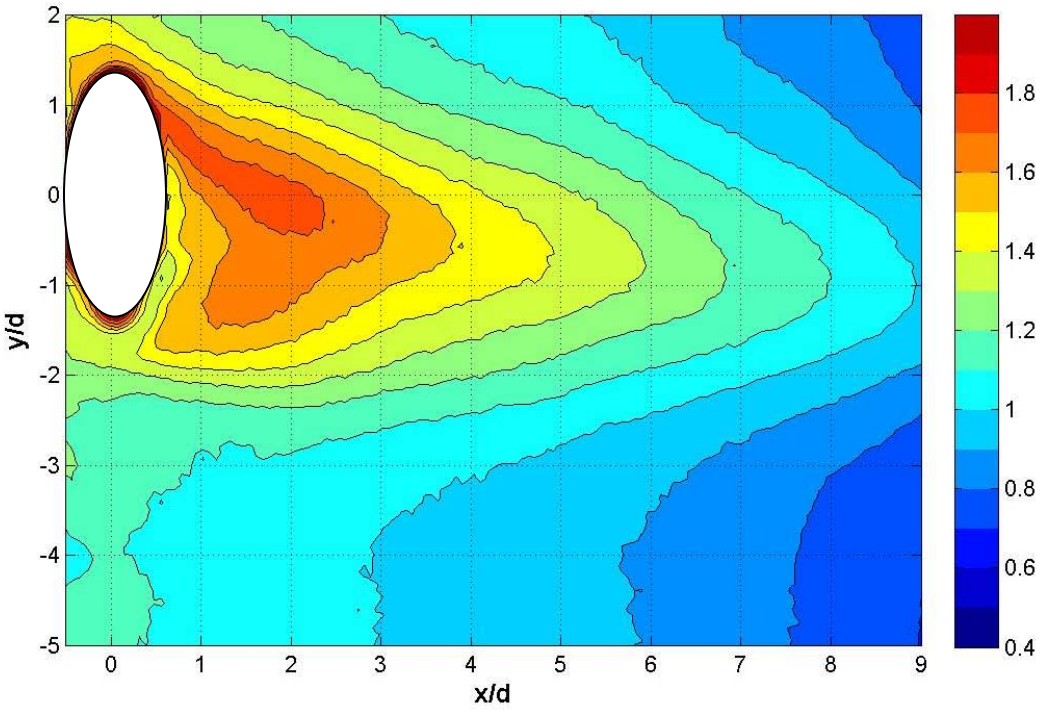

Fig 3.8 Contour of *Fr* with dimples at Re = 60k and high turbulence for M = 1.0

Once again, a MATLAB script was used to calculate the spanwise averaged values of *Fr*. An example of the spanwise averaged *Fr* plot calculated from Figure 3.8 can be seen in Figure 3.9. As evidenced in the contour plot, the value of *h* decreases moving from left to right. The spanwise averaged *Fr* plot in Figure 3.9 also confirms this result. Of particular interest in Figure 3.9 is that the value of *Fr* is approximately equal for both the case with and without dimples. This result is counterintuitive, as the heat transfer coefficient was expected to increase as a result of the dimples. The cause will be explained in the following pages.

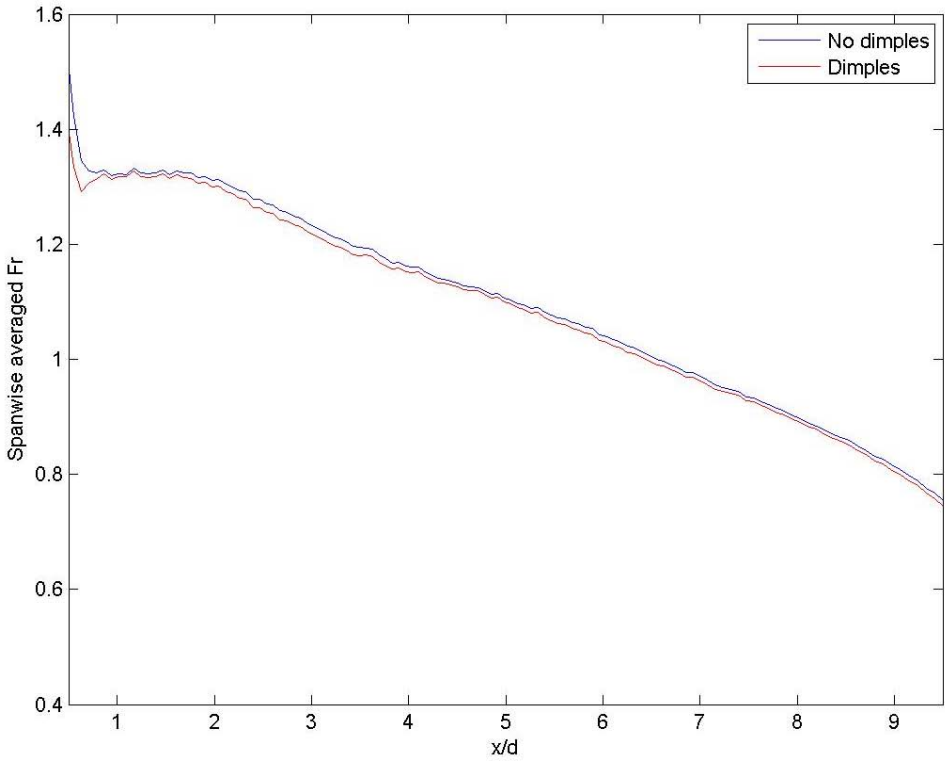

Fig 3.9 Spanwise averaged *Fr* at Re = 60k and high turbulence for M = 1.0

The area averaged Fr values can be found in Table 3, but are also provided in Figures 3.10-3.13. These figures prove that the Frössling number is unaffected by the presence of dimples downstream of the coolant hole. Generally, the data with dimples is equivalent to the data without dimples. The sole exception being M = 0.75 at a Re = 30k and low turbulence seen in Figure 3.13. This result is in, all probability, due to human error. The blowing ratio may have inadvertently been read incorrectly. In any case, given the remainder of the evidence, it can be concluded that the heat transfer coefficient is not dependent on the presence of dimples at locations downstream of the coolant hole.

Table 3 Area averaged Frössling number

	Case	M = 0.25	M = 0.5	M = 0.75	M = 1.0	M = 1.25	M = 1.5
Re = 60k, high Tu	No dimples	0.97	1.02	1.06	1.11	1.14	1.16
	Dimples	0.97	1.02	1.06	1.10	1.13	1.16
	Difference	0.00	0.00	0.00	0.01	0.01	0.00
Re = 30k, high Tu	No dimples	0.88	0.93	0.96	1.00	1.04	1.06
	Dimples	0.88	0.92	0.96	1.00	1.03	1.07
	Difference	0.00	0.01	0.00	0.00	0.01	-0.01
Re = 30k, low Tu	No dimples	0.75	0.83	0.87	0.91	0.94	0.97
	Dimples	0.75	0.82	0.84	0.90	0.93	0.96
	Difference	0.00	0.01	0.03	0.01	0.01	0.01
Re = 60k, low Tu	No dimples	0.79	0.87	0.92	0.96	1.00	1.03
	Dimples	0.80	0.87	0.92	0.96	0.99	1.01
	Difference	-0.01	0.00	0.00	0.00	0.01	0.02

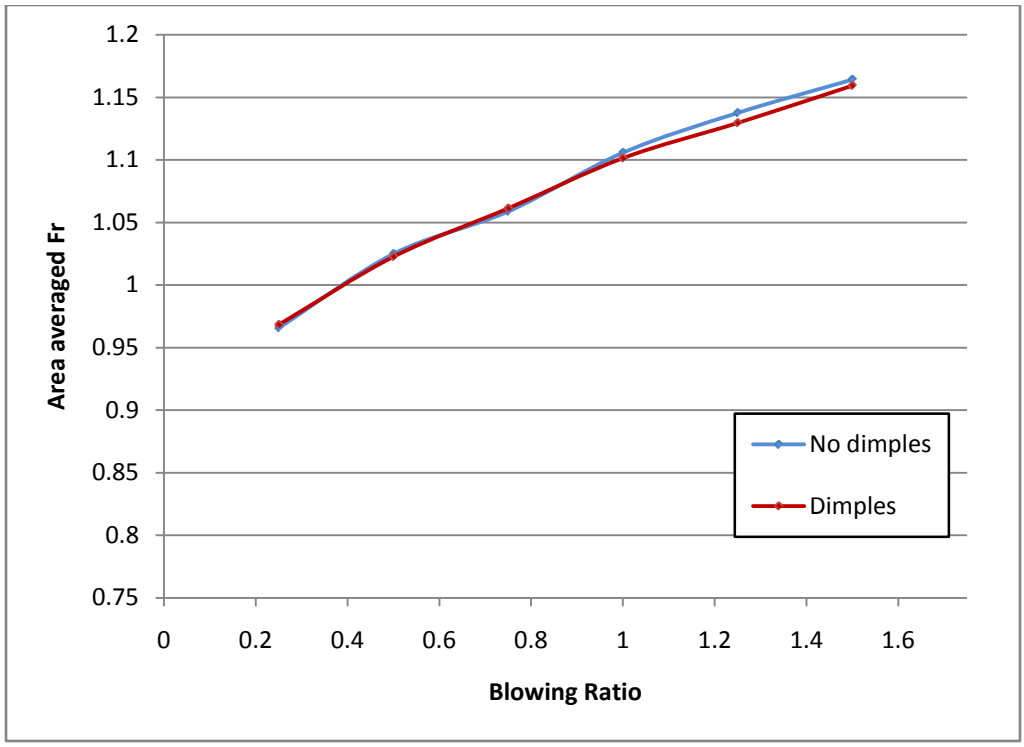

Fig 3.10 Area averaged *Fr* at Re = 60k and high Turbulence

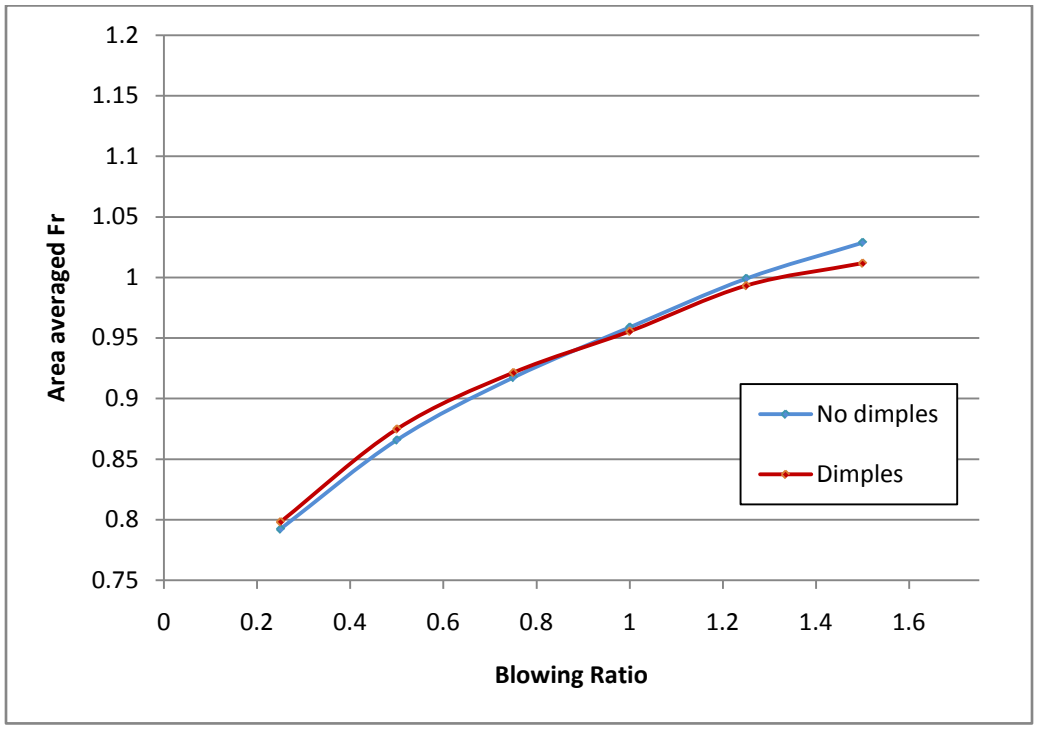

Fig 3.11 Area averaged *Fr* at Re = 60k and low Turbulence

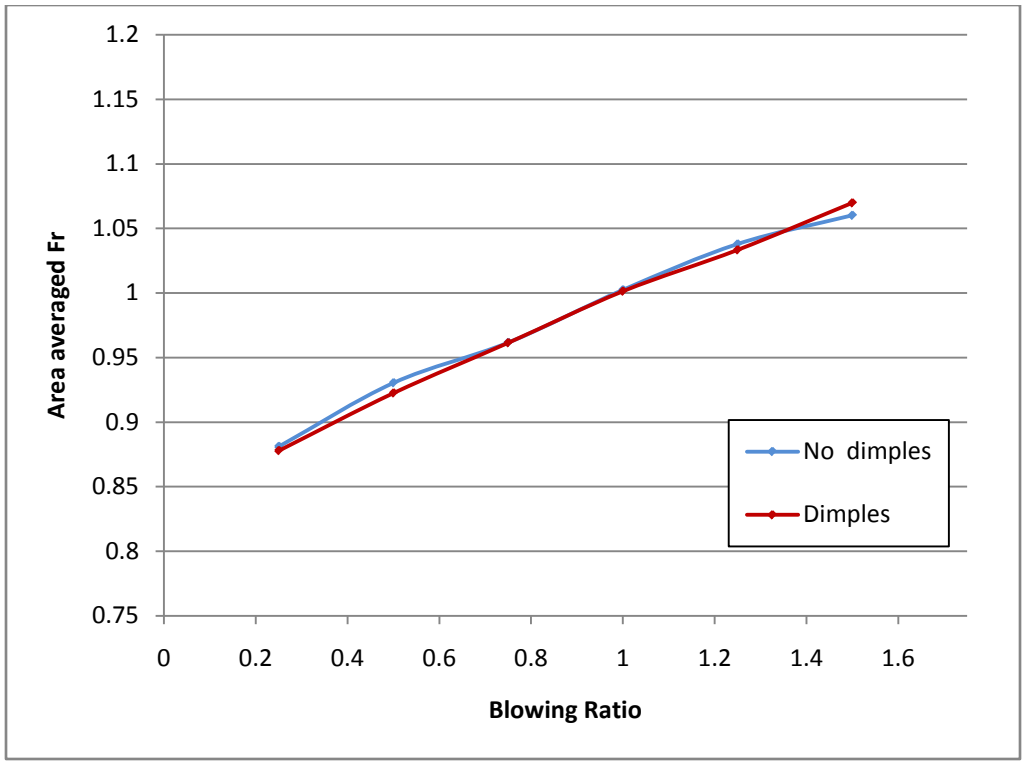

Fig 3.12 Area averaged *Fr* at Re = 30k and high Turbulence

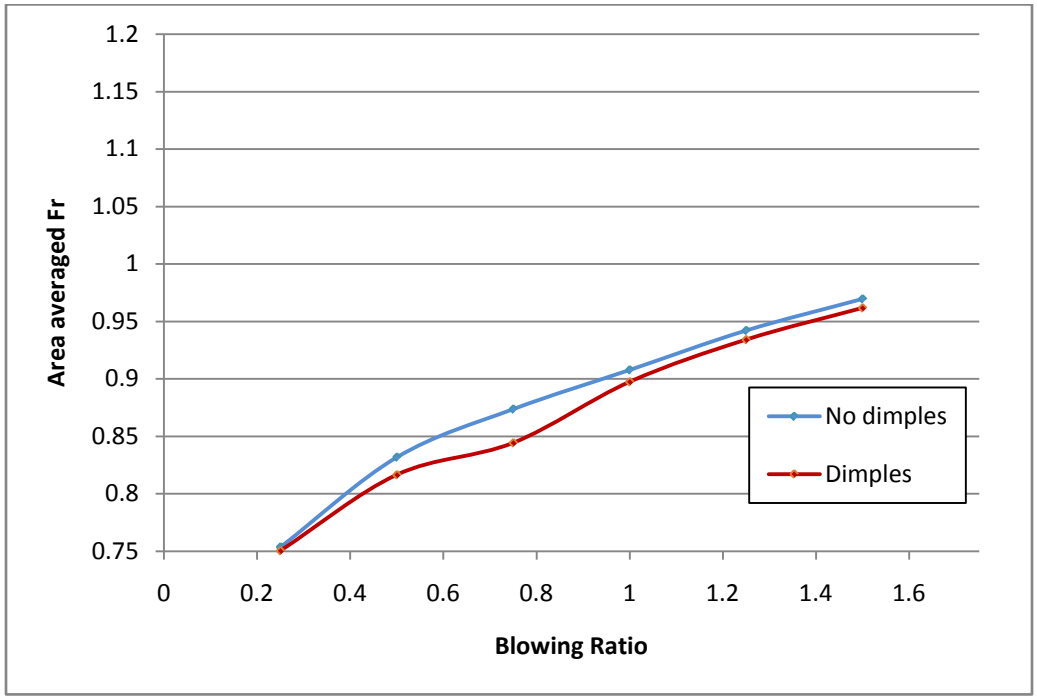

Fig 3.13 Area averaged *Fr* at Re = 30k and lowTurbulence

3.2.1 The Effect of Blowing Ratio on *Fr*

As the blowing ratio increases, the Frössling number, and therefore *h*, increases. As mentioned previously, more coolant is emitted from the coolant hole, more mixing occurs with the freestream fluid. This elevated mixing causes an increase in *h*.

3.2.2 The Effect of Reynolds number on *Fr*

Decreasing the Reynolds number causes the area averaged Frössling number, $\overline{\overline{Fr}}$, to decrease. For the high turbulence cases, the decrease is approximately 0.09 for all blowing ratios, whereas the lower turbulence cases yielded an average decrease of 0.05 across all blowing ratios. The value of the heat transfer coefficient is dependent on the velocity of the freestream, surface roughness, surface location, and fluid properties. Because the velocity of the freestream fluid decreases at Re = 30k, it can be concluded that the lower velocity causes a reduction in *h*.

3.2.3 The Effect of Turbulence on *Fr*

An elevated level of turbulence causes a significant increase in the Frössling number. The energy of the fluid increases as turbulence increases; generating amplified mixing with the freestream. At a Reynolds number of 30,000, the increase in turbulence causes an average increase in $\Delta\overline{\overline{Fr}}$ of 0.22. An average increase of $\Delta\overline{\overline{Fr}}$ = 0.32 was observed at the higher Reynolds number.

3.2.4 Dimples' Effect on the Heat Transfer Coefficient

To investigate how dimples affect, if at all, the heat transfer coefficient, contour plots were created with a larger view to accommodate the dimples. If the dimples did, in fact, increase the heat transfer coefficient, a higher value of the Frössling number would be present downstream of the dimple. Two contour plots were generated without film cooling to prevent any effects of the coolant plume from interfering with data downstream of the dimples. Figure 3.14 shows an enlarged view of the surface for the case where the dimples were covered with Kapton tape. Keep in mind, however, that data inside the dimples is unreliable because negligible heat flux was present at the dimple locations as the heat

flux plate had holes to accommodate the dimples. The Frössling number contour plot where the dimples were uncovered can be seen in Figure 3.15.

Evidence suggests that the dimples increase the heat transfer coefficient downstream of the dimples. Figure 3.15 has elevated values of *Fr* approximately 3 dimple diameters downstream. These results are not revealed in the spanwise averaged *Fr* plots because the increase in *h* can only be seen in a localized region downstream of the dimples, but upstream of x/d = 0.5. For this reason the heat transfer coefficient appears to be identical for both cases with and without dimples.

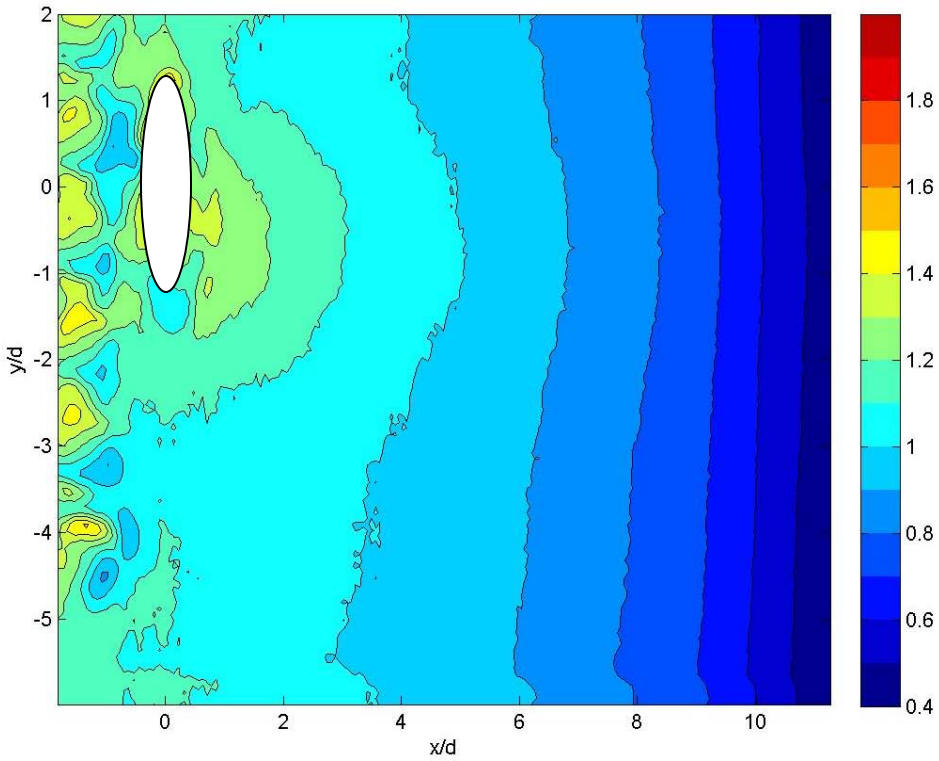

Fig 3.14 Contour of Fr without dimples at Re = 60k and high turbulence for no film cooling (M = 0)

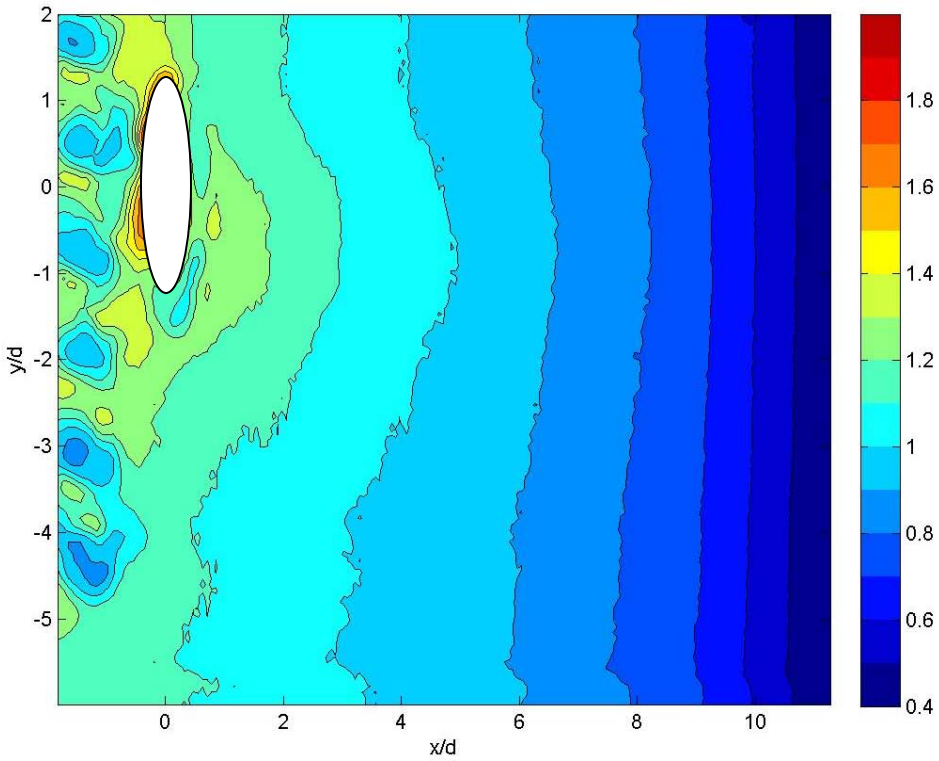

Fig 3.15 Contour of Fr with dimples at Re = 60k and high turbulence for no film cooling (M = 0)

3.3 DIMPLES' EFFECT ON NET HEAT FLUX REDUCTION

To adequately compare the net heat flux cases with and without dimples, Equations 2.3 and 2.4, repeated below, were applied. Both equations make use of a reference condition, defined by the case without film cooling or dimples. If the two were compared to this reference condition, the two resulting net heat flux reductions could be compared to one another. The higher value of the two would denote a case where the heat load is less than the other. In this case η_n is equal to zero because the adiabatic effectiveness is defined to be zero where no film cooling is present. The two resulting net heat flux reductions are shown in Equations 2.3 and 2.4.

$$\Delta q_{rd} = 1 - \frac{q_d}{q_o} = 1 - \frac{h_d\left(T_{aw_d} - T_w\right)}{h_o\left(T_{aw_o} - T_w\right)} = 1 - \frac{h_d(\eta_d - \phi)}{h_o(-\phi)} = 1 - \frac{h_d}{h_o}\left(1 - \frac{\eta_d}{\phi}\right) \quad 2.3$$

$$\Delta q_{rn} = 1 - \frac{q_n}{q_o} = 1 - \frac{h_n\left(T_{aw_n} - T_w\right)}{h_o\left(T_{aw_o} - T_w\right)} = 1 - \frac{h_n(\eta_n - \phi)}{h_o(-\phi)} = 1 - \frac{h_n}{h_o}\left(1 - \frac{\eta_n}{\phi}\right) \quad 2.4$$

These two equations are used to determine the values for the net heat flux reduction at each pixel location. The values were then spanwise averaged and area averaged using a MATLAB script program. The area averaged values are provided in Table 4, as well as, in Figures 3.16-3.19.

Table 4 Area averaged net heat flux reduction

	Case	M = 0.25	M = 0.5	M = 0.75	M = 1.0	M = 1.25	M = 1.5
Re = 60k, high Tu	No dimples	0.2200	0.20	0.17	0.12	0.08	0.03
	Dimples	0.23	0.21	0.17	0.13	0.08	0.04
	Difference	0.01	0.01	0.00	0.01	0.00	0.01
Re = 30k, high Tu	No dimples	0.21	0.22	0.16	0.10	0.05	0.02
	Dimples	0.20	0.22	0.16	0.10	0.04	0.00
	Difference	-0.01	0.00	0.00	0.00	-0.01	-0.02
Re = 30k, low Tu	No dimples	0.26	0.24	0.14	0.07	0.01	-0.04
	Dimples	0.25	0.23	0.15	0.06	-0.01	-0.07
	Difference	-0.01	-0.01	0.01	-0.01	-0.02	-0.03
Re = 60k, low Tu	No dimples	0.27	0.19	0.13	0.06	-0.01	-0.07
	Dimples	0.30	0.20	0.14	0.07	0.01	-0.04
	Difference	0.03	0.01	0.01	0.01	0.02	0.03

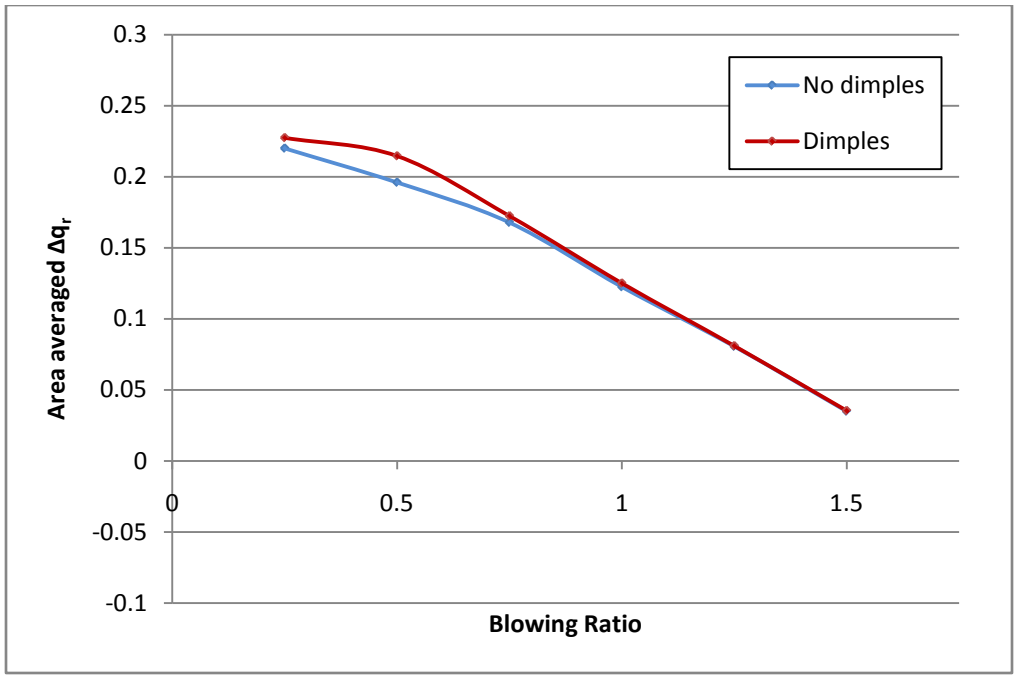

Fig 3.16 Area averaged Δq_r at Re = 60k and high Turbulence

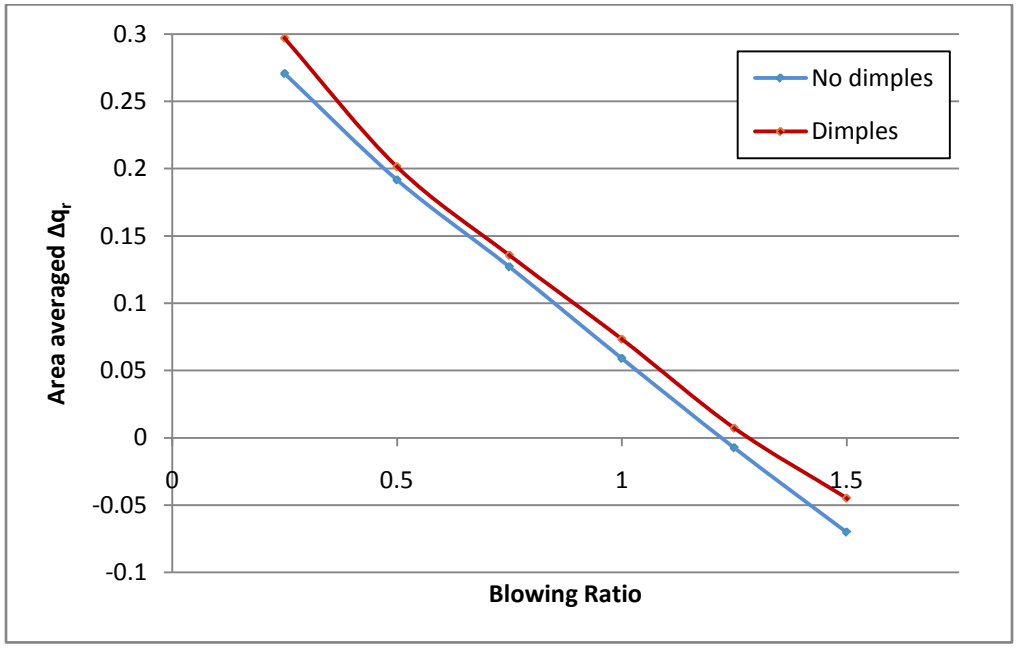

Fig 3.17 Area averaged Δq_r at Re = 60k and low Turbulence

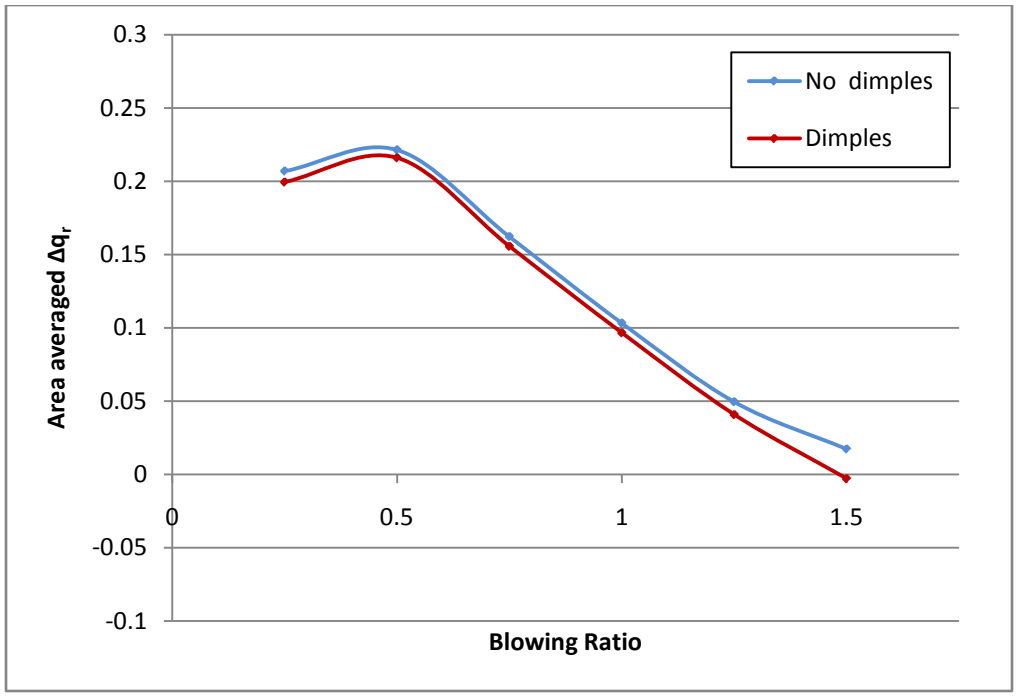

Fig 3.18 Area averaged Δq_r at Re = 30k and high Turbulence

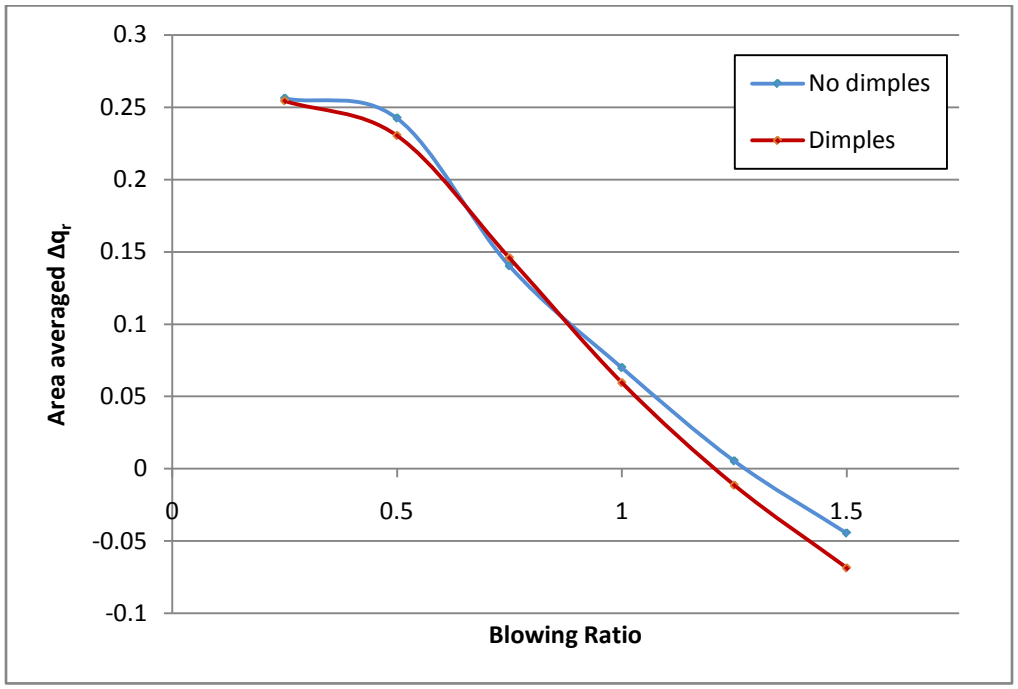

Fig 3.19 Area averaged Δq_r at Re = 30k and low Turbulence

3.3.1 The Effect of Blowing Ratio on Δq_r

The trends of the net heat flux reduction followed the adiabatic effectiveness trends very closely because the heat transfer coefficient changed very little. Similar to the $\bar{\bar{\eta}}$ results, $\overline{\overline{\Delta q_r}}$ decreased as the blowing ratio increased. As the blowing ratio is increased the lift off phenomenon becomes more prominent resulting in a trend that approaches zero. A net heat flux reduction of zero indicates a case where the combination of the film cooling and increased heat transfer coefficient performing equally to the case without film cooling or dimples. The negative values for the cases at low turbulence and high blowing ratios of M = 1.25 and M = 1.5 in Figures 3.17 and 3.19, indicate that the presence of film cooling is actually increasing the heat load compared to the case without film cooling or dimples.

3.3.2 The Effect of Reynolds number on Δq_r

For the low turbulence case, evidence suggests that the cases with and without dimples switch roles at blowing ratios of M = 0.75 and higher. At the lower Reynolds number, the non-dimpled case performs slightly better, while at Re = 60k, the dimpled case performs better. This is analogous to the adiabatic effectiveness cases where the Re = 60k cases performed better with dimples.

Decreasing the Reynolds number yields a smaller net heat flux reduction when comparing the high turbulence cases. This is a result of the adiabatic effectiveness having a greater value for the higher Reynolds number case.

3.3.3 The Effect of Turbulence on Δq_r

Generally, as turbulence increases, the adiabatic effectiveness increases and results in a greater net heat flux reduction. This is especially true for the higher blowing ratios. At a blowing ratio of M = 0.5, the results are far less dramatic. The average difference is less than $\overline{\overline{\Delta q_r}}$ =0.02. Conversely, at a blowing ratio of M = 0.25, the lower turbulence case outperforms the higher turbulence case at both Reynolds numbers by an average of $\overline{\overline{\Delta q_r}}$ =0.03. This is confirmed by the adiabatic effectiveness being greater for low turbulence for M = 0.25.

CHAPTER 4. CONCLUSIONS AND RECOMMENDATIONS

The information gathered from this experiment has provided interesting results regarding the use of dimples in enhancing film cooling performance. Although the parameter space was relatively limited, it has provided a foundation for future researchers to build on. Many more parameters could be studied to determine their influence on film cooling performance.

4.1 CONCLUSIONS

The blowing ratio was observed to be the most influential parameter in determining the effectiveness for a particular freestream condition. As the blowing ratio is increased, greater momentum normal to the surface exists which is more likely to cause lift off of the coolant fluid. As the coolant film loses contact with the surface, the area downstream is no longer protected by the coolant fluid causing a reduction in the observed adiabatic effectiveness.

The Reynolds number also demonstrated an influence on the adiabatic effectiveness. Doubling the Reynolds number produced slightly improved η, and is believed to be caused by slightly stronger vortices generated by the dimples.

The turbulence level seemed to affect only the two lower blowing ratios, as the higher blowing ratios had less cooling film to entrain due to lift off. Increasing the turbulence at blowing ratios of M = 0.25 and M = 0.5 significantly decreased the adiabatic effectiveness caused by increased mixing with the freestream.

The Frössling number, thus *h*, exhibited negligible change with or without dimples. Although the dimpled case showed elevated heat transfer immediately downstream of the dimple, the effects were washed out prior to x/d = 0.5. The resulting spanwise averaged *Fr* plots showed negligible change with or without dimples. Each freestream condition possessed different values of *Fr*, but the cases with and without dimples at each condition showed little difference. Because the heat transfer coefficient

changed very little, the net heat flux reduction result was almost exclusively dependent on the adiabatic effectiveness.

Even though, at Re = 60k, the dimpled case's adiabatic effectiveness is greater than the non-dimpled case, the change is relatively small. The value of $\bar{\bar{\eta}}$ changes less than 0.005 at the four higher blowing ratios at every freestream condition tested. At the two lower blowing ratios, the difference is slightly more significant with typical values ranging from 0.005 to a maximum of 0.02 at Re = 60k and low turbulence for blowing ratio of M = 0.25.

The small increase in adiabatic effectiveness is responsible for increasing the net heat flux reduction at the higher Reynolds number. At the lower Reynolds number, where the adiabatic effectiveness is neither distinctly better nor worse, the net heat flux reduction is essentially identical for the cases with and without dimples.

It can be concluded that any perceived advantage of the dimples was generally less than the uncertainty of the measurement suggesting that the dimples' effect was negligible.

4.2 RECOMMENDATIONS FOR FUTURE RESEARCH

This scientific investigation was able to demonstrate that dimples placed upstream of a film cooling hole can increase the adiabatic effectiveness, and as a result the net heat flux reduction for particular freestream conditions.

Upstream dimples were chosen because previous experiments found them to be more effective; however, the model used had two film cooling holes.[24] This model was abandoned in this experiment because the blowing ratios exhibited by the two holes differed by a sizeable margin due to unforeseen aerodynamic effects within the frame of the model. A possibility that downstream dimples might be more effective exists and could be tested using methods described in Chapter 2 to ensure data comparison is accurate.

Other parameters involving the dimple geometry should be tested to determine their effect on the net heat flux reduction. The dimple diameter, height, height-to -diameter ratio, quantity, location upstream or downstream, and pitch could possibly affect the turbine blade's temperature distribution.

Flow visualization experiments and CFD may aid in ascertaining the flow field's behavior off the surface of the model and could reveal evidence to optimize the geometric configuration of dimples.

Appendix A. Adiabatic Effectiveness Contour Plots

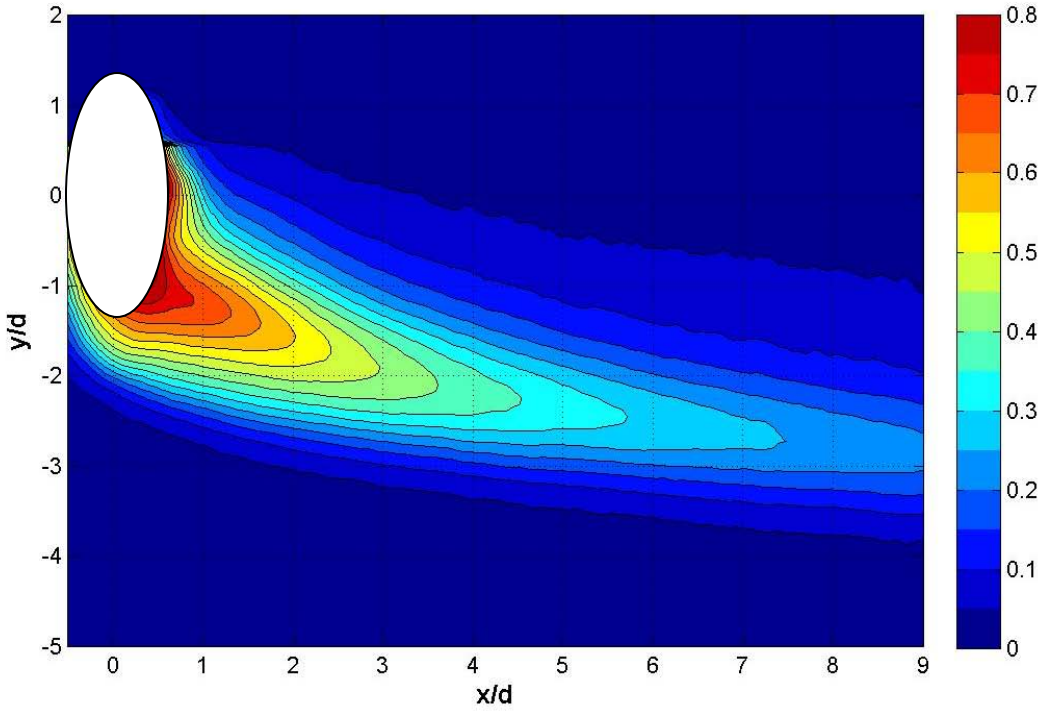

Fig A.1 Contour of η with dimples at Re = 60k and high turbulence for M = 1.5

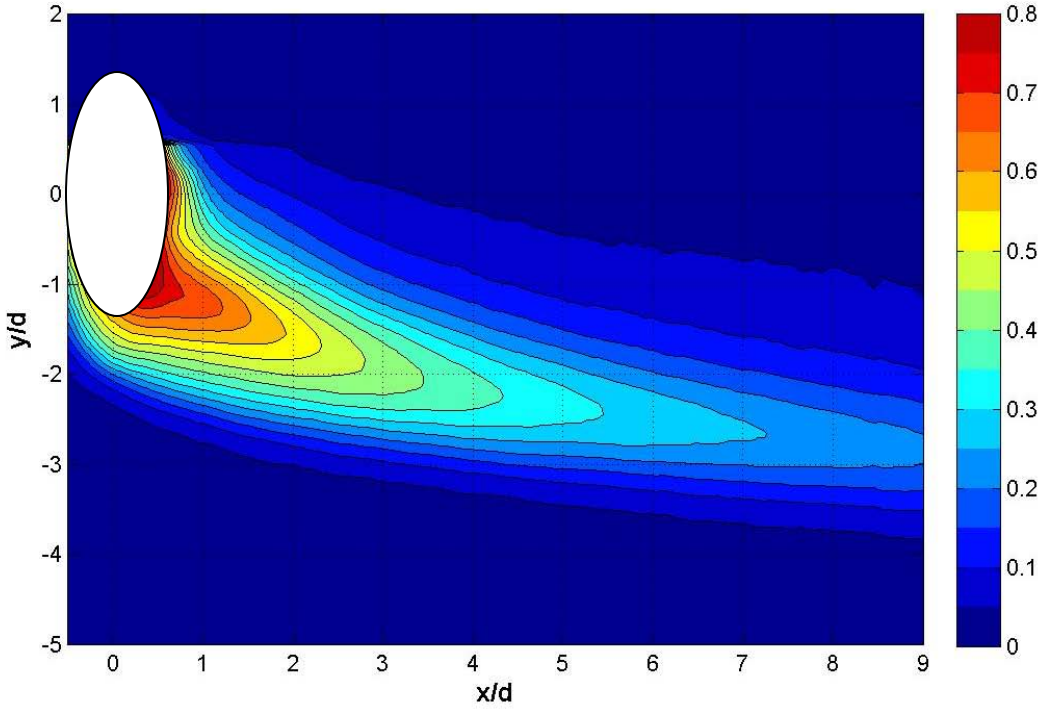

Fig A.2 Contour of η without dimples at Re = 60k and high turbulence for M = 1.5

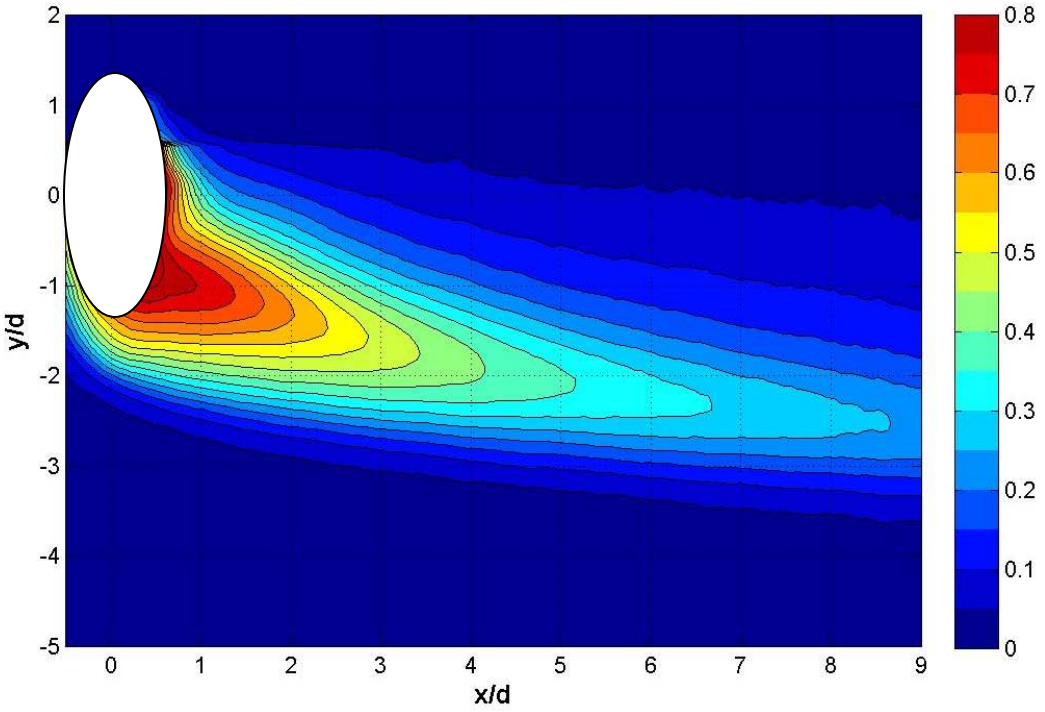

Fig A.3 Contour of η with dimples at Re = 60k and high turbulence for M = 1.25

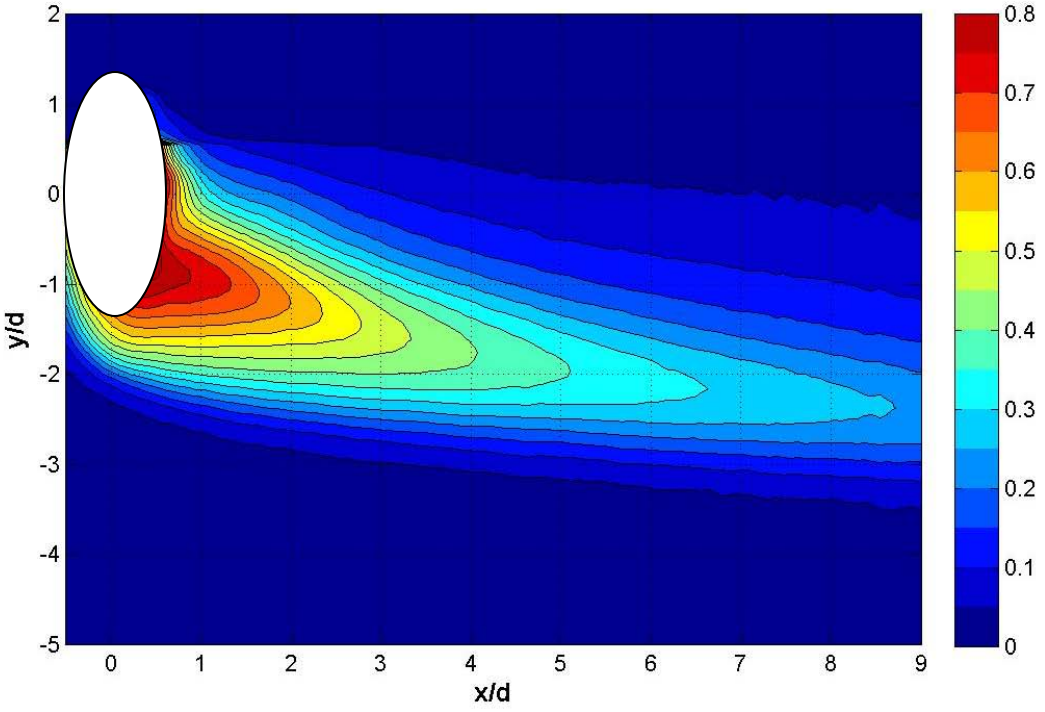

Fig A.4 Contour of η without dimples at Re = 60k and high turbulence for M = 1.25

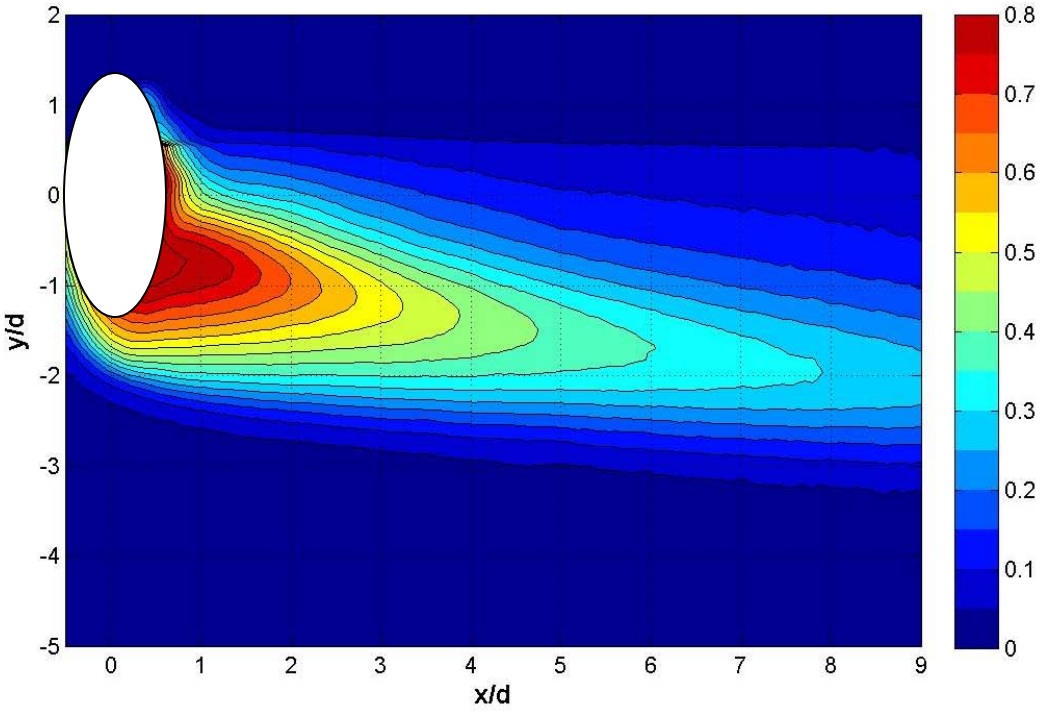

Fig A.5 Contour of η with dimples at Re = 60k and high turbulence for M = 1.0

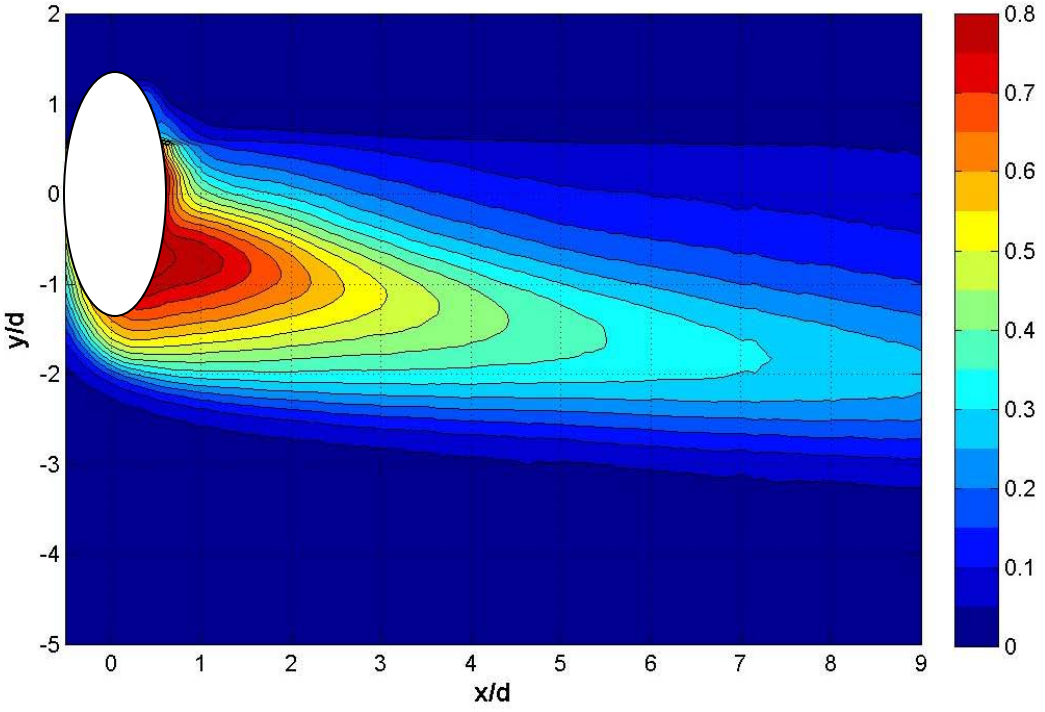

Fig A.6 Contour of η without dimples at Re = 60k and high turbulence for M = 1.0

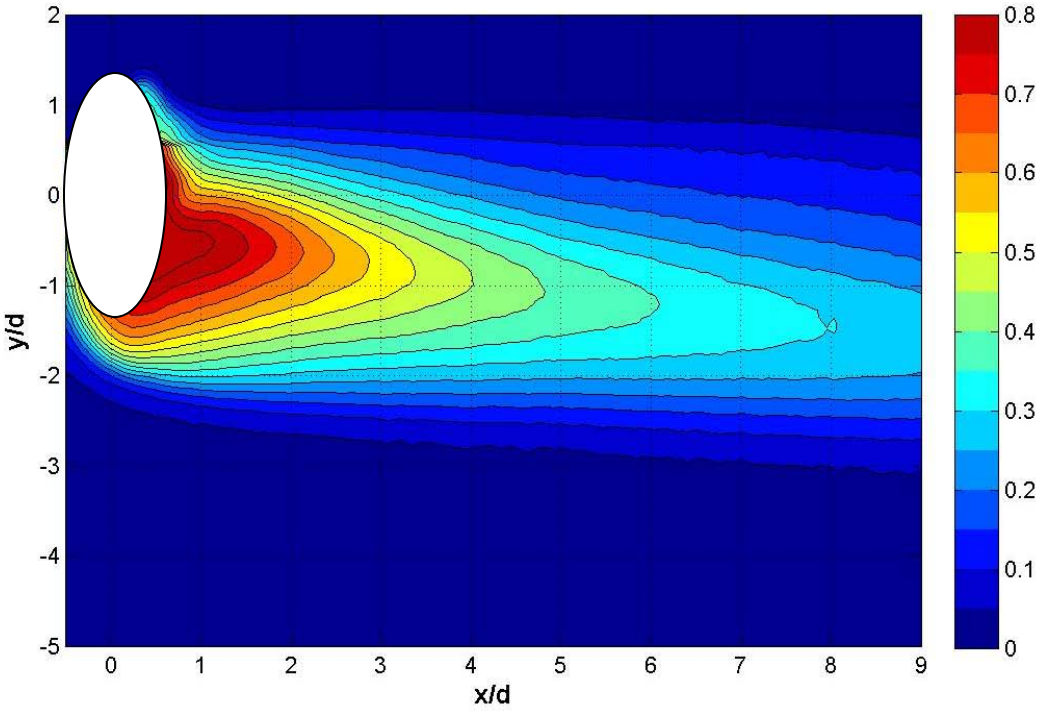

Fig A.7 Contour of η with dimples at Re = 60k and high turbulence for M = 0.75

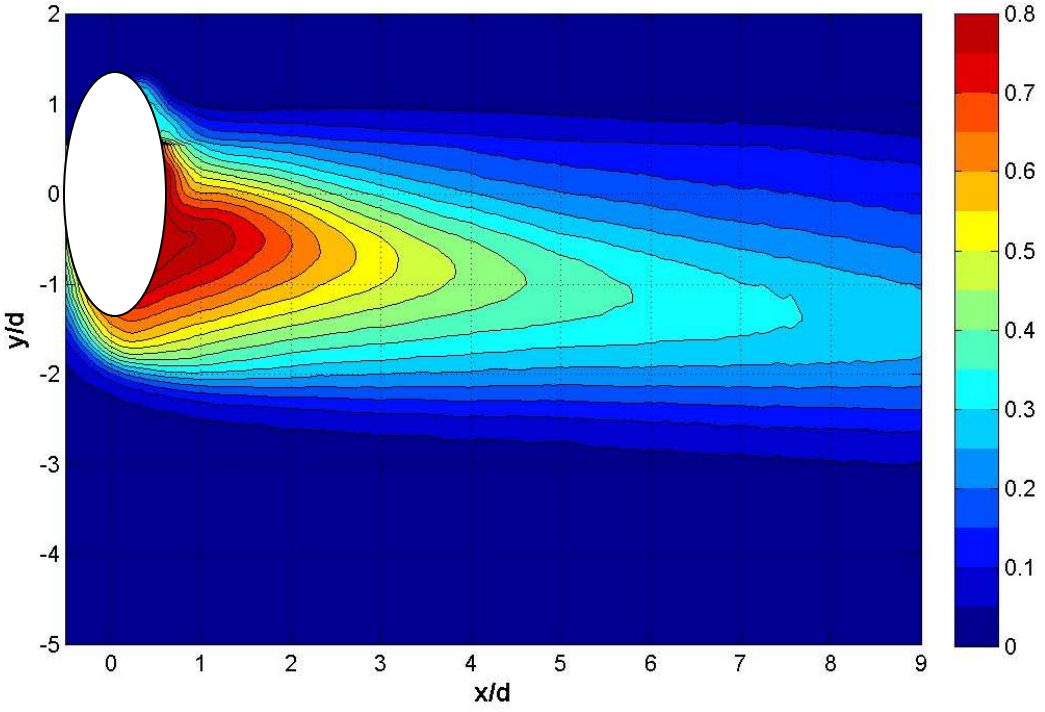

Fig A.8 Contour of η without dimples at Re = 60k and high turbulence for M = 0.75

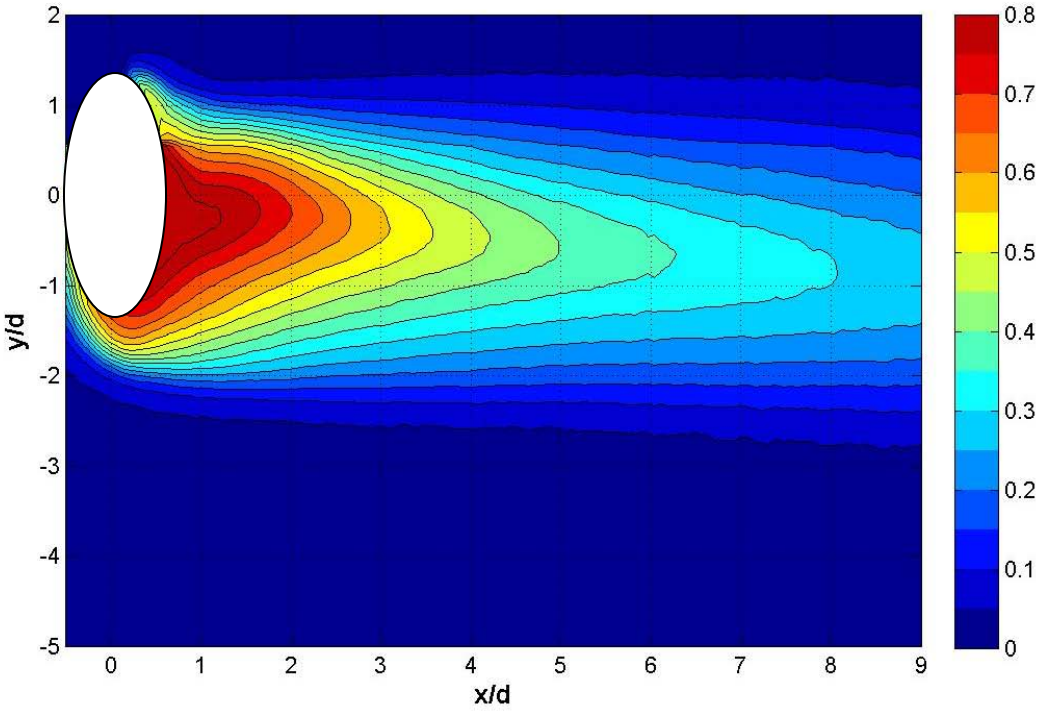

Fig A.9 Contour of η with dimples at Re = 60k and high turbulence for M = 0.5

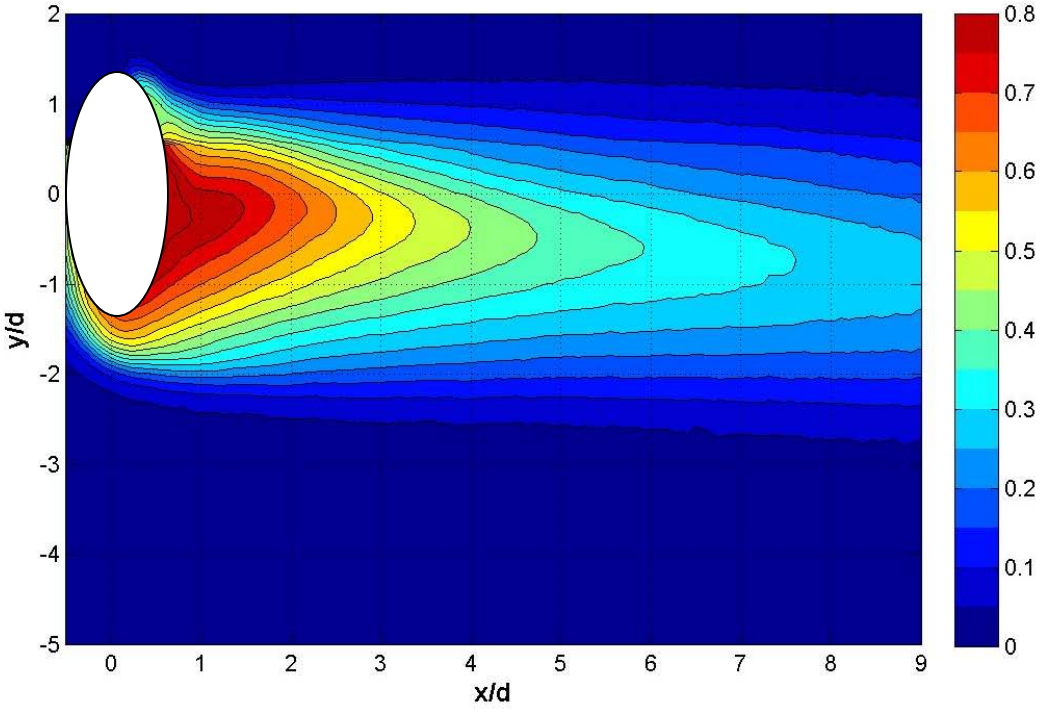

Fig A.10 Contour of η without dimples at Re = 60k and high turbulence for M = 0.5

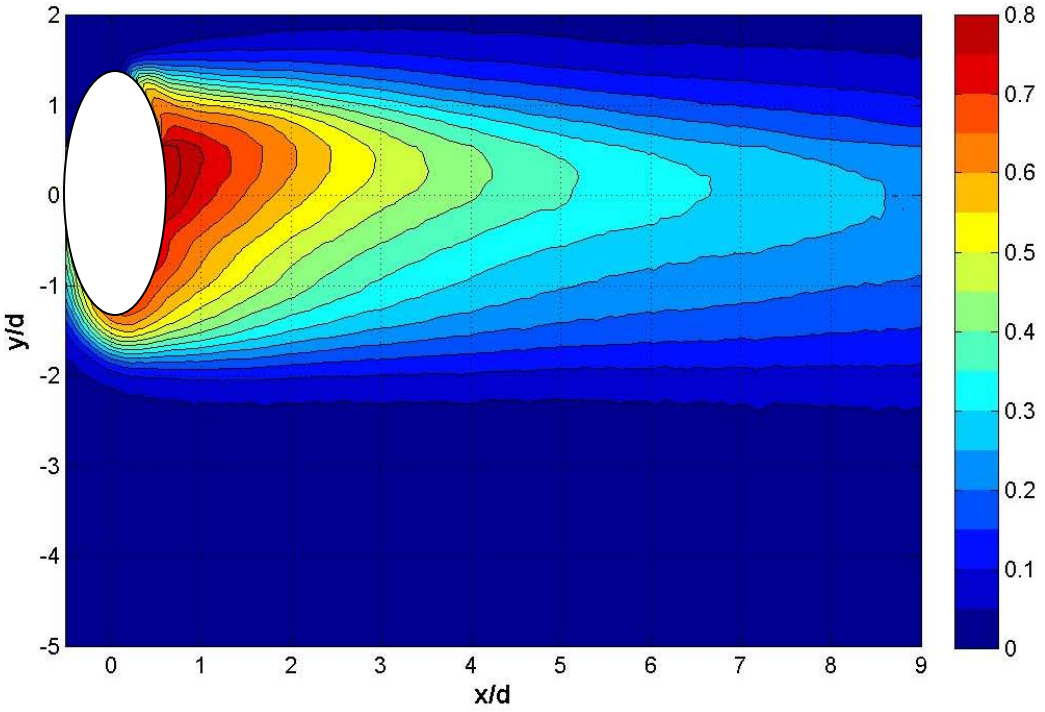

Fig A.11 Contour of η with dimples at Re = 60k and high turbulence for M = 0.25

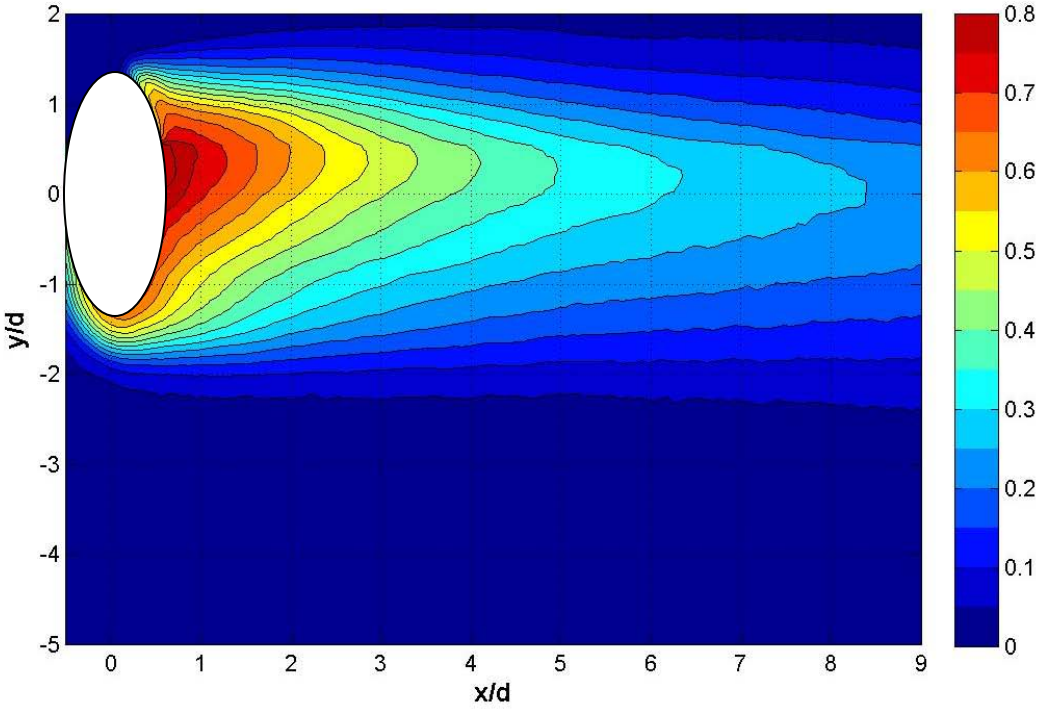

Fig A.12 Contour of η without dimples at Re = 60k and high turbulence for M = 0.25

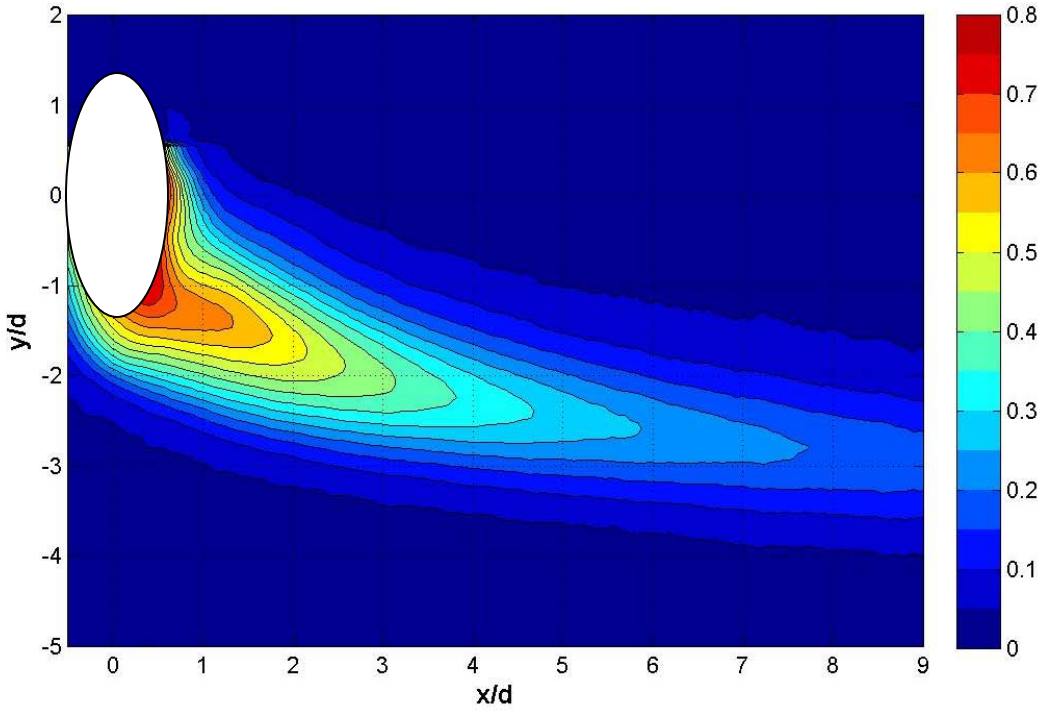

Fig A.13 Contour of η with dimples at Re = 30k and high turbulence for M = 1.5

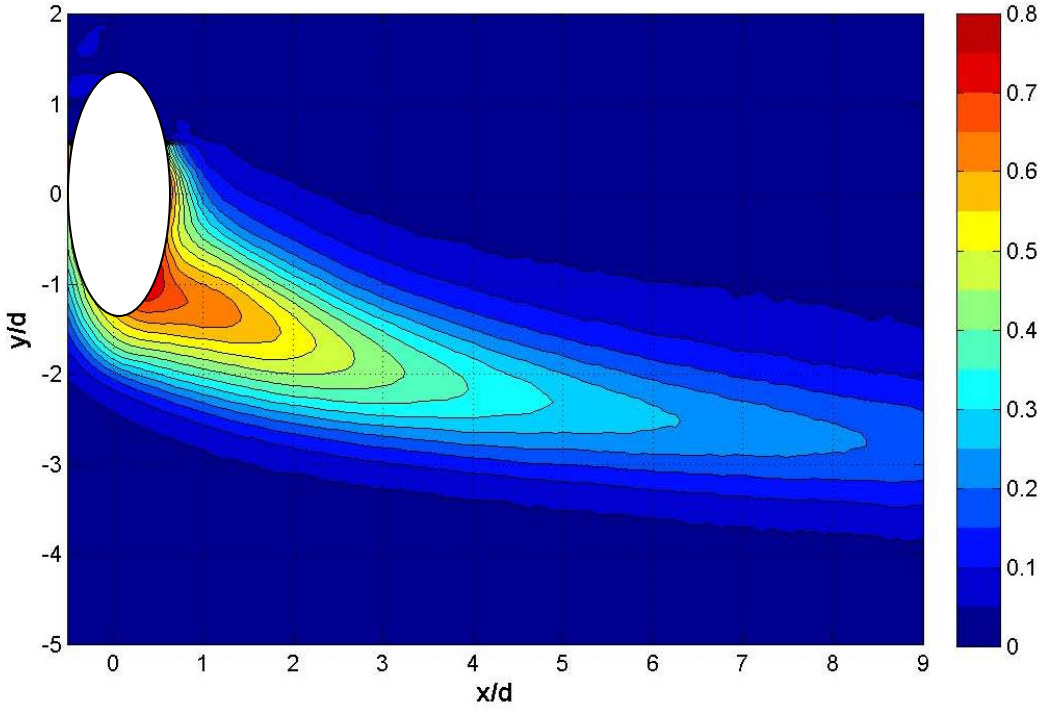

Fig A.14 Contour of η without dimples at Re = 30k and high turbulence for M = 1.5

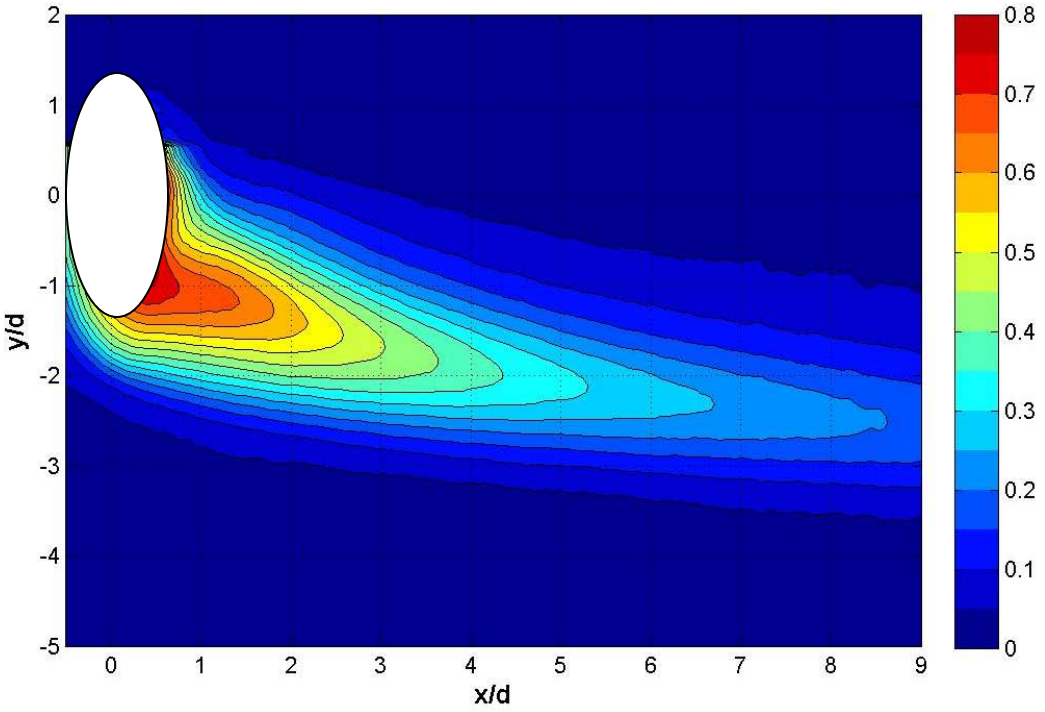

Fig A.15 Contour of η with dimples at Re = 30k and high turbulence for M = 1.25

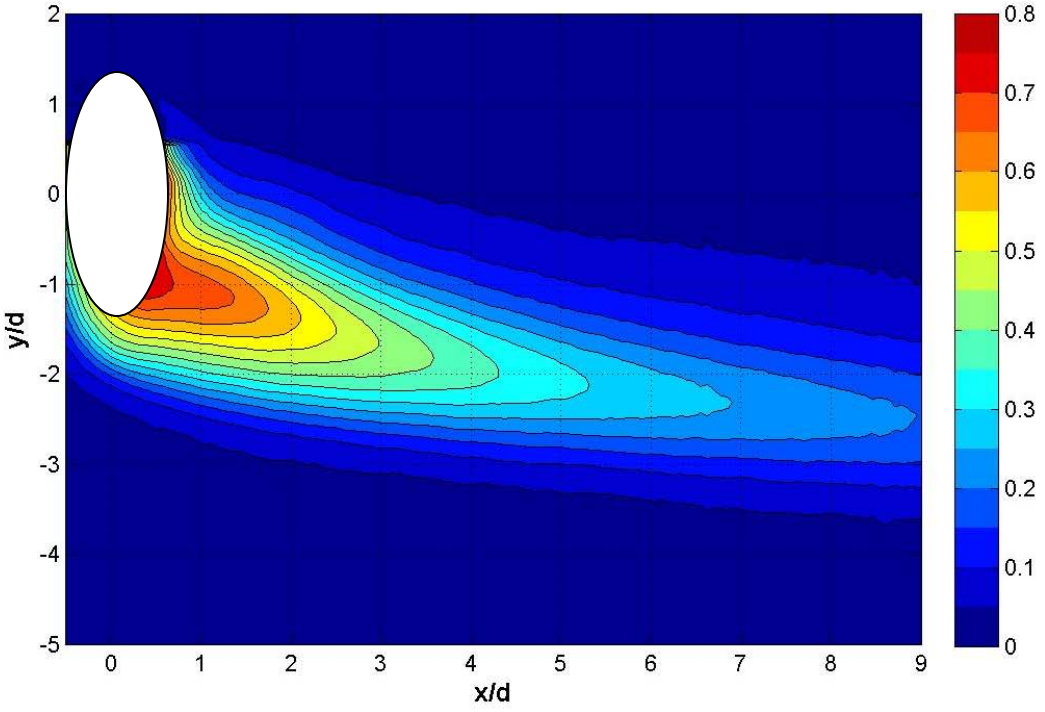

Fig A.16 Contour of η without dimples at Re = 30k and high turbulence for M = 1.25

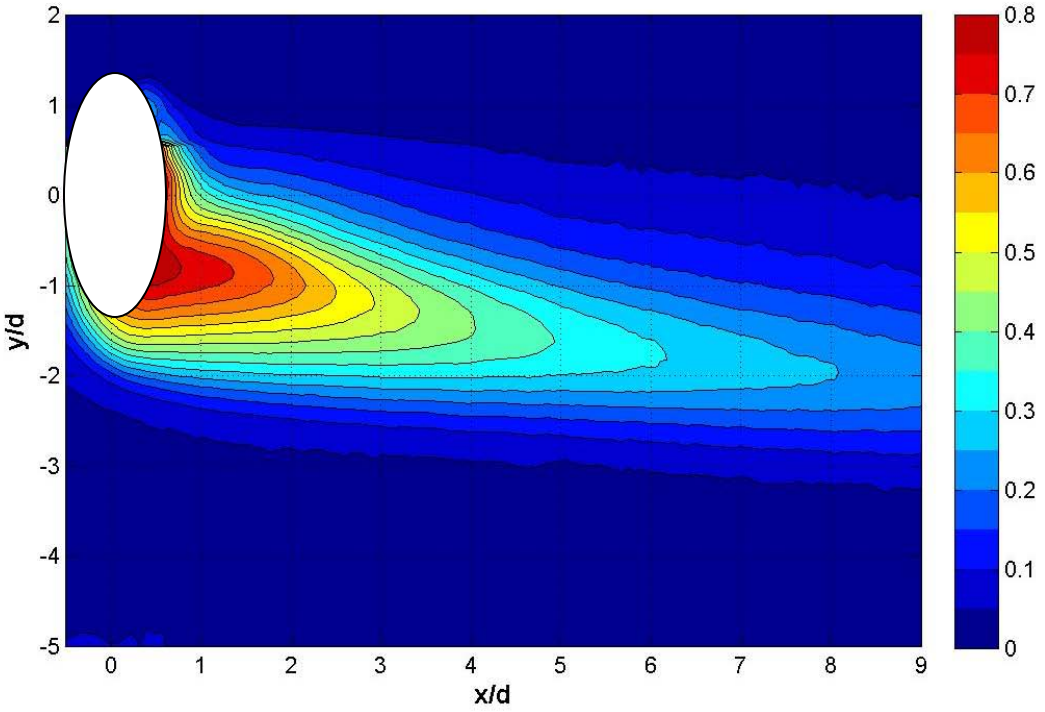

Fig A.17 Contour of η with dimples at Re = 30k and high turbulence for M = 1.0

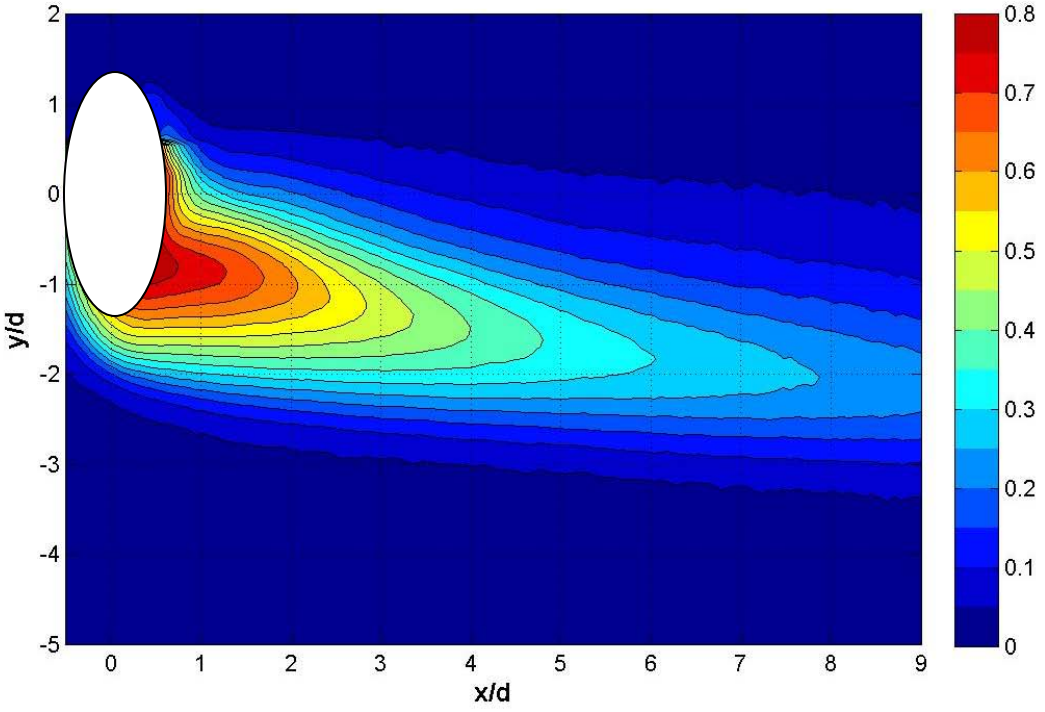

Fig A.18 Contour of η without dimples at Re = 30k and high turbulence for M = 1.0

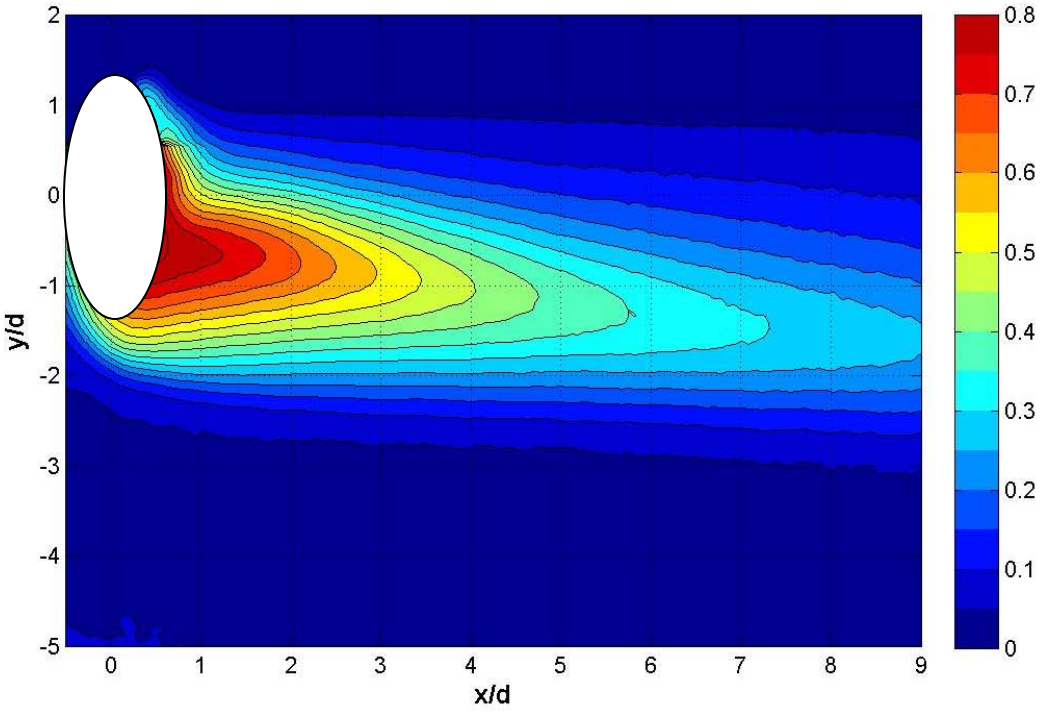

Fig A.19 Contour of η with dimples at Re = 30k and high turbulence for M = 0.75

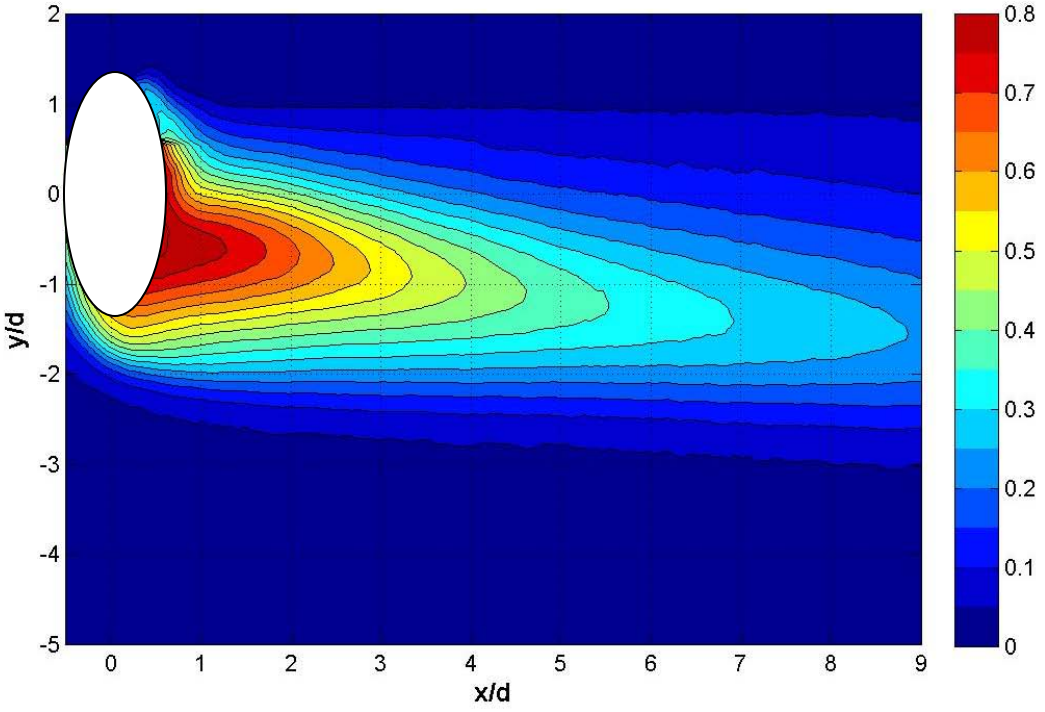

Fig A.20 Contour of η without dimples at Re = 30k and high turbulence for M = 0.75

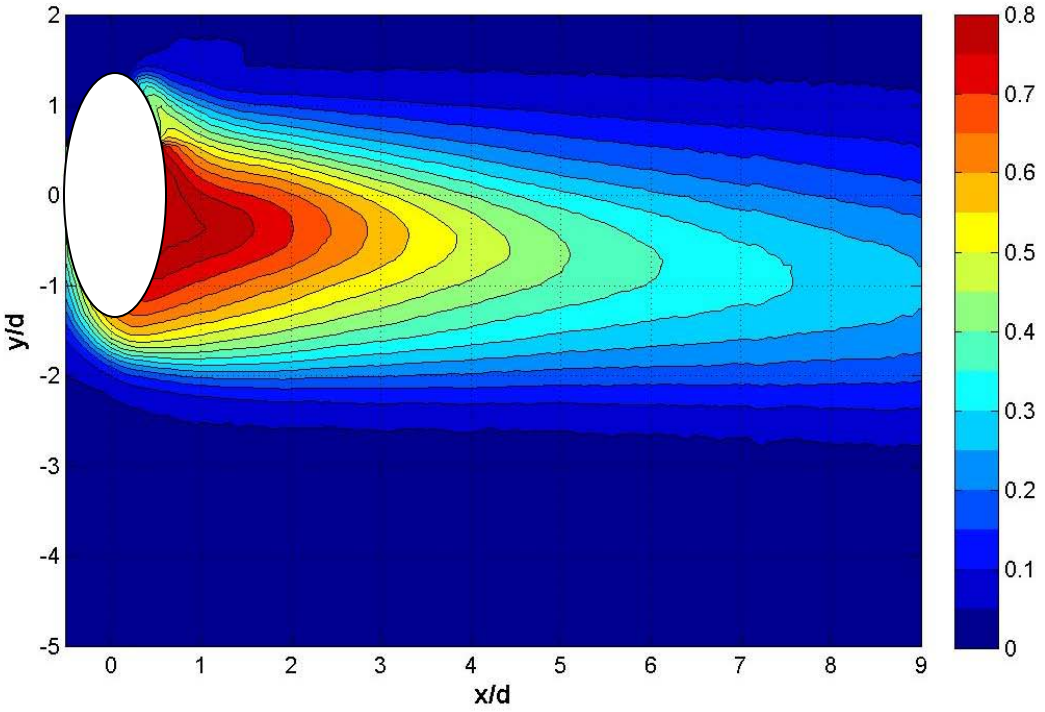

Fig A.21 Contour of η with dimples at Re = 30k and high turbulence for M = 0.5

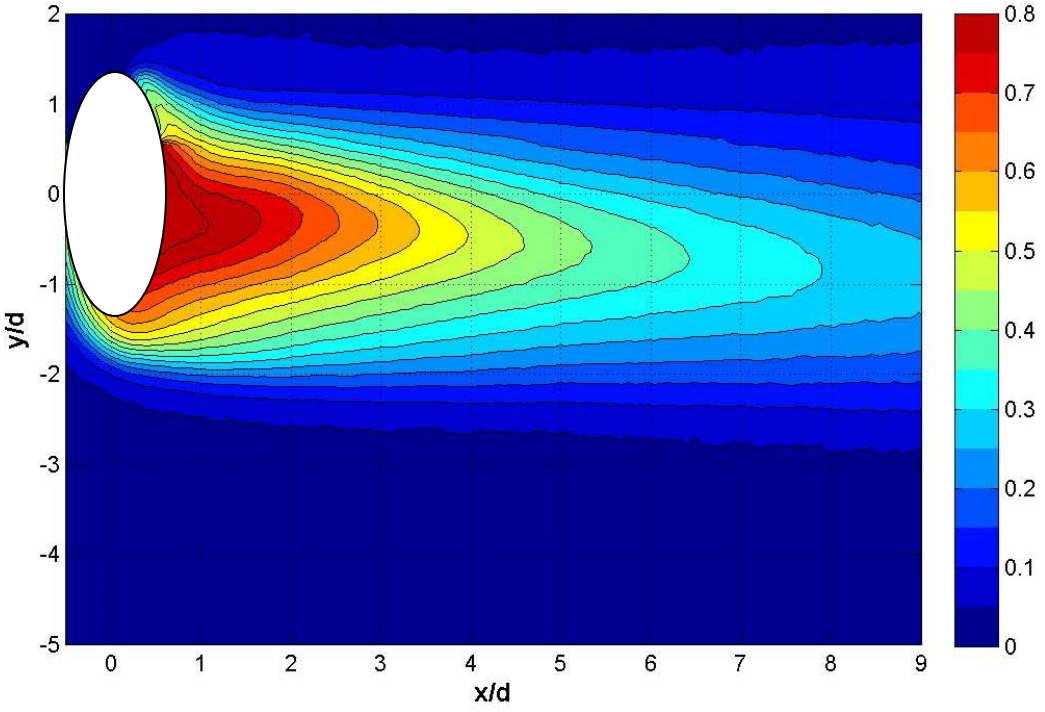

Fig A.22 Contour of η without dimples at Re = 30k and high turbulence for M = 0.5

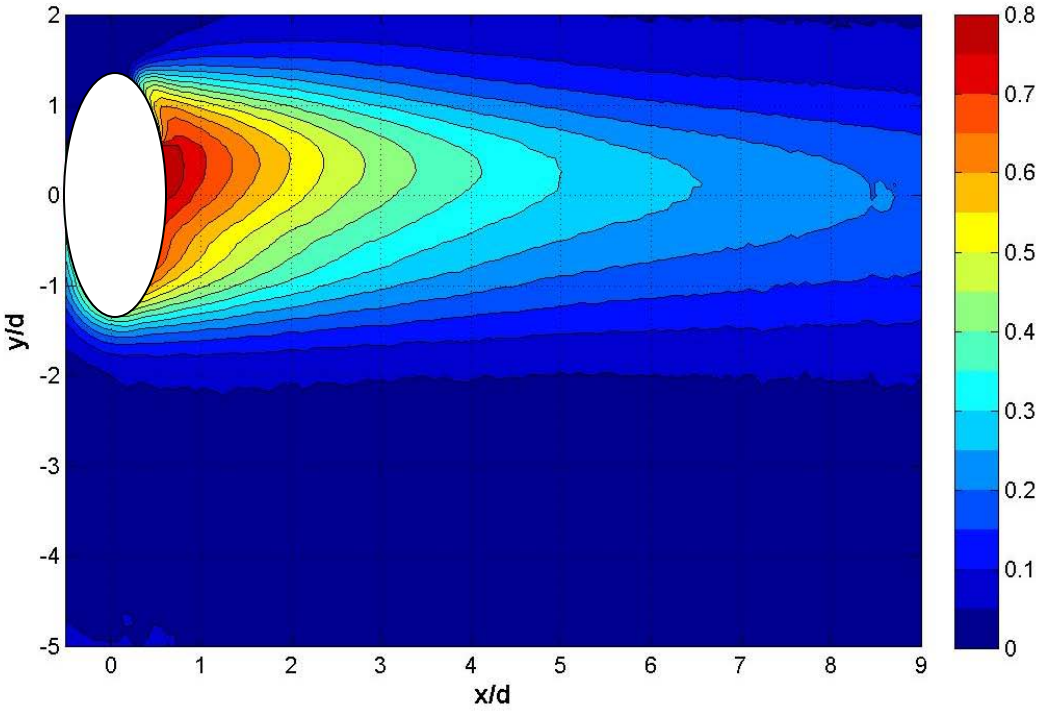

Fig A.23 Contour of η with dimples at Re = 30k and high turbulence for M = 0.25

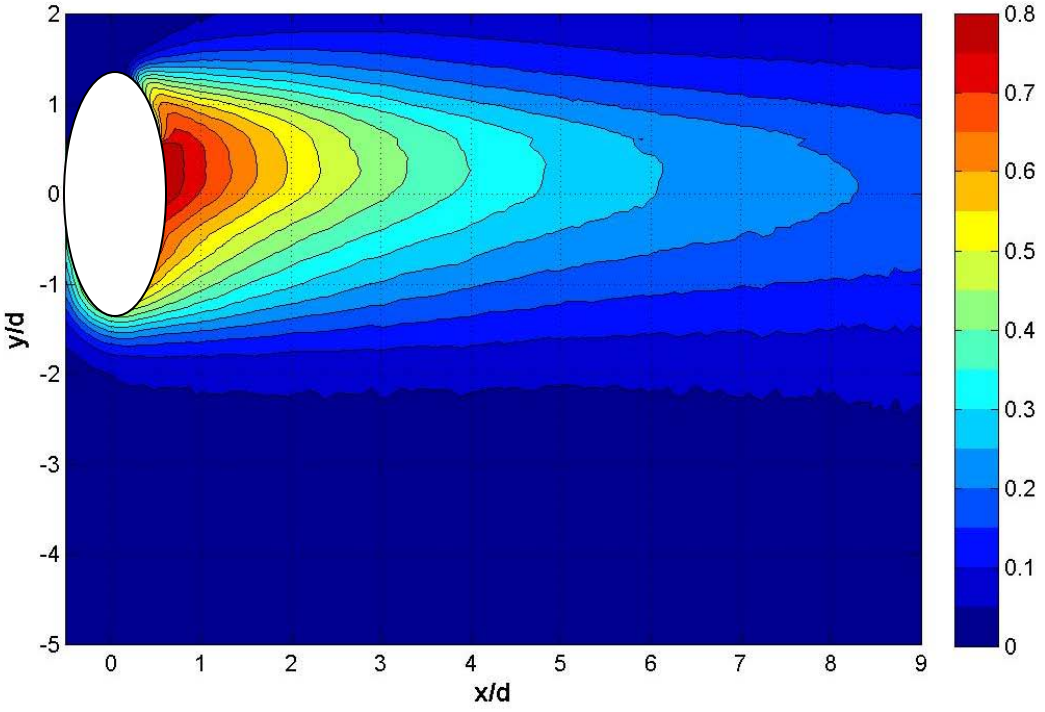

Fig A.24 Contour of η without dimples at Re = 30k and high turbulence for M = 0.25

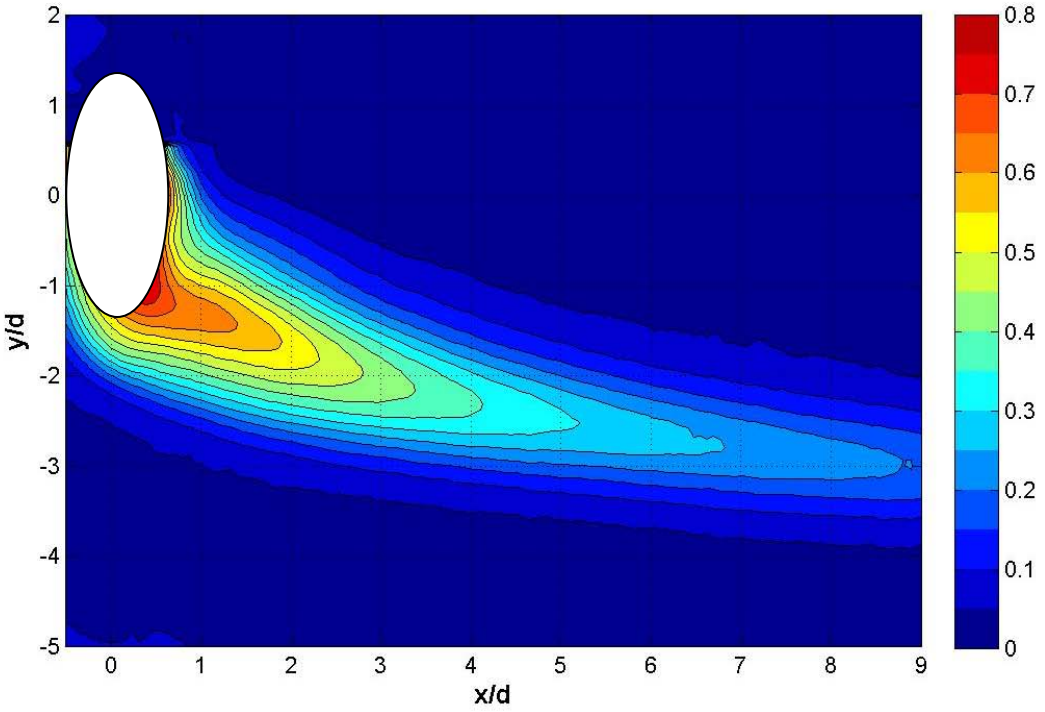

Fig A.25 Contour of η with dimples at Re = 30k and low turbulence for M = 1.5

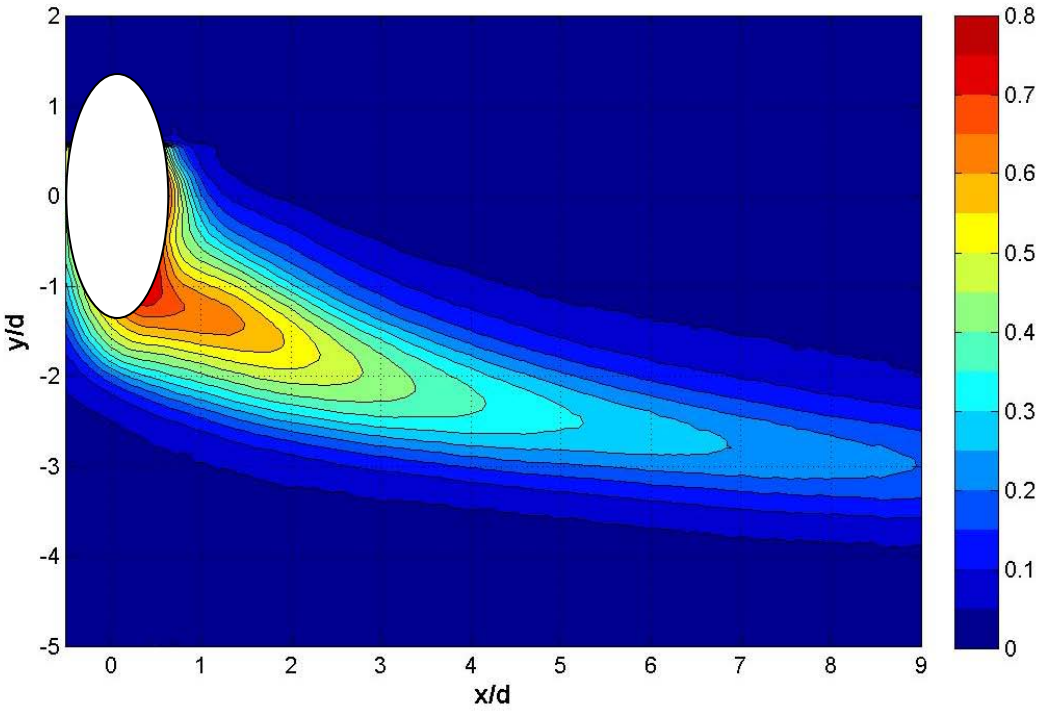

Fig A.26 Contour of η without dimples at Re = 30k and low turbulence for M = 1.5

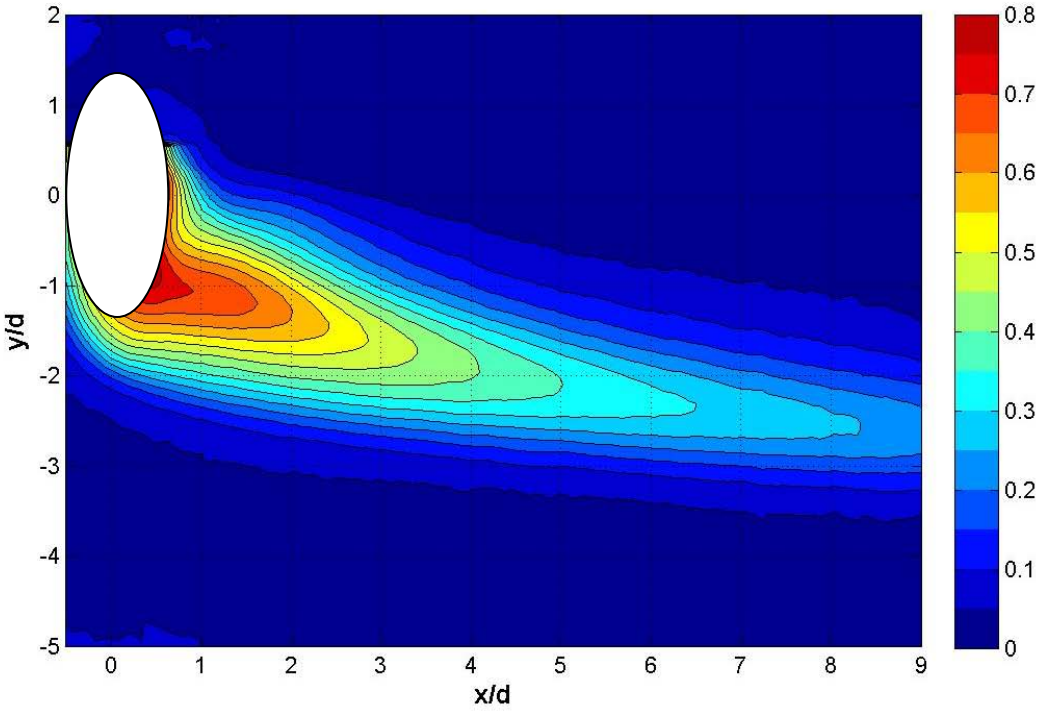

Fig A.27 Contour of η with dimples at Re = 30k and low turbulence for M = 1.25

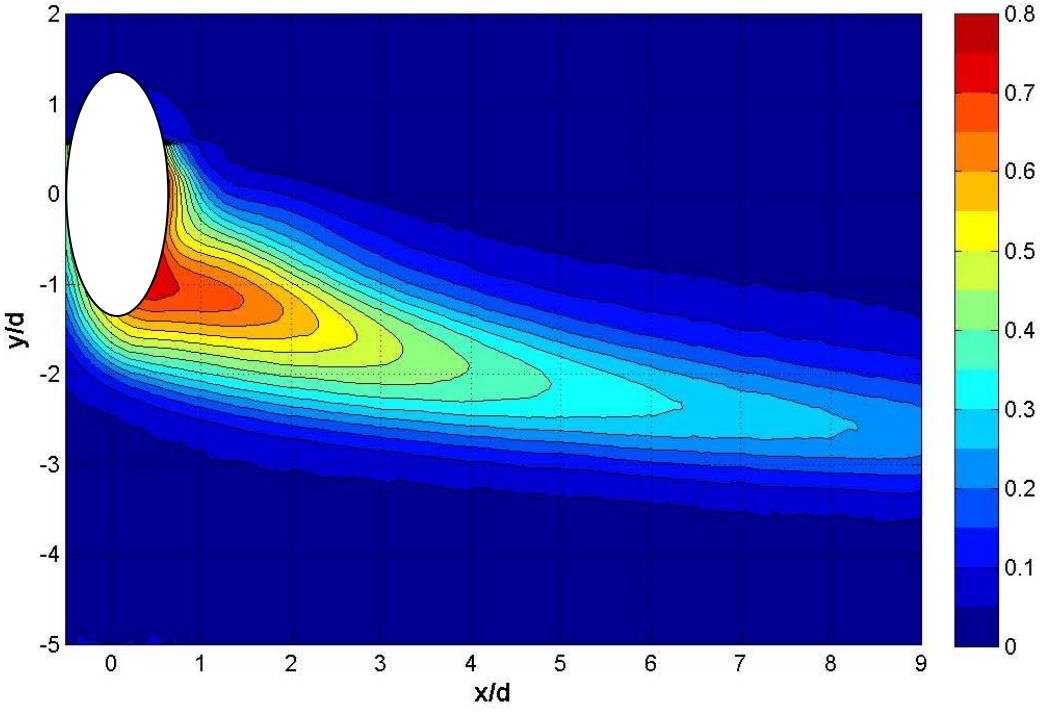

Fig A.28 Contour of η without dimples at Re = 30k and low turbulence for M = 1.25

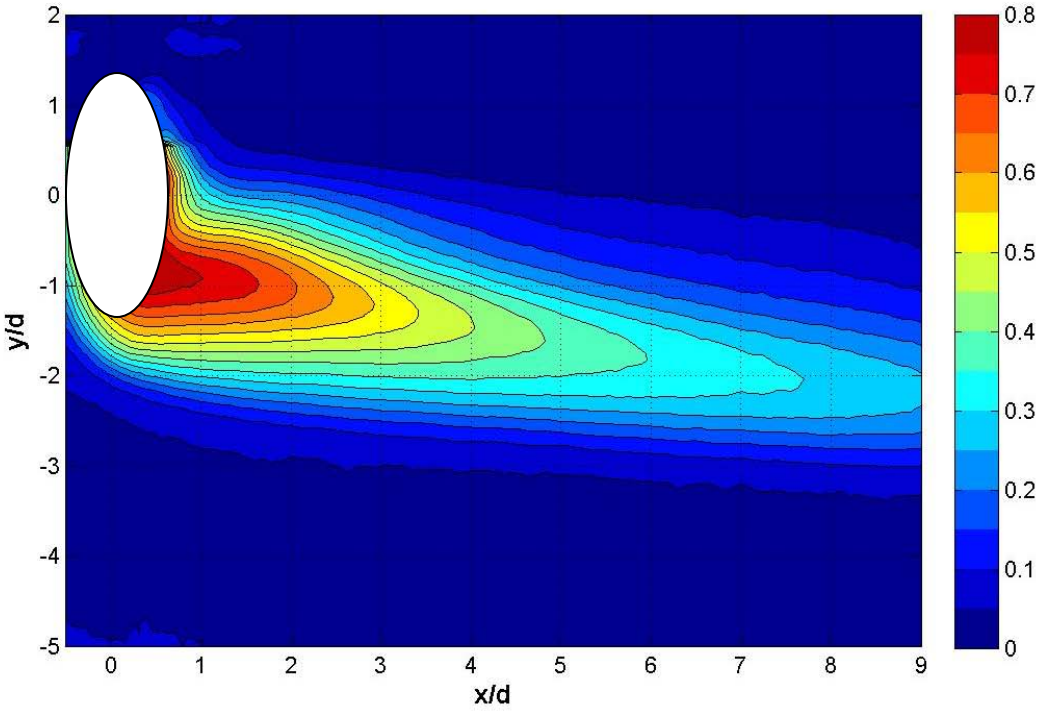

Fig A.29 Contour of η with dimples at Re = 30k and low turbulence for M = 1.0

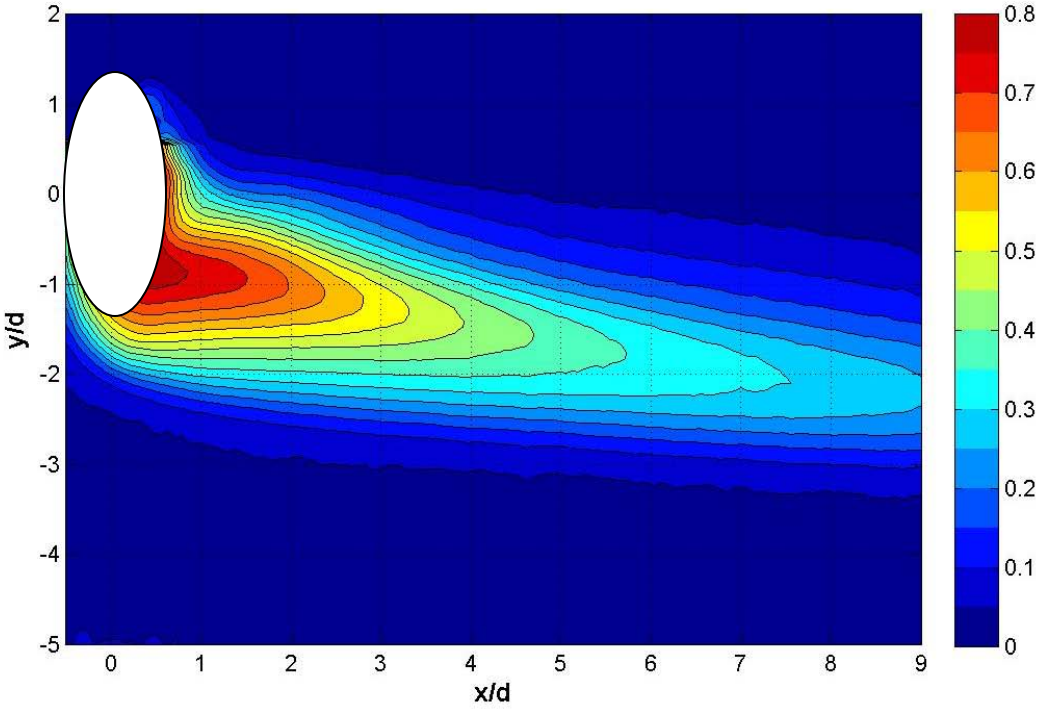

Fig A.30 Contour of η without dimples at Re = 30k and low turbulence for M = 1.0

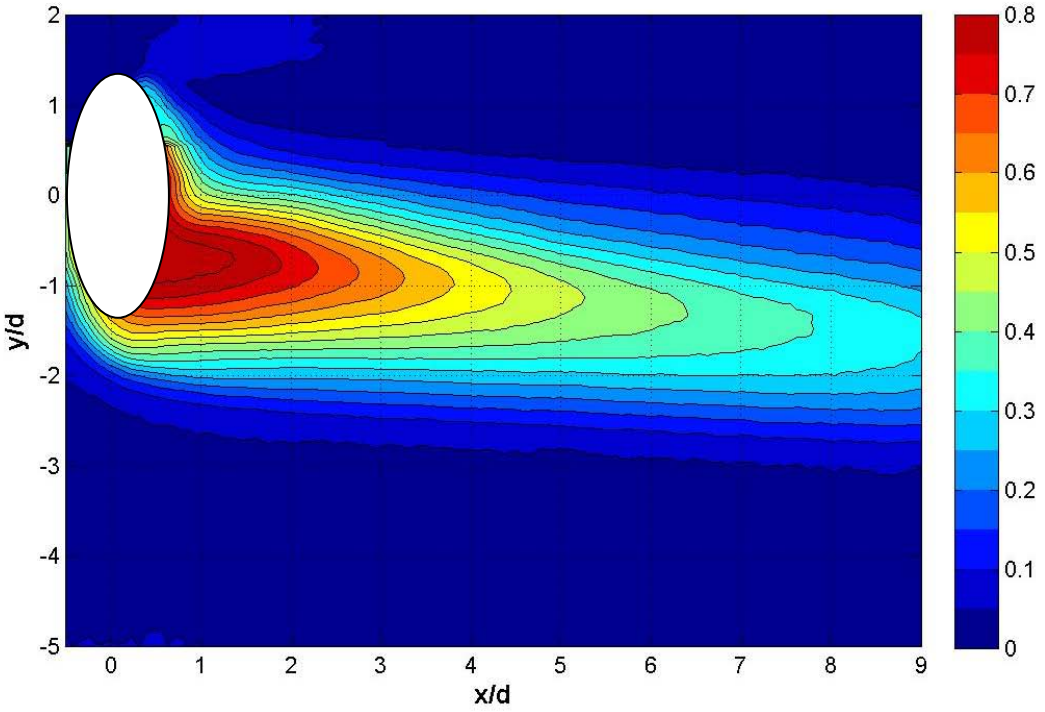

Fig A.31 Contour of η with dimples at Re = 30k and low turbulence for M = 0.75

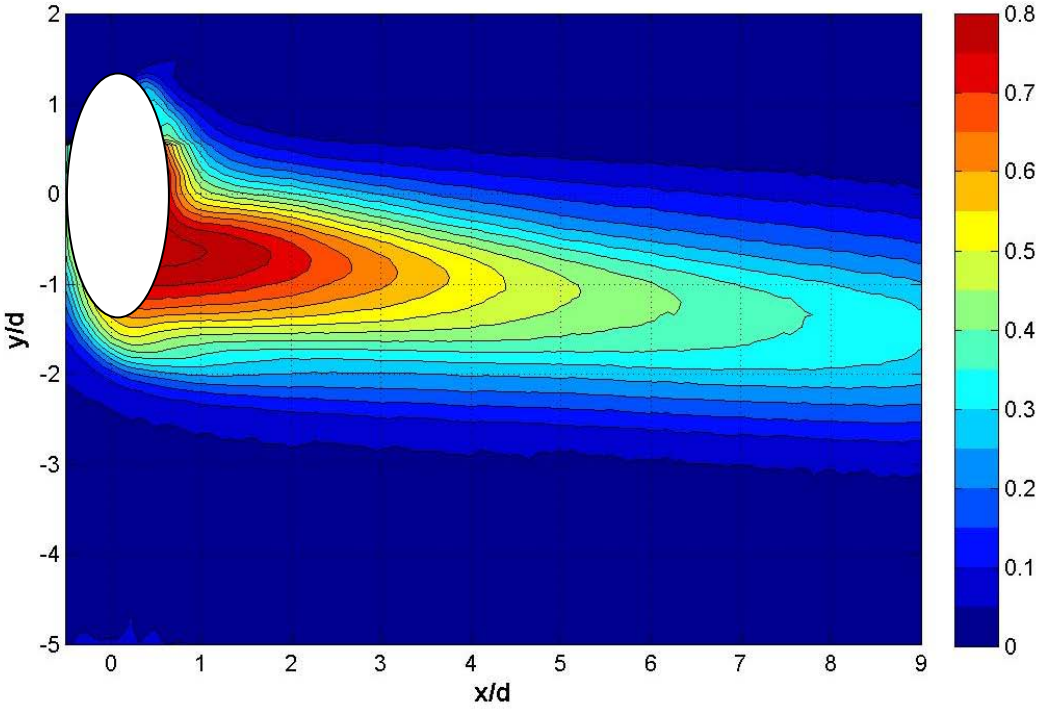

Fig A.32 Contour of η without dimples at Re = 30k and low turbulence for M = 0.75

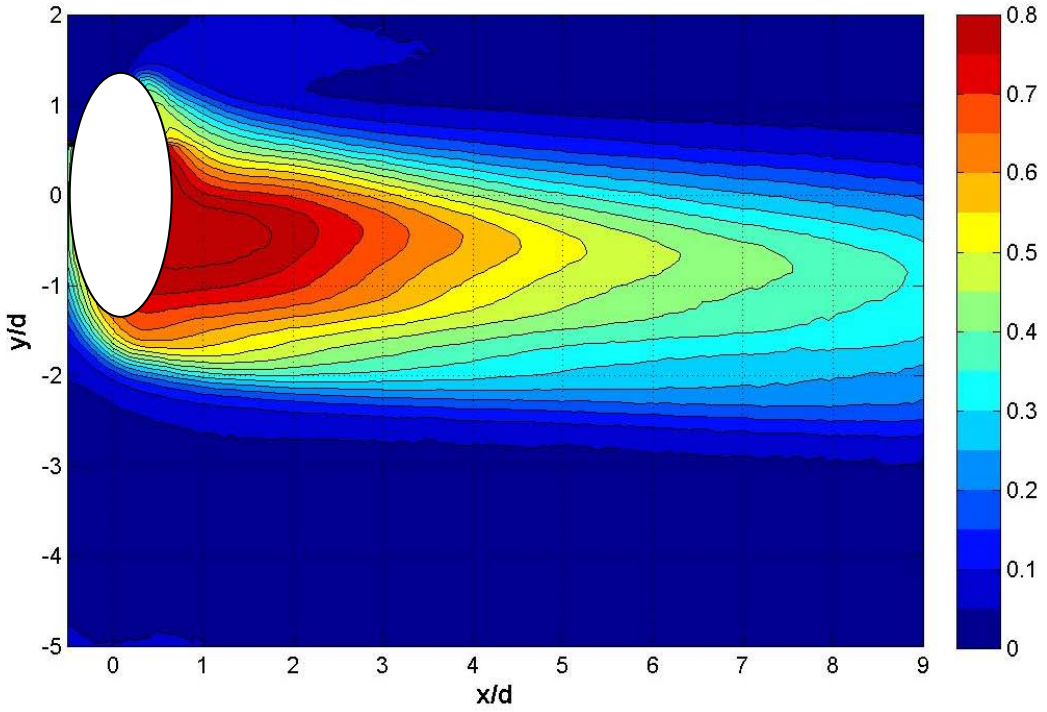

Fig A.33 Contour of η with dimples at Re = 30k and low turbulence for M = 0.5

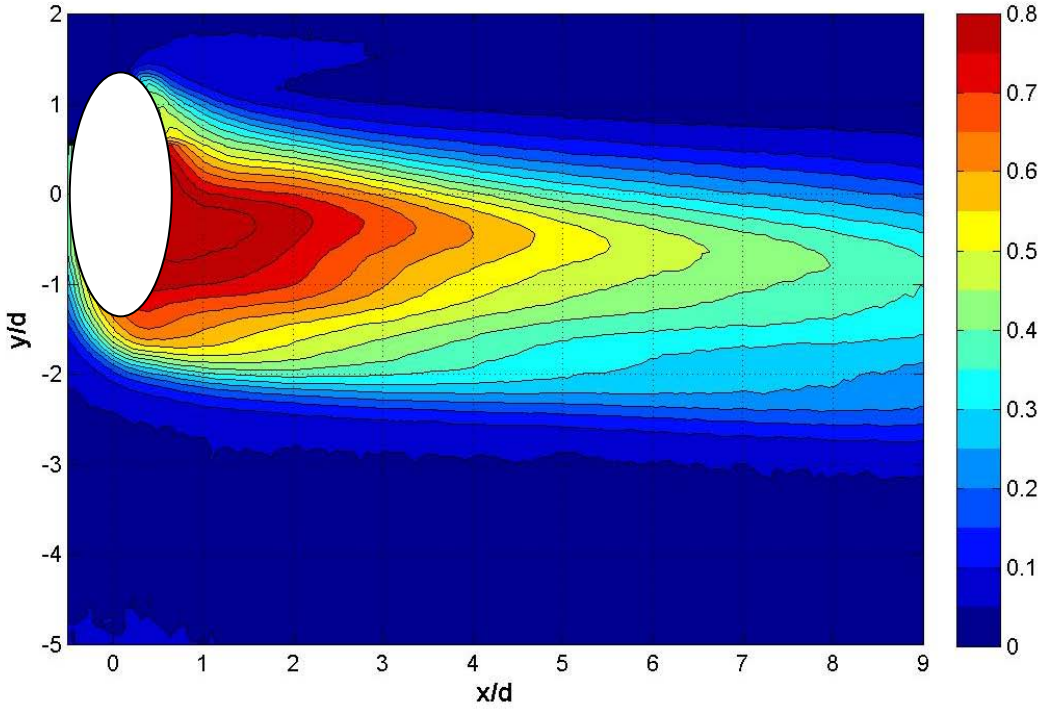

Fig A.34 Contour of η without dimples at Re = 30k and low turbulence for M = 0.5

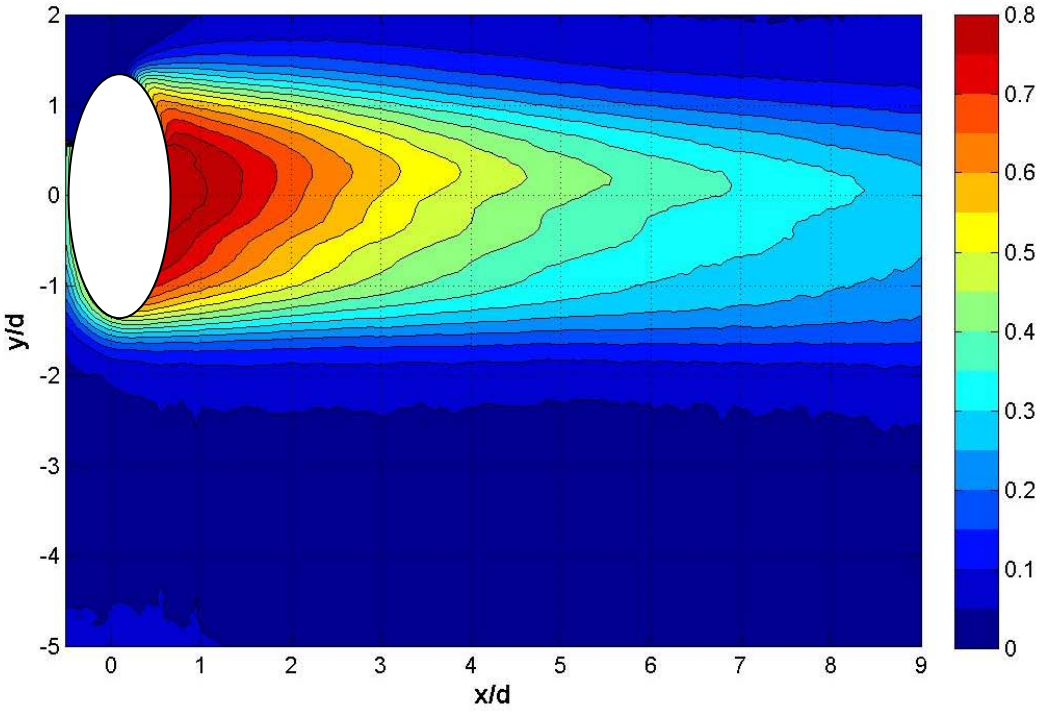

Fig A.35 Contour of η with dimples at Re = 30k and low turbulence for M = 0.25

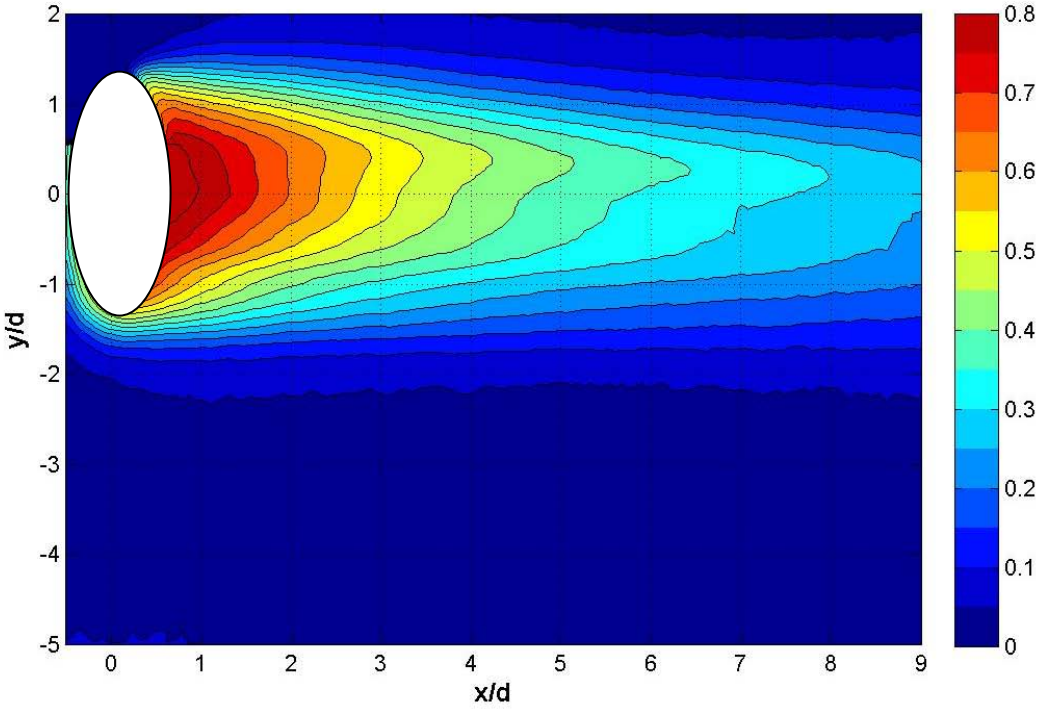

Fig A.36 Contour of η without dimples at Re = 30k and low turbulence for M = 0.25

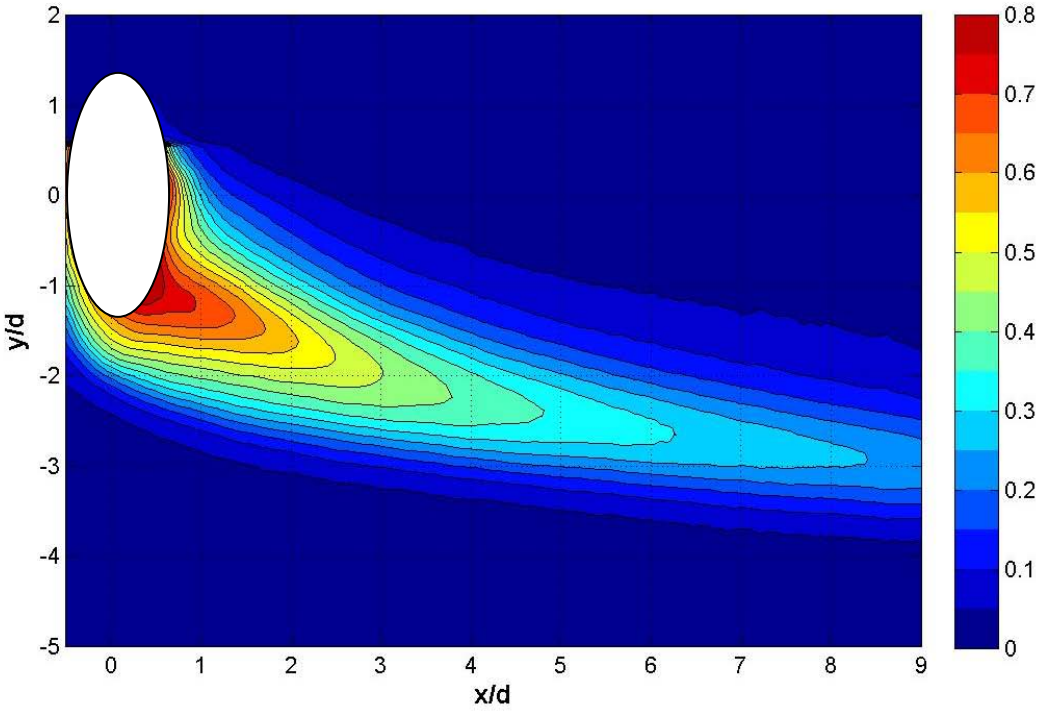

Fig A.37 Contour of η with dimples at Re = 60k and low turbulence for M = 1.5

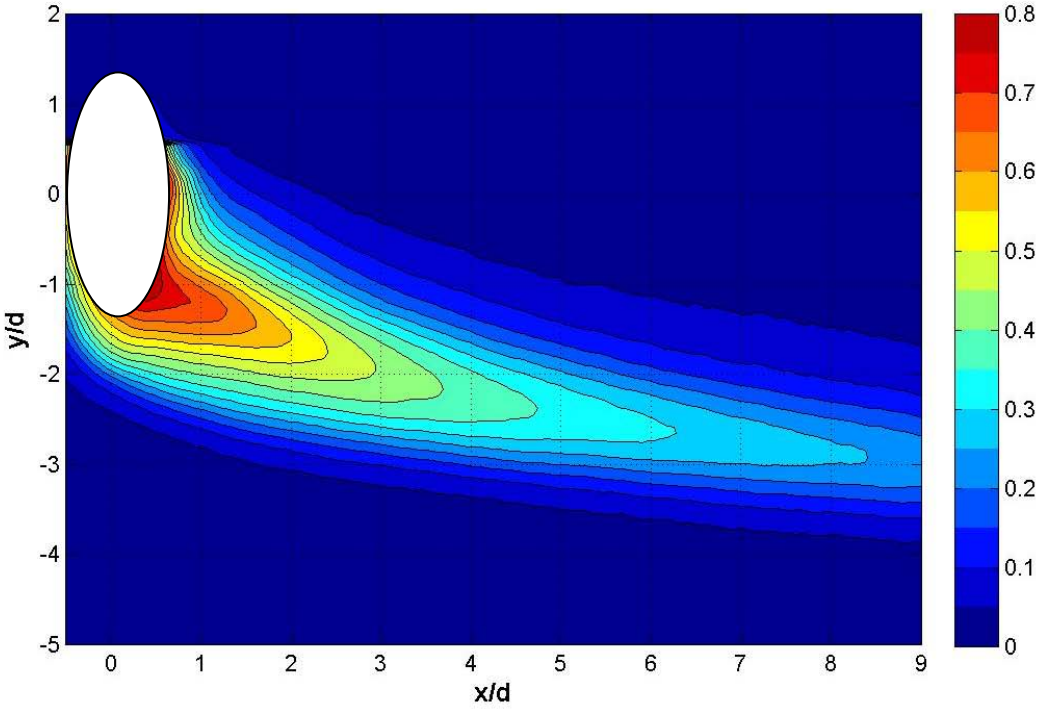

Fig A.38 Contour of η without dimples at Re = 60k and low turbulence for M = 1.5

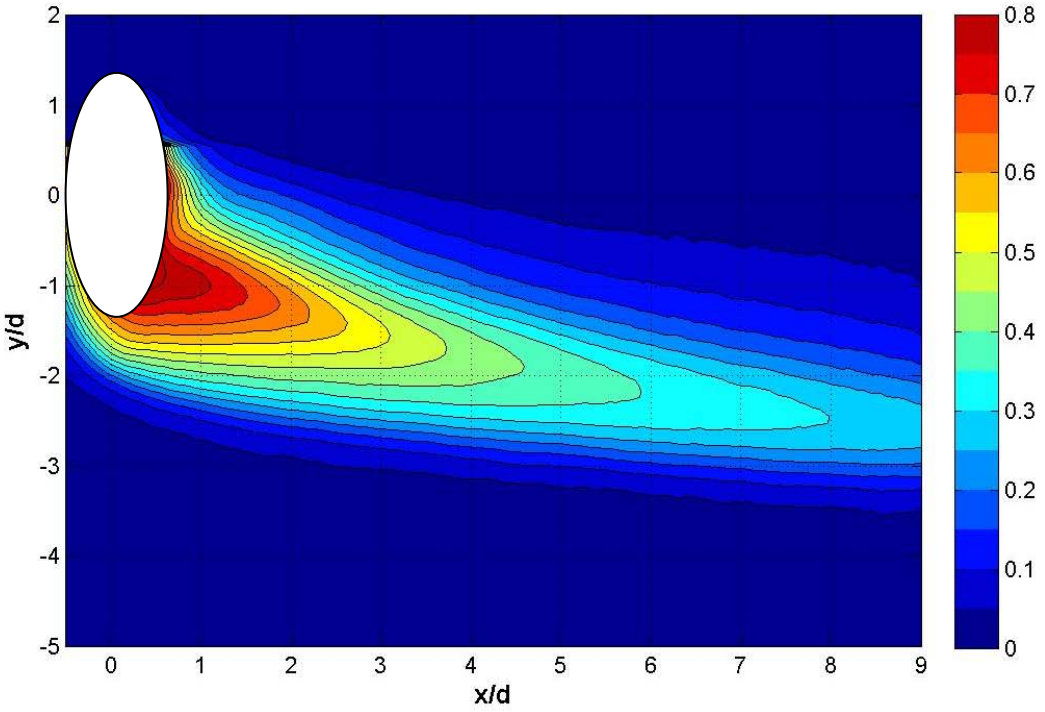

Fig A.39 Contour of η with dimples at Re = 60k and low turbulence for M = 1.25

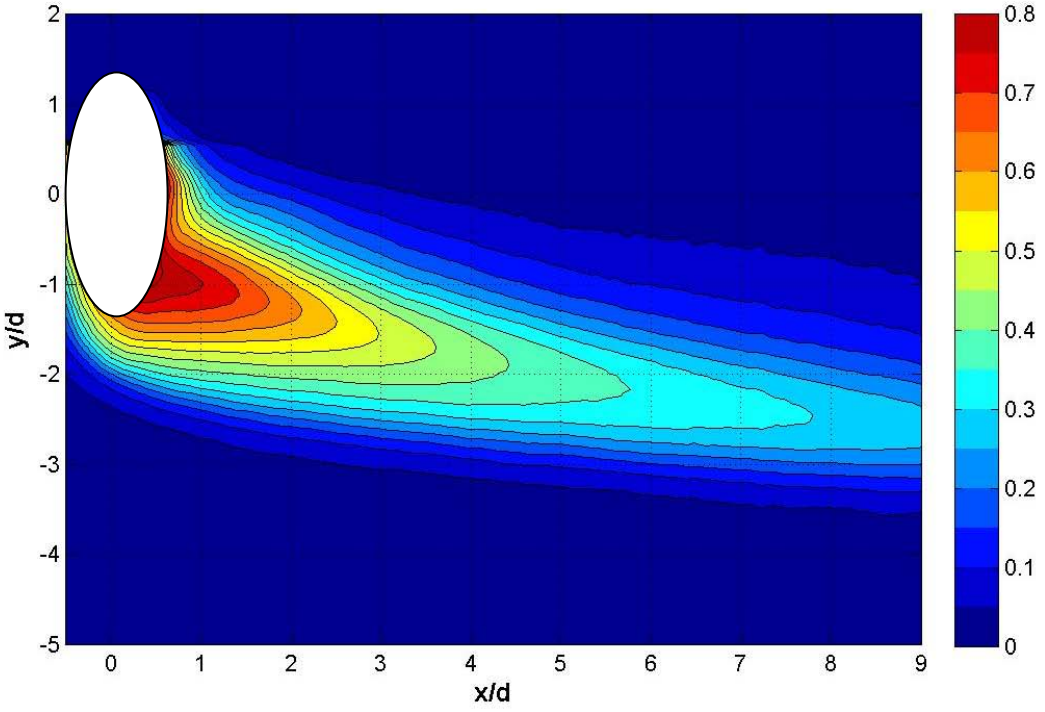

Fig A.40 Contour of η without dimples at Re = 60k and low turbulence for M = 1.25

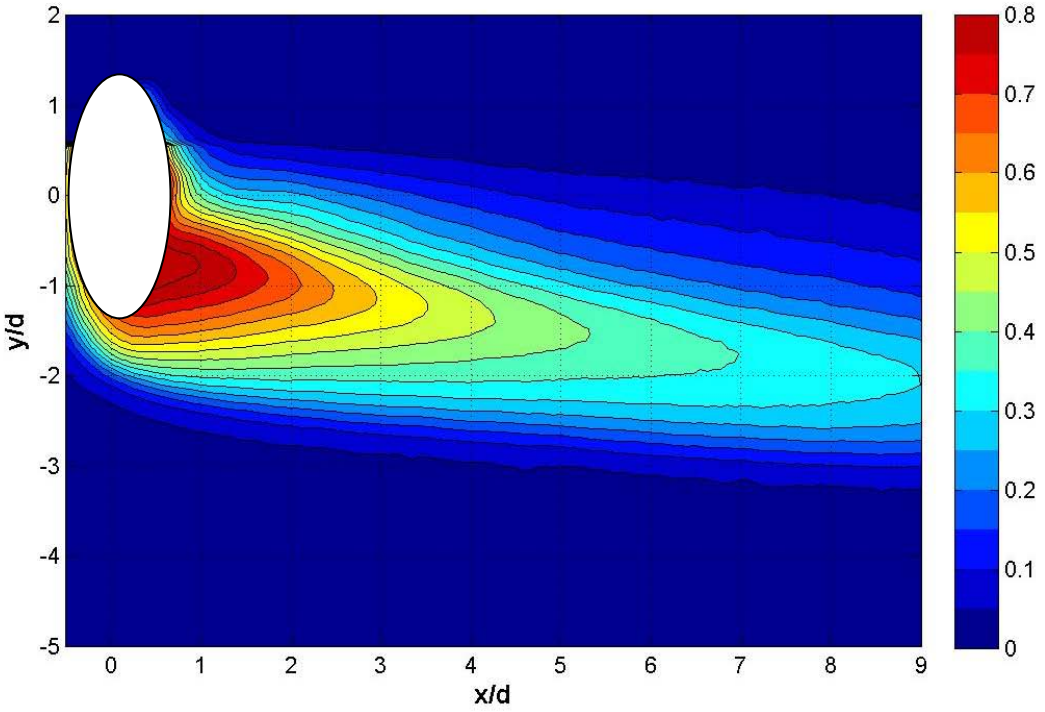

Fig A.41 Contour of η with dimples at Re = 60k and low turbulence for M = 1.0

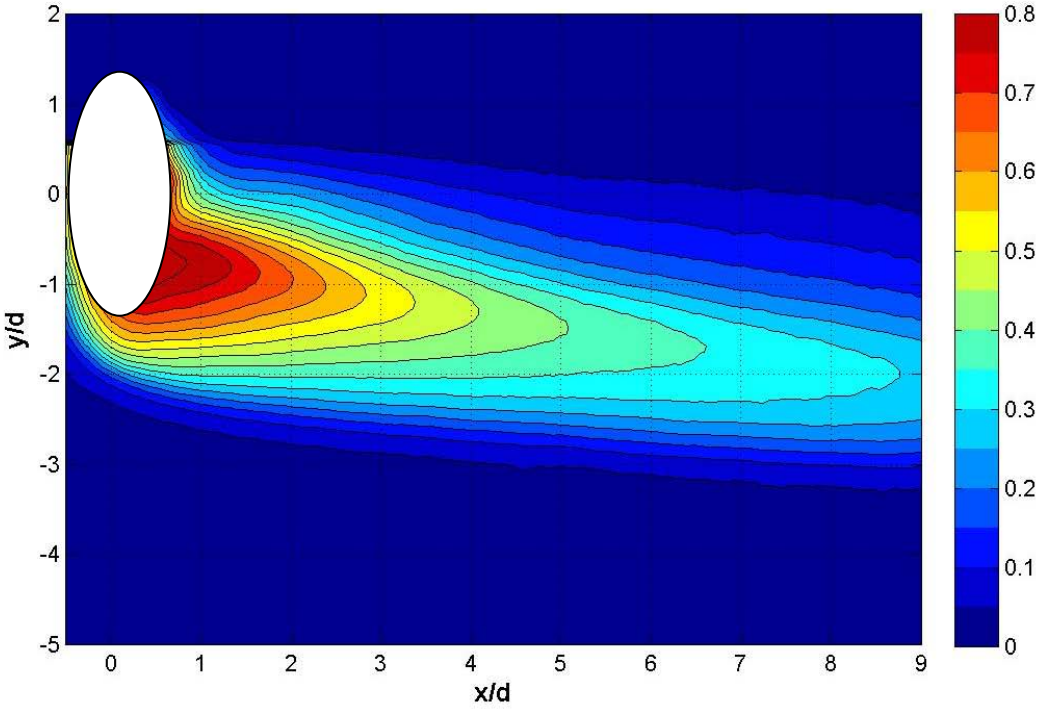

Fig A.42 Contour of η without dimples at Re = 60k and low turbulence for M = 1.0

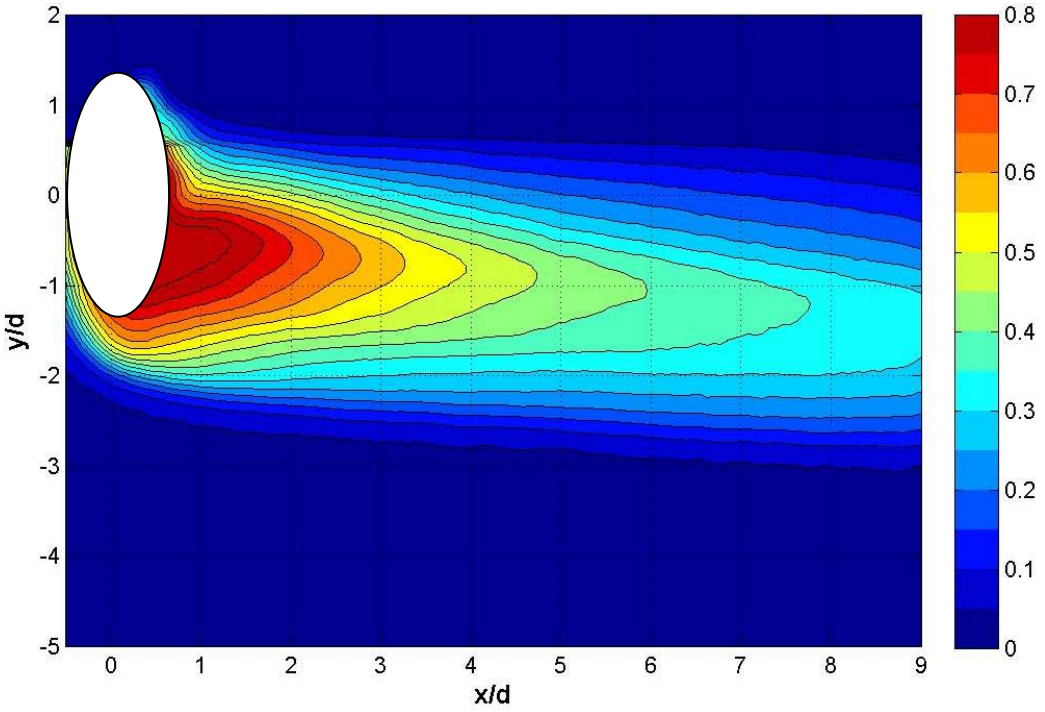

Fig A.43 Contour of η with dimples at Re = 60k and low turbulence for M = 0.75

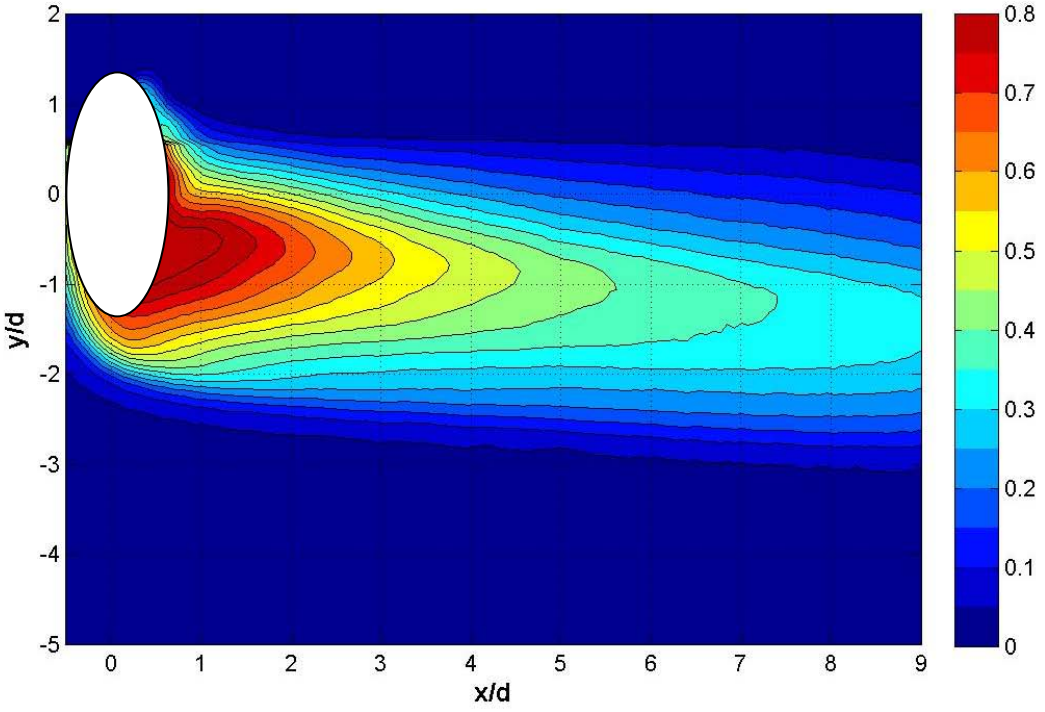

Fig A.44 Contour of η without dimples at Re = 60k and low turbulence for M = 0.75

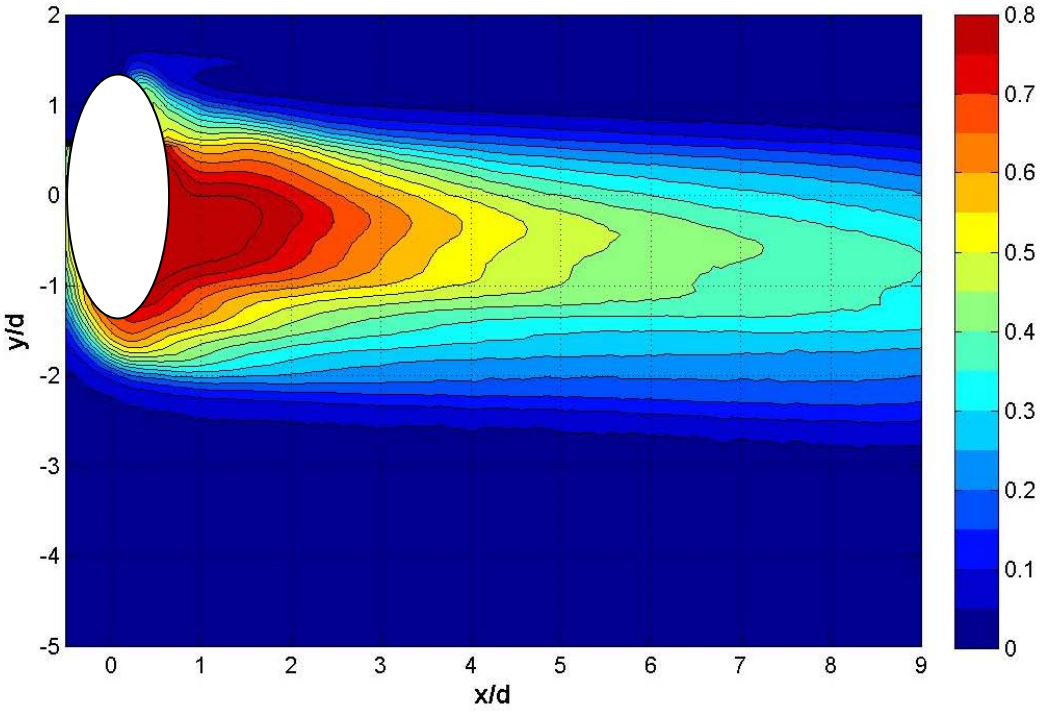

Fig A.45 Contour of η with dimples at Re = 60k and low turbulence for M = 0.5

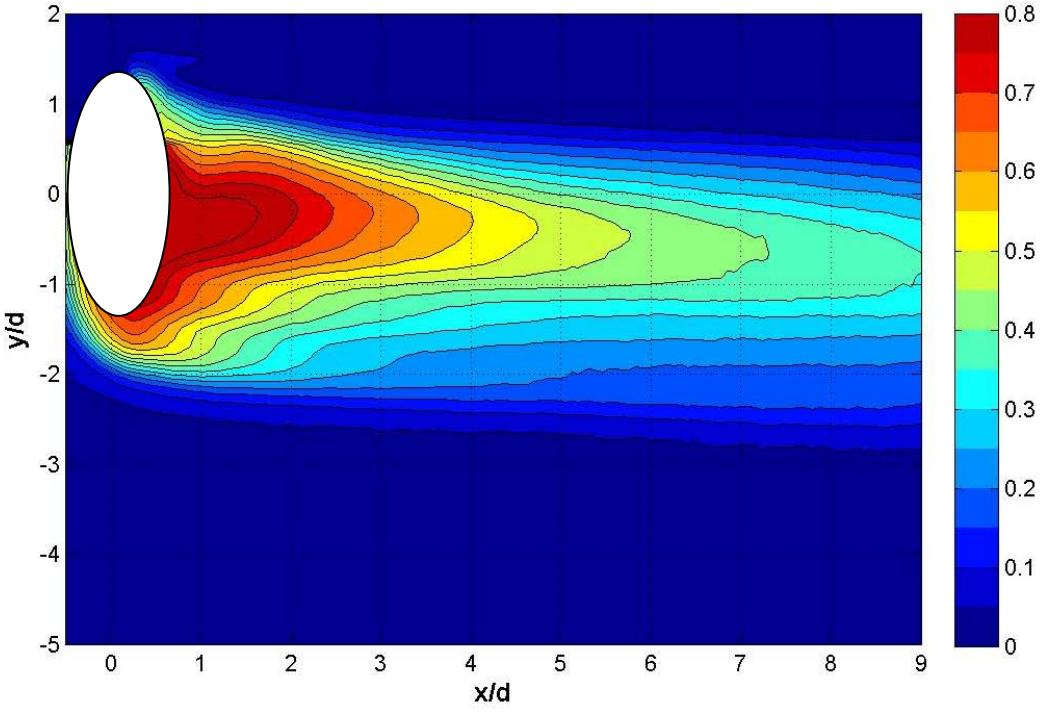

Fig A.46 Contour of η without dimples at Re = 60k and low turbulence for M = 0.5

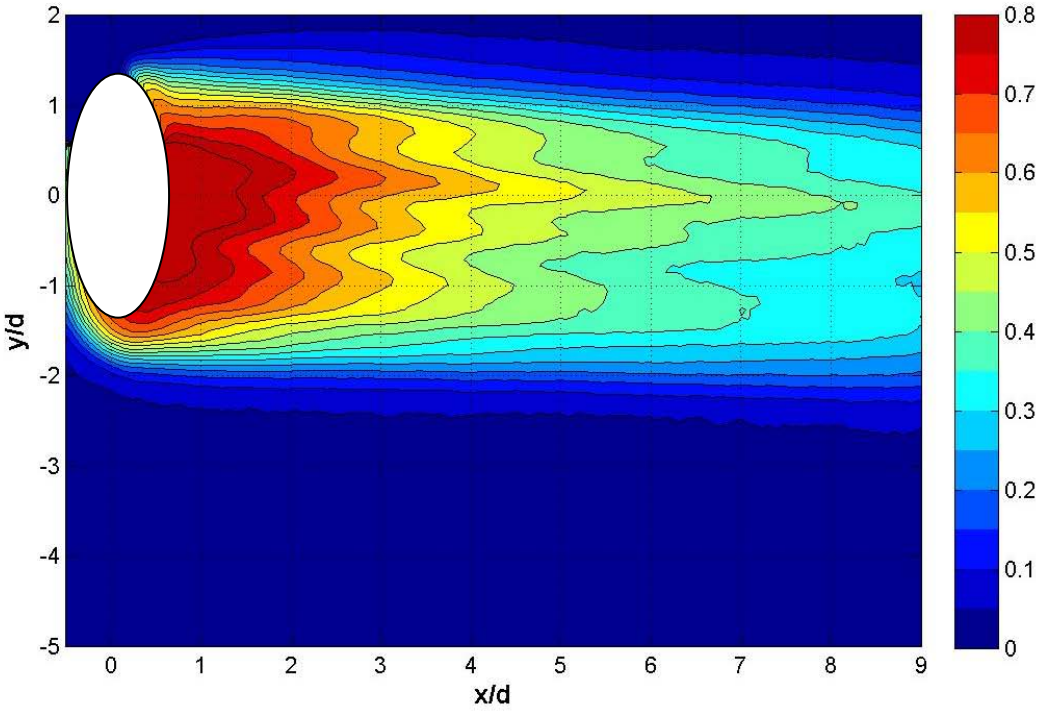

Fig A.47 Contour of η with dimples at Re = 60k and low turbulence for M = 0.25

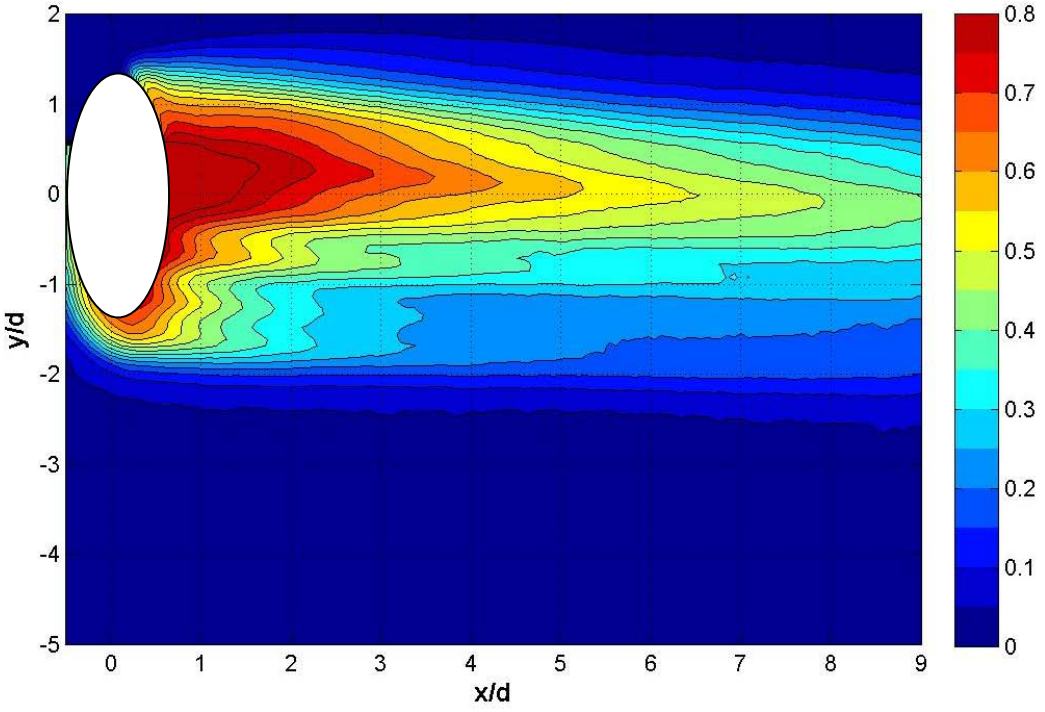

Fig A.48 Contour of η without dimples at Re = 60k and low turbulence for M = 0.25

Appendix B. Spanwise averaged adiabatic effectiveness plots

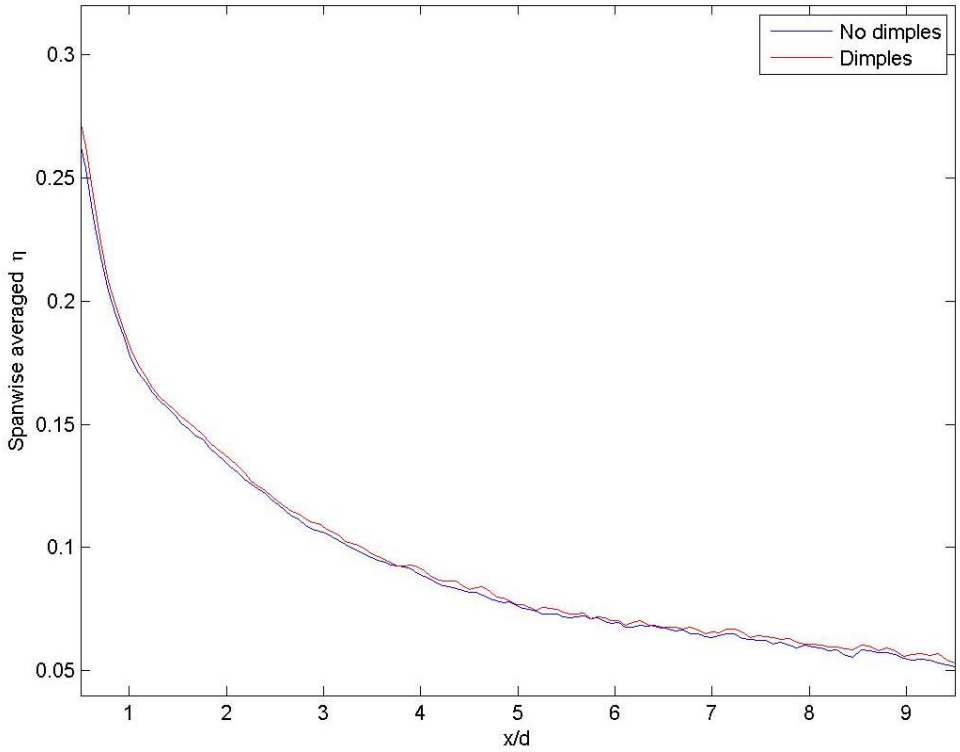

Fig B.1 Spanwise averaged η at Re = 60k and high turbulence for M = 1.5

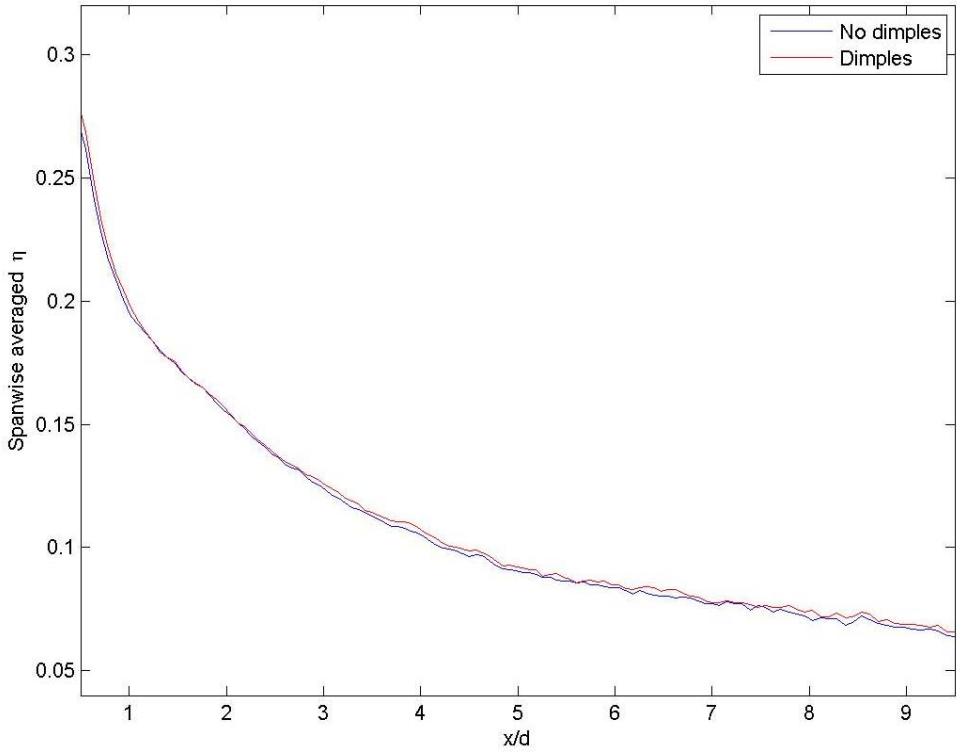

Fig B.2 Spanwise averaged η at Re = 60k and high turbulence for M = 1.25

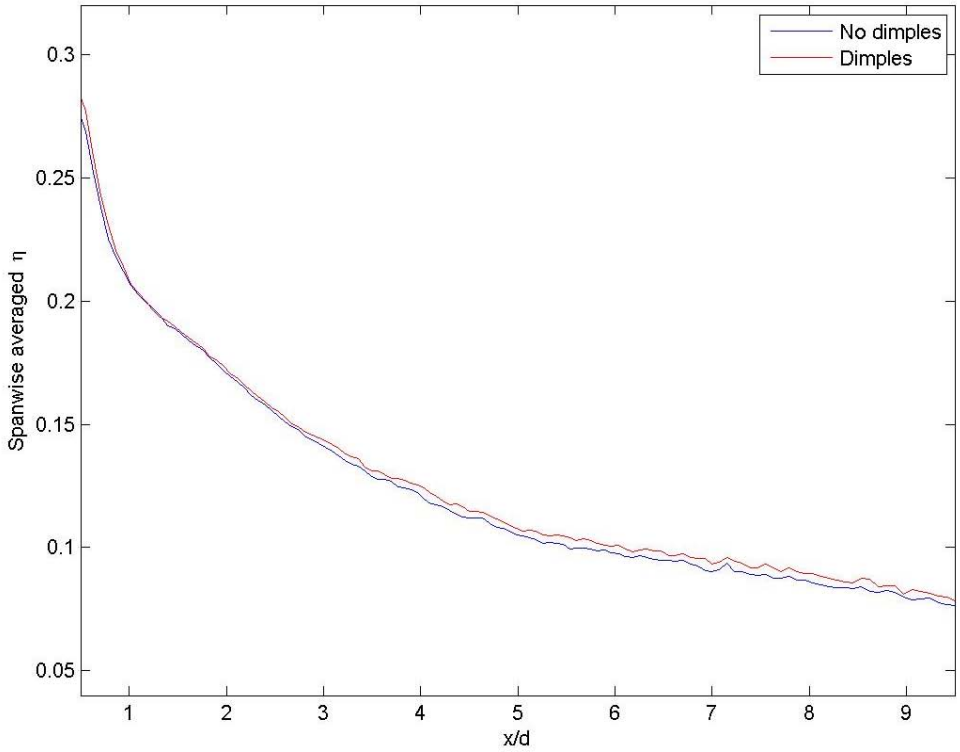

Fig B.3 Spanwise averaged η at Re = 60k and high turbulence for M = 1.0

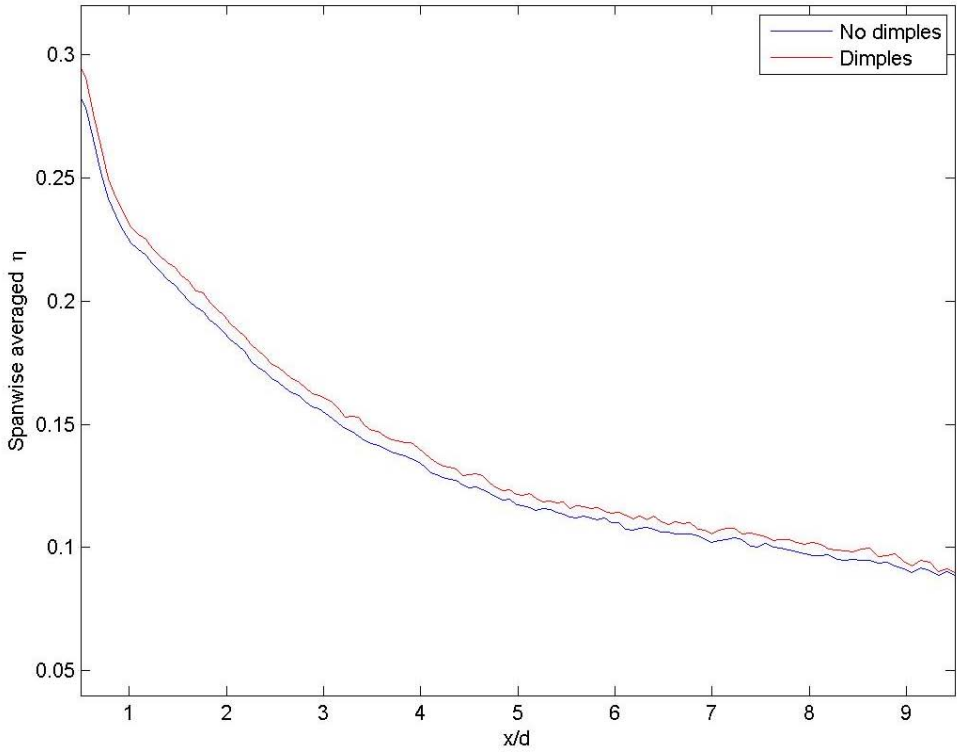

Fig B.4 Spanwise averaged η at Re = 60k and high turbulence for M = 0.75

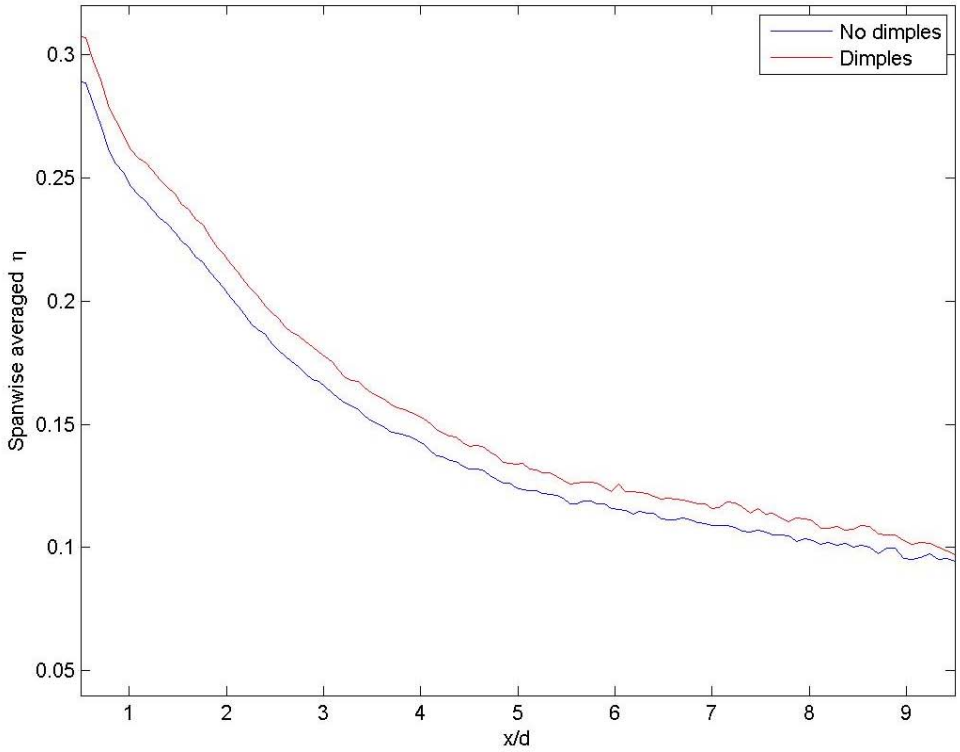

Fig B.5 Spanwise averaged η at Re = 60k and high turbulence for M = 0.5

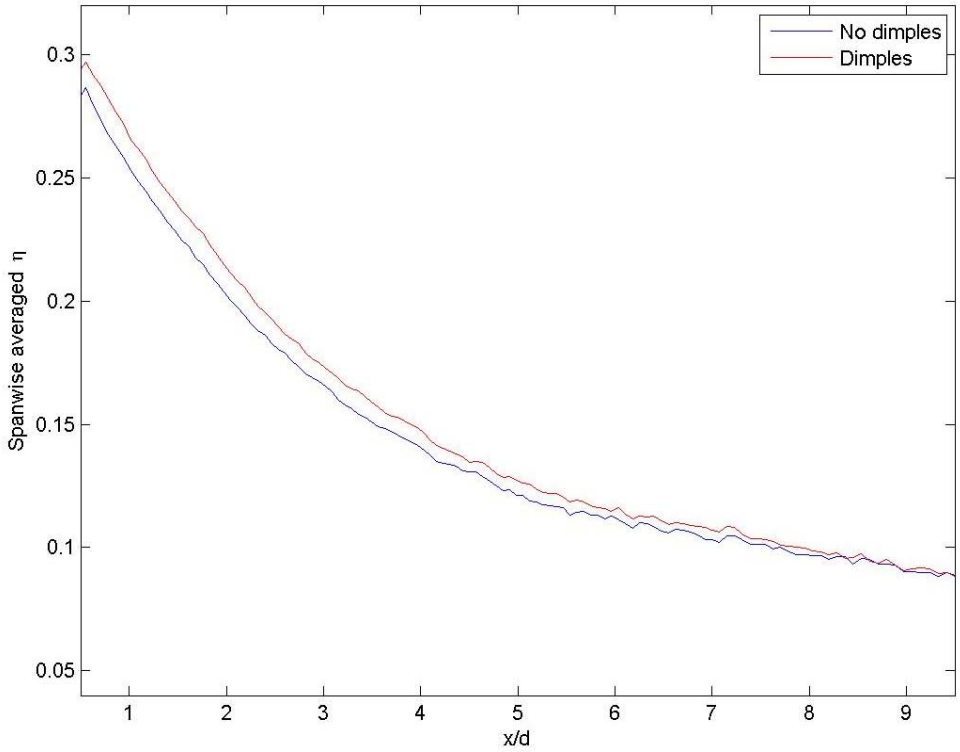

Fig B.6 Spanwise averaged η at Re = 60k and high turbulence for M = 0.25

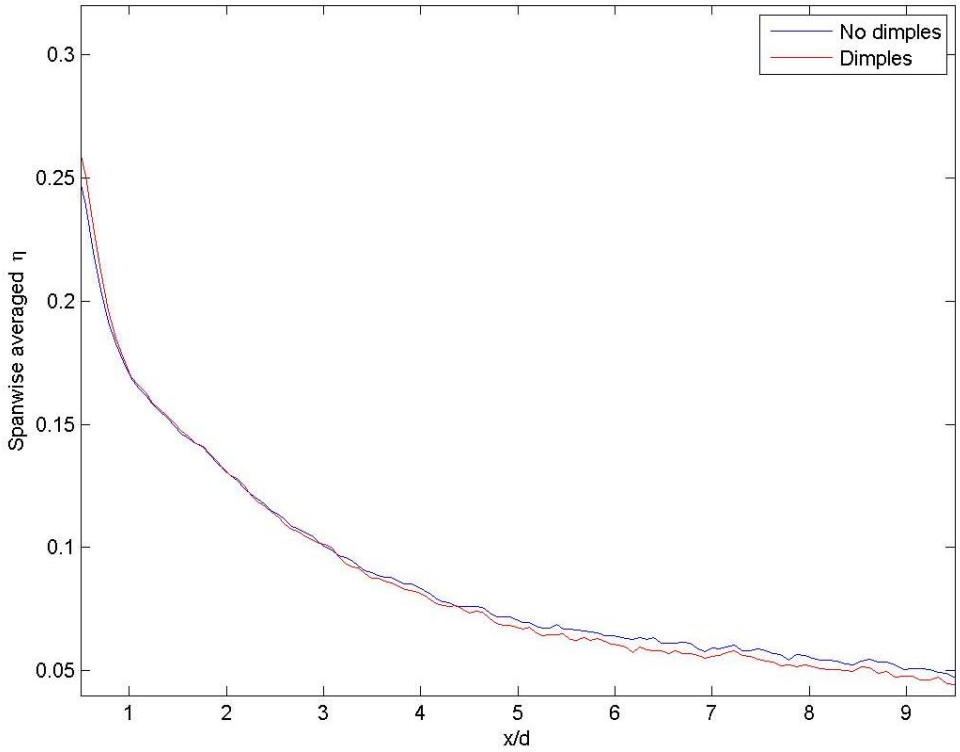

Fig B.7 Spanwise averaged η at Re = 30k and high turbulence for M = 1.5

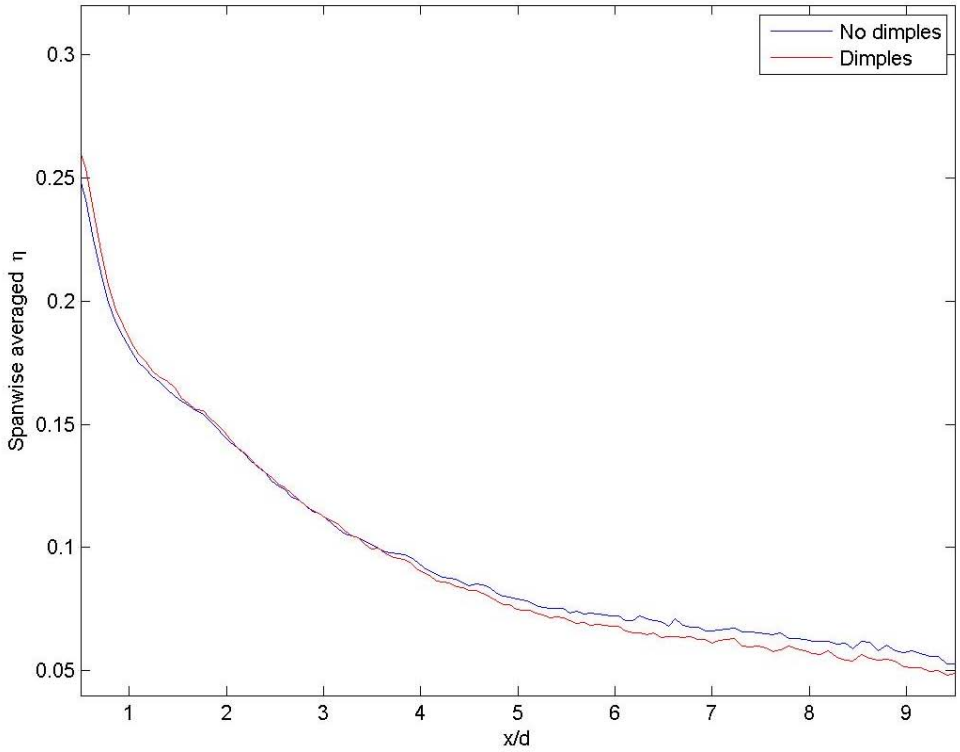

Fig B.8 Spanwise averaged η at Re = 30k and high turbulence for M = 1.25

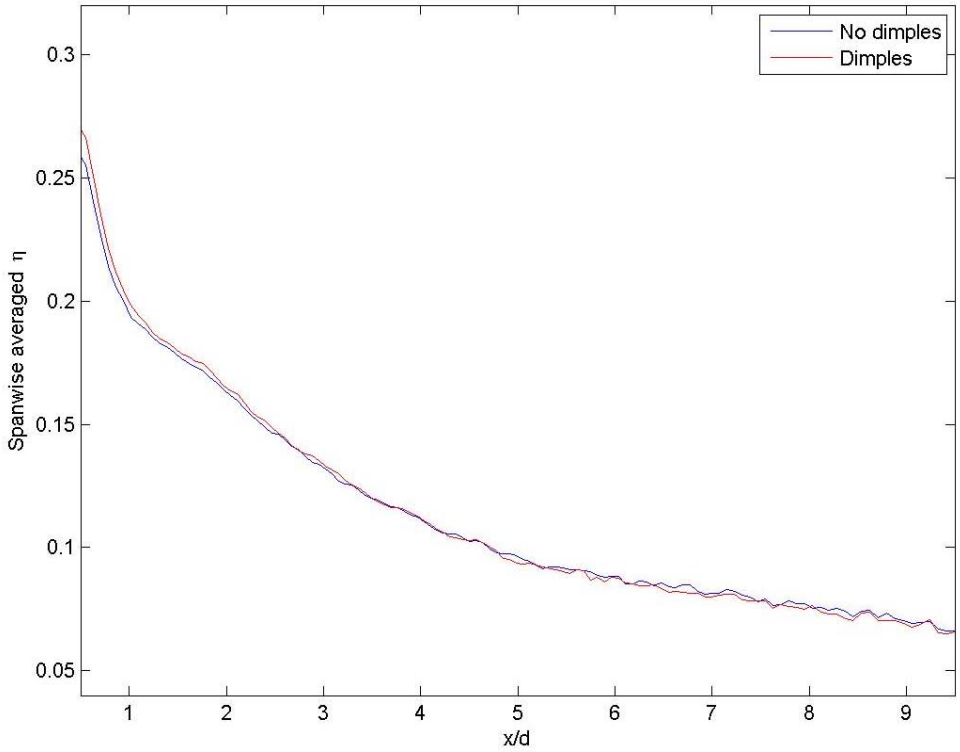

Fig B.9 Spanwise averaged η at Re = 30k and high turbulence for M = 1.0

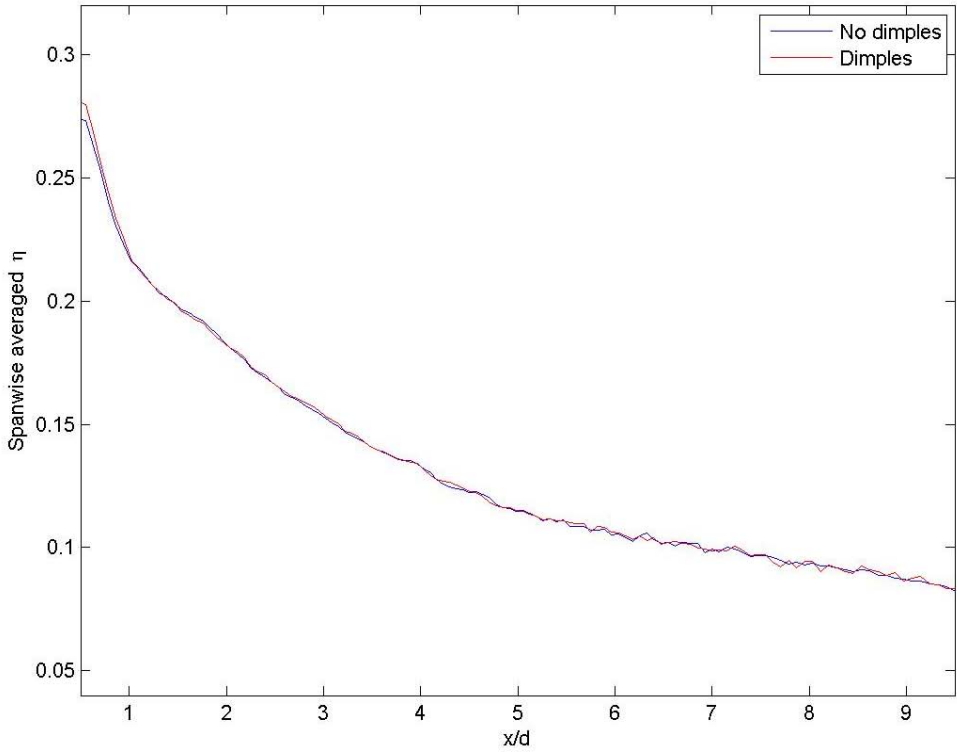

Fig B.10 Spanwise averaged η at Re = 30k and high turbulence for M = 0.75

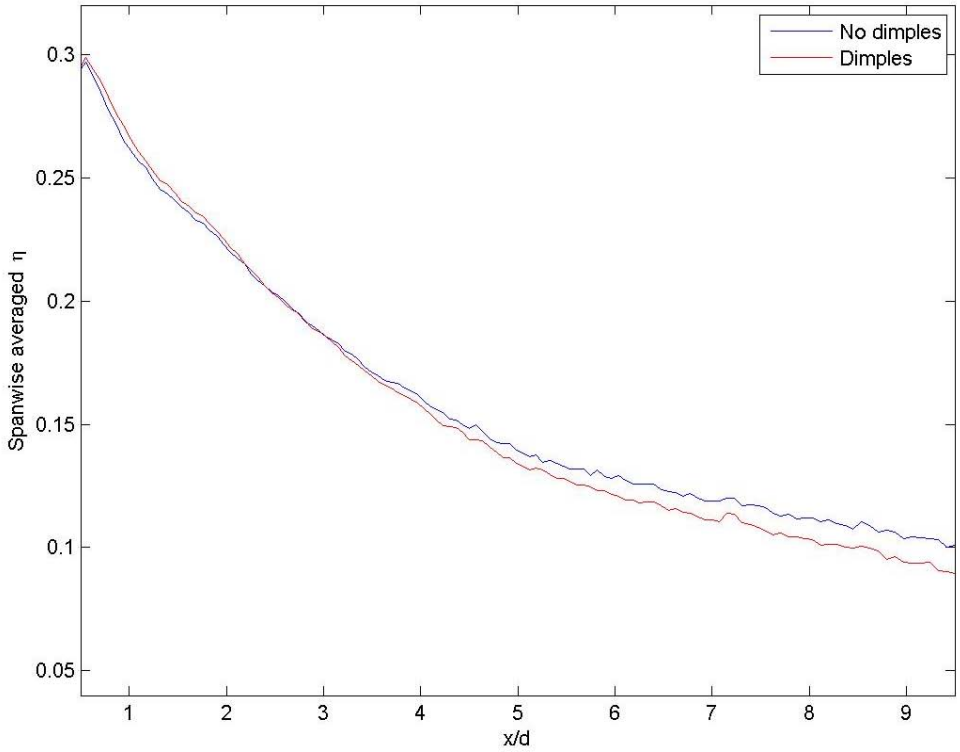

Fig B.11 Spanwise averaged η at Re = 30k and high turbulence for M = 0.5

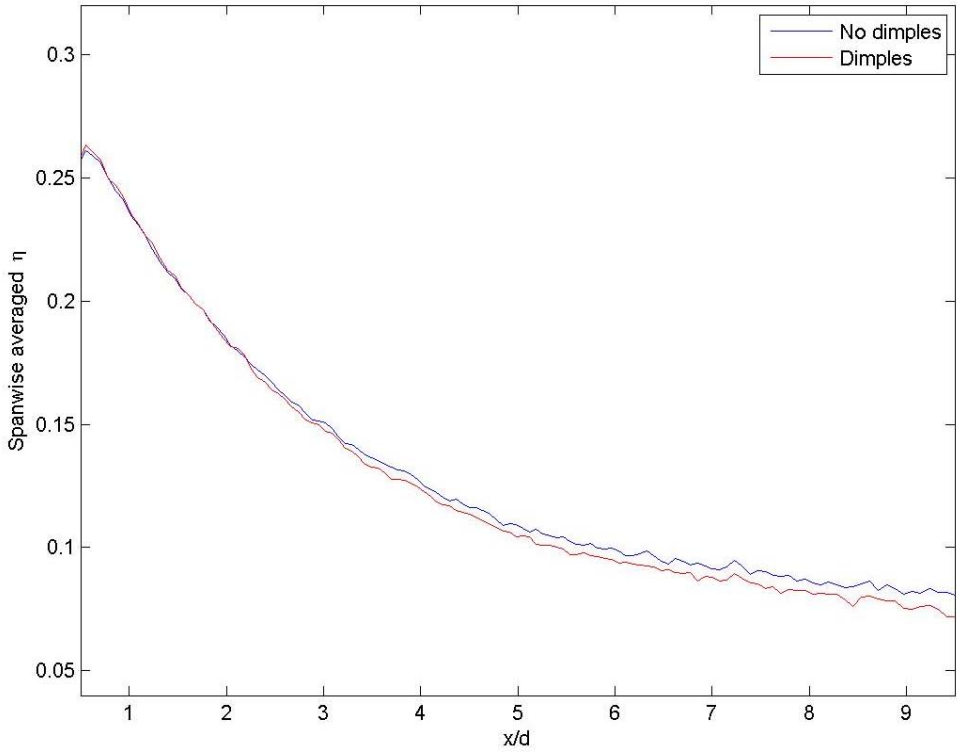

Fig B.12 Spanwise averaged η at Re = 30k and high turbulence for M = 0.25

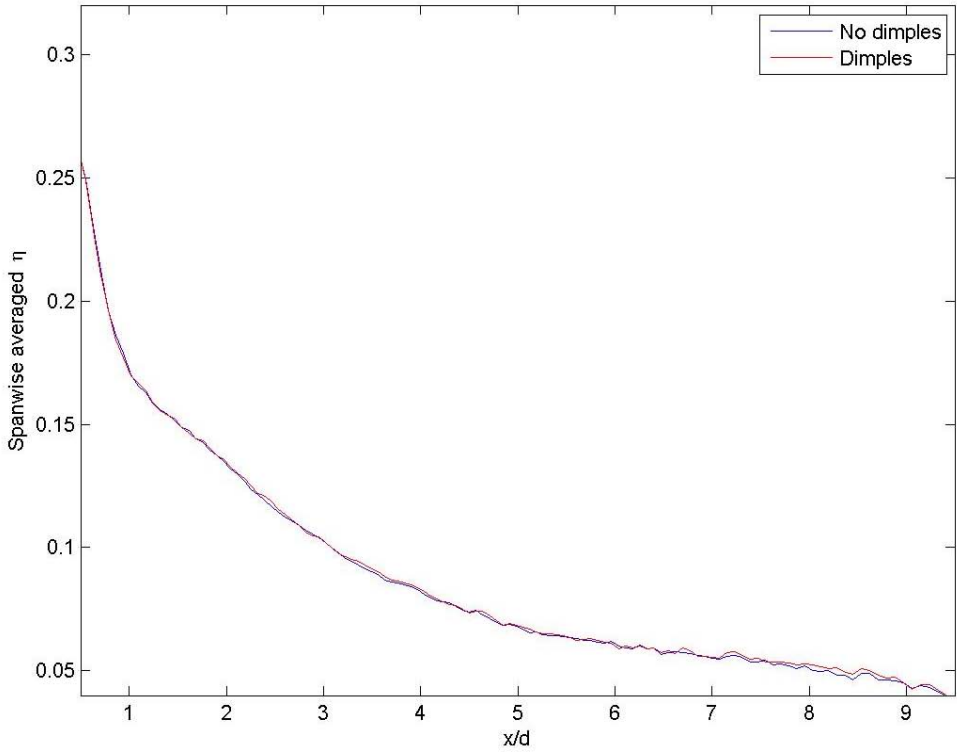

Fig B.13 Spanwise averaged η at Re = 30k and low turbulence for M = 1.5

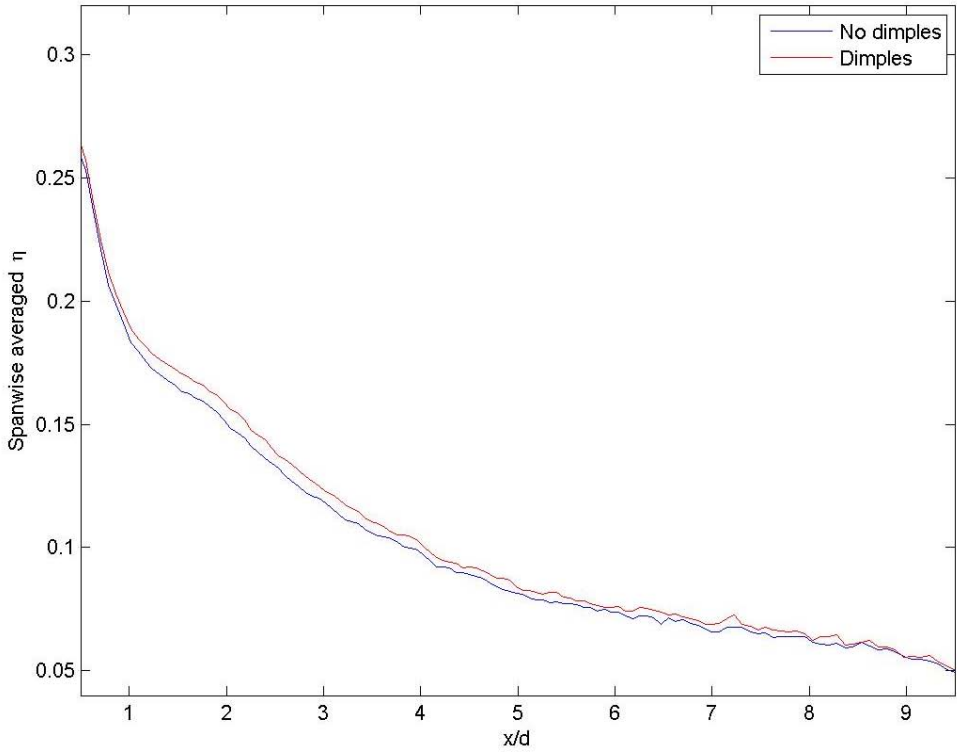

Fig B.14 Spanwise averaged η at Re = 30k and low turbulence for M = 1.25

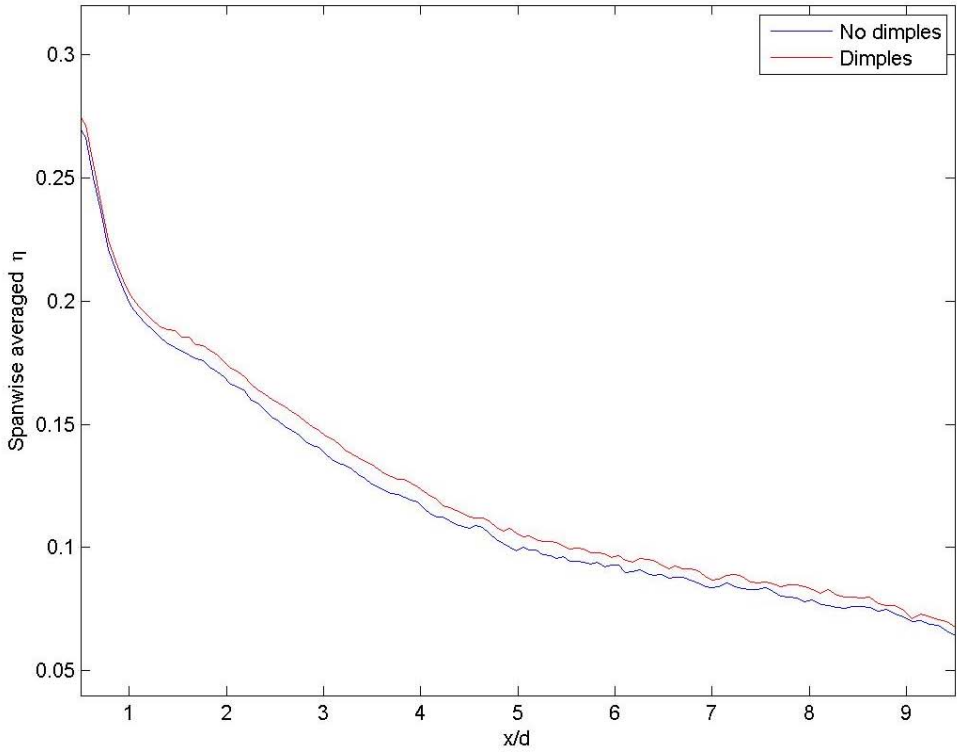

Fig B.15 Spanwise averaged η at Re = 30k and low turbulence for M = 1.0

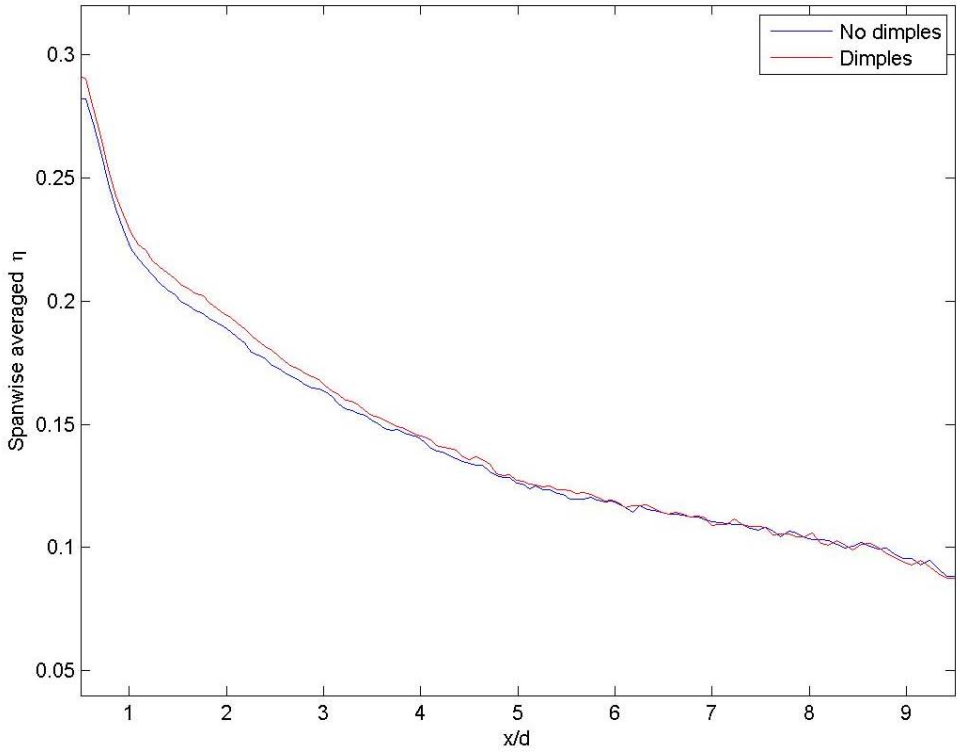

Fig B.16 Spanwise averaged η at Re = 30k and low turbulence for M = 0.75

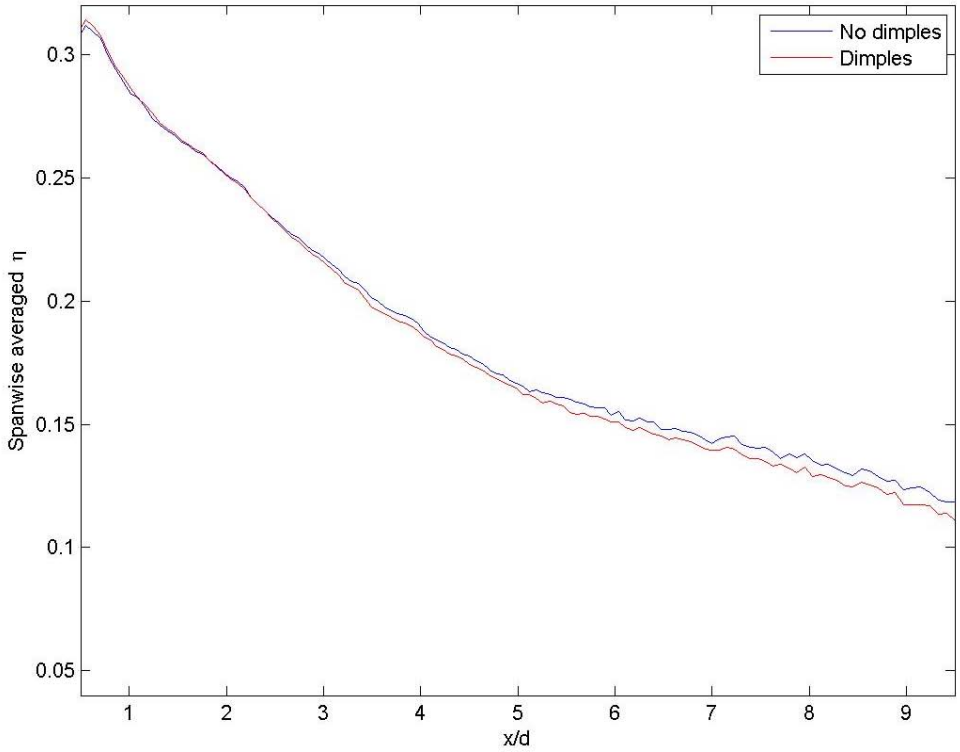

Fig B.17 Spanwise averaged η at Re = 30k and low turbulence for M = 0.5

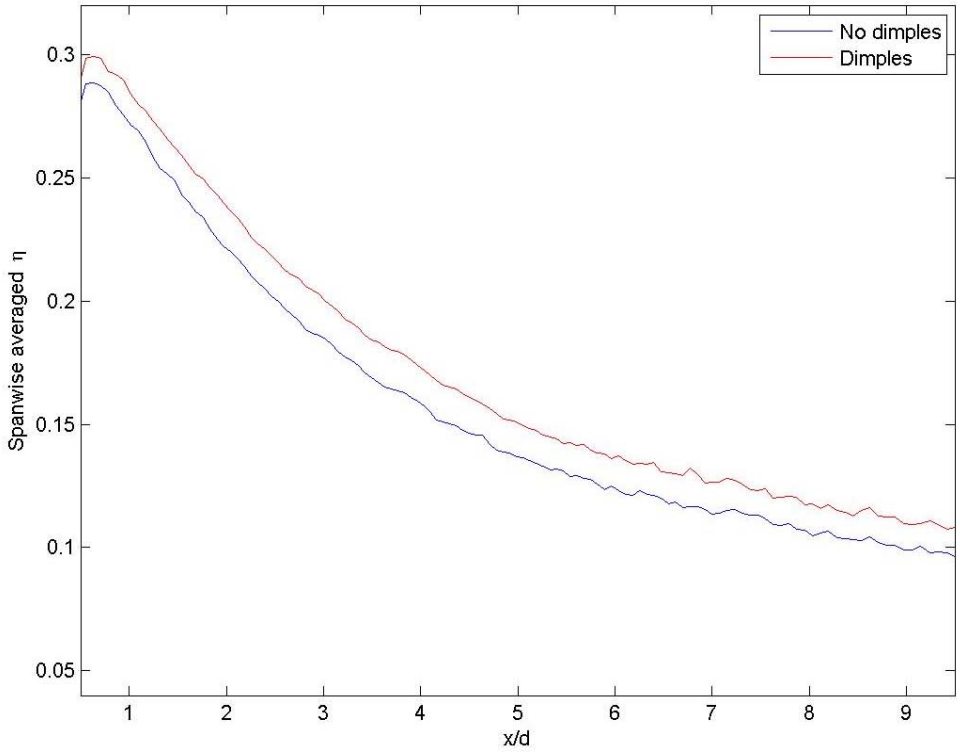

Fig B.18 Spanwise averaged η at Re = 30k and low turbulence for M = 0.25

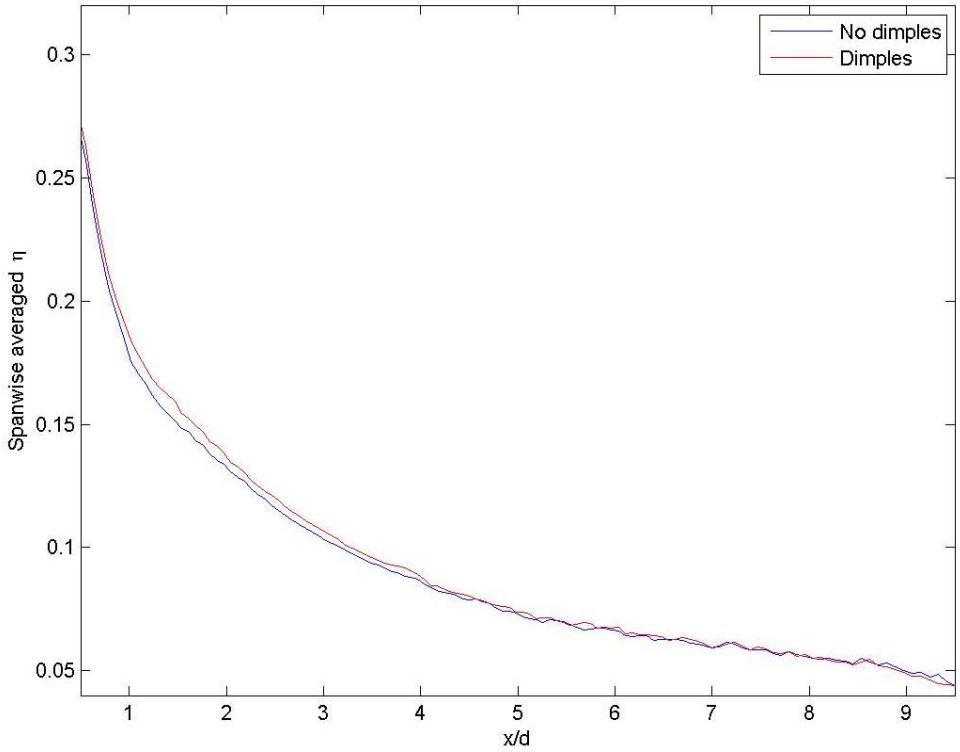

Fig B.19 Spanwise averaged η at Re = 60k and low turbulence for M = 1.5

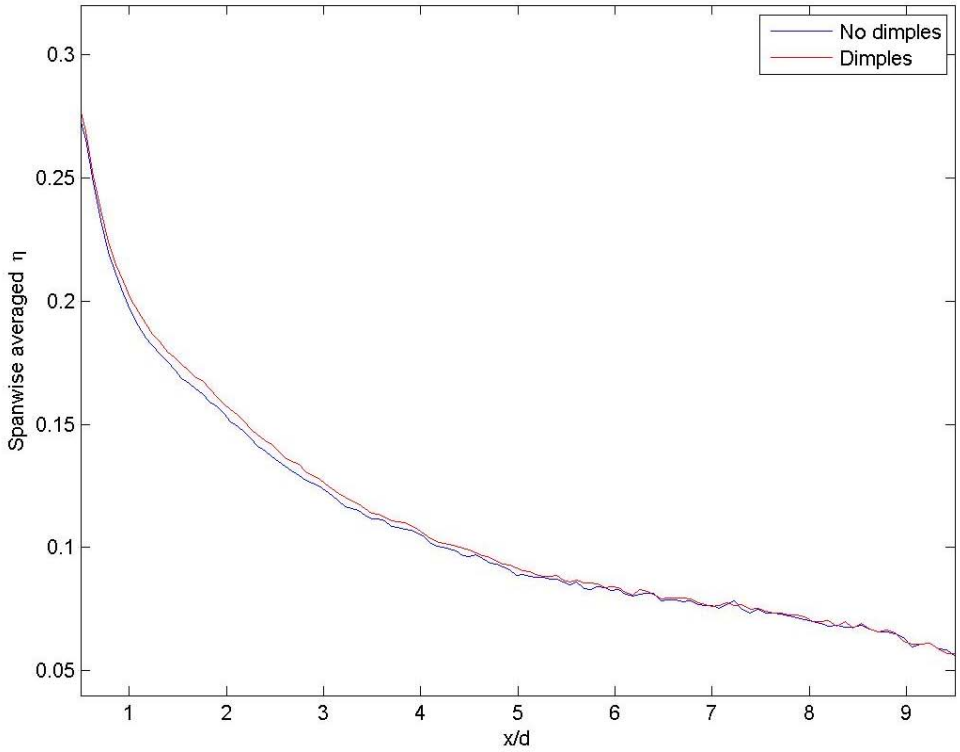

Fig B.20 Spanwise averaged η at Re = 60k and low turbulence for M = 1.25

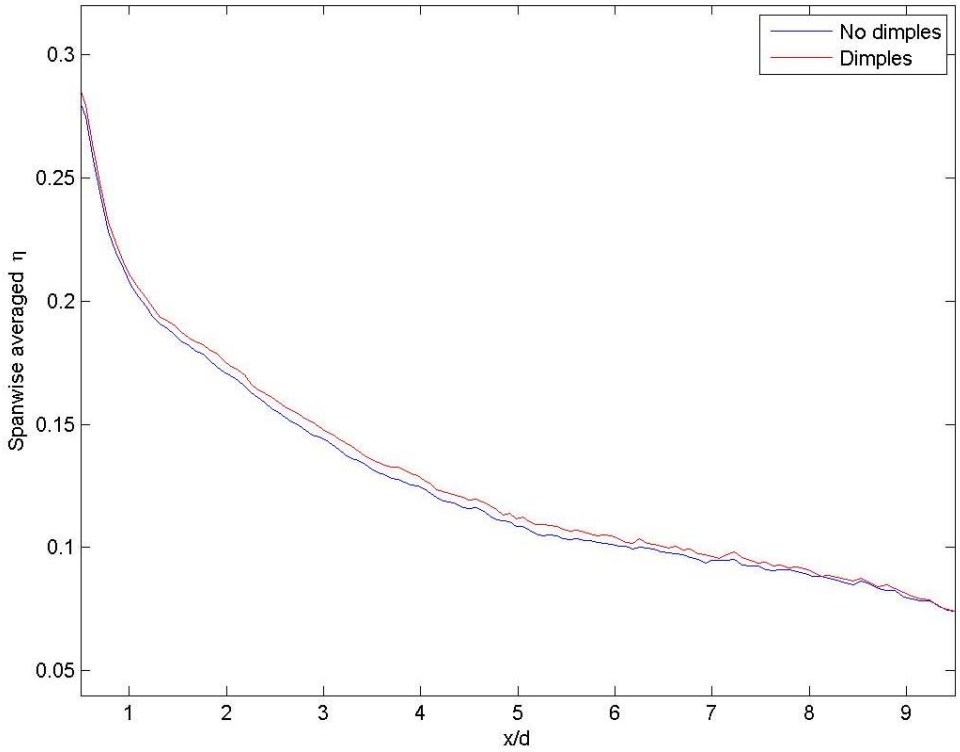

Fig B.21 Spanwise averaged η at Re = 60k and low turbulence for M = 1.0

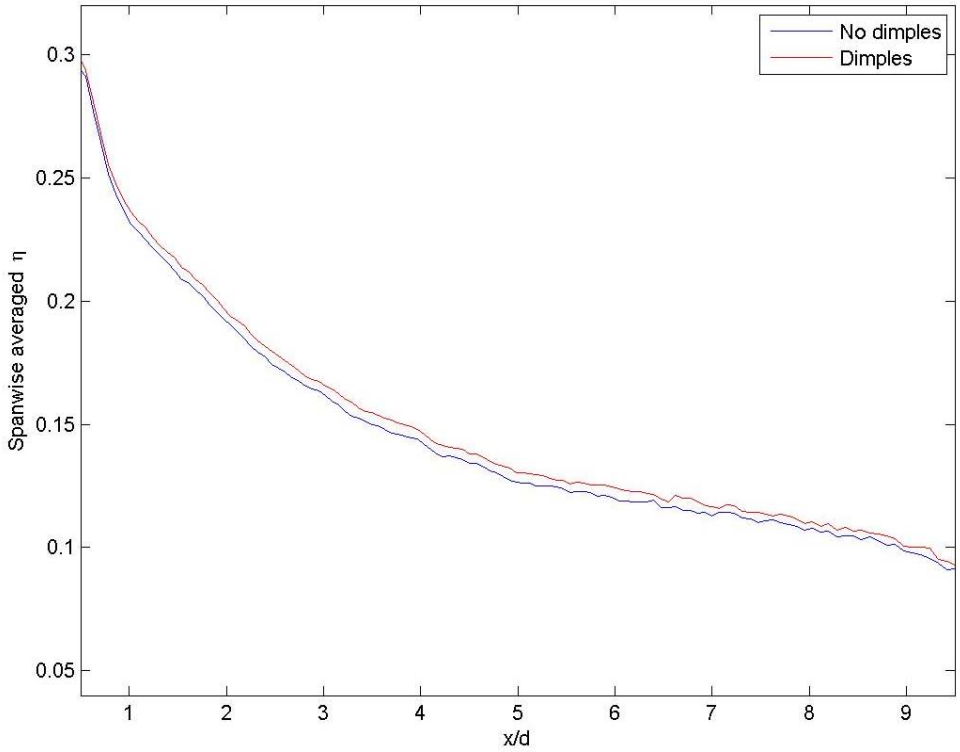

Fig B.22 Spanwise averaged η at Re = 60k and low turbulence for M = 0.75

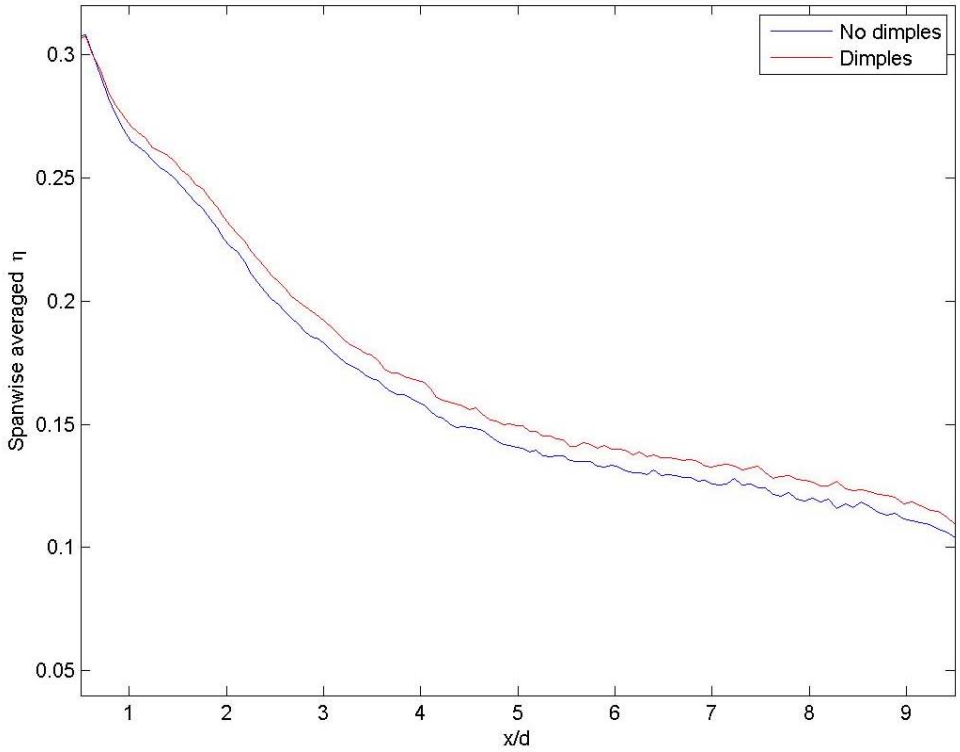

Fig B.23 Spanwise averaged η at Re = 60k and low turbulence for M = 0.5

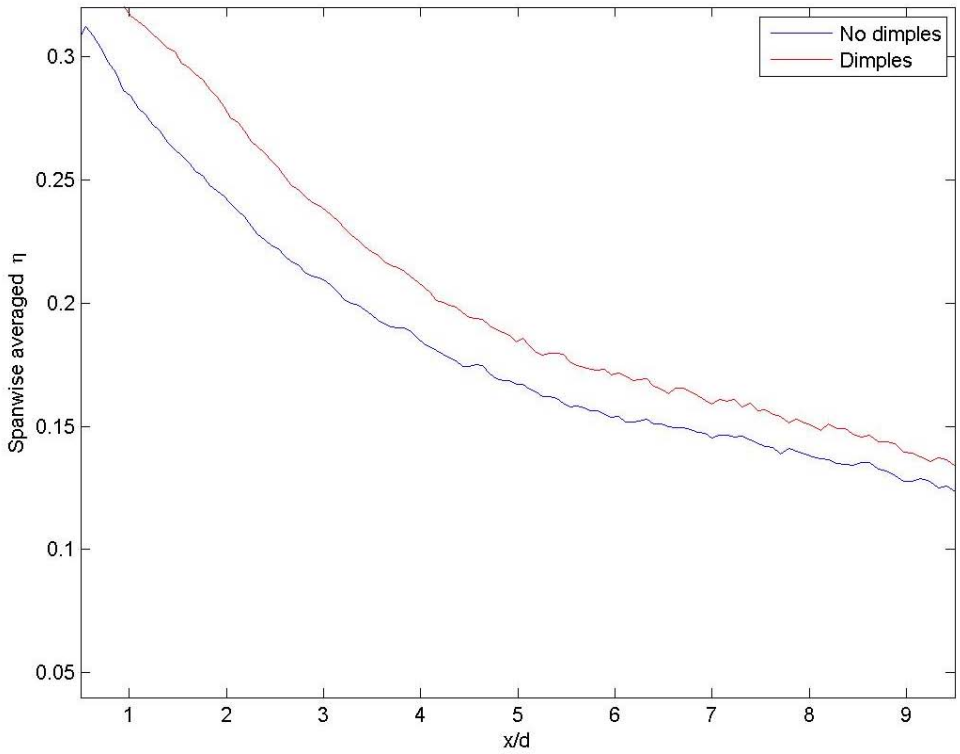

Fig B.24 Spanwise averaged η at Re = 60k and low turbulence for M = 0.25

Appendix C. Frössling Number Contour Plots

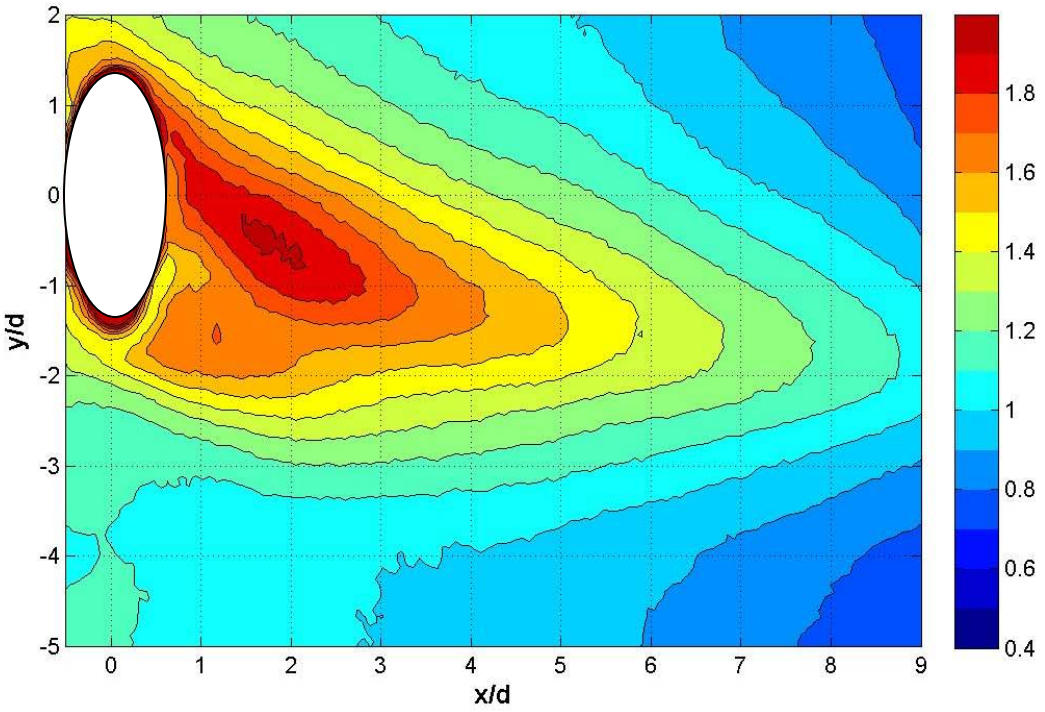

Fig C.1 Contour of *Fr* with dimples at Re = 60k and high turbulence for M = 1.5

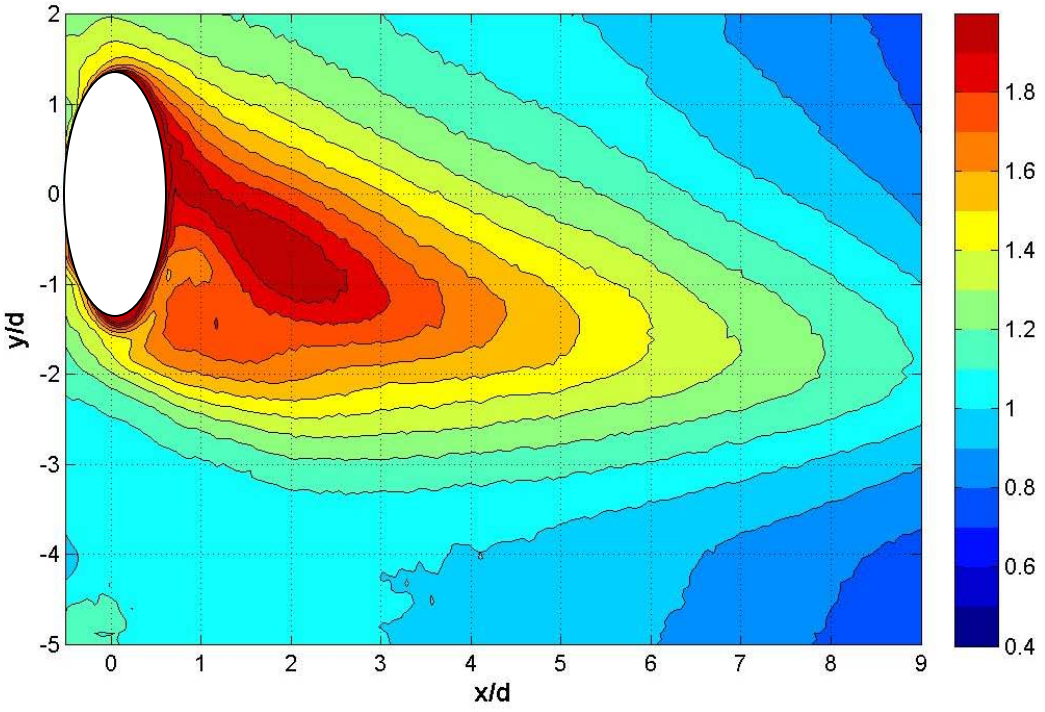

Fig C.2 Contour of *Fr* without dimples at Re = 60k and high turbulence for M = 1.5

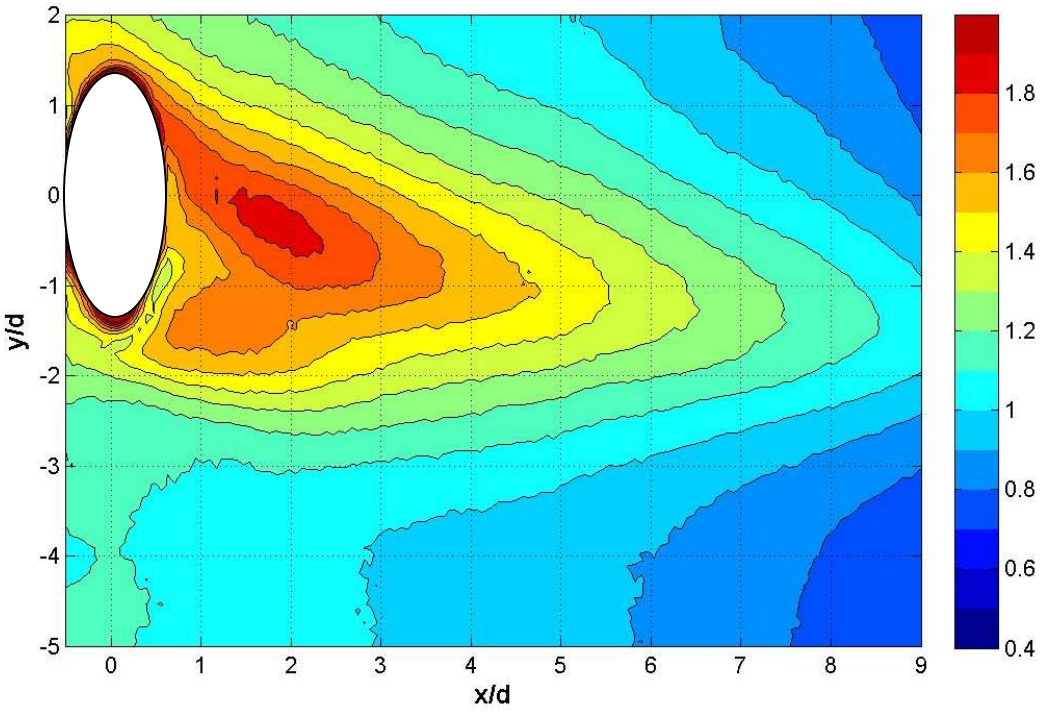

Fig C.3 Contour of *Fr* with dimples at Re = 60k and high turbulence for M = 1.25

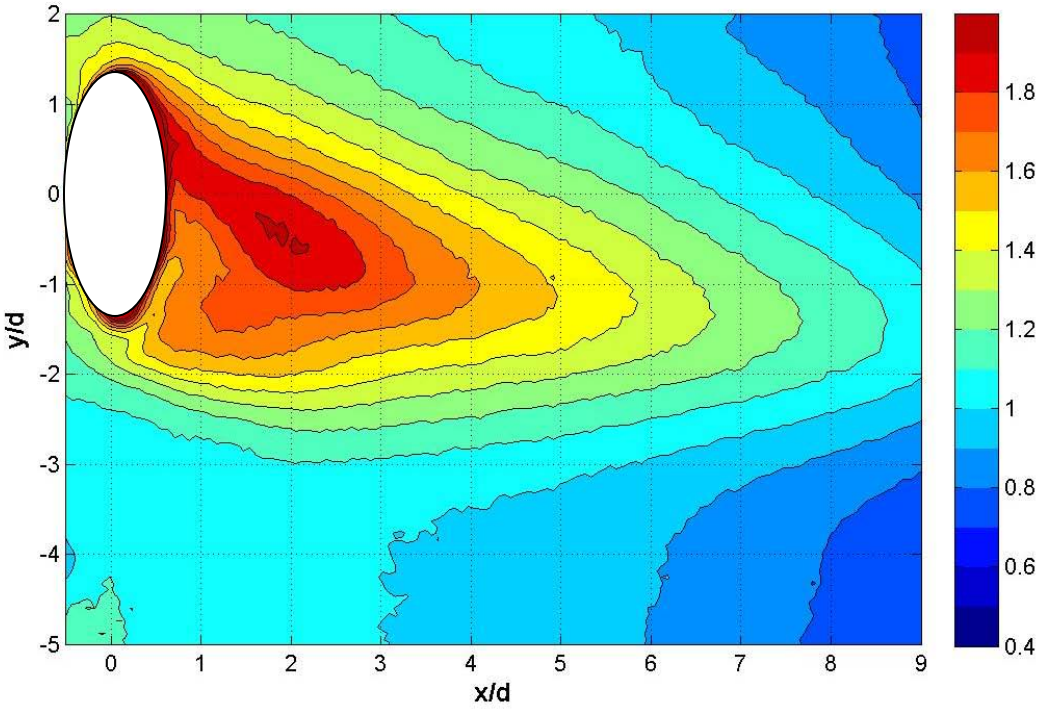

Fig C.4 Contour of *Fr* without dimples at Re = 60k and high turbulence for M = 1.25

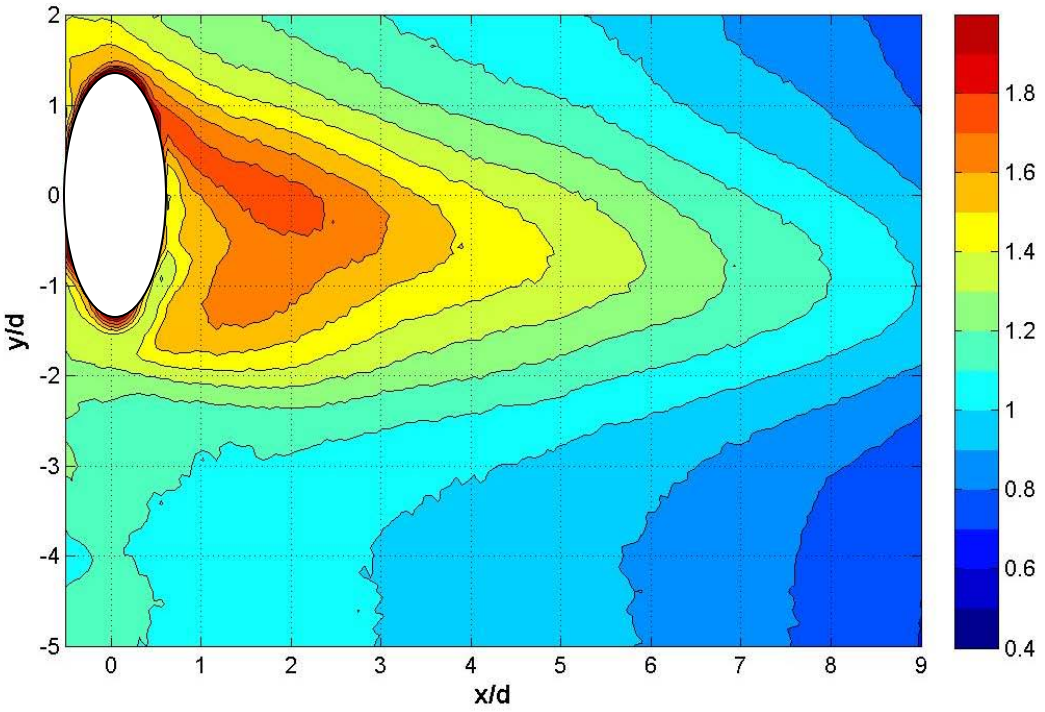

Fig C.5 Contour of *Fr* with dimples at Re = 60k and high turbulence for M = 1.0

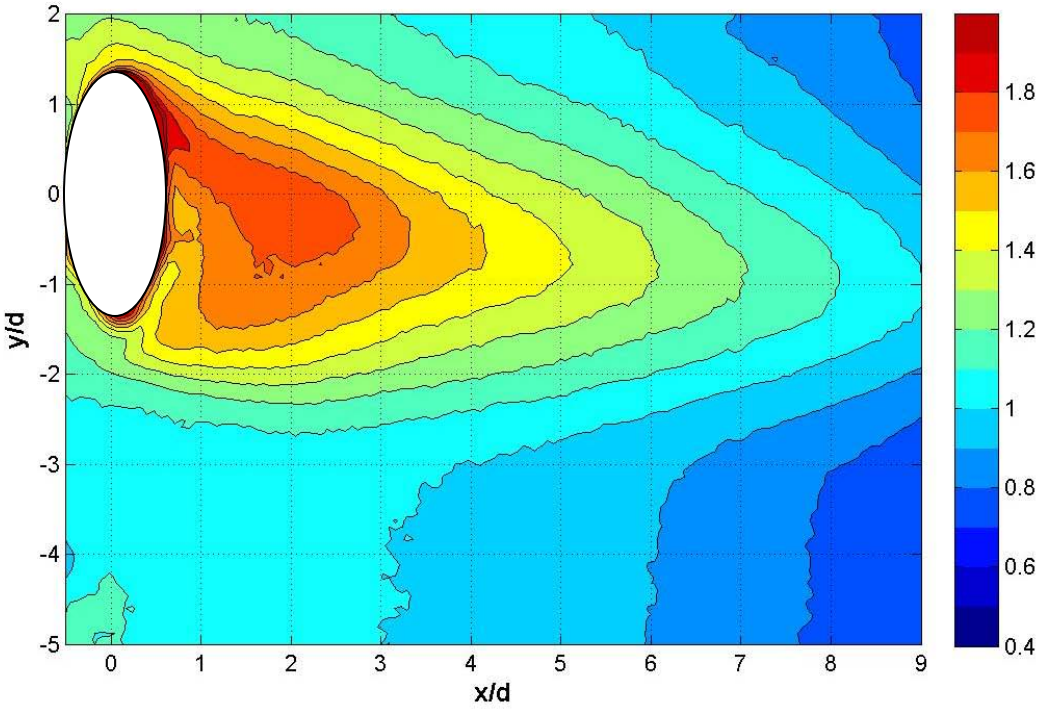

Fig C.6 Contour of *Fr* without dimples at Re = 60k and high turbulence for M = 1.0

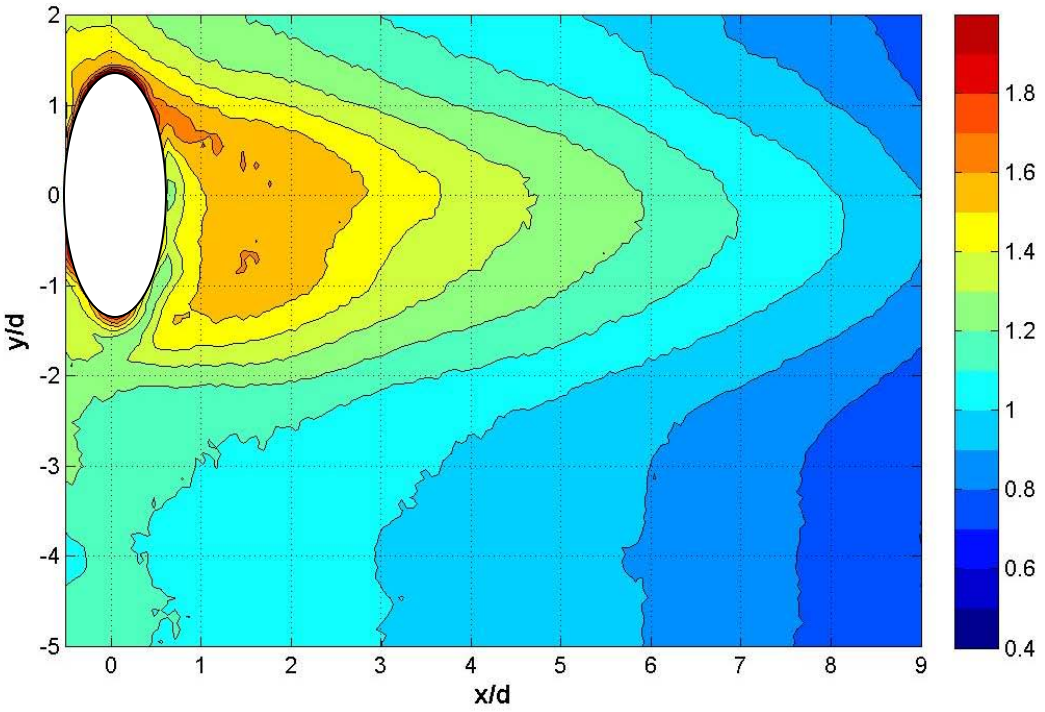

Fig C.7 Contour of *Fr* with dimples at Re = 60k and high turbulence for M = 0.75

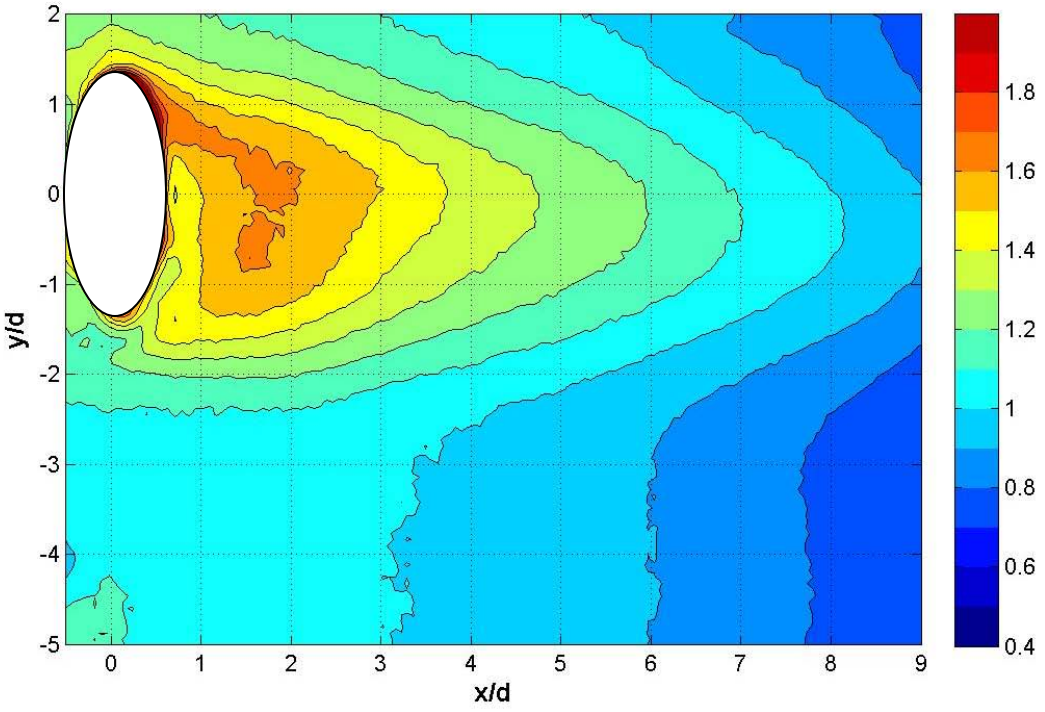

Fig C.8 Contour of *Fr* without dimples at Re = 60k and high turbulence for M = 0.75

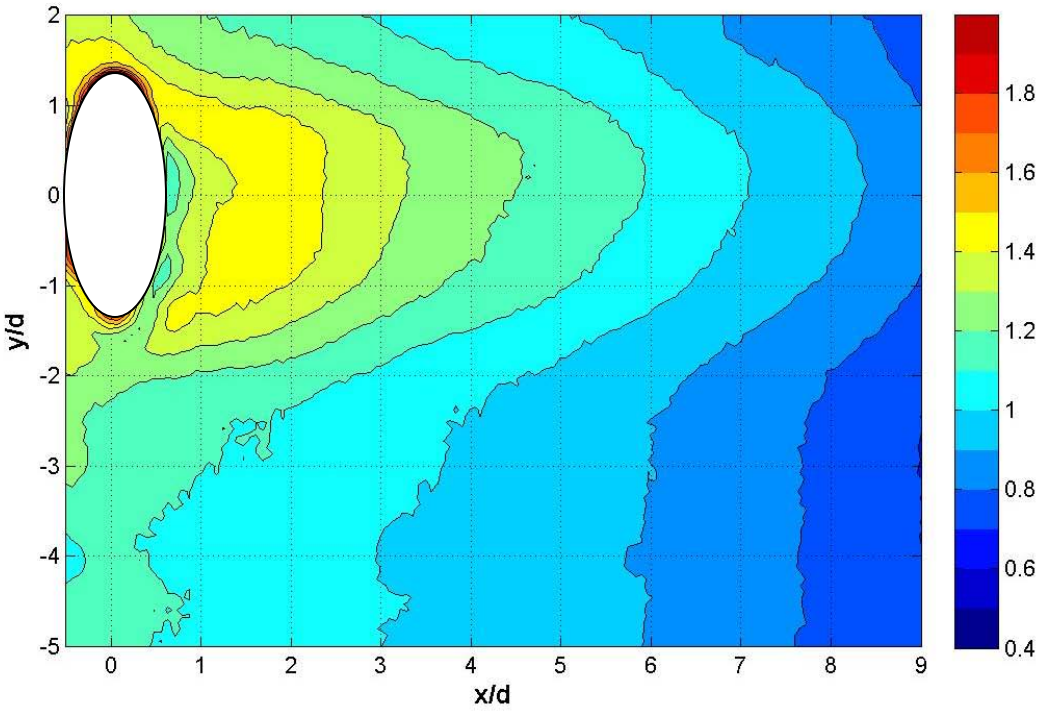

Fig C.9 Contour of *Fr* with dimples at Re = 60k and high turbulence for M = 0.5

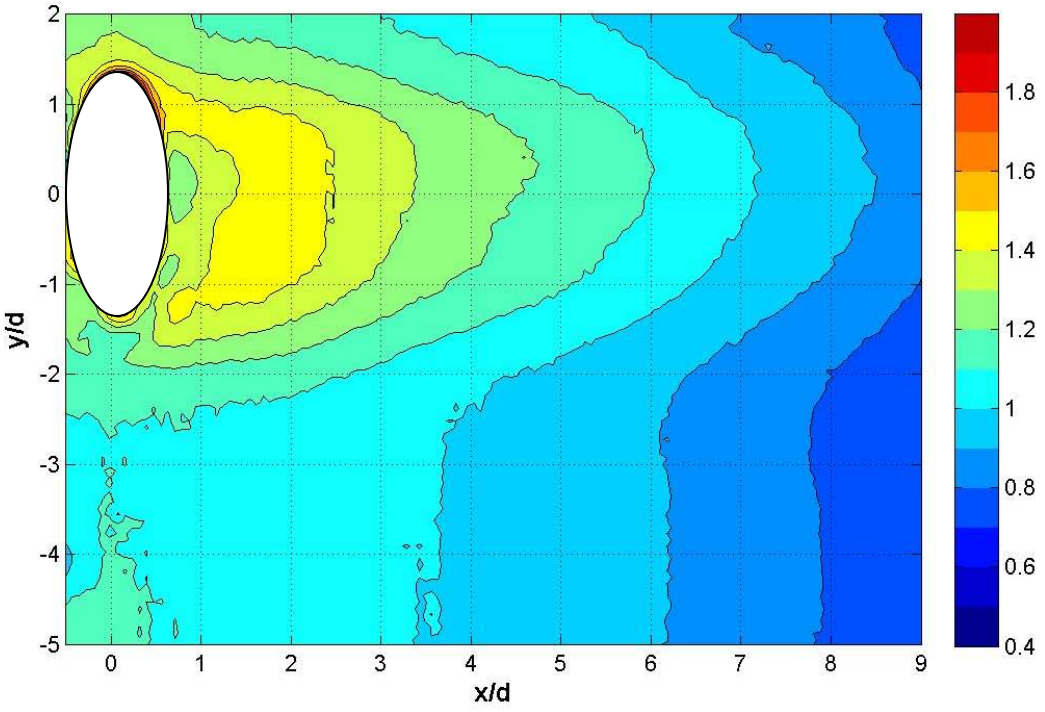

Fig C.10 Contour of *Fr* without dimples at Re = 60k and high turbulence for M = 0.5

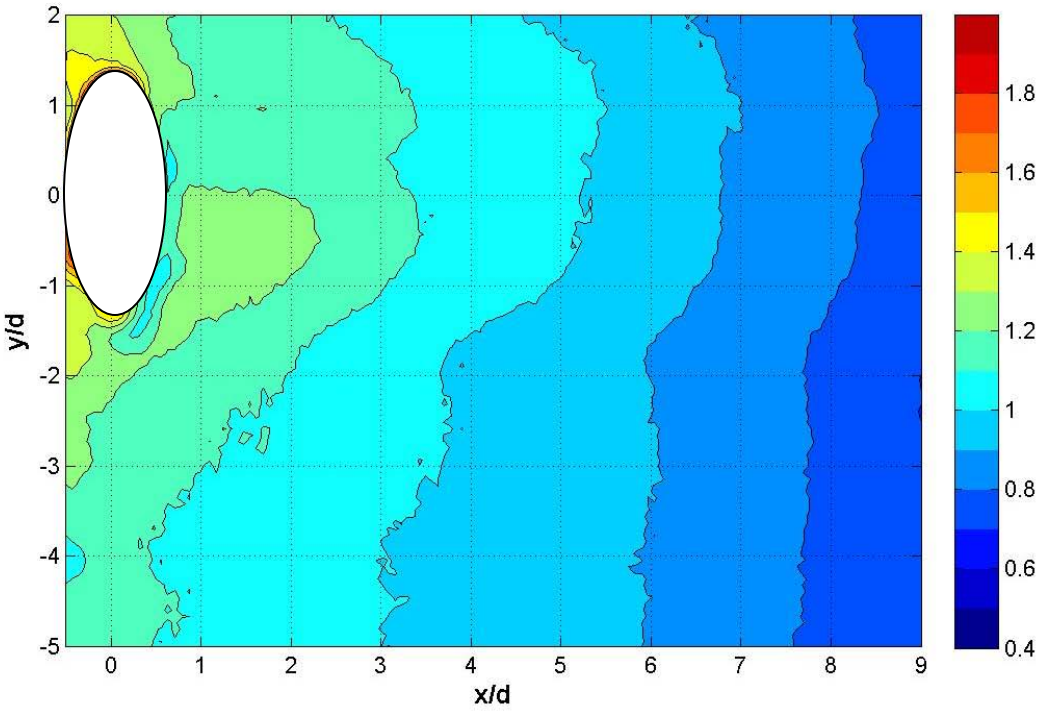

Fig C.11 Contour of *Fr* with dimples at Re = 60k and high turbulence for M = 0.25

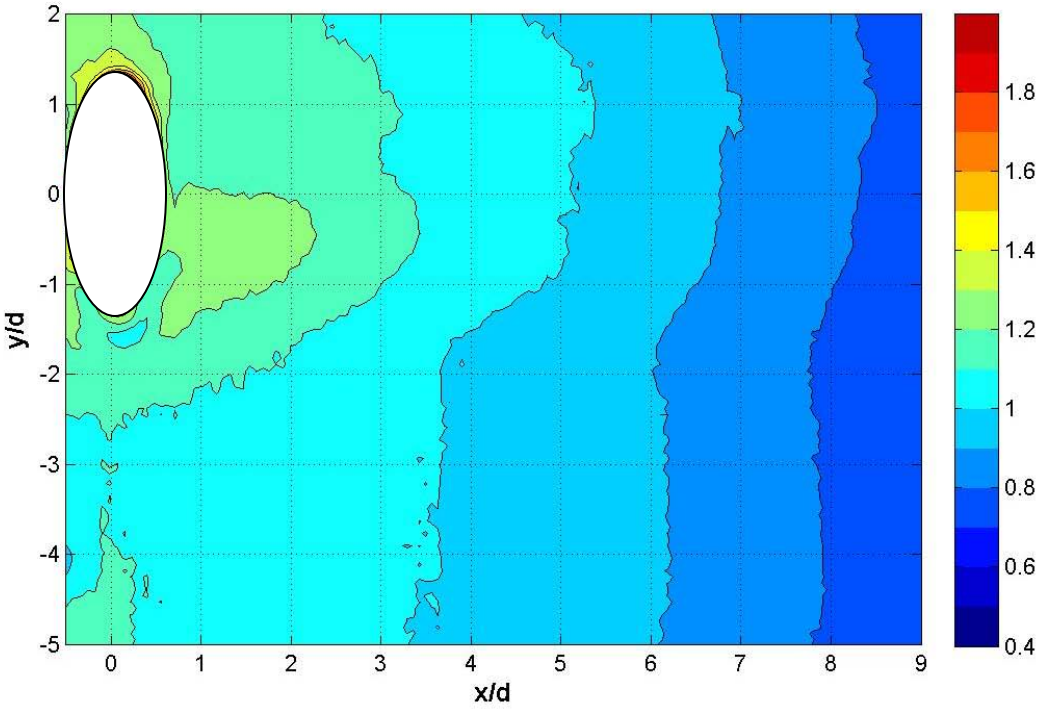

Fig C.12 Contour of *Fr* without dimples at Re = 60k and high turbulence for M = 0.25

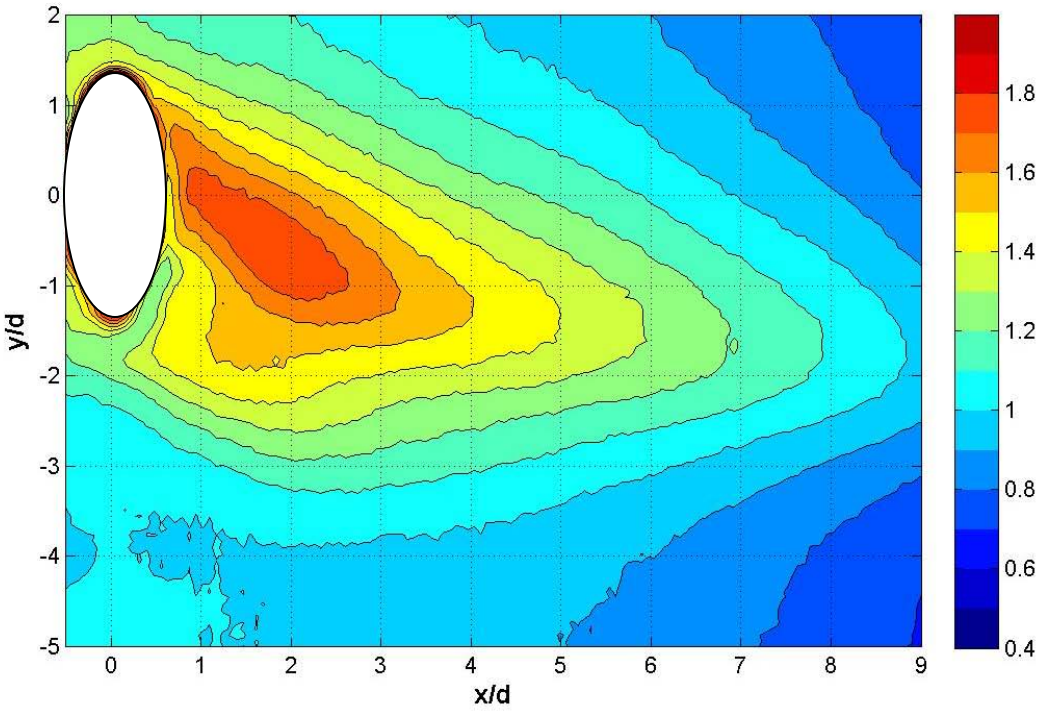

Fig C.13 Contour of *Fr* with dimples at Re = 30k and high turbulence for M = 1.5

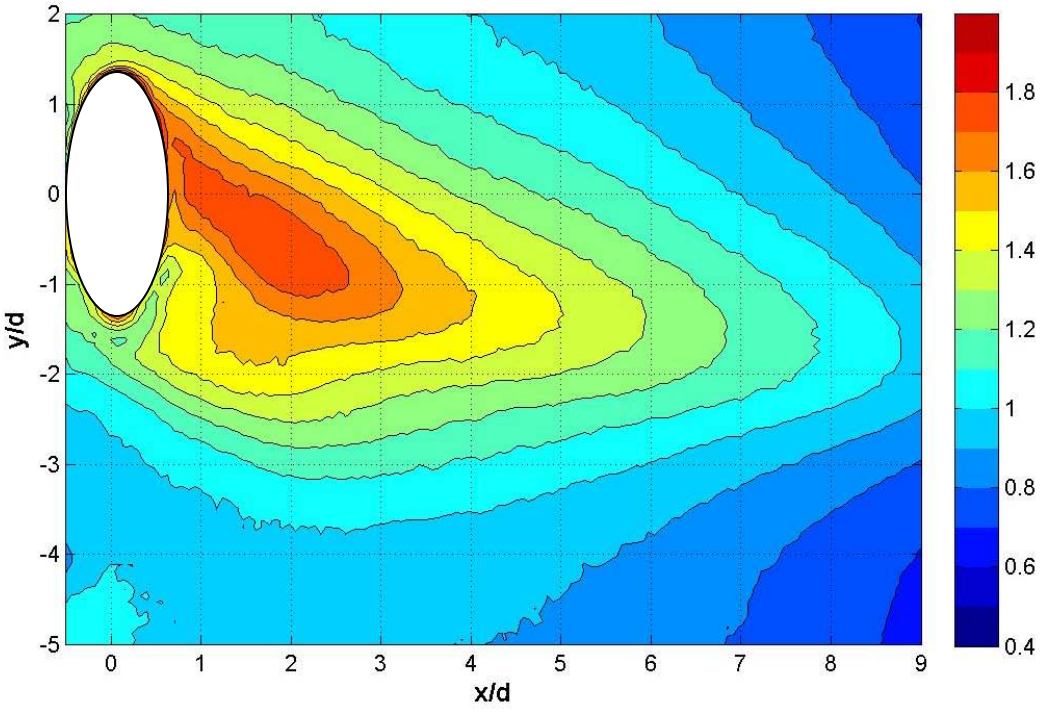

Fig C.14 Contour of *Fr* without dimples at Re = 30k and high turbulence for M = 1.5

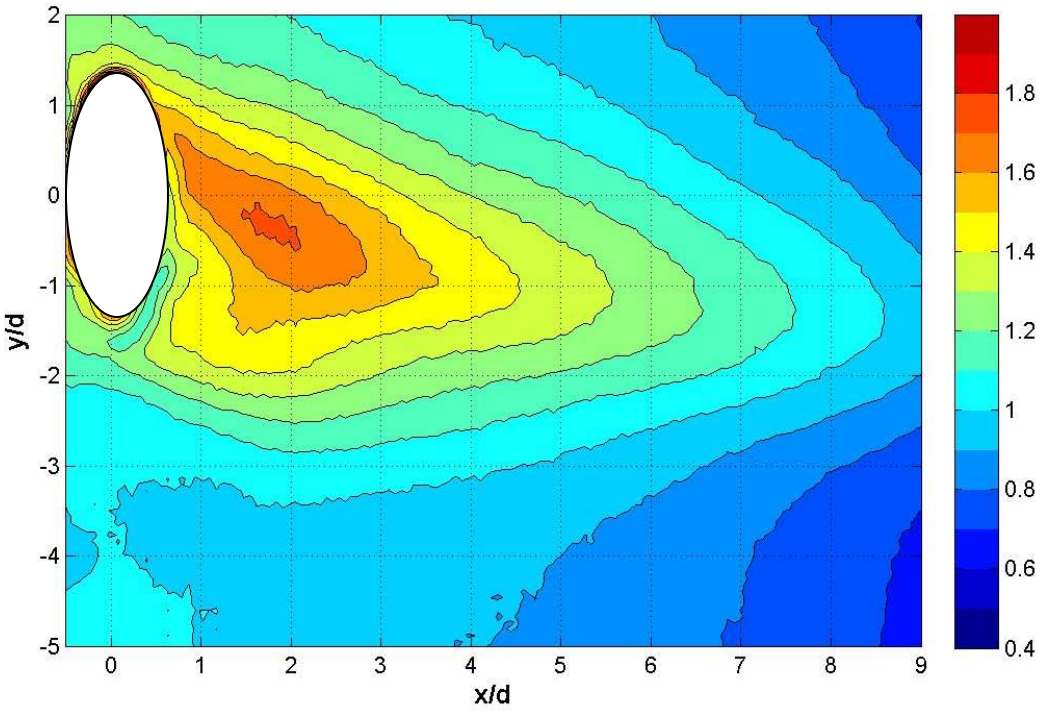

Fig C.15 Contour of *Fr* with dimples at Re = 30k and high turbulence for M = 1.25

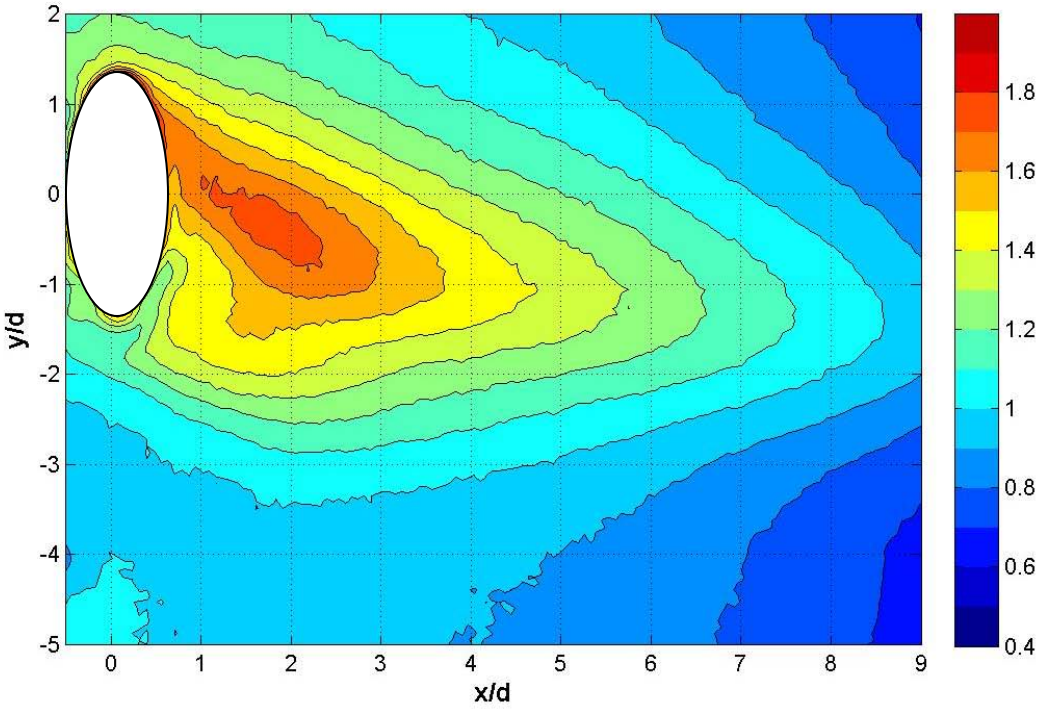

Fig C.16 Contour of *Fr* without dimples at Re = 30k and high turbulence for M = 1.25

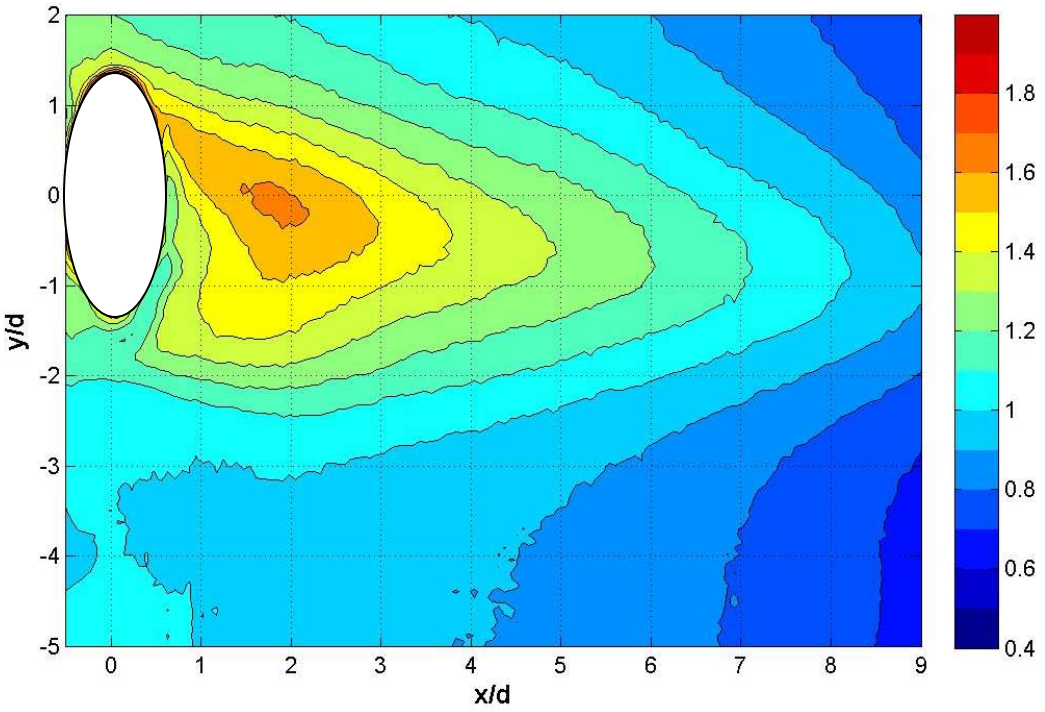

Fig C.17 Contour of *Fr* with dimples at Re = 30k and high turbulence for M = 1.0

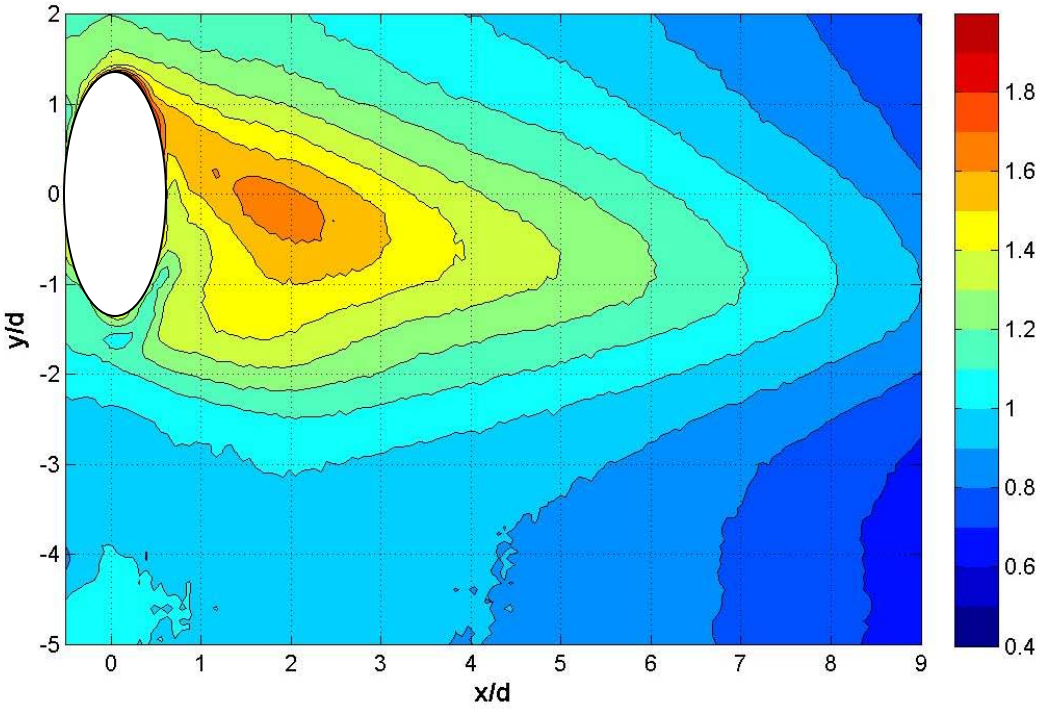

Fig C.18 Contour of *Fr* without dimples at Re = 30k and high turbulence for M = 1.0

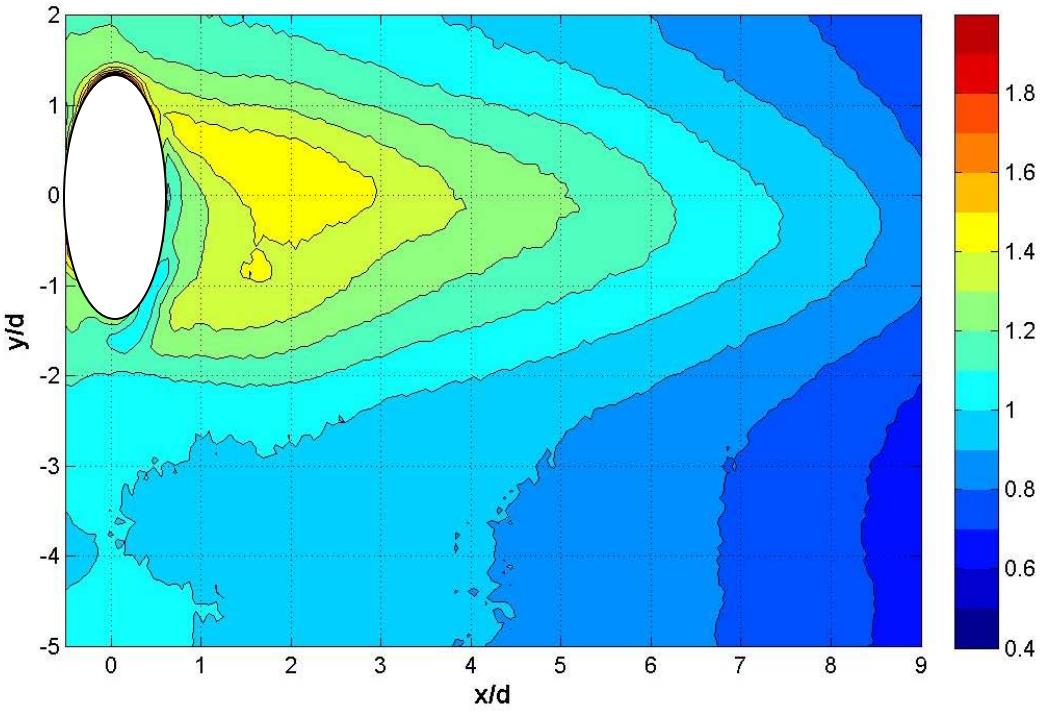

Fig C.19 Contour of *Fr* with dimples at Re = 30k and high turbulence for M = 0.75

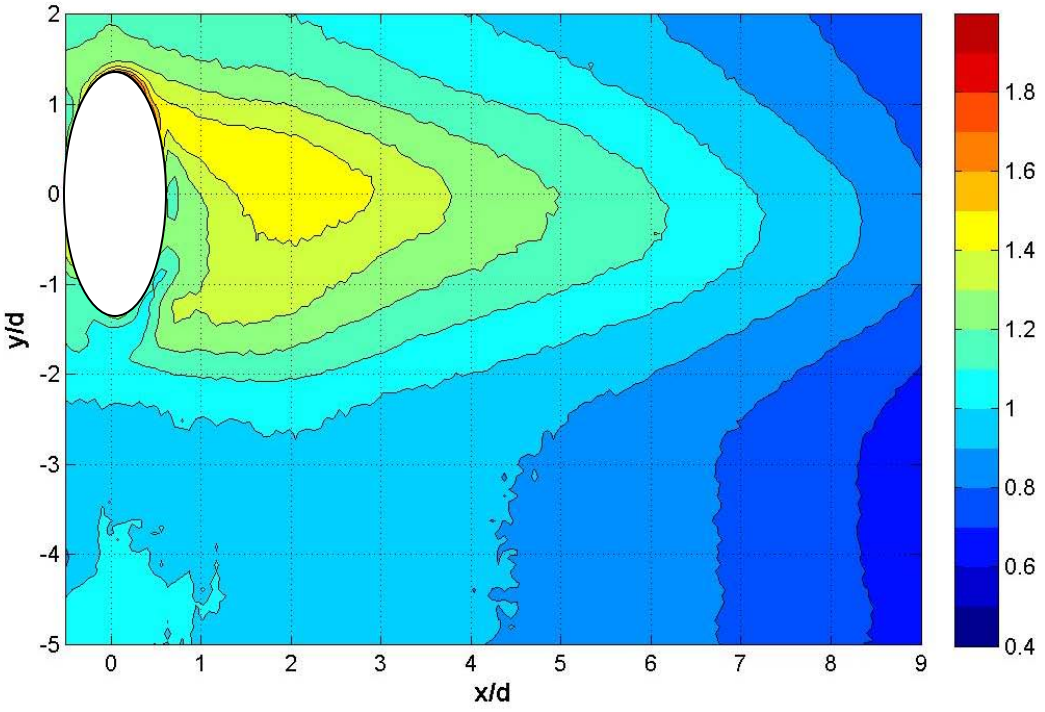

Fig C.20 Contour of *Fr* without dimples at Re = 30k and high turbulence for M = 0.75

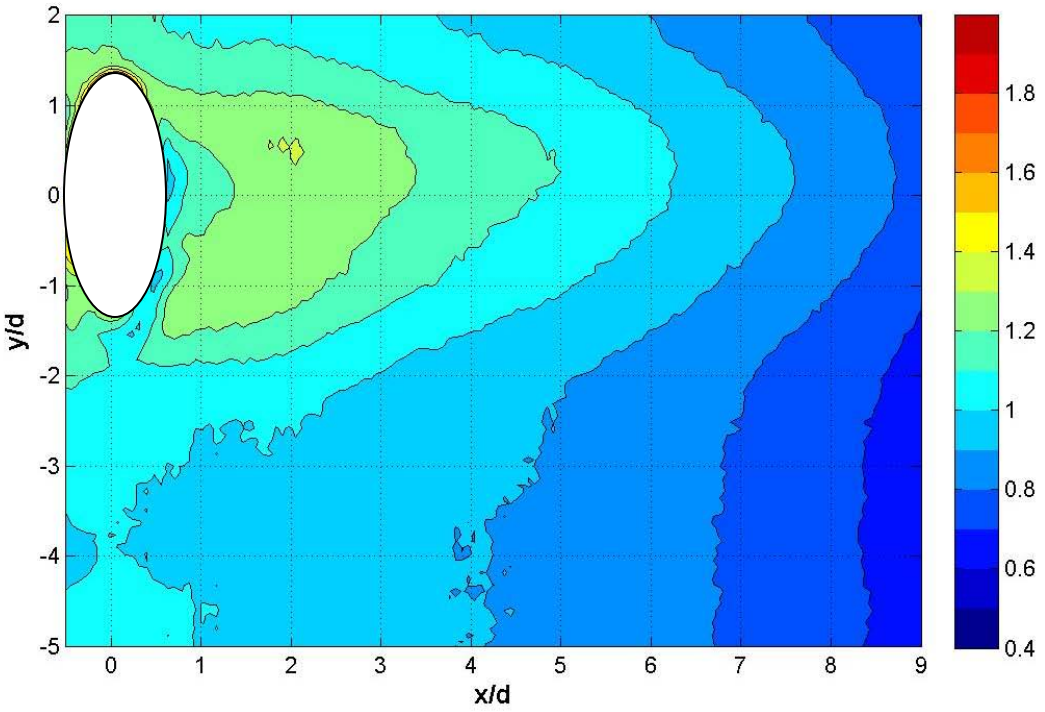

Fig C.21 Contour of *Fr* with dimples at Re = 30k and high turbulence for M = 0.5

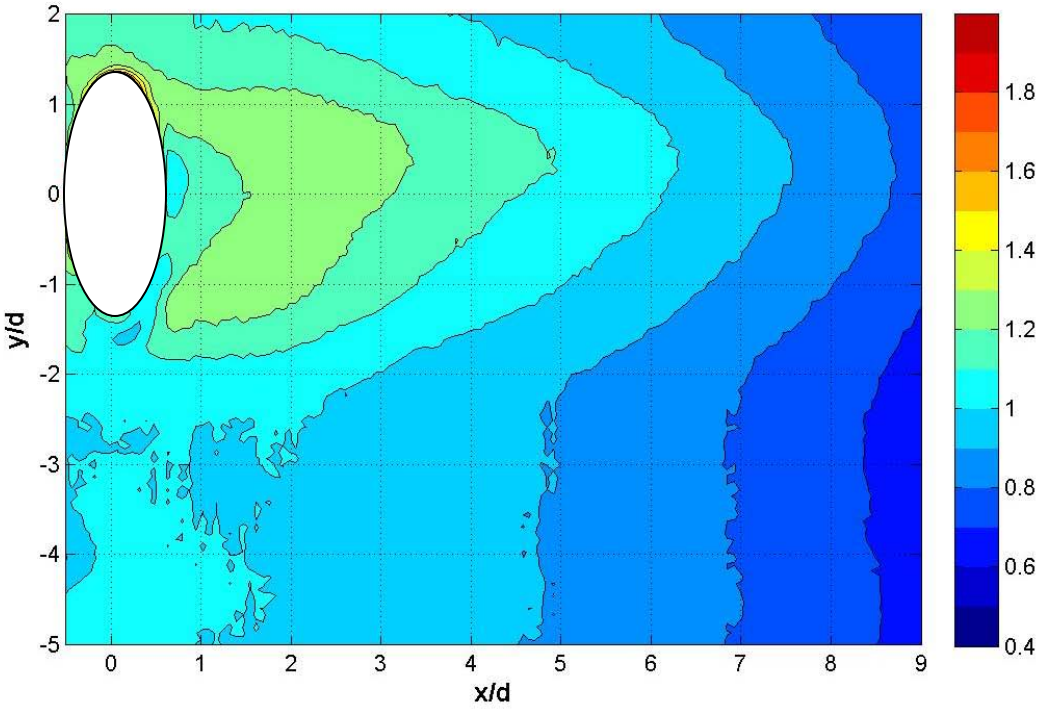

Fig C.22 Contour of *Fr* without dimples at Re = 30k and high turbulence for M = 0.5

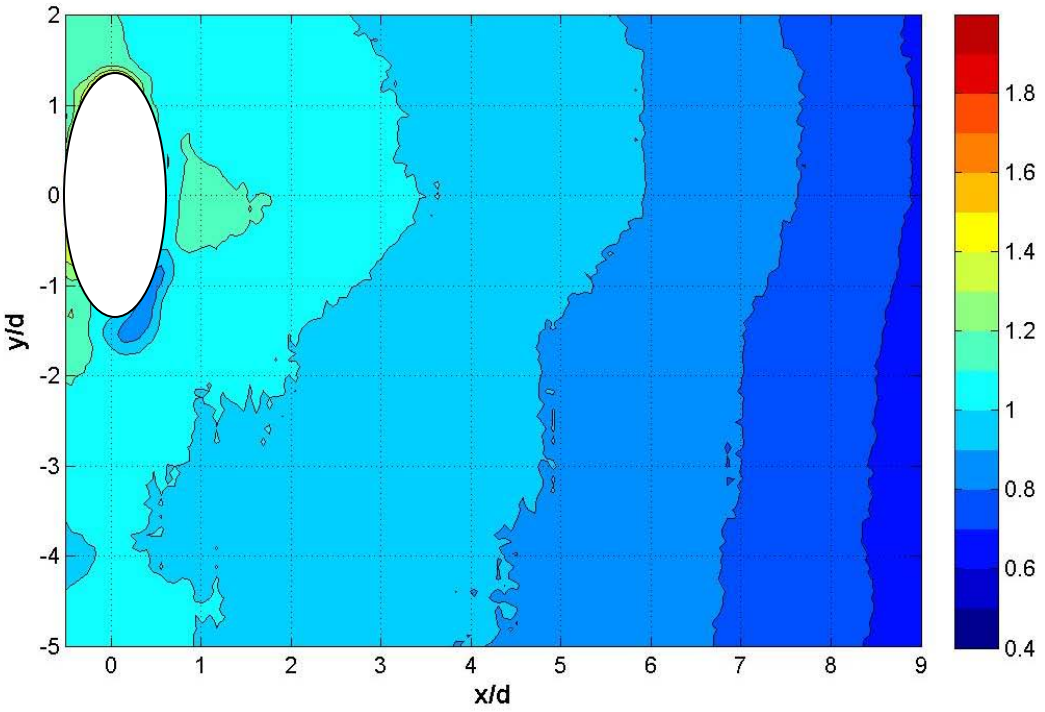

Fig C.23 Contour of *Fr* with dimples at Re = 30k and high turbulence for M = 0.25

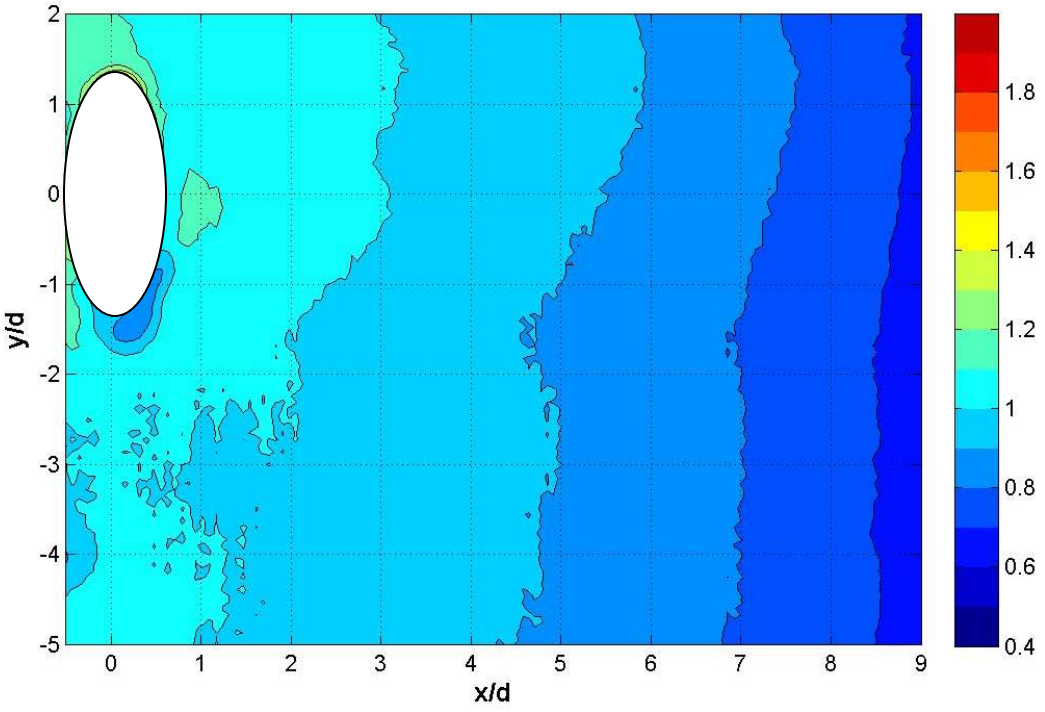

Fig C.24 Contour of *Fr* without dimples at Re = 30k and high turbulence for M = 0.25

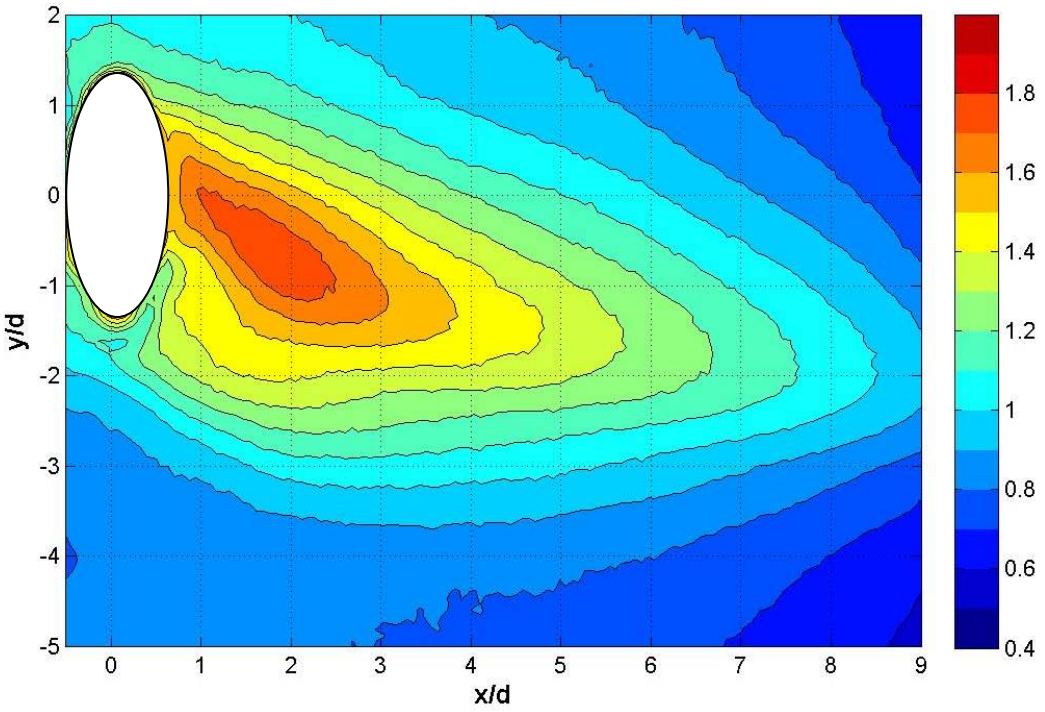

Fig C.25 Contour of *Fr* with dimples at Re = 30k and low turbulence for M = 1.5

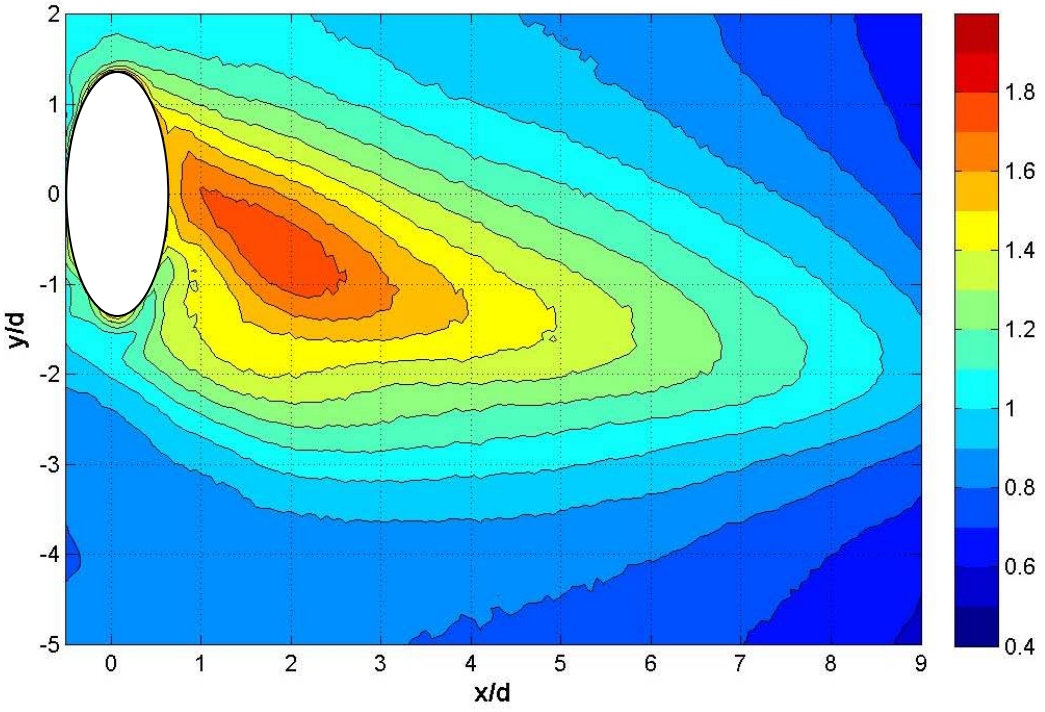

Fig C.26 Contour of *Fr* without dimples at Re = 30k and low turbulence for M = 1.5

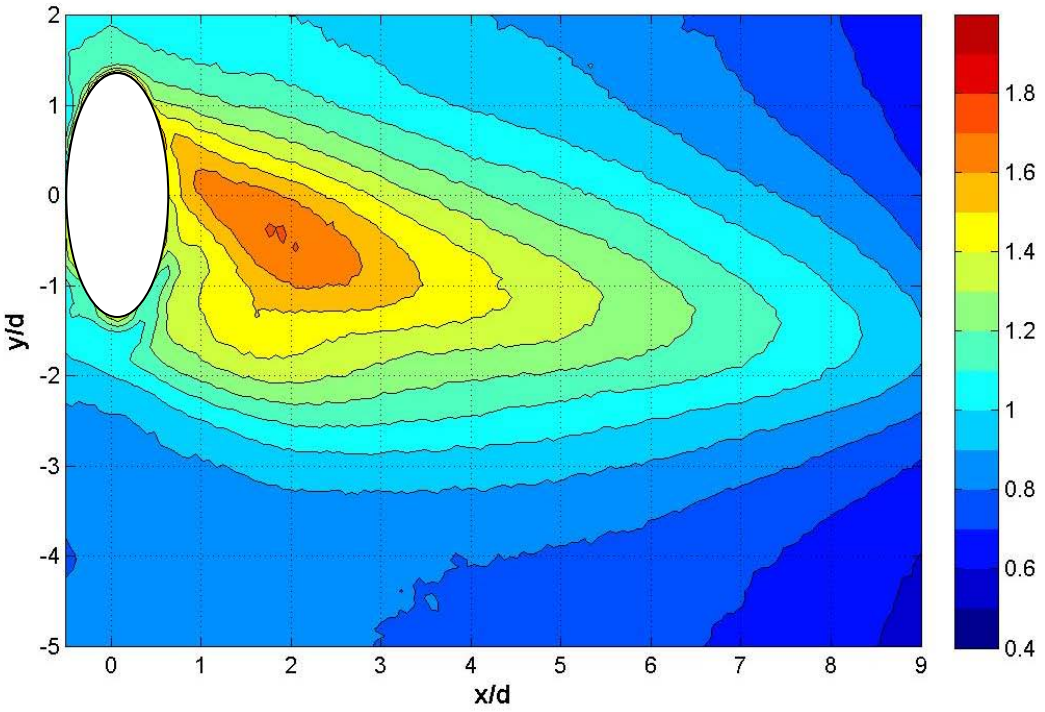

Fig C.27 Contour of *Fr* with dimples at Re = 30k and low turbulence for M = 1.25

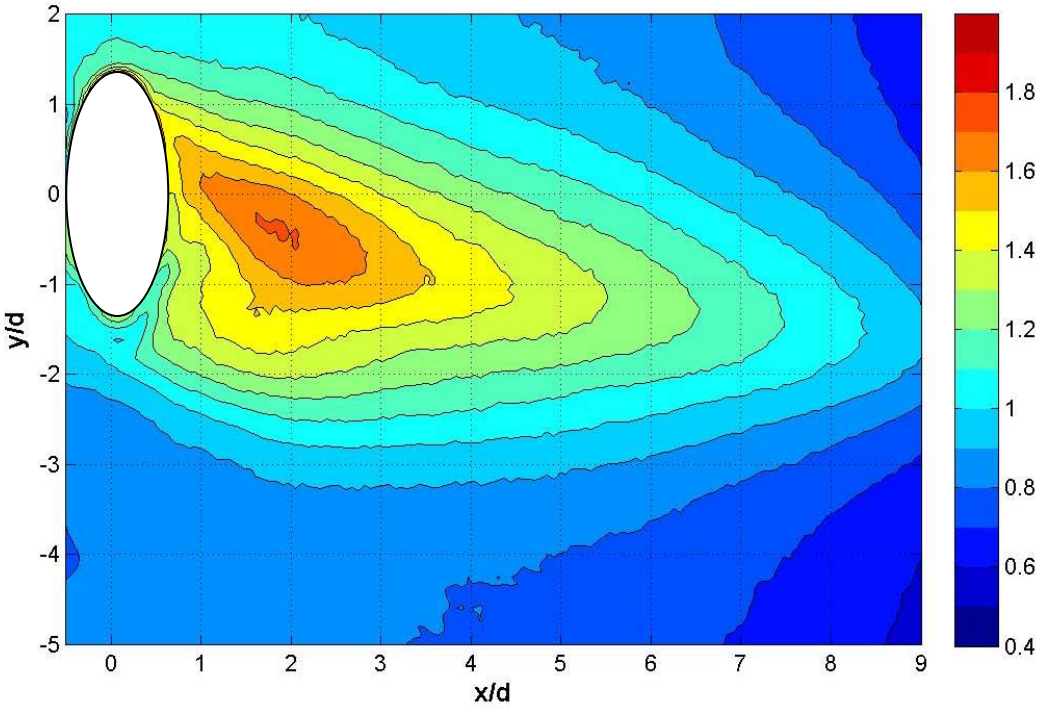

Fig C.28 Contour of *Fr* without dimples at Re = 30k and low turbulence for M = 1.25

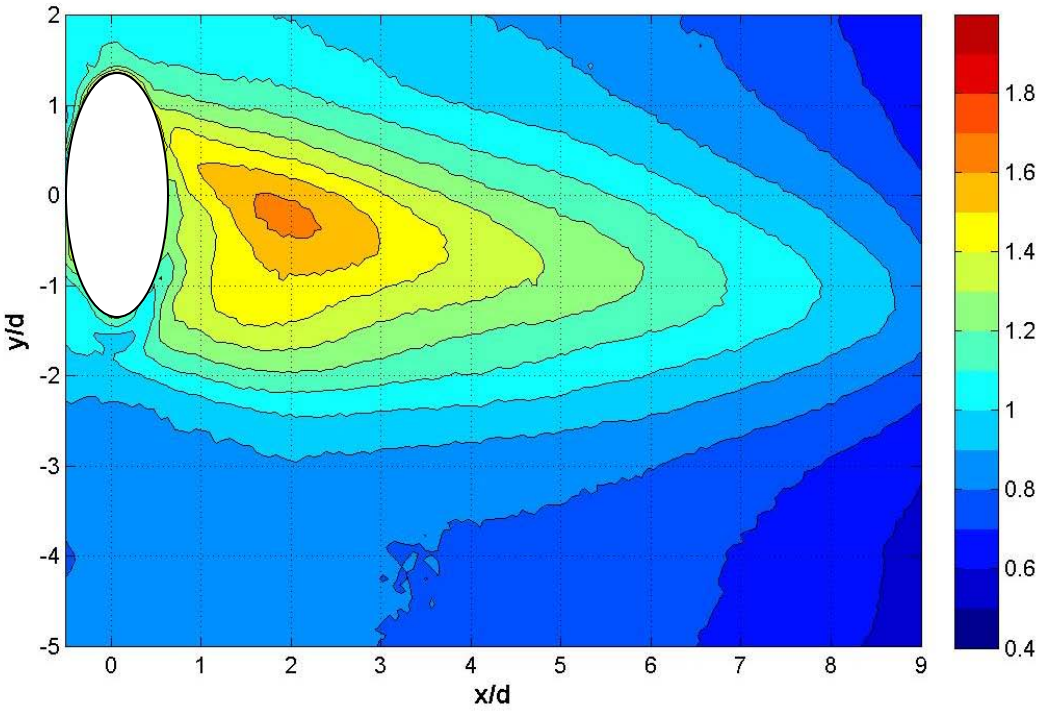

Fig C.29 Contour of *Fr* with dimples at Re = 30k and low turbulence for M = 1.0

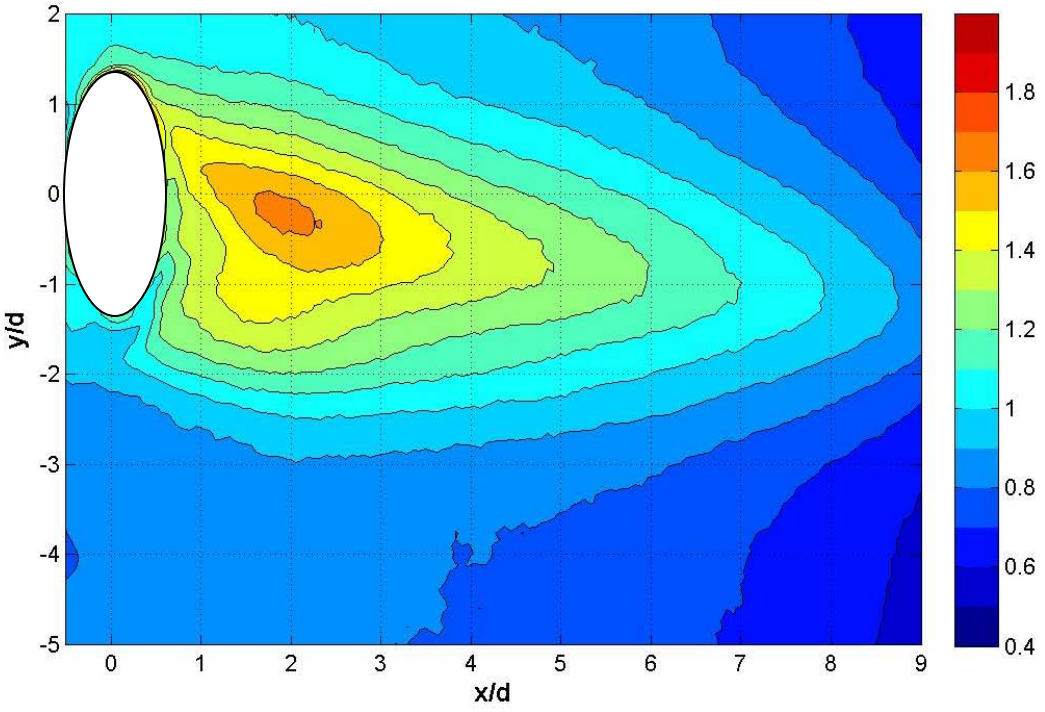

Fig C.30 Contour of *Fr* without dimples at Re = 30k and low turbulence for M = 1.0

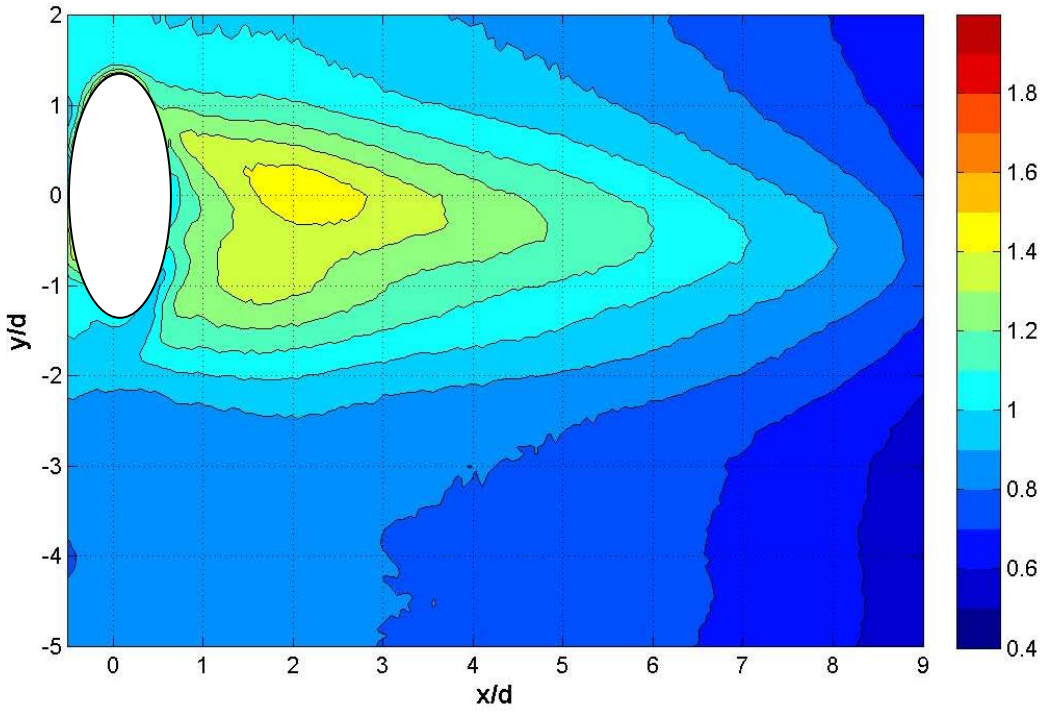

Fig C.31 Contour of *Fr* with dimples at Re = 30k and low turbulence for M = 0.75

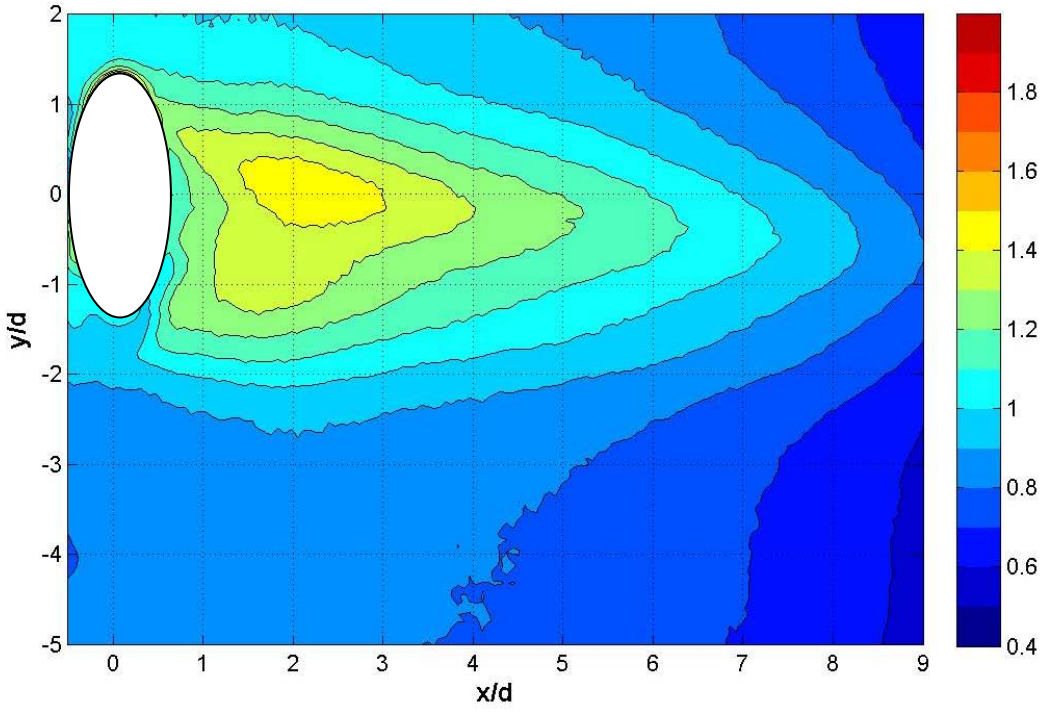

Fig C.32 Contour of *Fr* without dimples at Re = 30k and low turbulence for M = 0.75

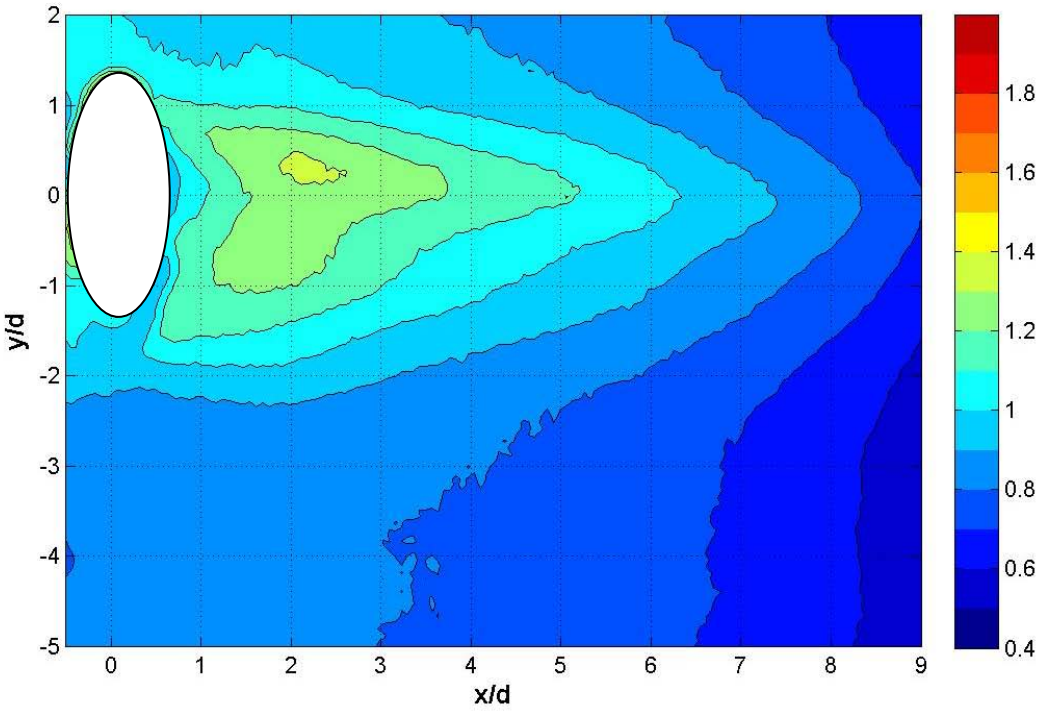

Fig C.33 Contour of *Fr* with dimples at Re = 30k and low turbulence for M = 0.5

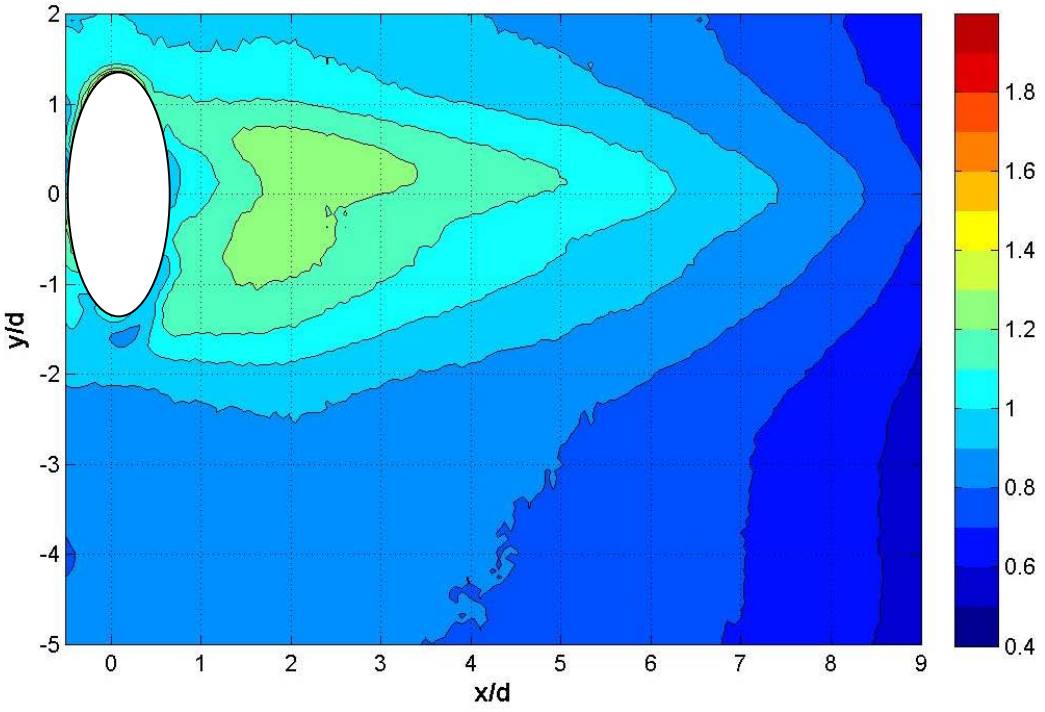

Fig C.34 Contour of *Fr* without dimples at Re = 30k and low turbulence for M = 0.5

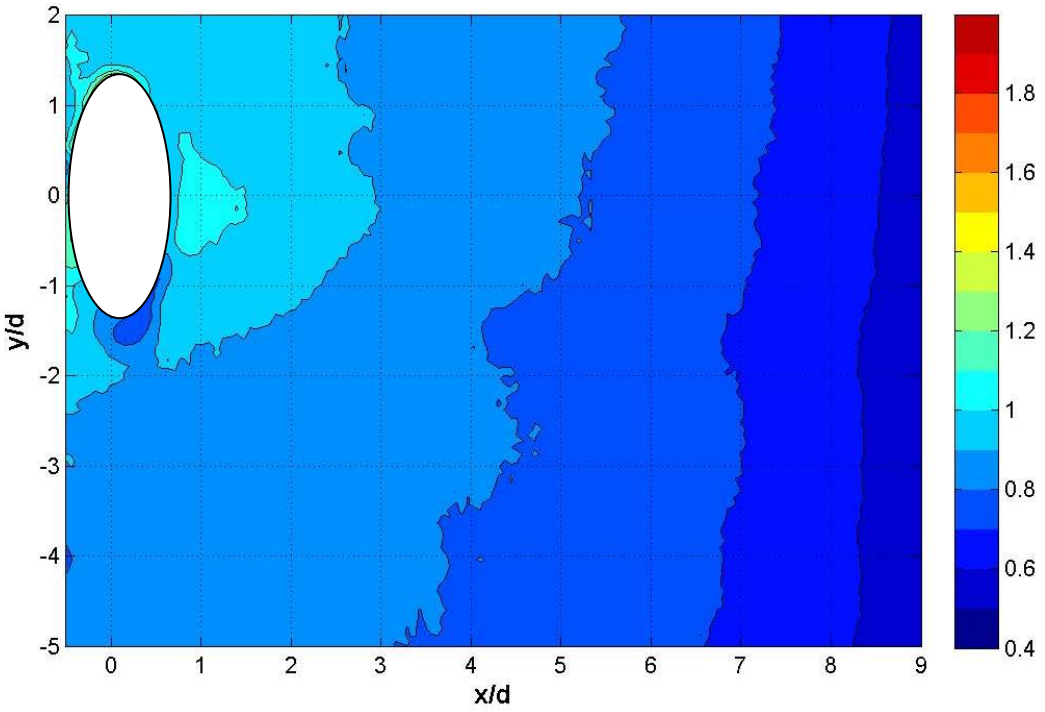

Fig C.35 Contour of *Fr* with dimples at Re = 30k and low turbulence for M = 0.25

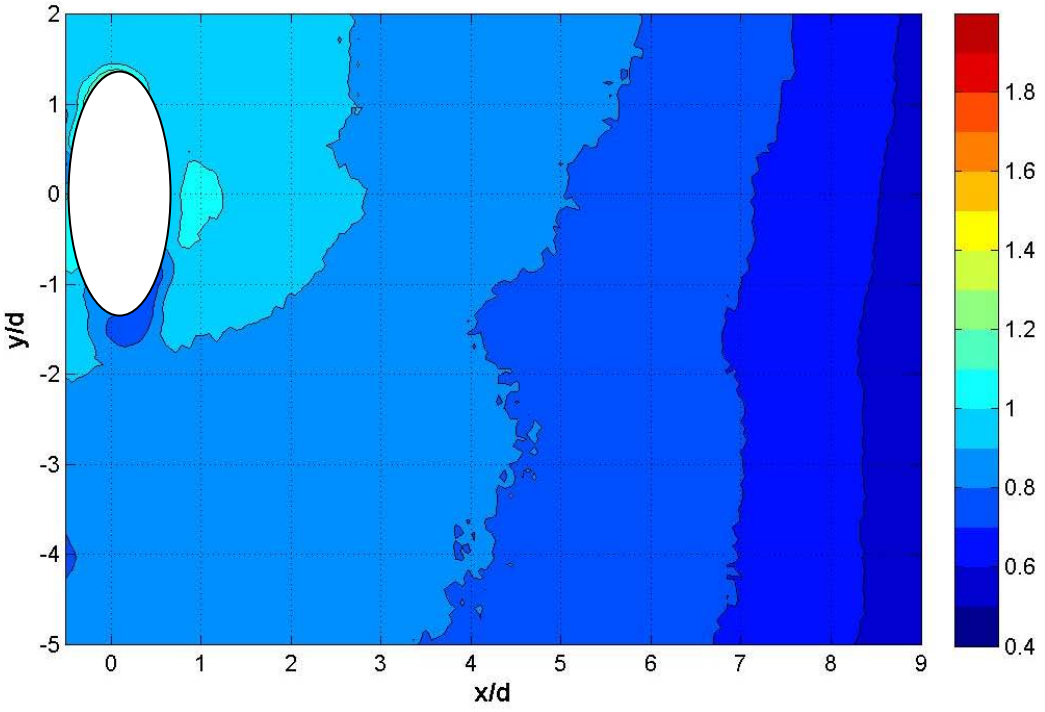

Fig C.36 Contour of *Fr* without dimples at Re = 30k and low turbulence for M = 0.25

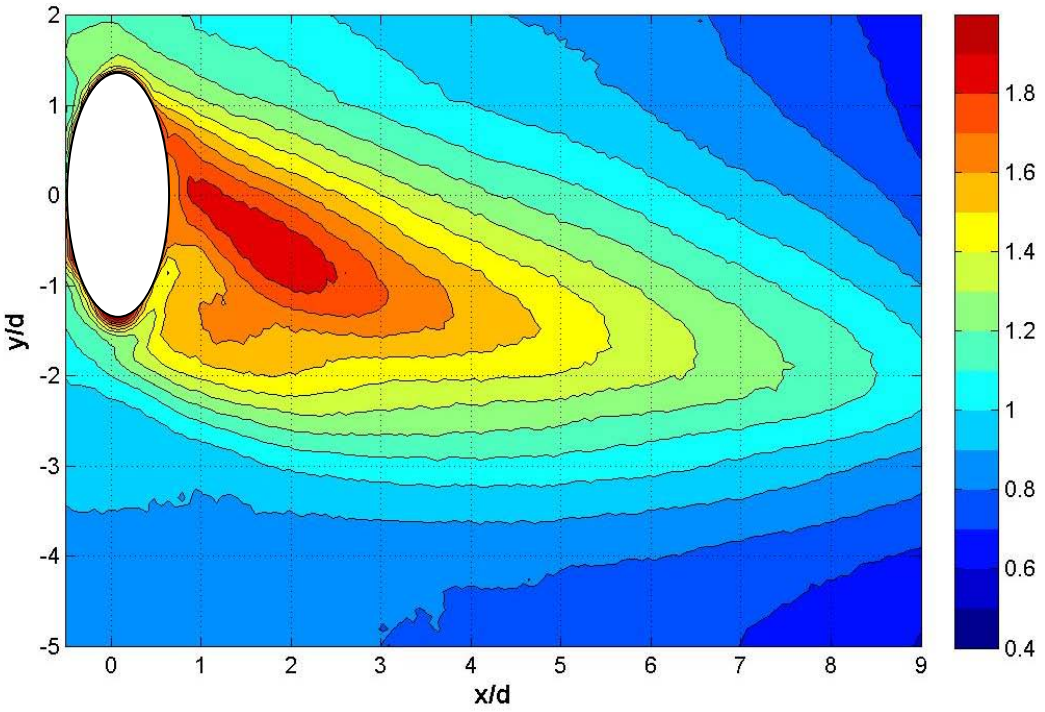

Fig C.37 Contour of *Fr* with dimples at Re = 60k and low turbulence for M = 1.5

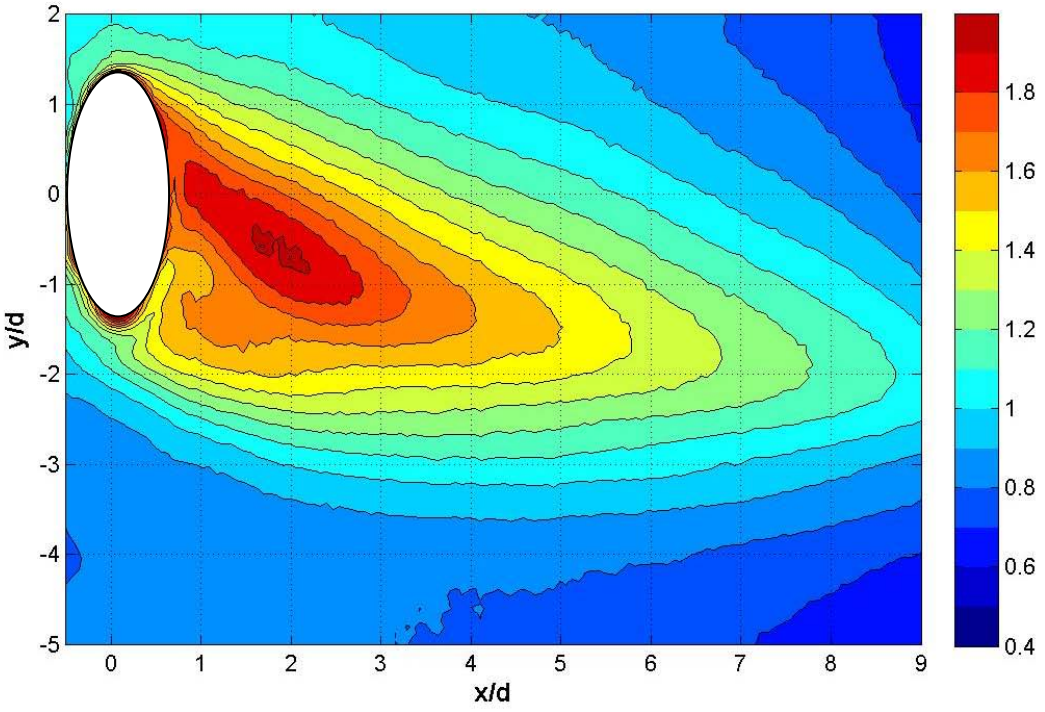

Fig C.38 Contour of *Fr* without dimples at Re = 60k and low turbulence for M = 1.5

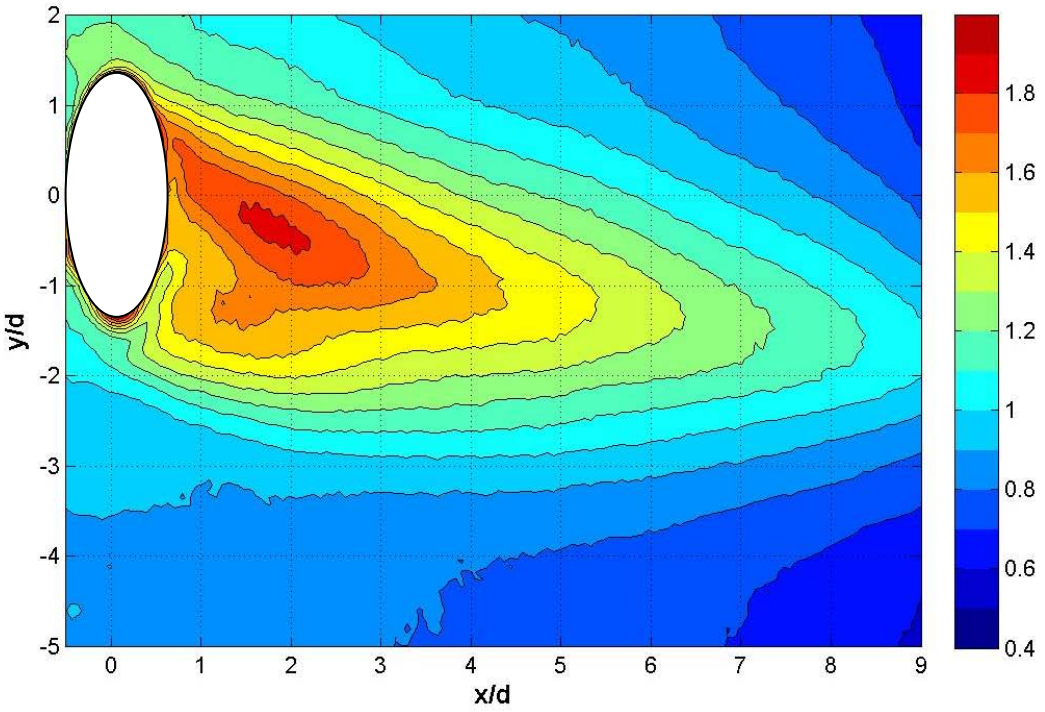

Fig C.39 Contour of *Fr* with dimples at Re = 60k and low turbulence for M = 1.25

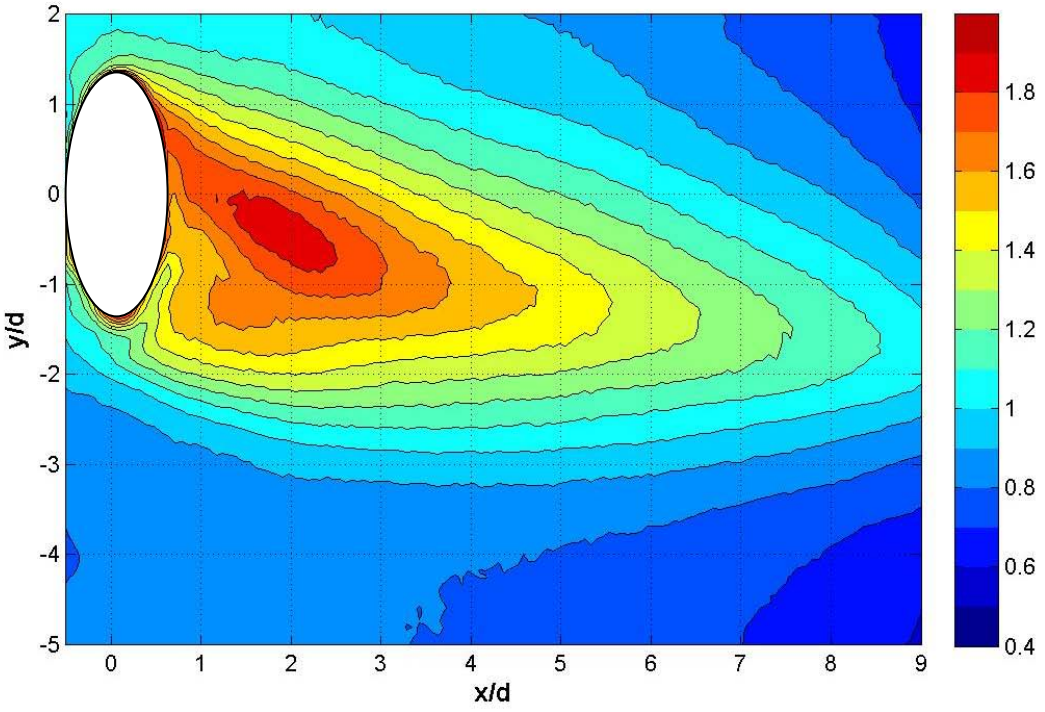

Fig C.40 Contour of *Fr* without dimples at Re = 60k and low turbulence for M = 1.25

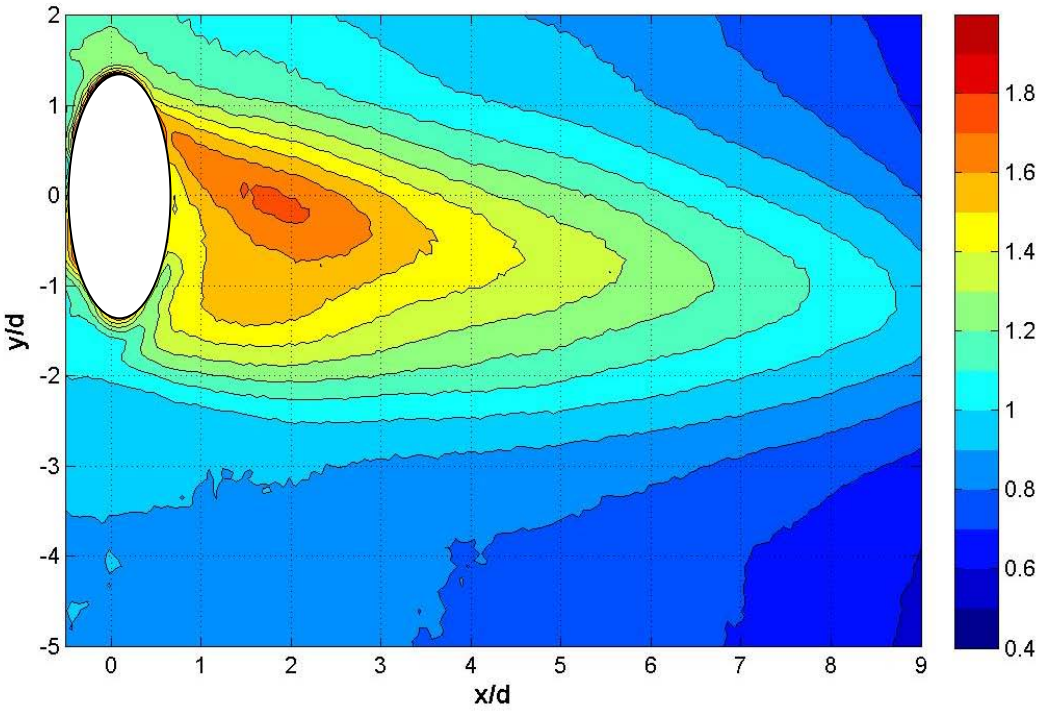

Fig C.41 Contour of *Fr* with dimples at Re = 60k and low turbulence for M = 1.0

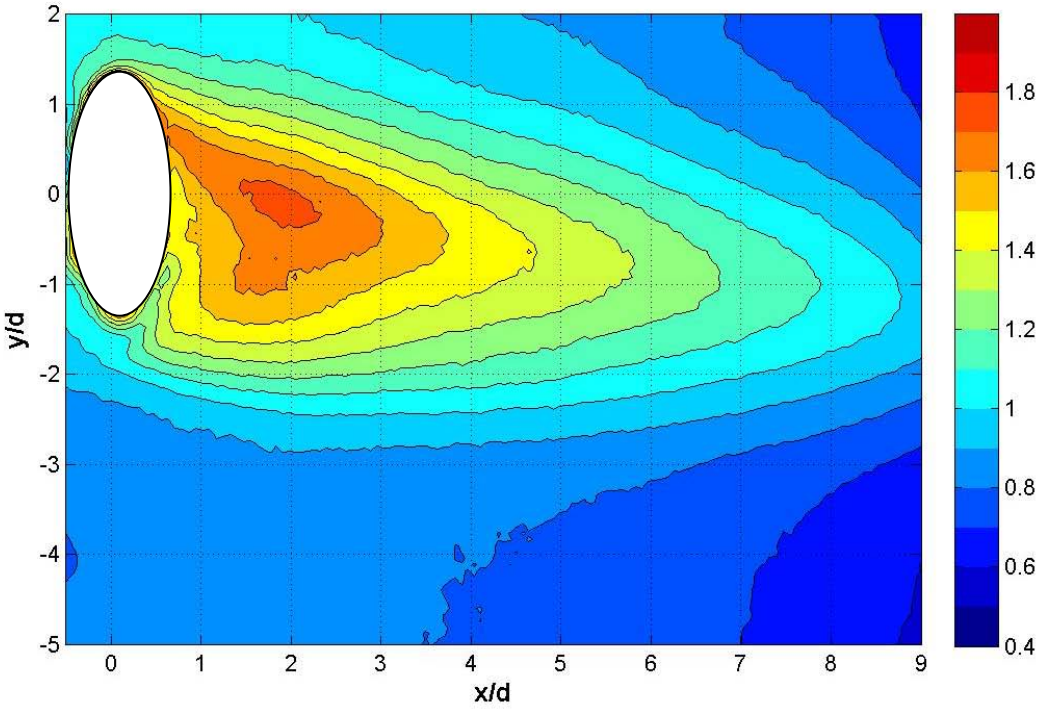

Fig C.42 Contour of *Fr* without dimples at Re = 60k and low turbulence for M = 1.0

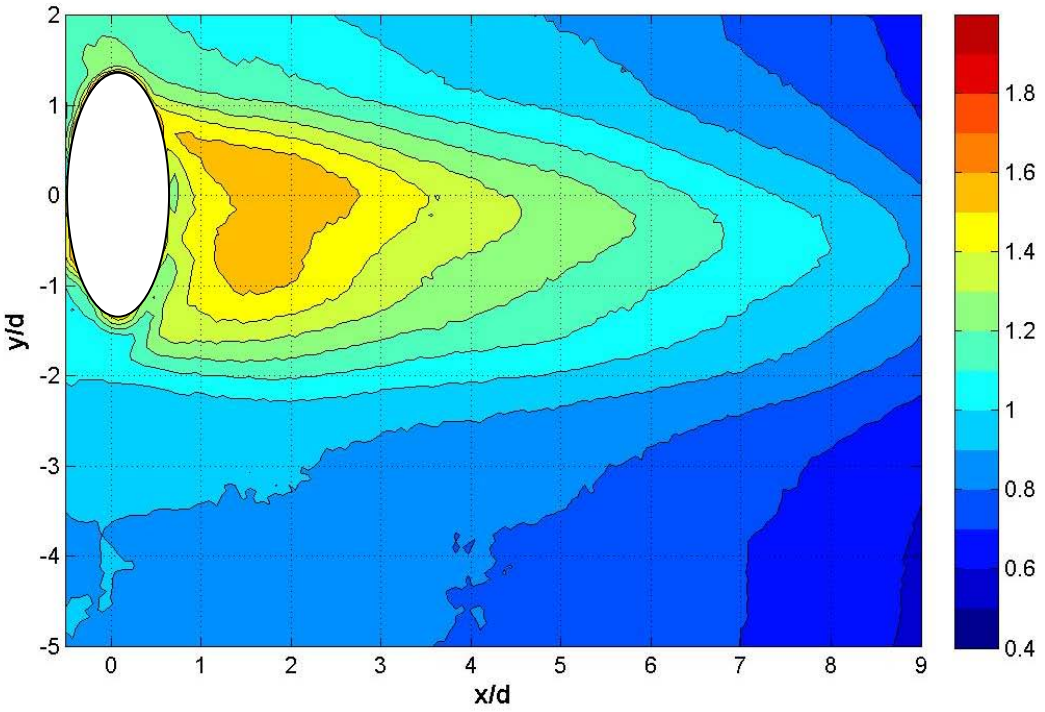

Fig C.43 Contour of *Fr* with dimples at Re = 60k and low turbulence for M = 0.75

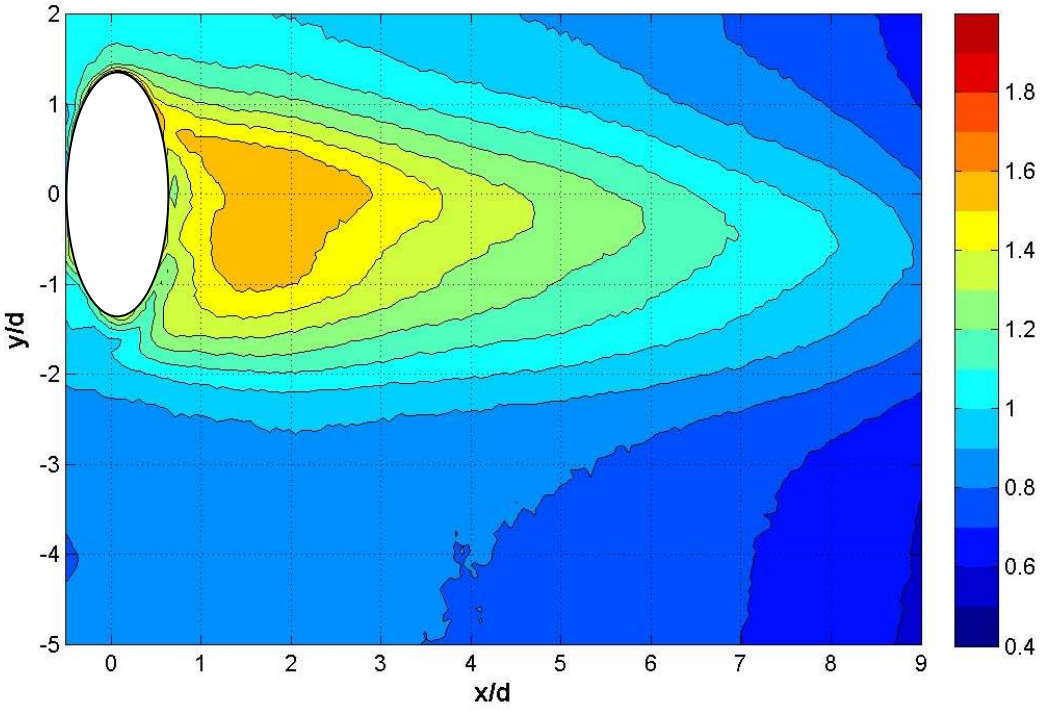

Fig C.44 Contour of *Fr* without dimples at Re = 60k and low turbulence for M = 0.75

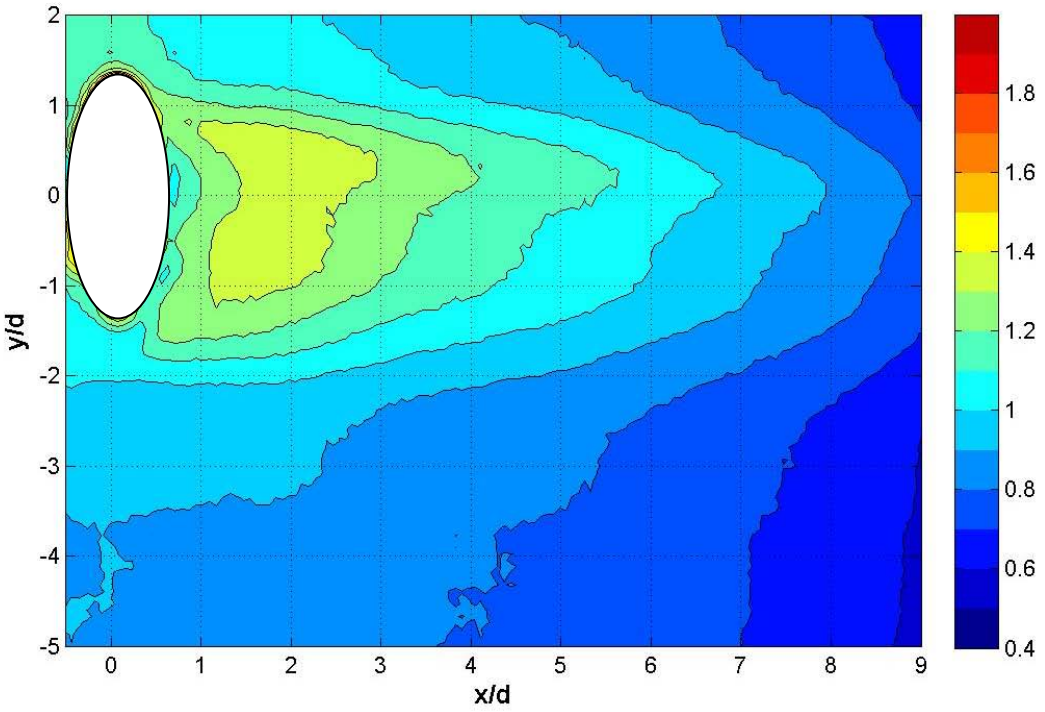

Fig C.45 Contour of *Fr* with dimples at Re = 60k and low turbulence for M = 0.5

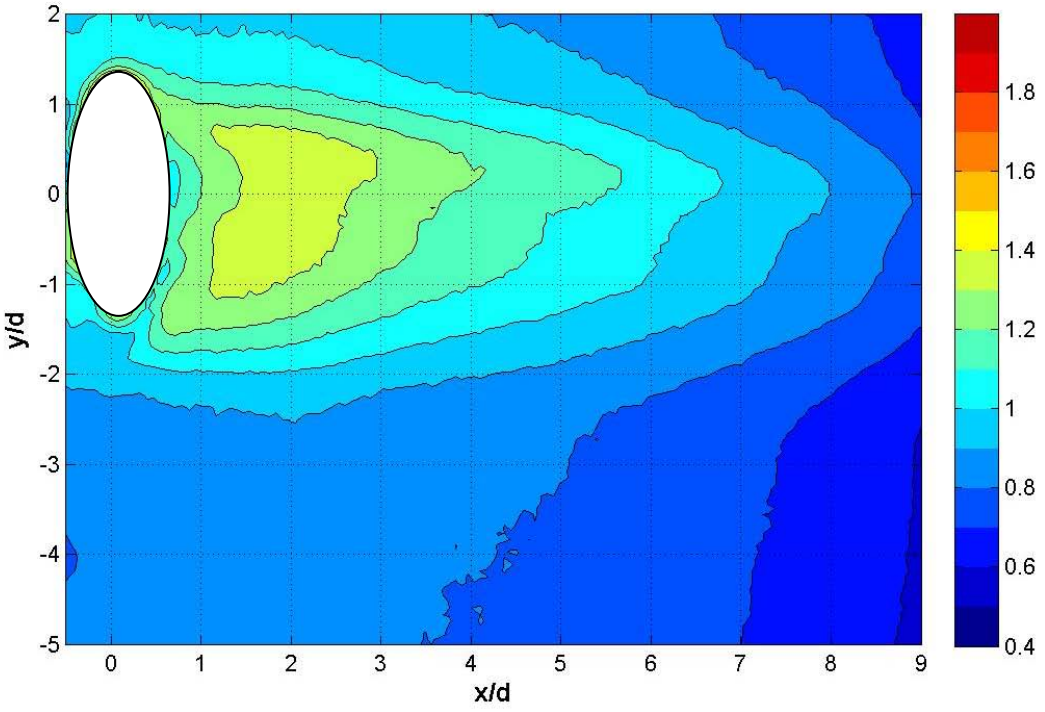

Fig C.46 Contour of *Fr* without dimples at Re = 60k and low turbulence for M = 0.5

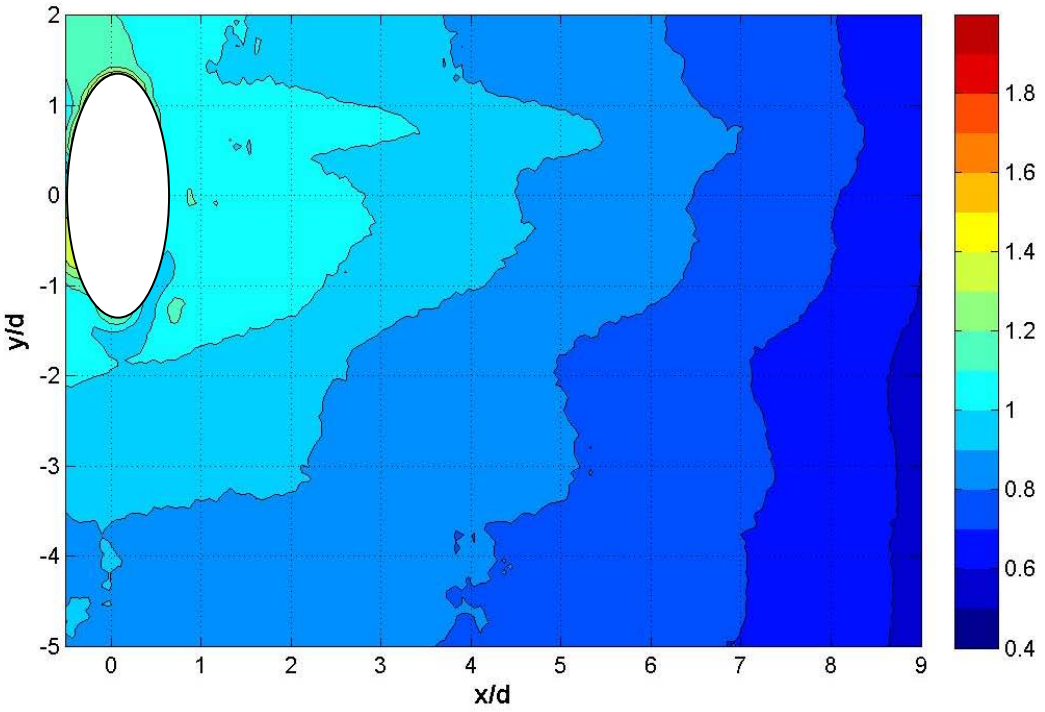

Fig C.47 Contour of *Fr* with dimples at Re = 60k and low turbulence for M = 0.25

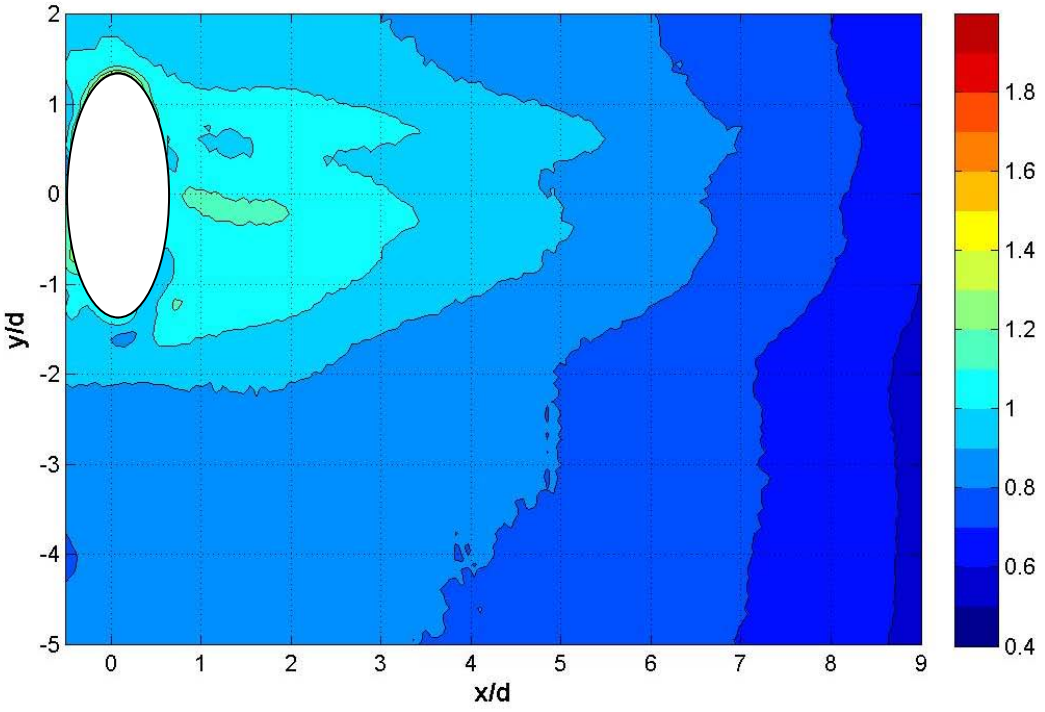

Fig C.48 Contour of *Fr* without dimples at Re = 60k and low turbulence for M = 0.25

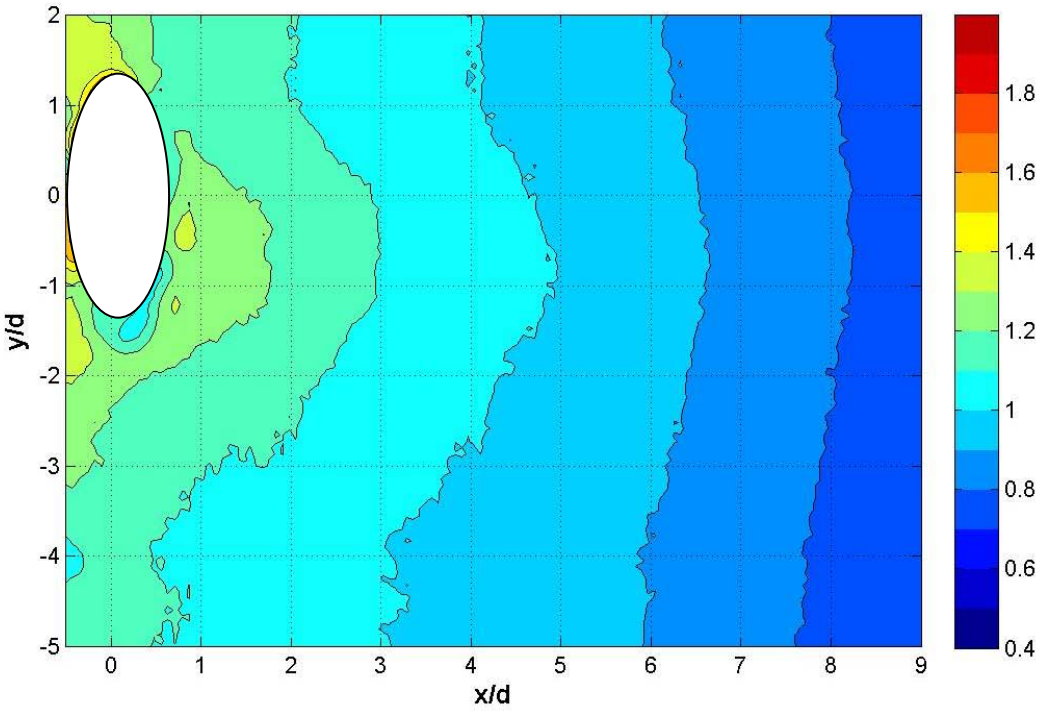

Fig C.49 Contour of *Fr* with dimples at Re = 60k and high turbulence for no film cooling (M = 0)

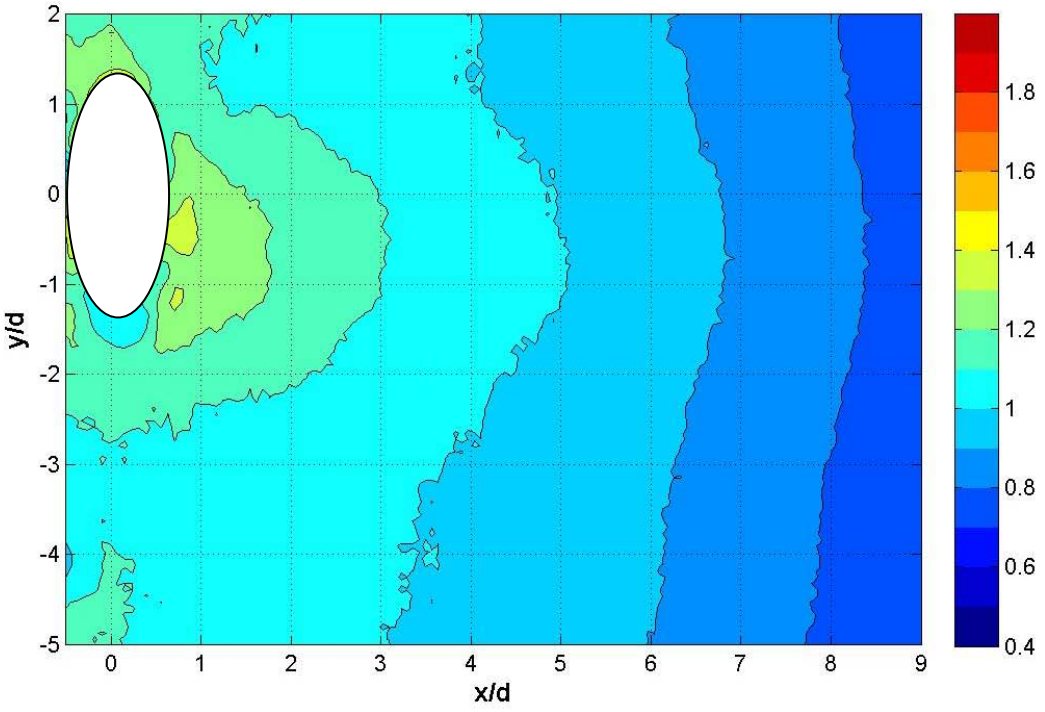

Fig C.50 Contour of *Fr* without dimples at Re = 60k and high turbulence for no film cooling (M = 0)

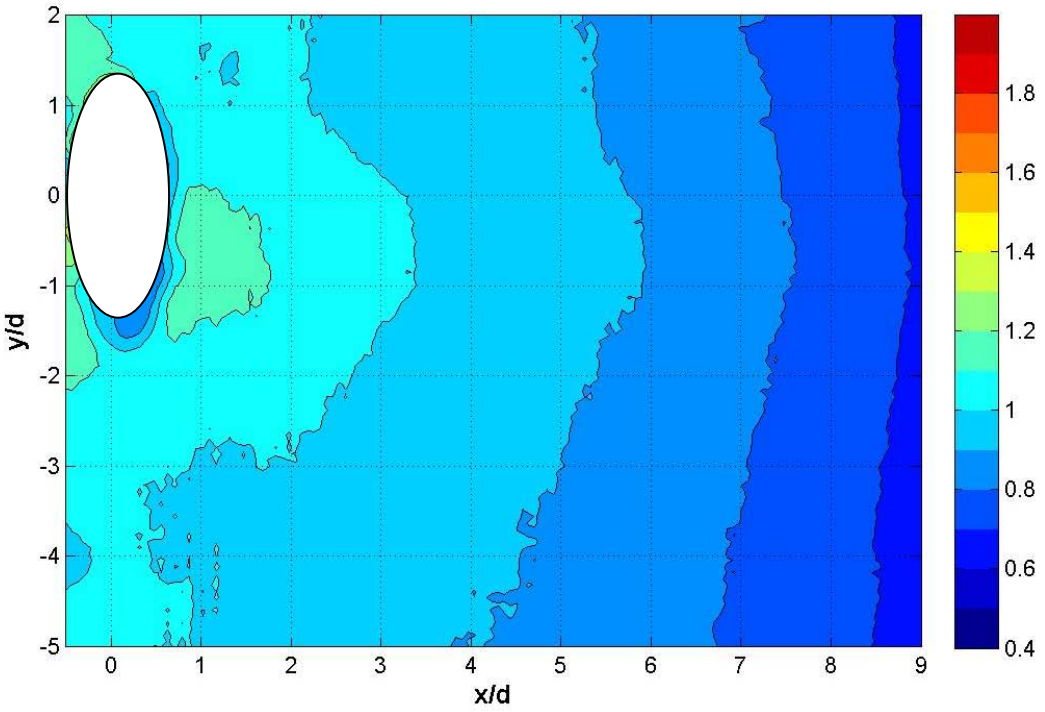

Fig C.51 Contour of *Fr* with dimples at Re = 30k and high turbulence for no film cooling (M = 0)

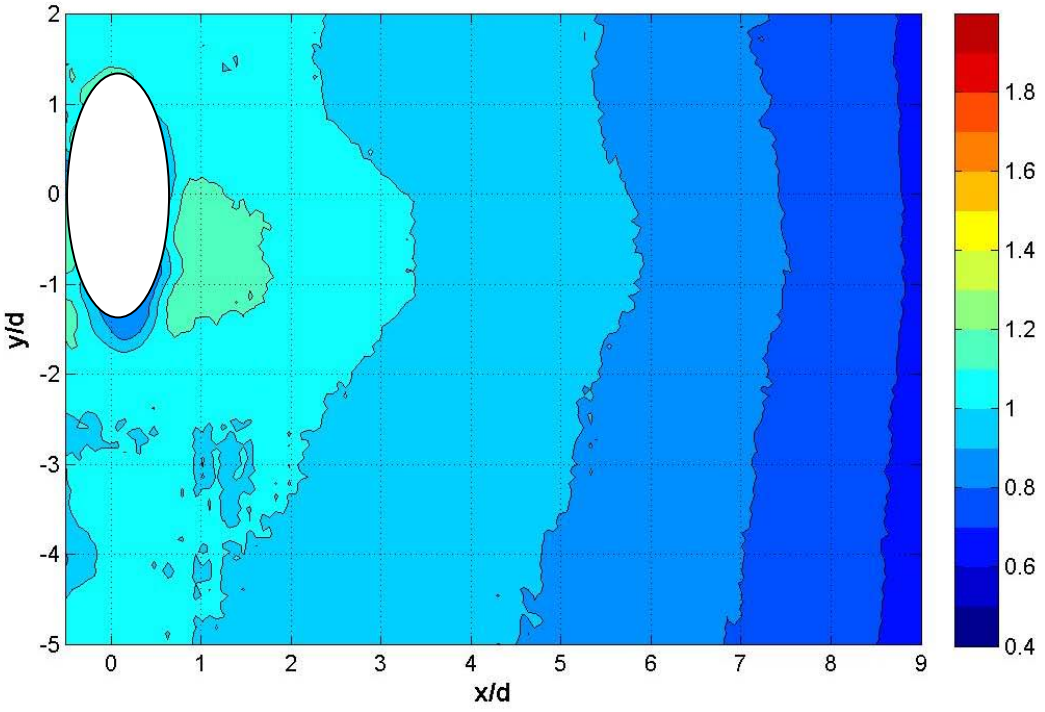

Fig C.52 Contour of *Fr* without dimples at Re = 30k and high turbulence for no film cooling (M = 0)

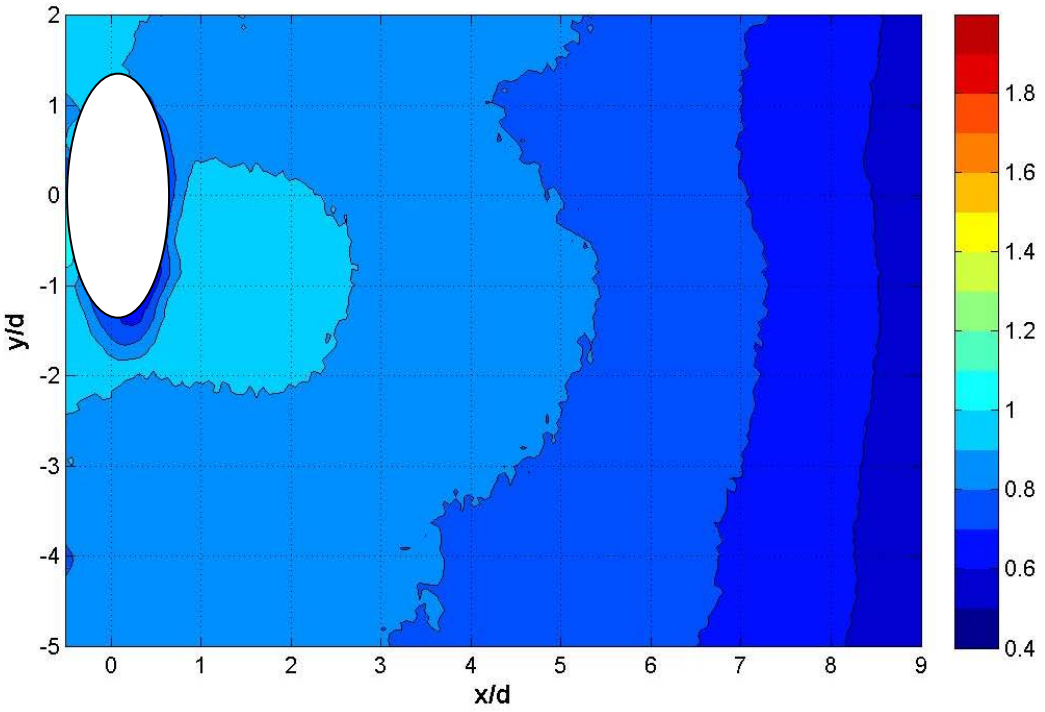

Fig C.53 Contour of *Fr* with dimples at Re = 30k and low turbulence for no film cooling (M = 0)

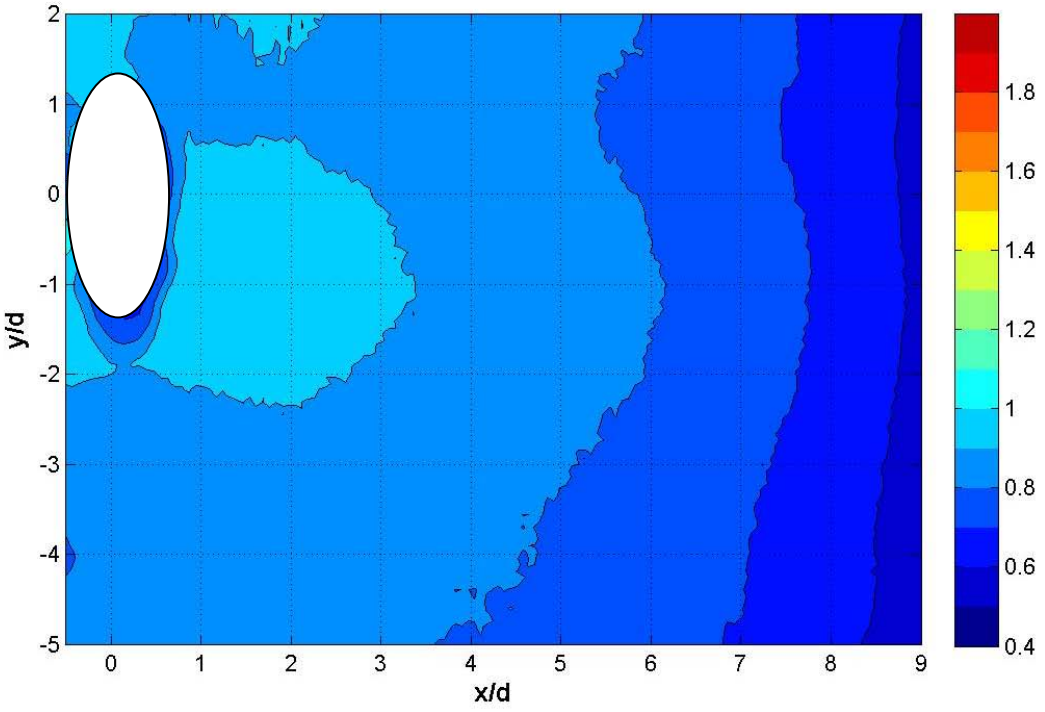

Fig C.54 Contour of *Fr* without dimples at Re = 60k and low turbulence for M = 0.25

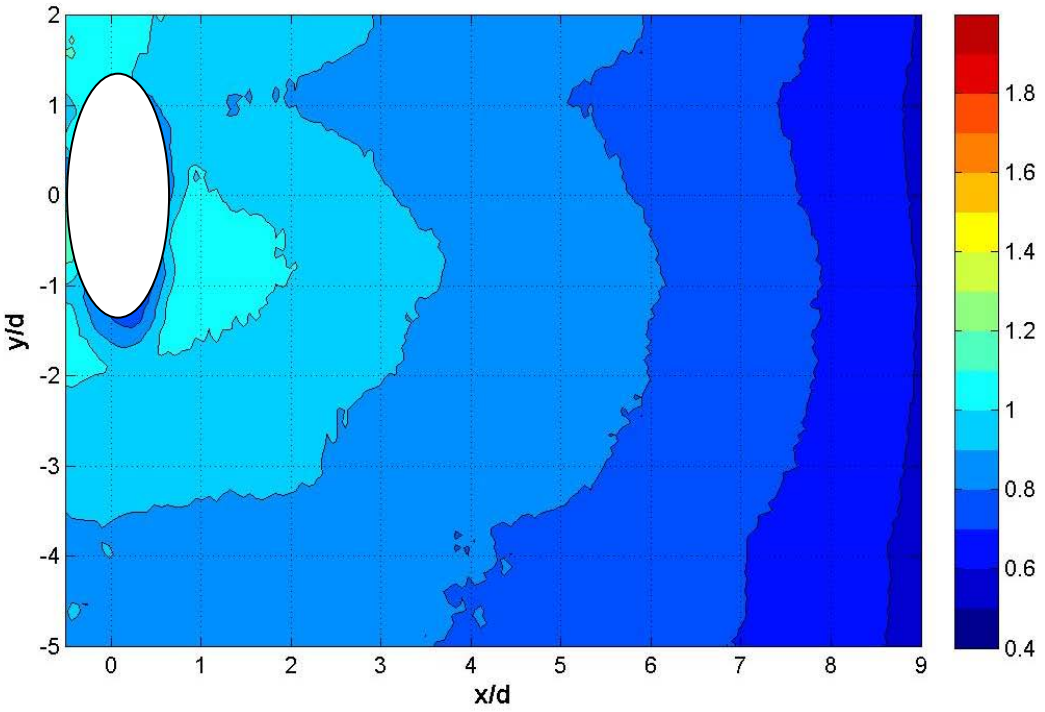

Fig C.55 Contour of *Fr* with dimples at Re = 60k and low turbulence for M = 0.25

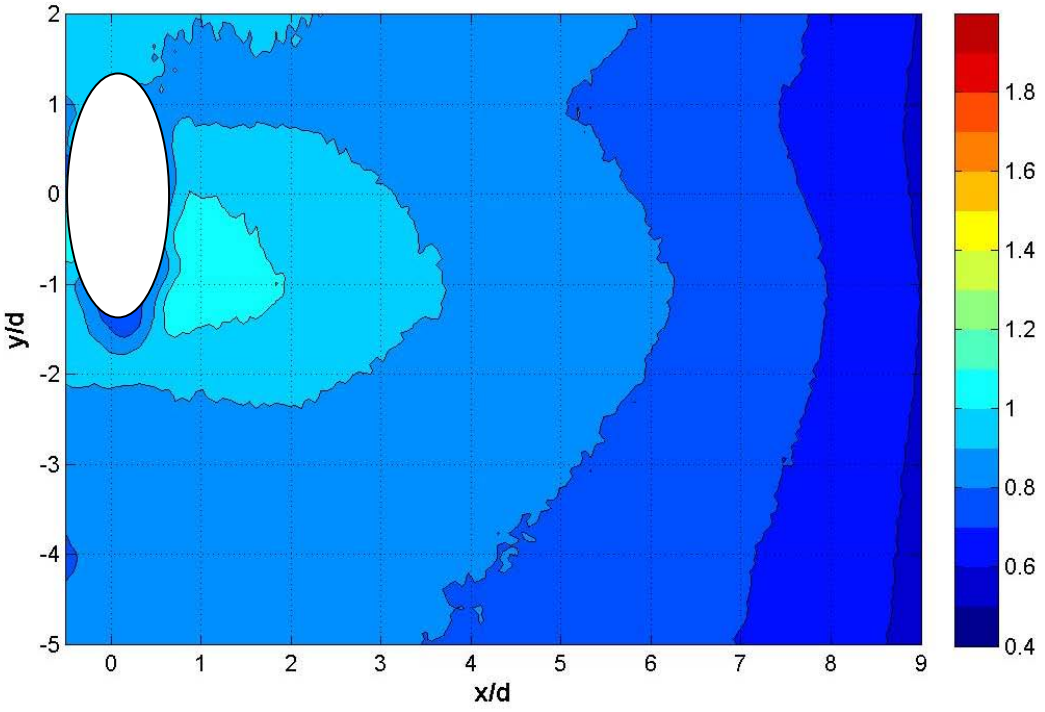

Fig C.56 Contour of *Fr* without dimples at Re = 60k and low turbulence for M = 0.25

Appendix D. Spanwise averaged Frössling number plots

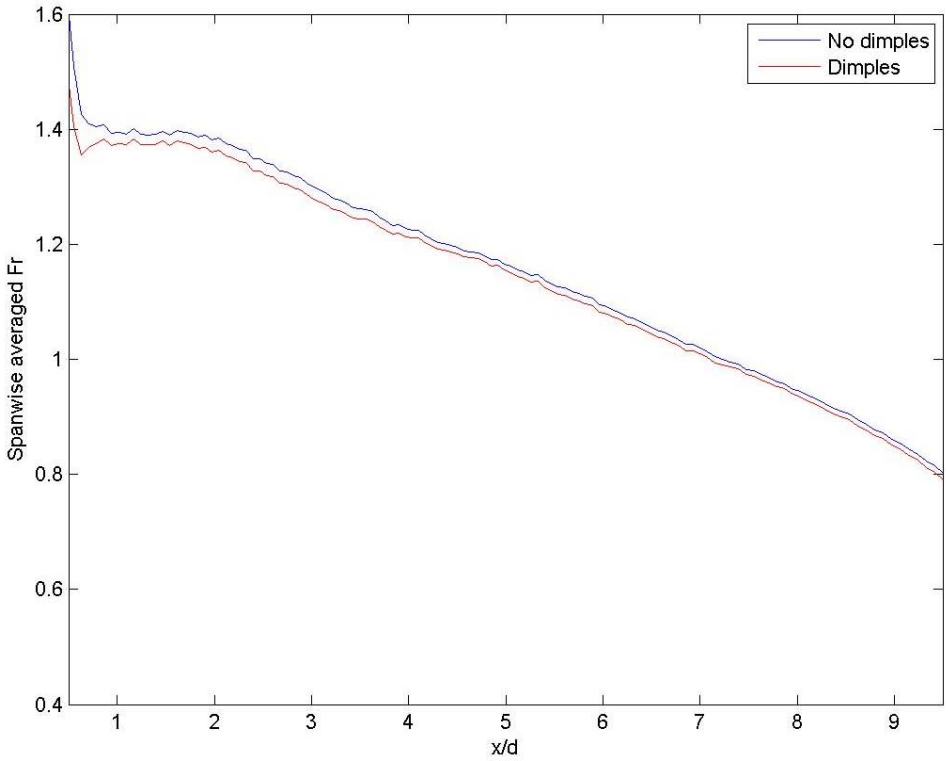

Fig D.1 Spanwise averaged *Fr* at Re = 60k and high turbulence for M = 1.5

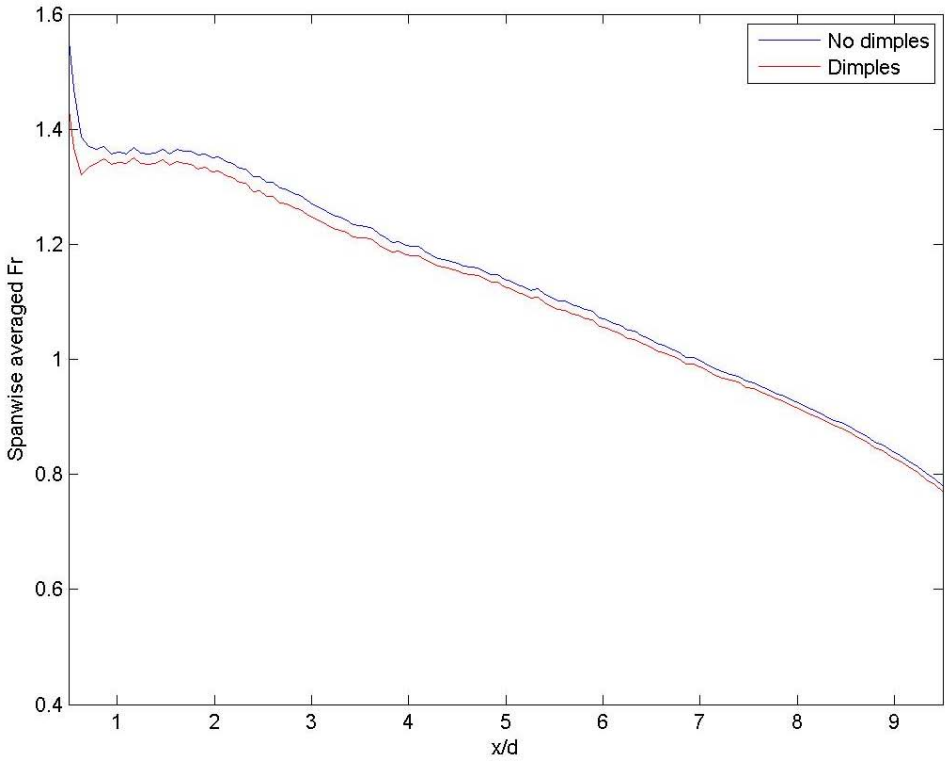

Fig D.2 Spanwise averaged *Fr* at Re = 60k and high turbulence for M = 1.25

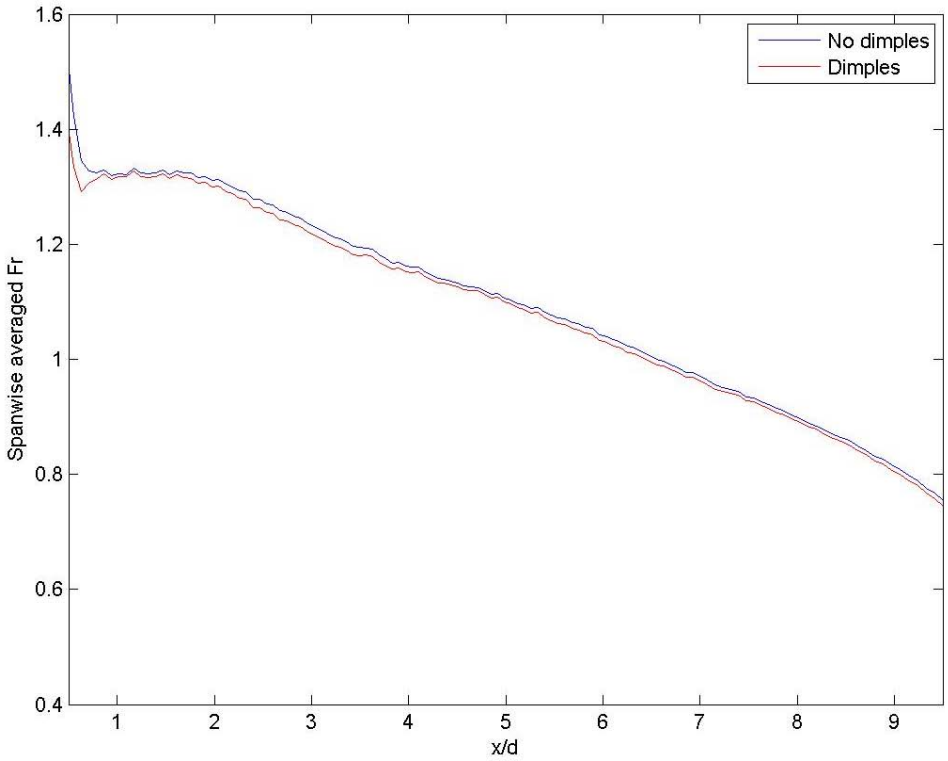

Fig D.3 Spanwise averaged *Fr* at Re = 60k and high turbulence for M = 1.0

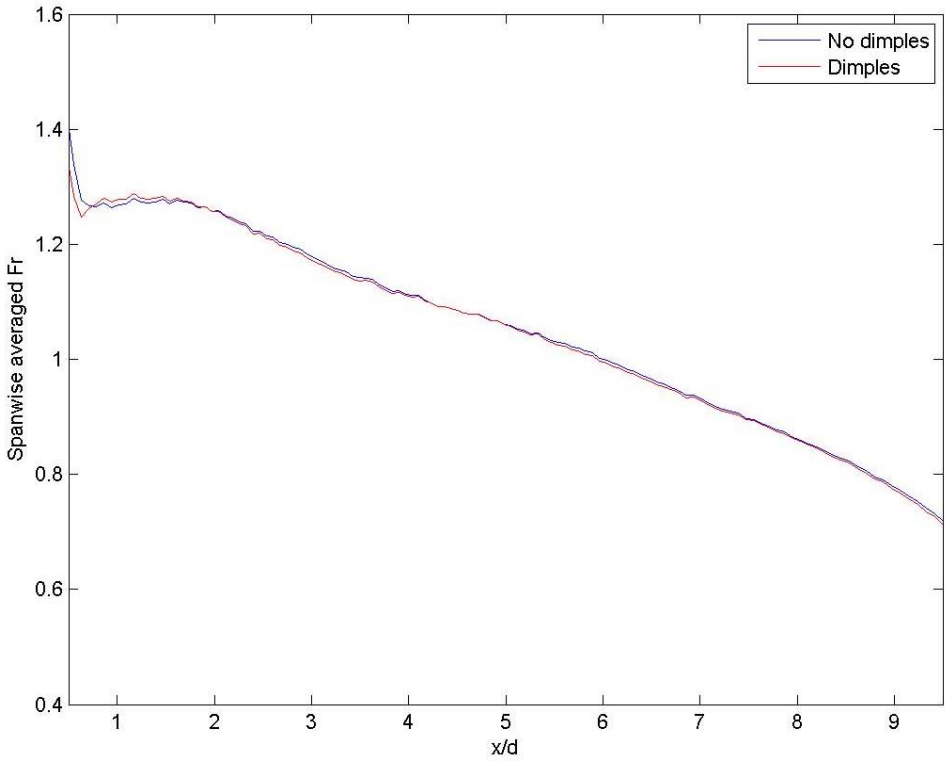

Fig D.4 Spanwise averaged *Fr* at Re = 60k and high turbulence for M = 0.75

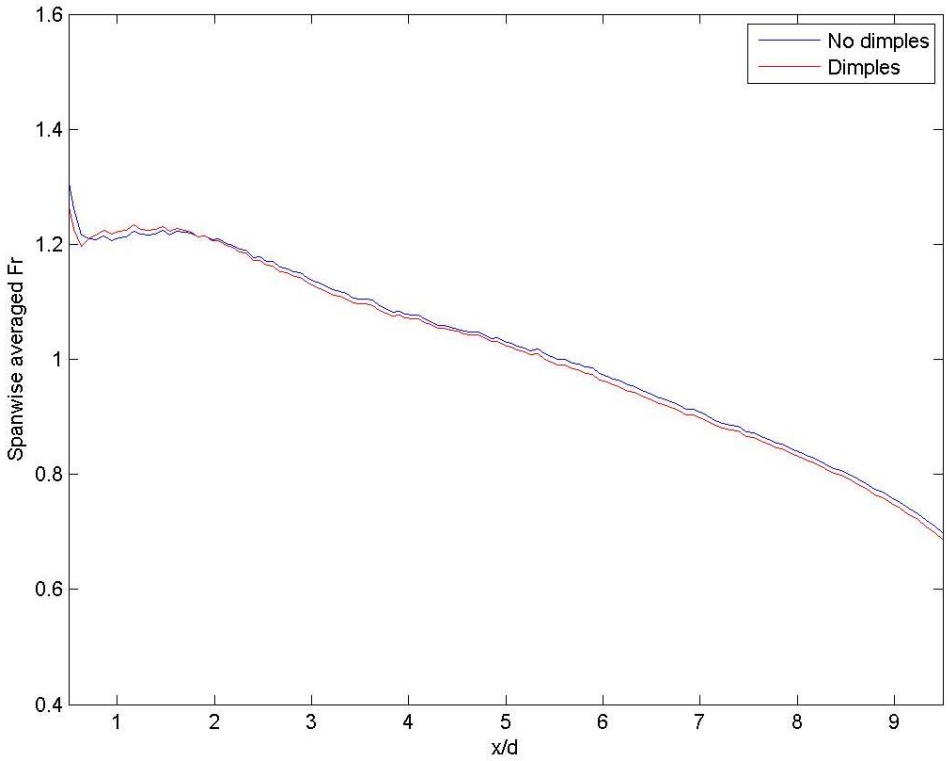

Fig D.5 Spanwise averaged *Fr* at Re = 60k and high turbulence for M = 0.5

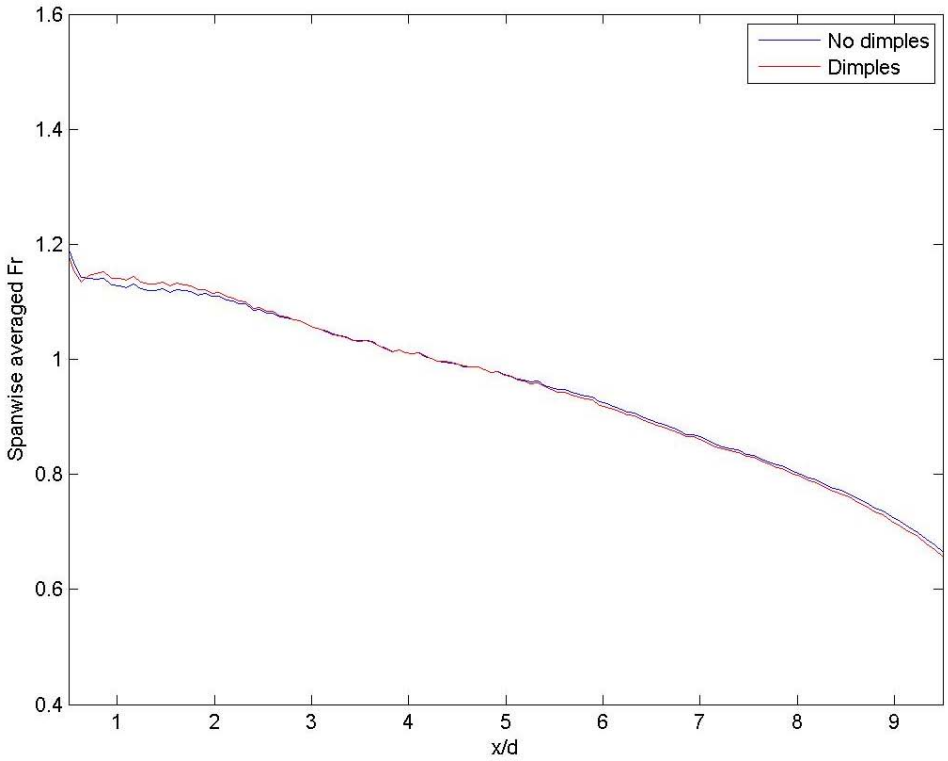

Fig D.6 Spanwise averaged *Fr* at Re = 60k and high turbulence for M = 0.25

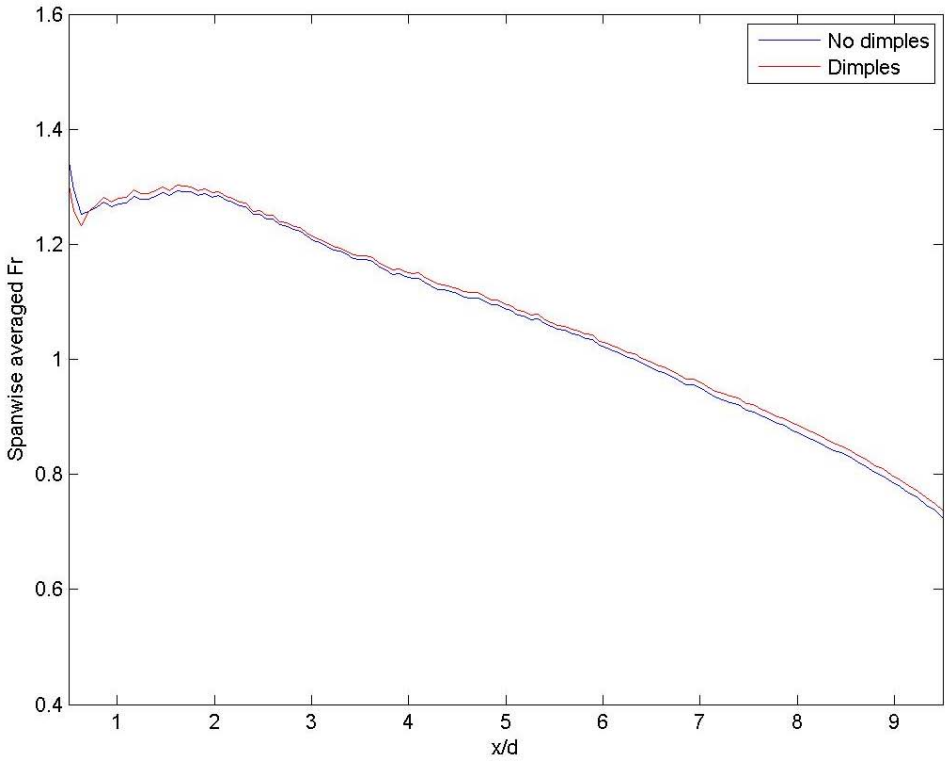

Fig D.7 Spanwise averaged *Fr* at Re = 30k and high turbulence for M = 1.5

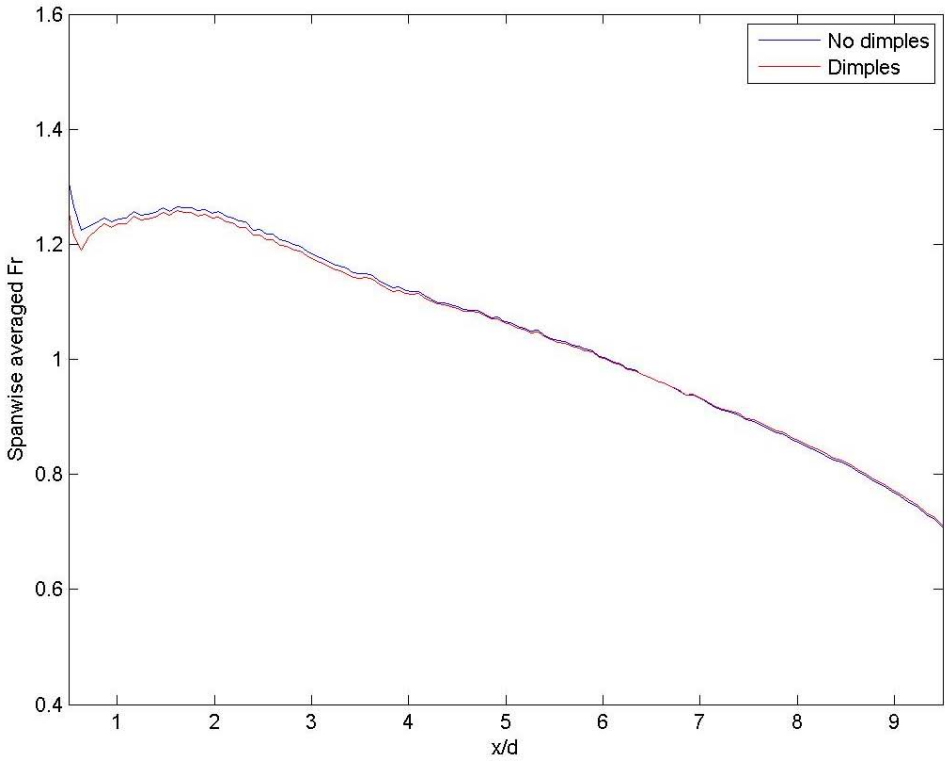

Fig D.8 Spanwise averaged η at Re = 30k and high turbulence for M = 1.25

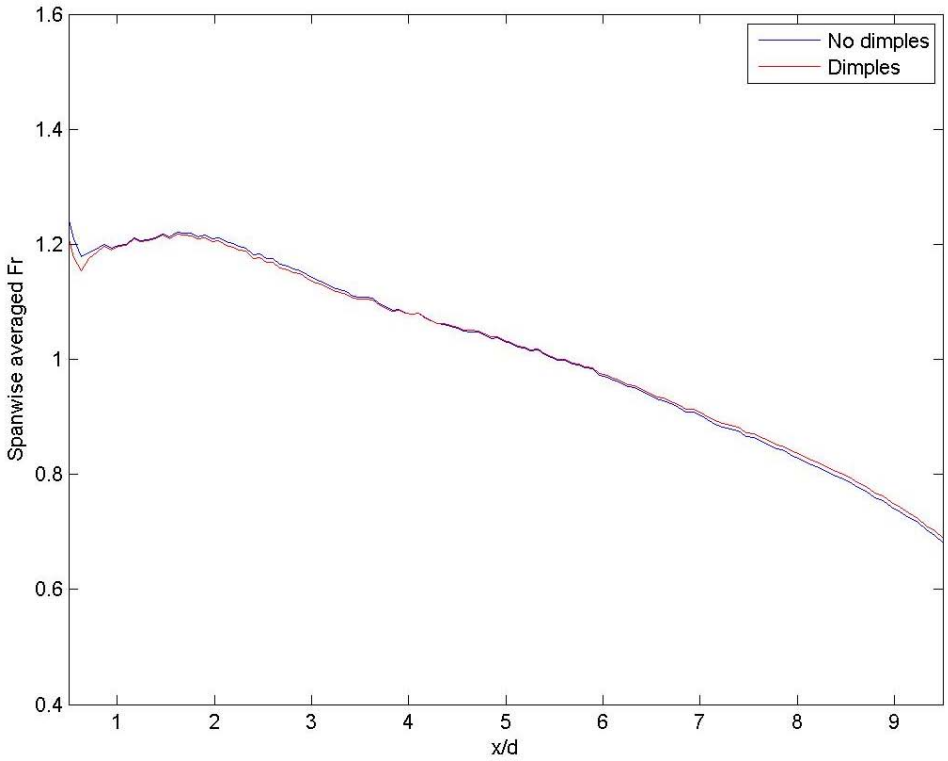

Fig D.9 Spanwise averaged *Fr* at Re = 30k and high turbulence for M = 1.0

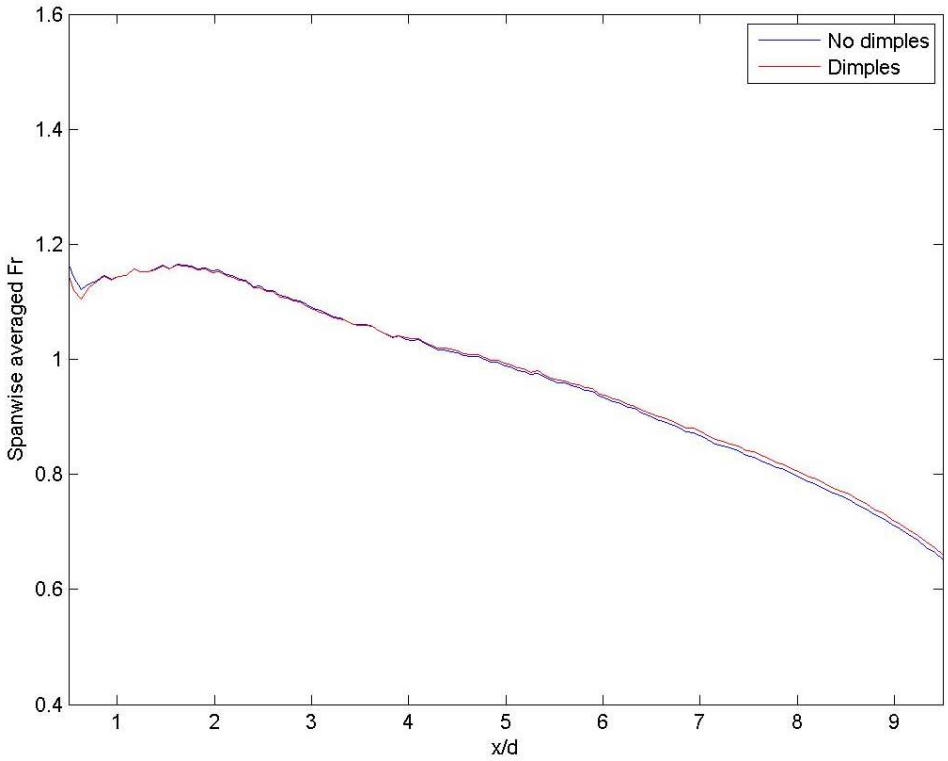

Fig D.10 Spanwise averaged *Fr* at Re = 30k and high turbulence for M = 0.75

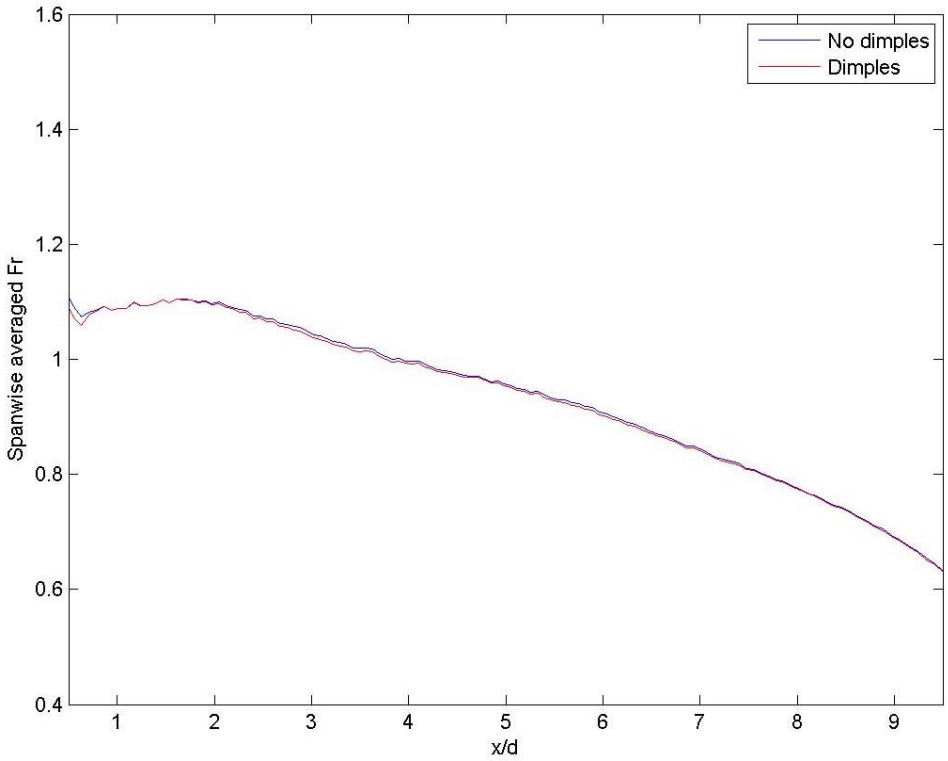

Fig D.11 Spanwise averaged *Fr* at Re = 30k and high turbulence for M = 0.5

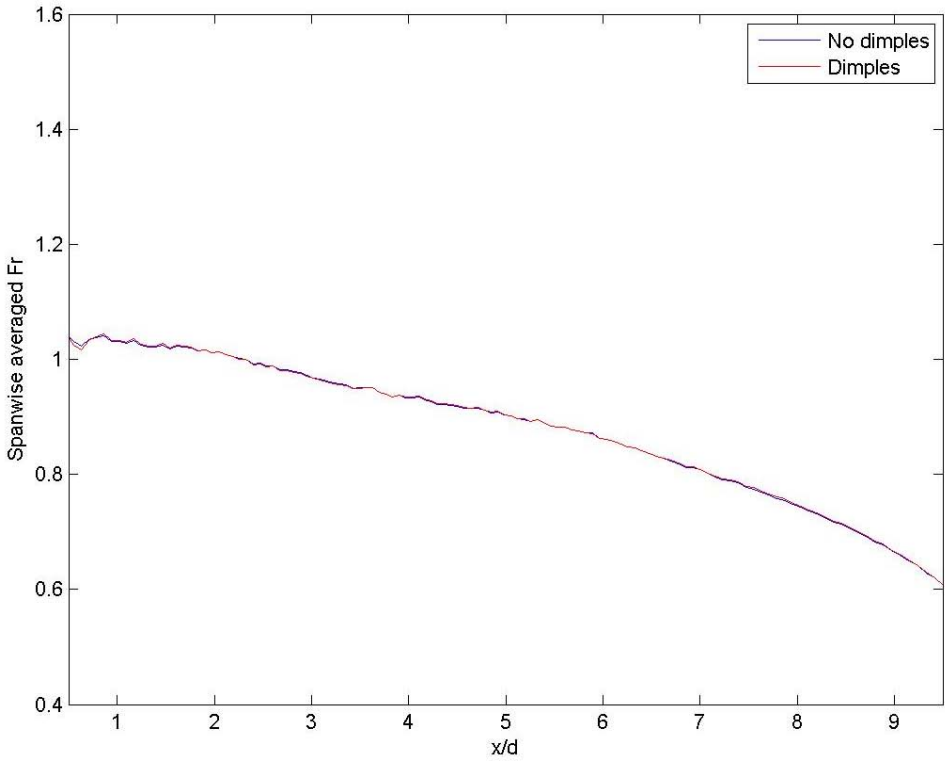

Fig D.12 Spanwise averaged *Fr* at Re = 30k and high turbulence for M = 0.25

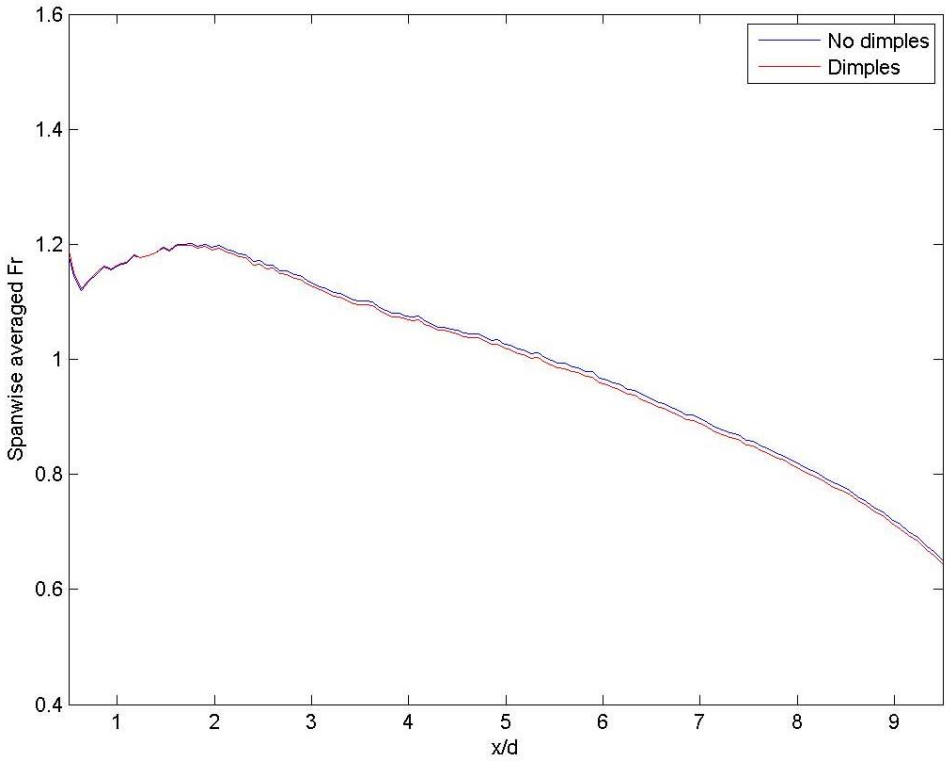

Fig D.13 Spanwise averaged *Fr* at Re = 30k and low turbulence for M = 1.5

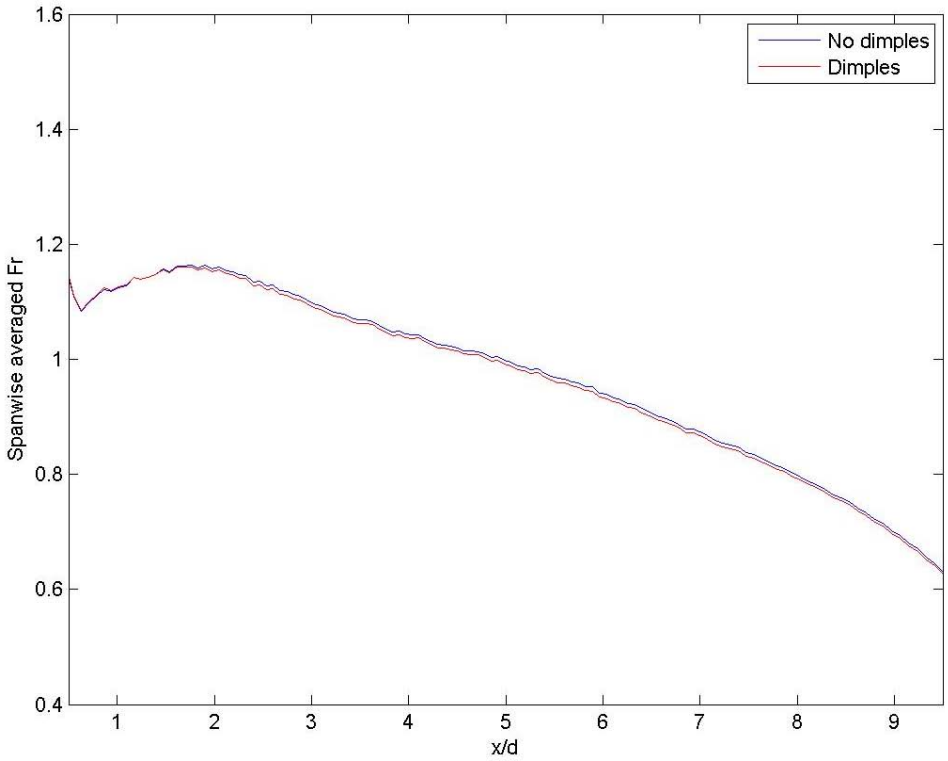

Fig D.14 Spanwise averaged *Fr* at Re = 30k and low turbulence for M = 1.25

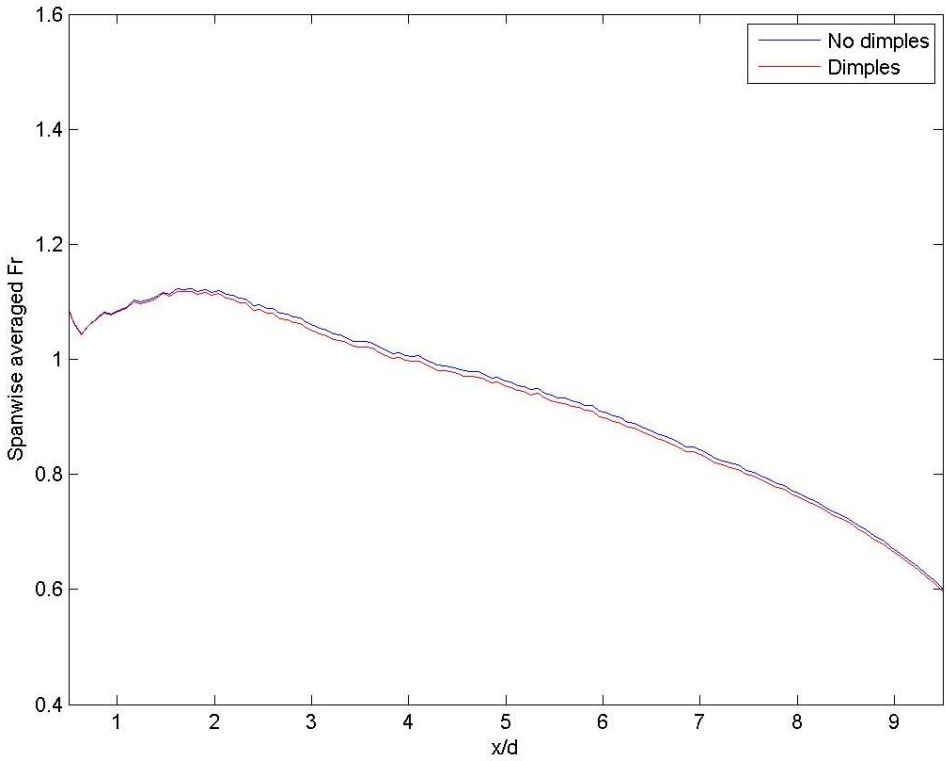

Fig D.15 Spanwise averaged *Fr* at Re = 30k and low turbulence for M = 1.0

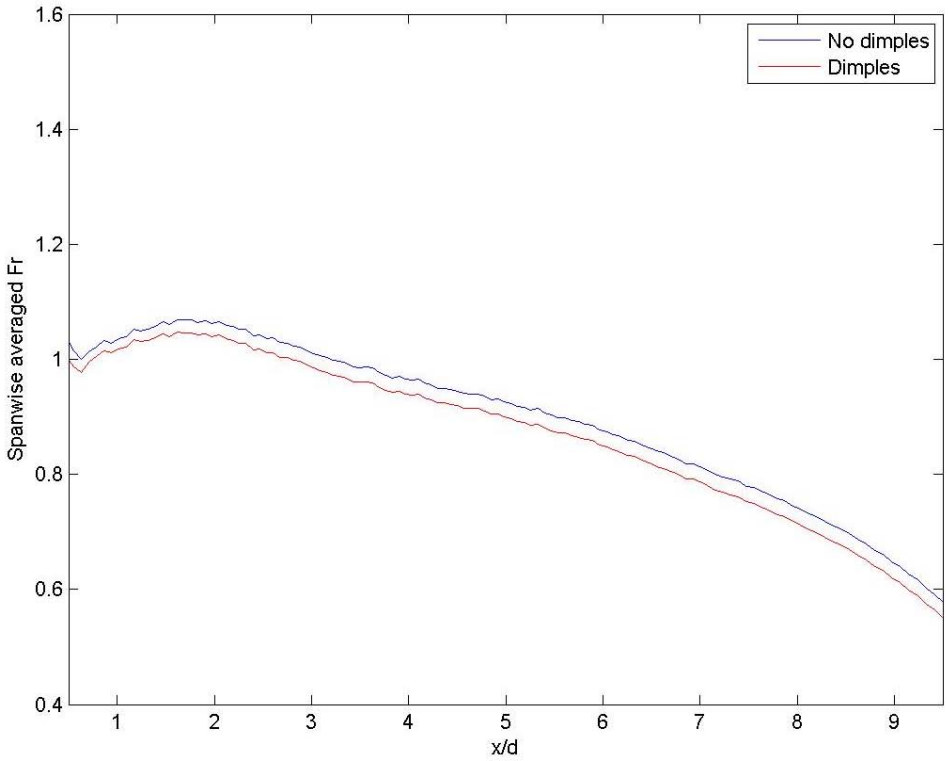

Fig D.16 Spanwise averaged *Fr* at Re = 30k and low turbulence for M = 0.75

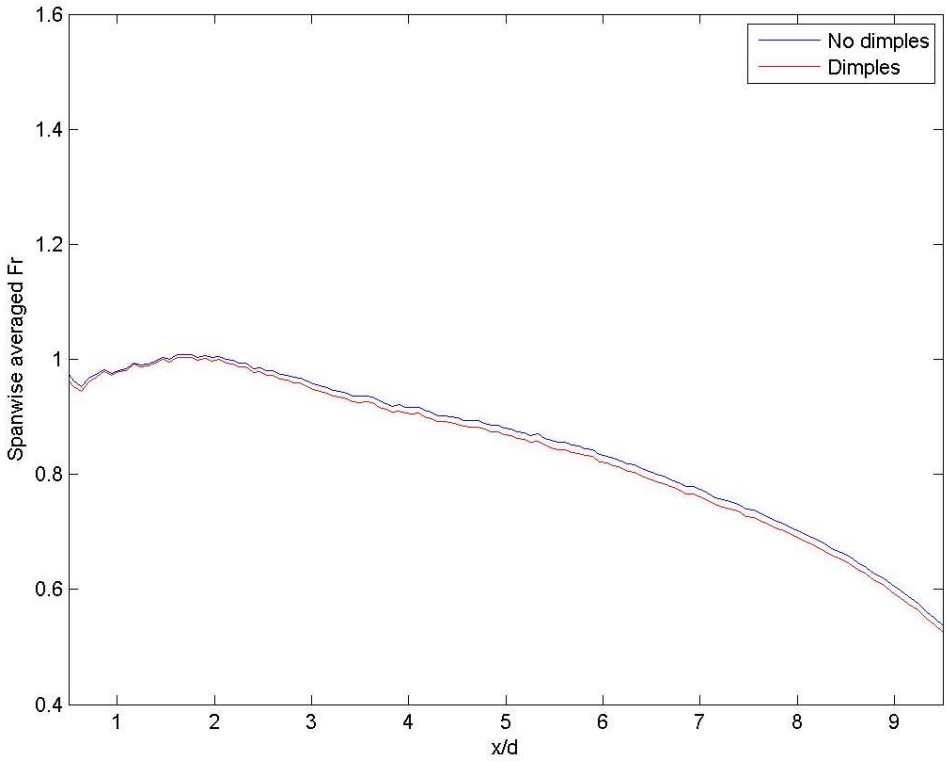

Fig D.17 Spanwise averaged *Fr* at Re = 30k and low turbulence for M = 0.5

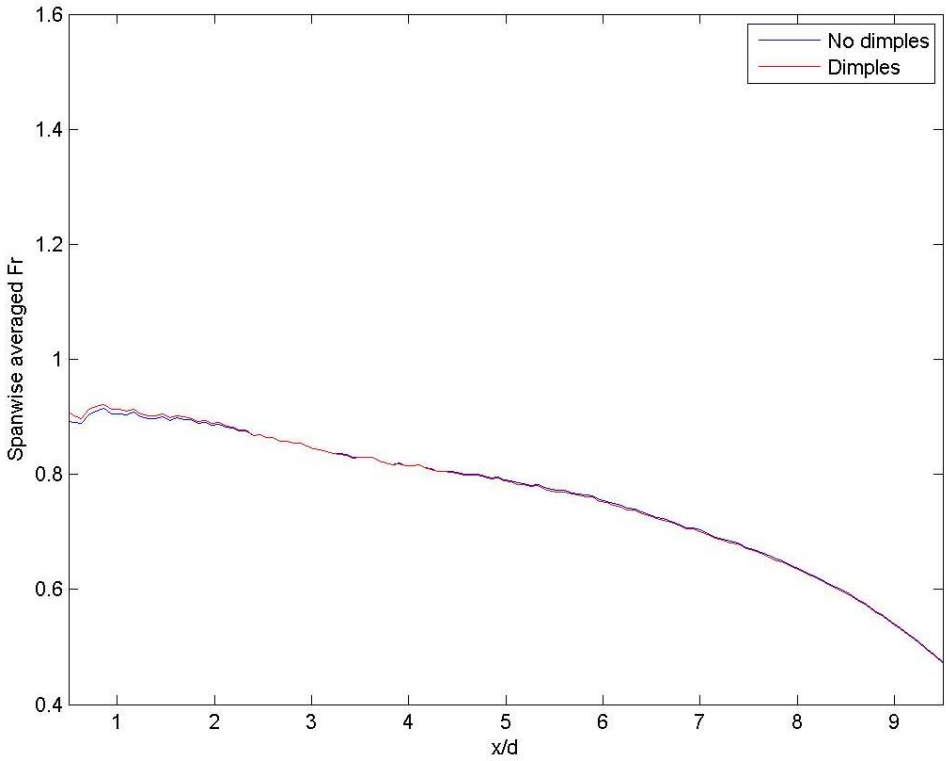

Fig D.18 Spanwise averaged *Fr* at Re = 30k and low turbulence for M = 0.25

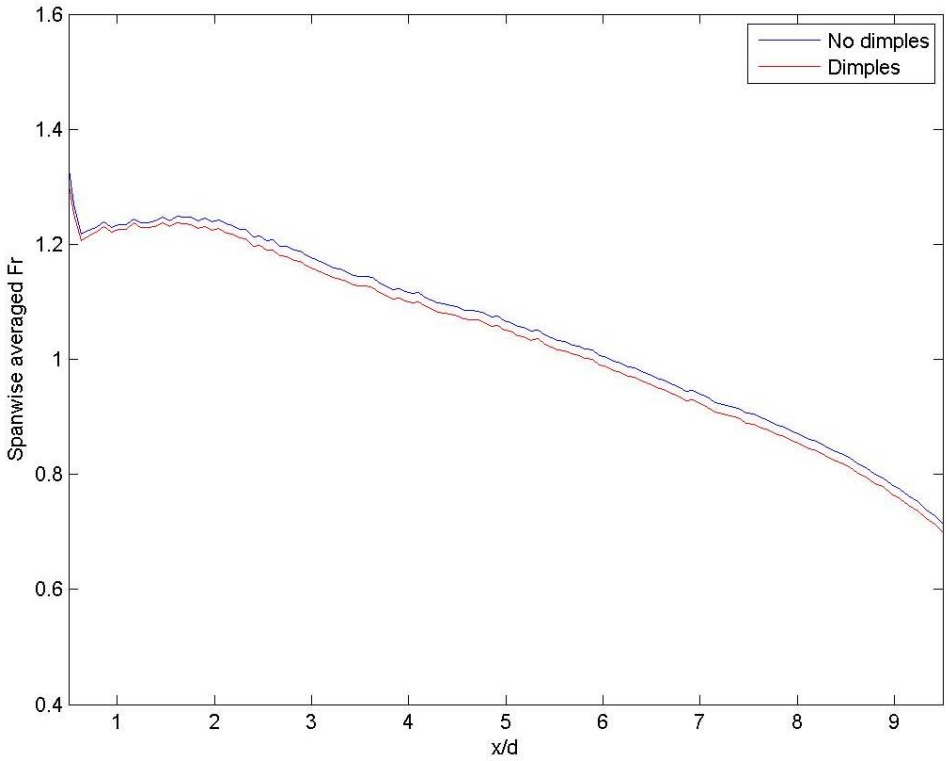

Fig D.19 Spanwise averaged *Fr* at Re = 60k and low turbulence for M = 1.5

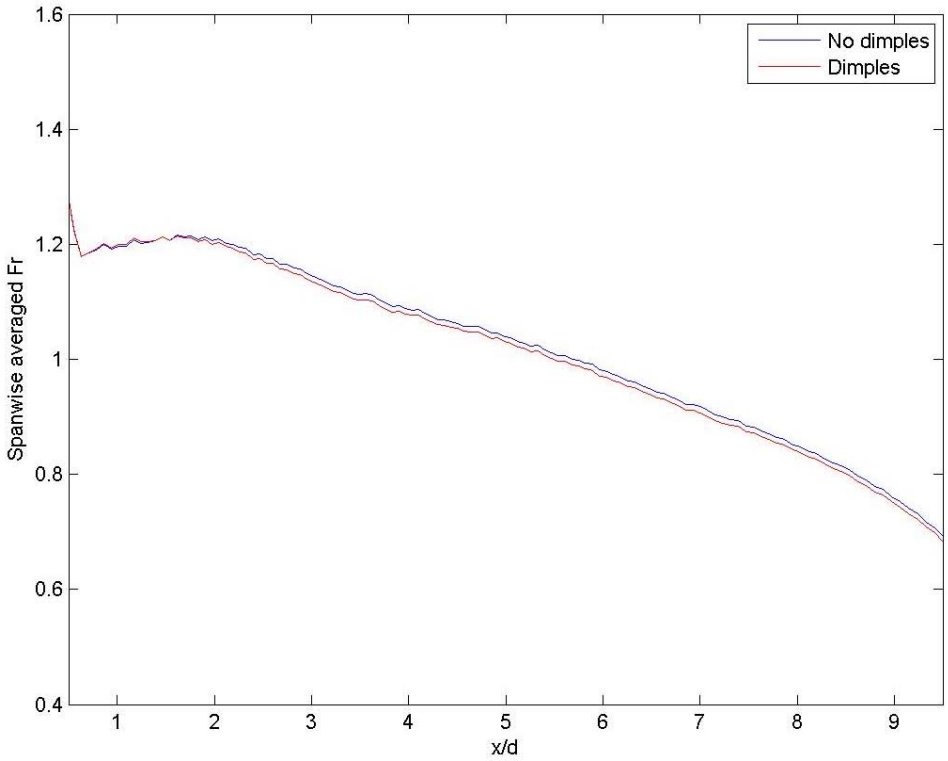

Fig D.20 Spanwise averaged *Fr* at Re = 60k and low turbulence for M = 1.25

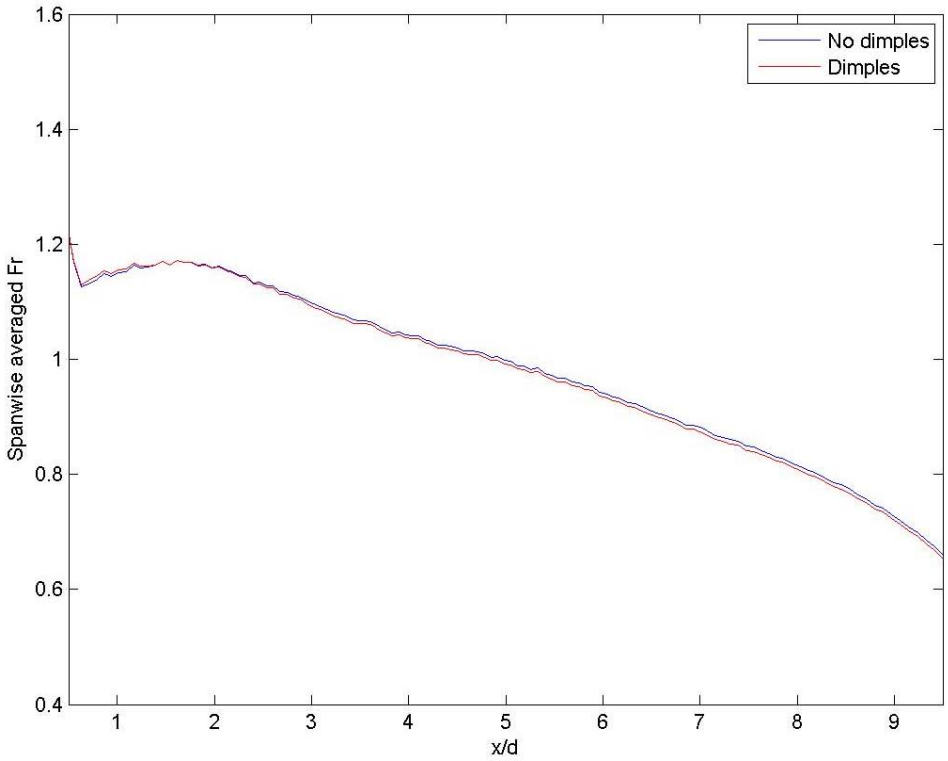

Fig D.21 Spanwise averaged *Fr* at Re = 60k and low turbulence for M = 1.0

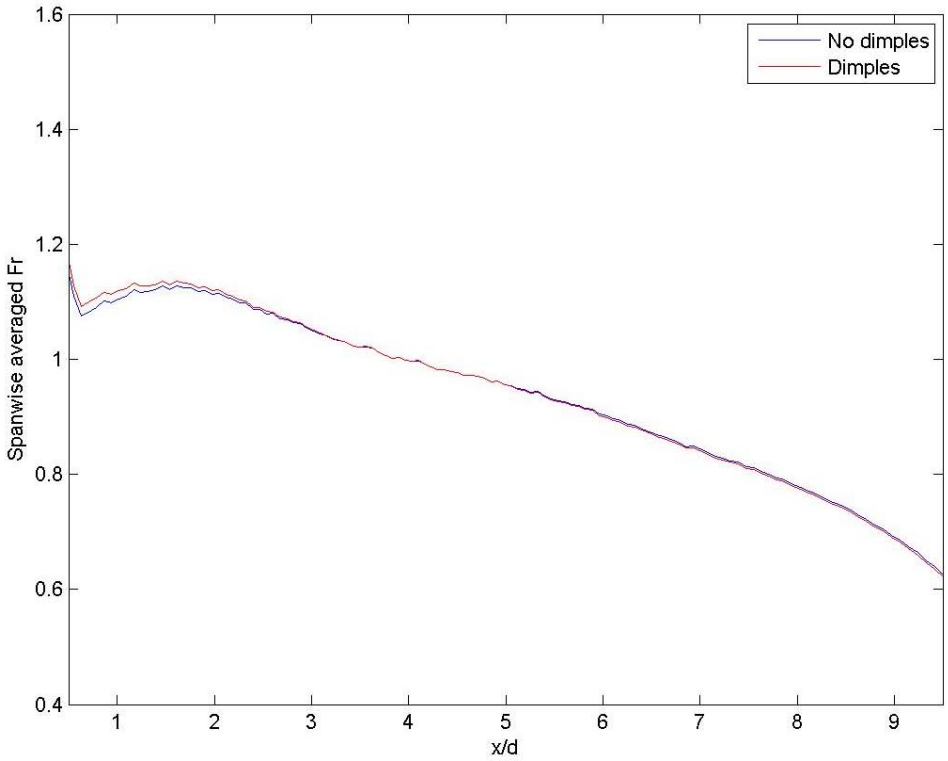

Fig D.22 Spanwise averaged *Fr* at Re = 60k and low turbulence for M = 0.75

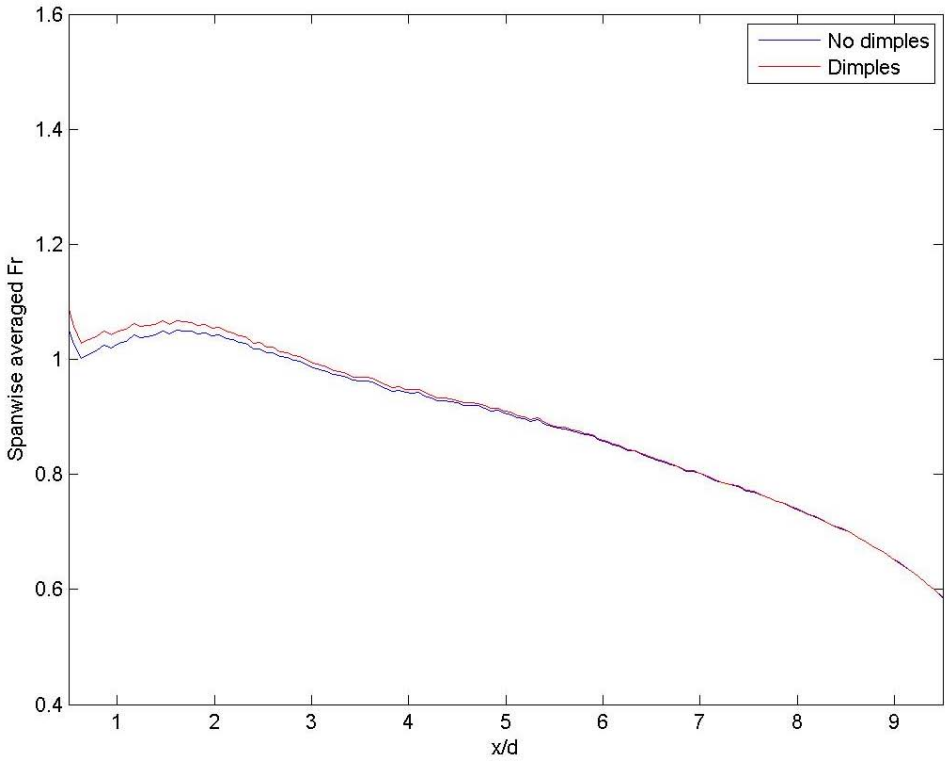

Fig D.23 Spanwise averaged *Fr* at Re = 60k and low turbulence for M = 0.5

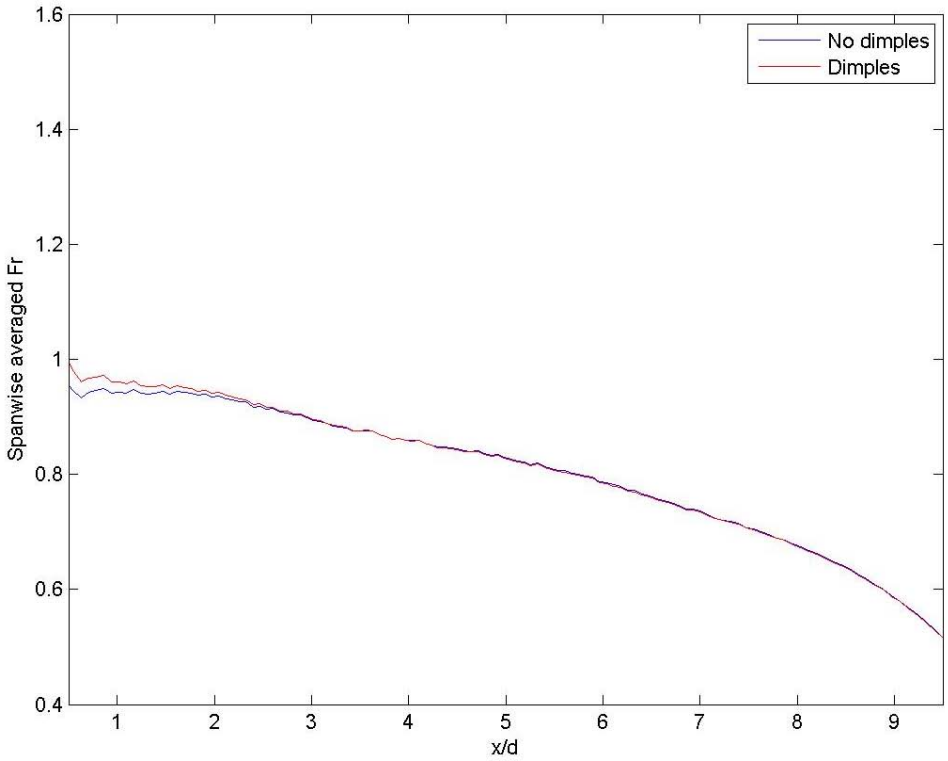

Fig D.24 Spanwise averaged *Fr* at Re = 60k and low turbulence for M = 0.25

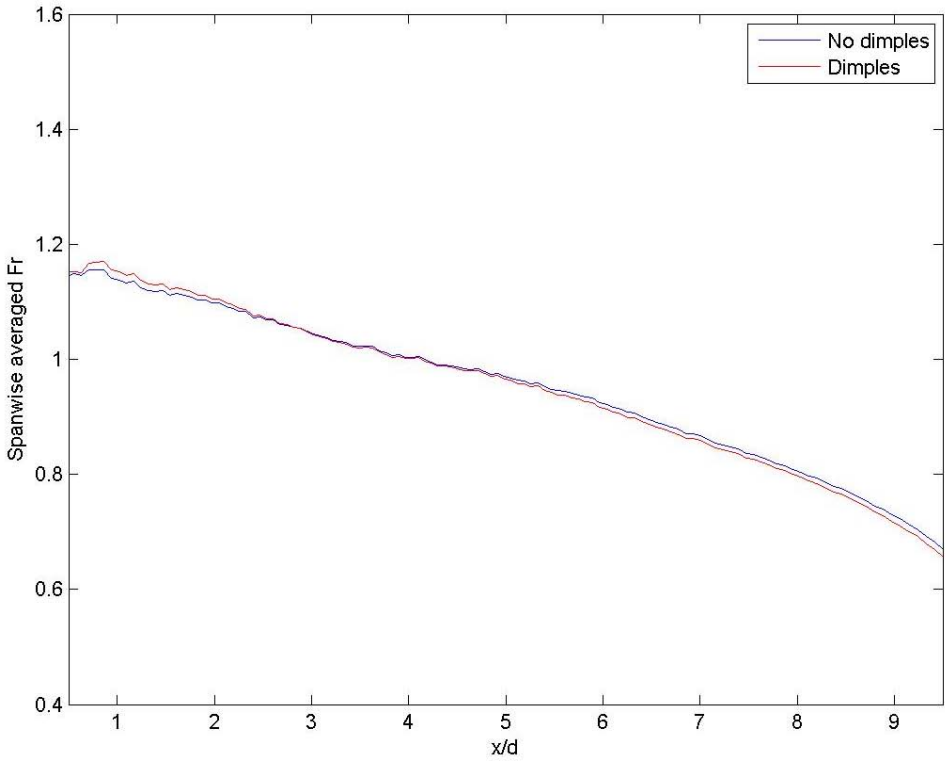

Fig D.25 Spanwise averaged *Fr* at Re = 60k and high turbulence for no film cooling (M = 0)

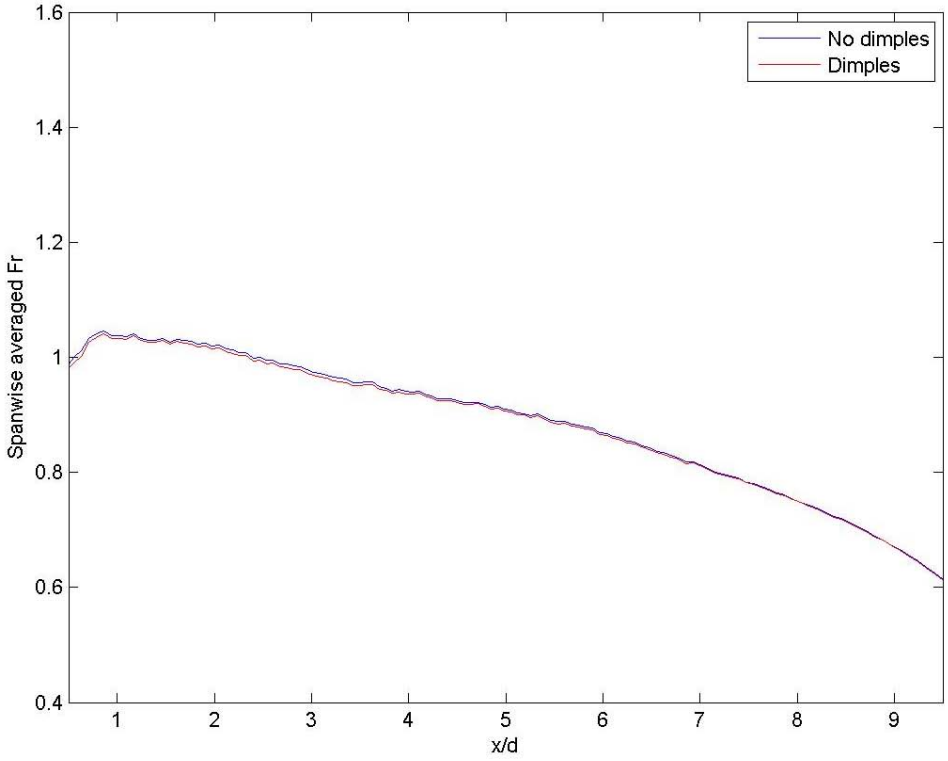

Fig D.26 Spanwise averaged *Fr* at Re = 30k and high turbulence for no film cooling (M = 0)

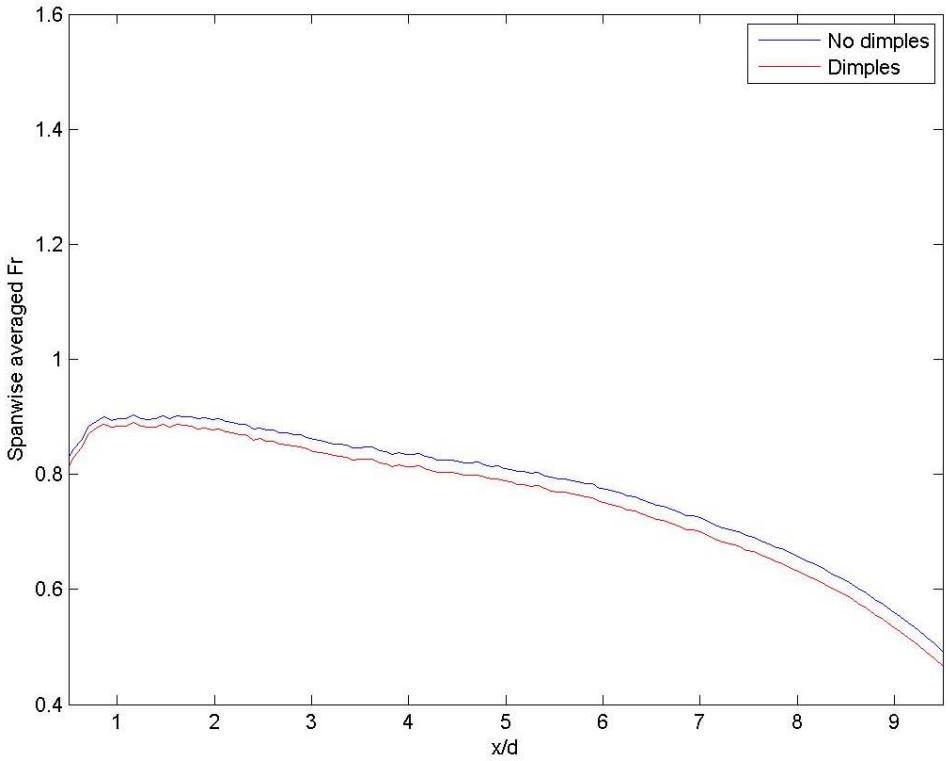

Fig D.27 Spanwise averaged *Fr* at Re = 30k and low turbulence for no film cooling (M = 0)

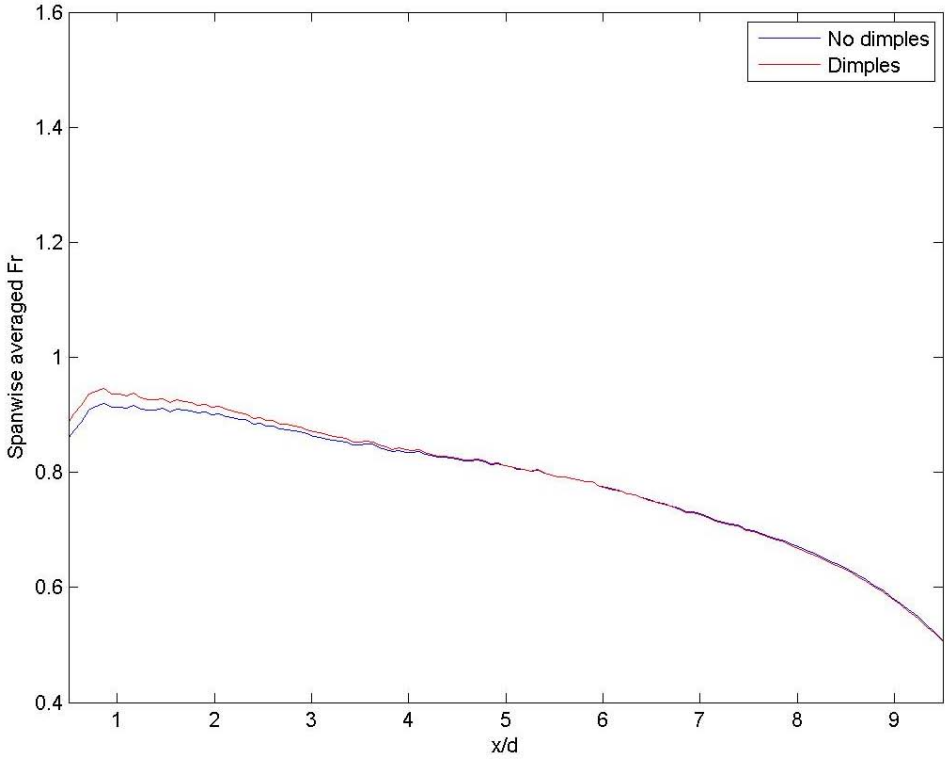

Fig D.28 Spanwise averaged *Fr* at Re = 60k and low turbulence for no film cooling (M = 0)

Appendix E. Model Drawings

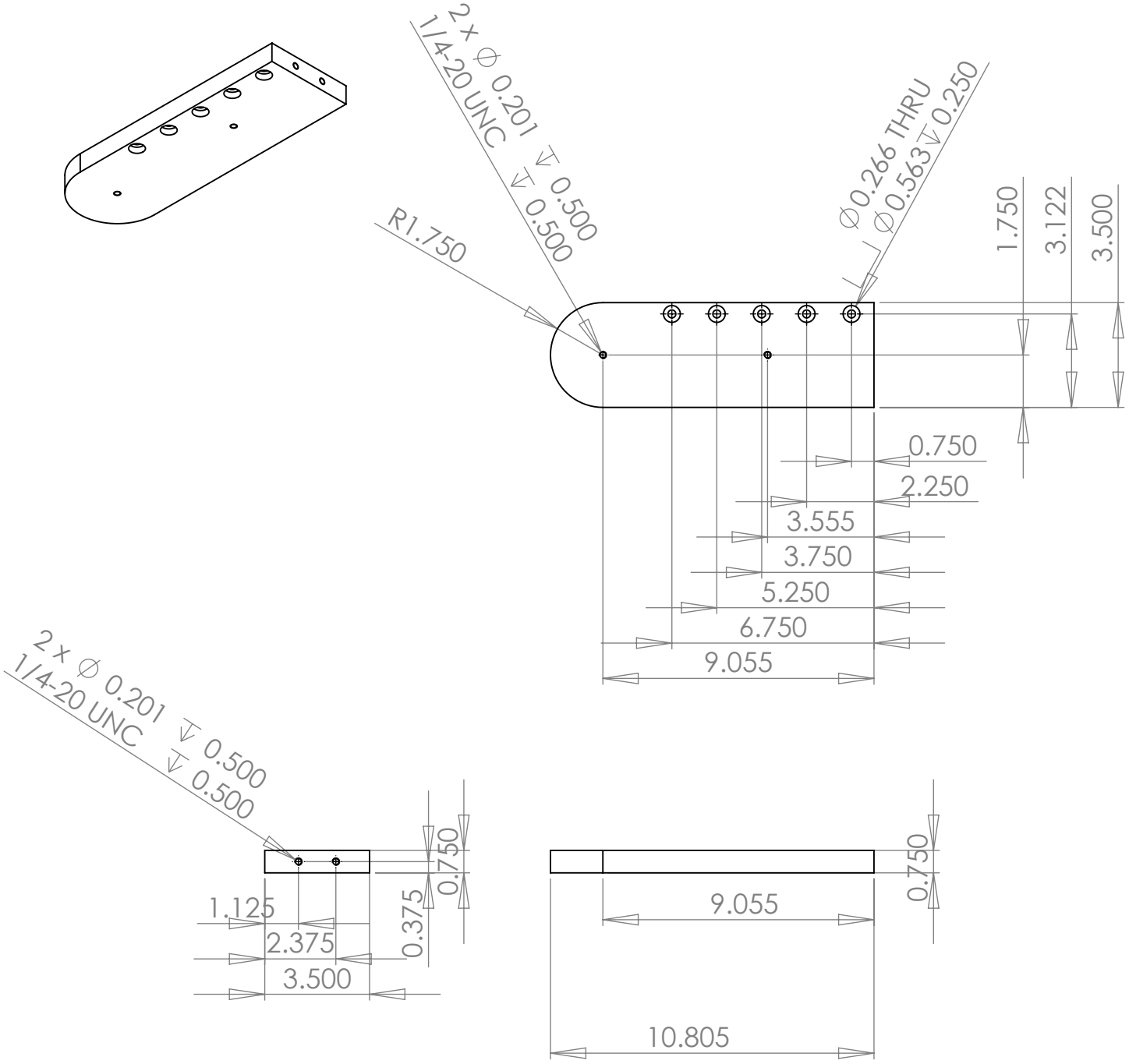

Part: Right Side Plate
Material: Plexiglass
Units: Inches

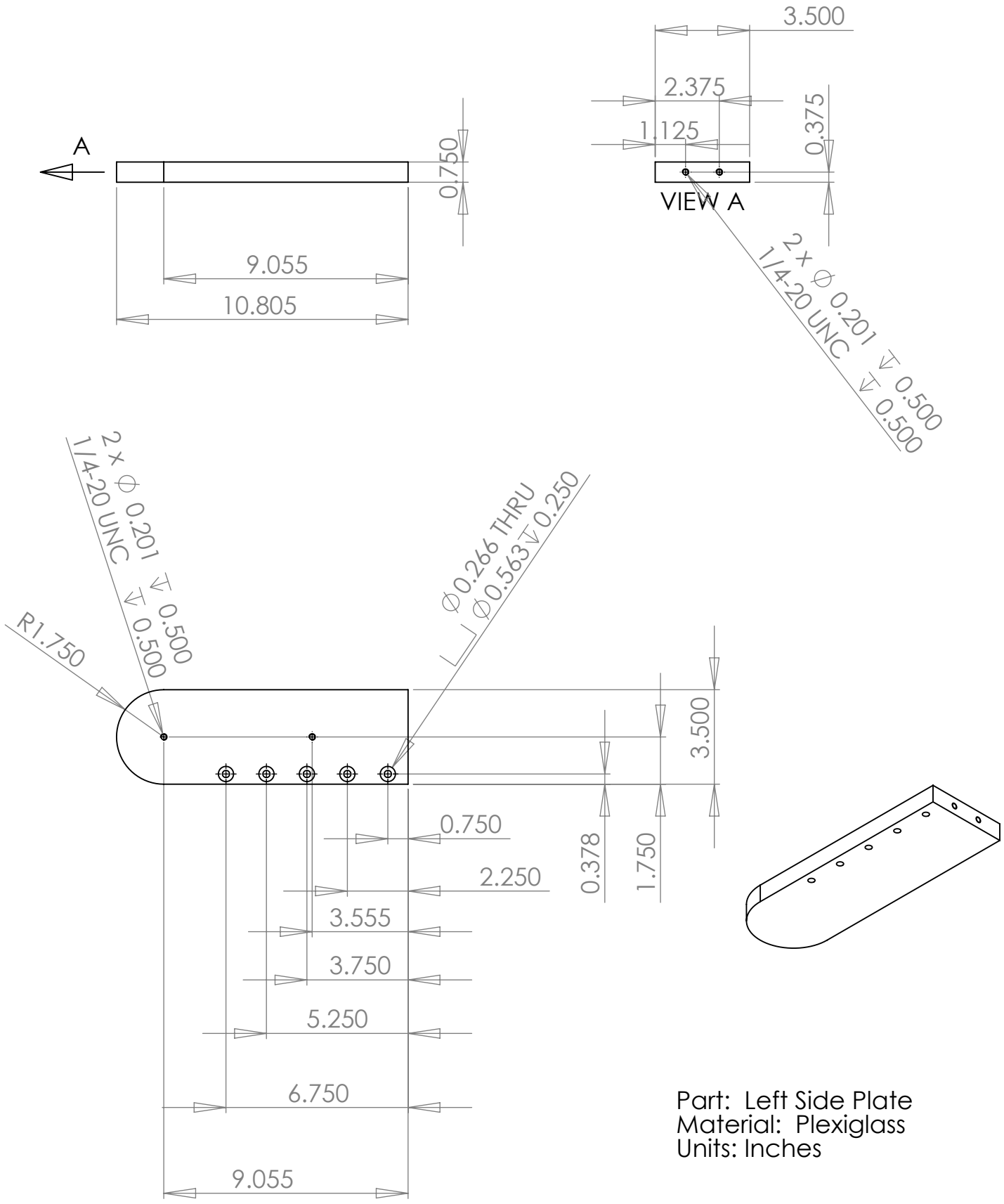

Part: Left Side Plate
Material: Plexiglass
Units: Inches

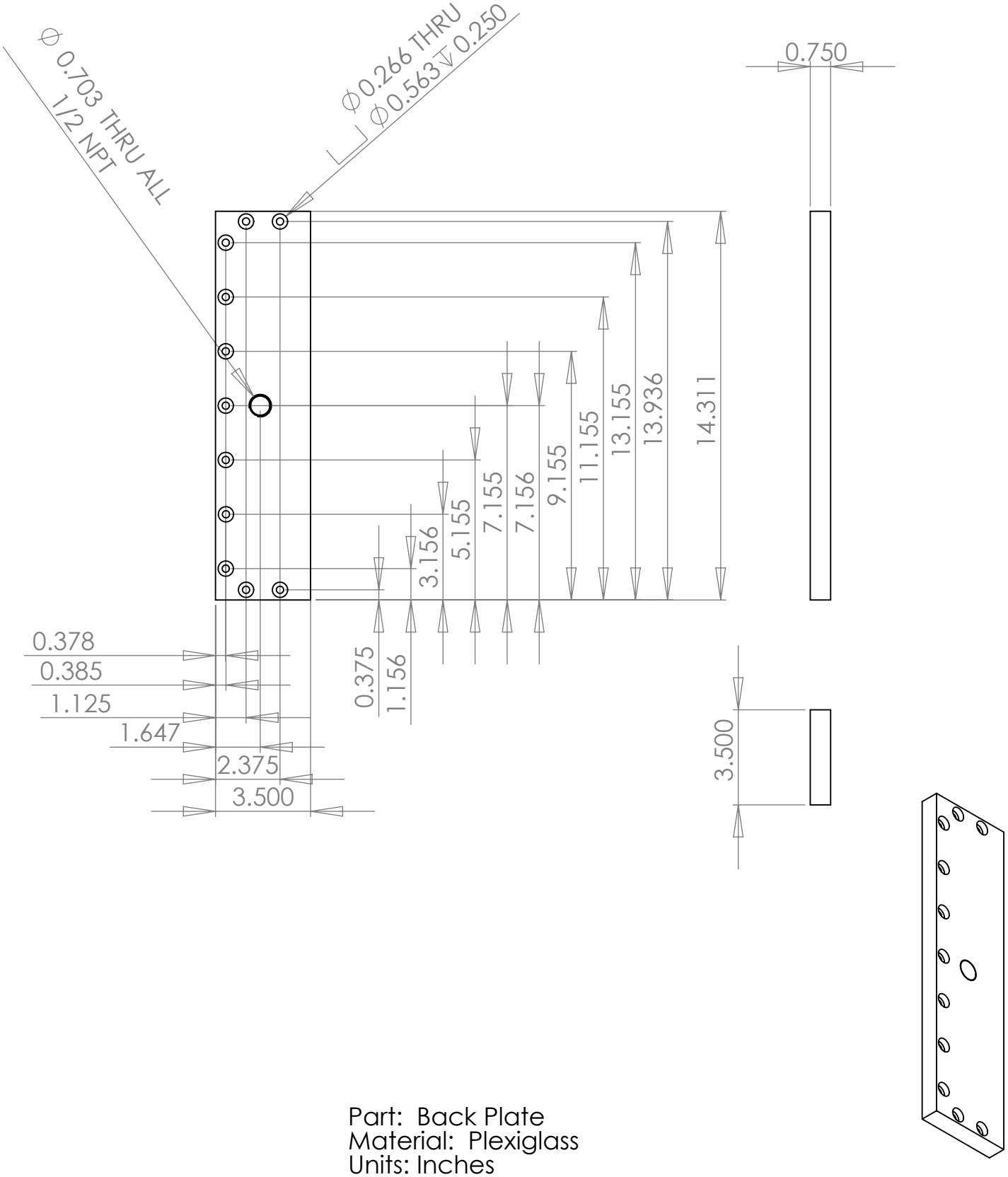

Part: Back Plate
Material: Plexiglass
Units: Inches

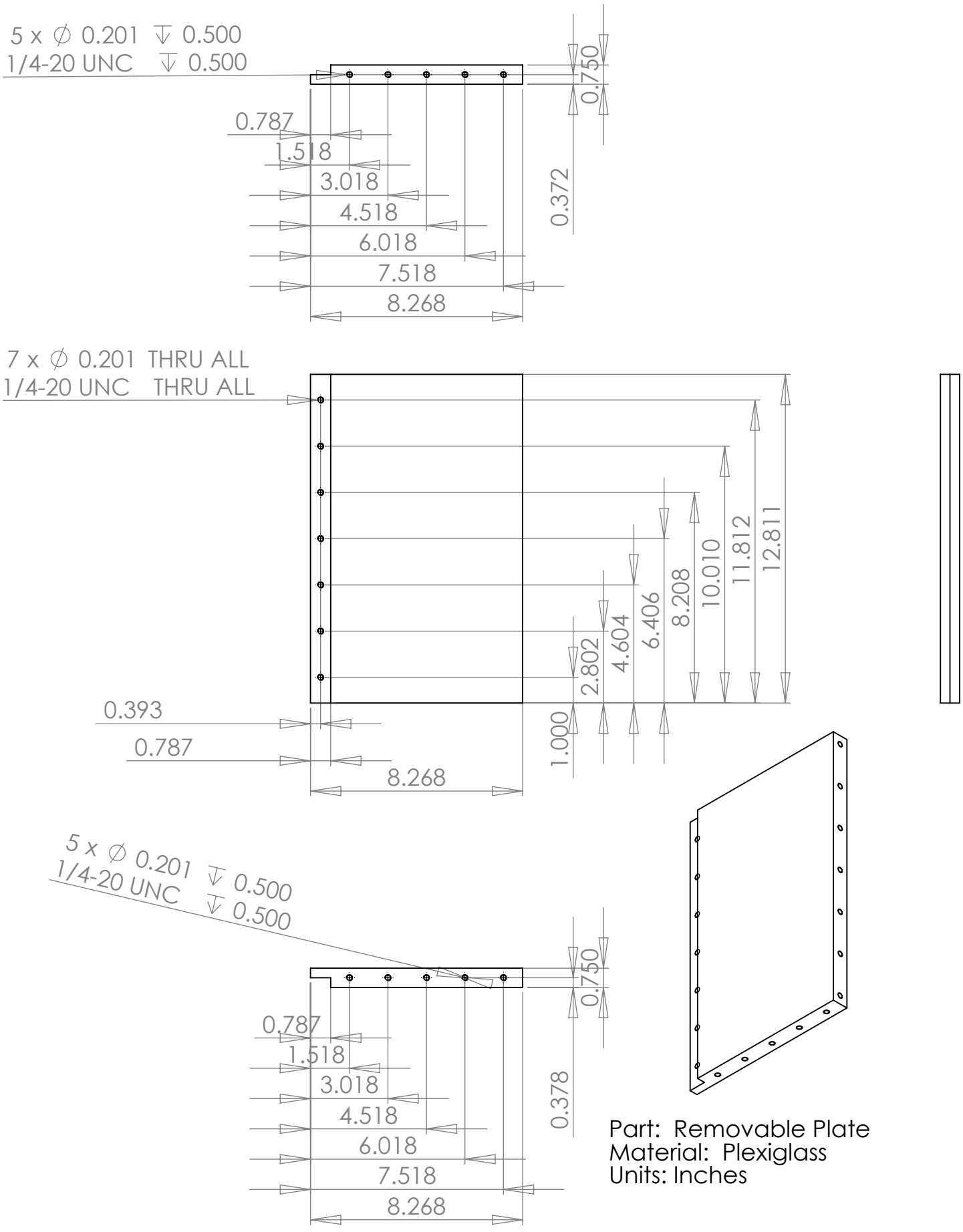

Part: Removable Plate
Material: Plexiglass
Units: Inches

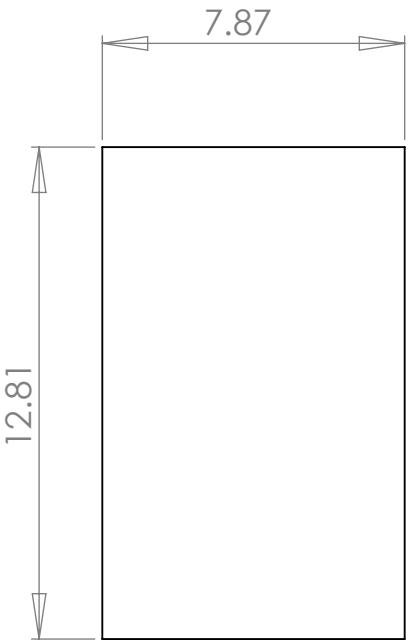

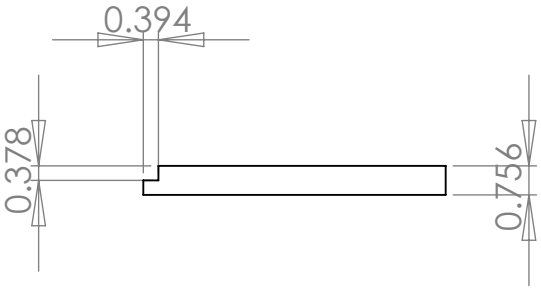

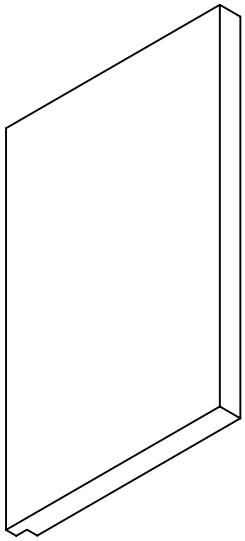

Part: Top Plate
Material: Plexiglass
Units: Inches

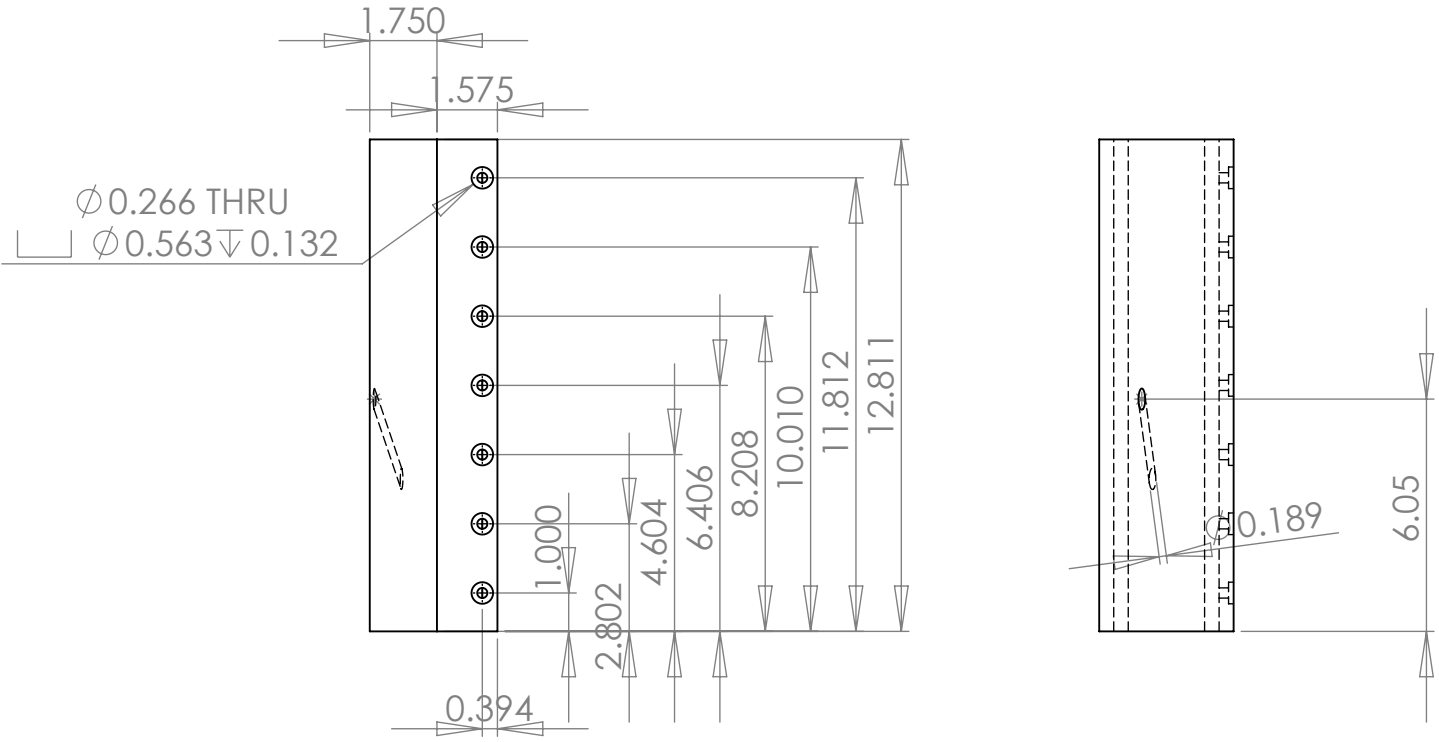

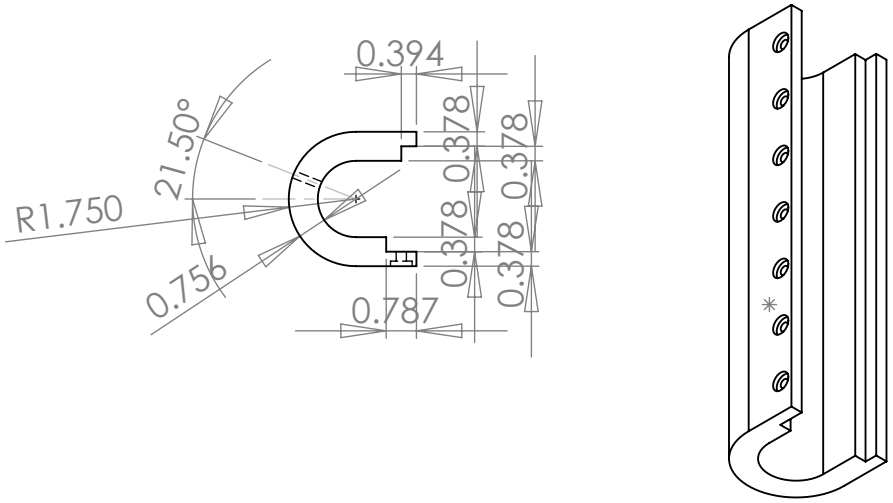

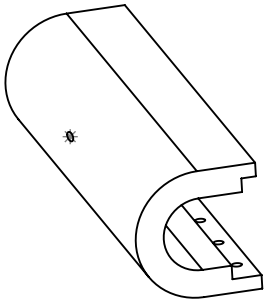

Part: Leading Edge
Material: Last-a-Foam
Units: Inches

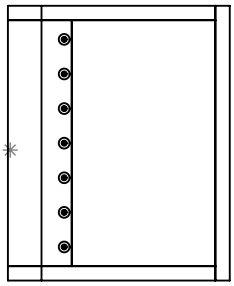

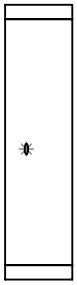

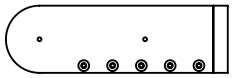

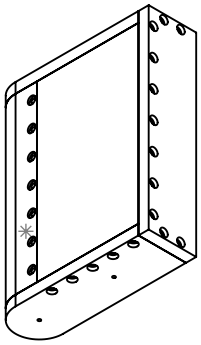

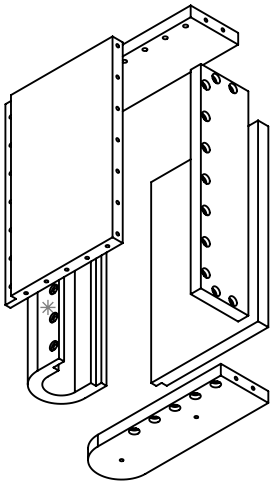

Leading Edge Model

1. Wilson, D.G., and Korakianitis, T. *The Design of High-Efficiency Turbomachinery and Gas Turbines*. Prentice Hall, Upper Saddle River, NJ, 1998.

2. Saravanamuttoo, H.I.H, Rogers,G.F.C, and Cohen, H. *Gas Turbine Theory*. Pearson Education Limited. Harlow, England, 2001.

3. Han, J.-C. "Turbine Blade Cooling Studies at Texas A&M University: 1980-2004," Journal of Thermophysics and Heat Transfer, Vol. 20, No. 2, April-June 2006.

4. Hah, C., B. Lakshminarayana. *Fluid Dynamics and Heat Transfer of Turbomachinery*. John Wiley & Sons, Inc., New York, NY, 1996.

5. Bogard, D.G., K.A. Thole, "Gas Turbine Film Cooling," *Journal of Propulsion and Power Vol. 22, No. 2*, March-April 2006.

6. Koff, B.L. "*Spanning the Globe with Jet Propulsion,"* AIAA Annual Meeting and Exhibit, Arlington, Virginia, Paper No. 2987. April 30-May 2, 1991.

7. Incropera, F.P., Dewitt, D.P., Bergman, T.L., and Lavine, A.S. *Fundamentals of Heat and Mass Transfer 6th ed*. John Riley and Sons, Inc. Hoboken, NJ, 2007.

8. Eckert, E.R.G., and R.M. Drake. *Analysis of Heat and Mass Transfer*. McGraw-Hill, Inc., New York, NY, 1972.

9. Goldstein, R.J. "Film Cooling," Advances in Heat Transfer, Vol. 7, pp. 321-379. Academic Press, 1971.

10. Choi, Jin, W.-P. Jeon, and H. Choi. "Method of Drag Reduction by Dimples on a Sphere," Physics of Fluids. American Institute of Physics, 2006.

11. Ligrani, P.M., J.L. Harrison, G.I. Mahmood, and M.L. Hill. "Flow Structure Due to Dimple Depressions on a Channel Surface," American Institute of Physics, 13, 2001.

12. Bearman, P.W., and Harvey, J.K. "Golf Ball Aerodynamics," Aeronautical Quarterly, Vol.27, May 1976

13. Lake, J.P. *Flow Separation Prevention on a Turbine Blade in Cascade at Low Reynolds Number*. PHD dissertation, AFIT/DS/ENY/99-01. School of Systems and Logistics, Air Force Institute of Technology (AU), Wright-Patterson AFB, OH, 2001.

14. Rouser, Kurt P. Use *of Dimples to Suppress Boundary Layer Separation on a Low Pressure Turbine Blade*. Master's Thesis, AFIT/GAE/ENY/02-13. School of Systems and Logistics, Air Force Institute of Technology (AU), Wright-Patterson AFB OH, 2002.

15. Khalatov, A., A. Byerley, D. Ochoa, Seong-Ki Min. "Flow Characteristics Within and Downstream of Spherical and Cylindrical Dimple on a Flat Plate at Low Reynolds Numbers," Vol. 3, Proceedings of ASME Turbo Expo Power for Land, Sea, and Air, pp. 589-601, June 2004.

16. Khalatov, A., A. Byerley, R. Vincent. "Flow Characteristics Within and Downstream of a Single Shallow Cylindrical and Spherical Dimple: Effect of Pre-Dimple Boundary Layer Thickness," Proceedings of GT2005 ASME Turbo Expo 2005: Power for Land, Sea, and Air," pp. 61-77, June 2005.

17. Bearman, P.W., and J.K. Harvey. "Control of Circular Cylinder Flow," AIAA Journal, Vol. 31, pp. 1753-1756, October 1993.

18. Vincent, Robert C. *CFD Investigation of Flow Dynamics Inside a Spherical Surface Indentation*. Master's Thesis, AFIT/GAE/ENY/06-M31. School of Systems and Logistics, Air Force Institute of Technology (AU), Wright-Patterson AFB OH, 2006.

19. Etter, Robert B. *CFD Investigation of Effect of Depth to Diameter Ratio on Dimples Flow Dynamics*. Master's Thesis, AFIT/GAE/ENY/07-J07. School of Systems and Logistics, Air Force Institute of Technology (AU), Wright-Patterson AFB OH, July 2007.

20. Mahmood, G.I., M.L. Hill, D.L. Nelson, P.M. Ligrani, H.-K. Moon, B. Glezer. "Local Heat Transfer and Flow Structures on and Above a Dimple Surface in a Channel," Journal of Turbomachinery, Vol. 123, January 2001.

21. Syred, N., A. Khalatov. "Effect of Surface Curvature on Heat Transfer and Hydrodynamics Within a Single Hemispherical Dimple,: Journal of Turbomachinery, Vol. 123, 2001.

22. Griffith, T.S., L. Al-Hadhrami, and J.C. Han. "Heat Transfer in Rotating Rectangular Cooling Channels (AR=4) with Dimples," Journal of Turbomachinery, Vol. 125, July 2003.

23. Hiwada, M. and T. Kawamura. "Some Characteristics of Flow Pattern and Heat Transfer Past a Circular Cylindrical Cavity," Bulletin of JSME, Vol. 26, No. 220, 1744-1752, October 1983.

24. Roland, I. An *Experimental Investigation of the Effect of Dimples on Turbine Adiabatic Film Cooling*. Master's Thesis, AFIT/GAE/ENY/08-M24. School of Engineering and Management, Air Force Institute of Technology (AU), Wright-Patterson AFB OH, March 2008.

25. Jung, I.S., J.S. Lee, and P.M. Ligrani. "Effects of Bulk Flow Pulsations on Film Cooling With Compound Angle Holes: Heat Transfer Coefficient Ratio and Heat Flux Ratio," Journal of Turbomachinery, Vol. 124, No.1, pp. 142-151, January 2002.

26. Rutledge, J.L., D. Robertson, and D.G. Bogard. "Degradation of Film Cooling Performance on a Turbine Vane Suction Side due to Surface Roughness," Journal of Turbomachinery, Vol. 128, pp. 547-554, July 2006.

27. Cruise, M.W., U.M. Yuki, and D.G. Bogard. "Investigation of Various Parametric Influences on Leading Edge Film Cooling," ASME Paper 97-GT-296, 1997.

28. Rutledge, J.L., King, P.I., Rivir, R., "Net Heat Flux Reduction of Pulsed Film Cooling on a Turbine Blade Leading Edge," AIAA/ASME/SAE/ASEE Joint Propulsion Conference & Exhibit, 2009.

29. Ekkad, S. V., Ou, S., Rivir, R. B., "Effect of Jet Pulsation and Duty Cycle on Film Cooling From a Single Jet on a Leading Edge Model," *Journal of Turbomachinery*, Vol. 128, Jul., 2006, pp. 564-571.

30. Rutledge, James L. Air Force Institute of Technology PhD student, personal communication

Vita

Captain Paul G. Frisinger graduated from Dripping Springs High School in Dripping Springs, Texas in May 1999. He entered undergraduate studies at the University of Texas at Austin where he graduated with a Bachelor of Science degree in Aerospace engineering in May 2003. After earning his commission from Officer Training School at Maxwell AFB, Alabama in November 2004, he supported the F-22 program at Wright-Patterson AFB, Ohio as the Maintenance Training Systems Engineer. In August 2007 he entered the Graduate School of Engineering and Management at the Air Force Institute of Technology. Upon graduation he will be assigned to Kirtland AFB, New Mexico where he will serve in the Space Vehicle Directorate, Air Force Research Laboratory.

REPORT DOCUMENTATION PAGE

Form Approved
OMB No. 0704–0188

1. REPORT DATE (DD–MM–YYYY)	2. REPORT TYPE	3. DATES COVERED *(From — To)*
26-03-2009	Master's Thesis	Sep 2009 – Mar 2009

4. TITLE AND SUBTITLE
An Experimental Investigation Studying the Influence of Dimples on a Film Cooled Turbine Blade Leading Edge

5a. CONTRACT NUMBER

5b. GRANT NUMBER

5c. PROGRAM ELEMENT NUMBER

6. AUTHOR(S)
Paul G. Frisinger, Capt, USAF

5d. PROJECT NUMBER

5e. TASK NUMBER

5f. WORK UNIT NUMBER

7. PERFORMING ORGANIZATION NAME(S) AND ADDRESS(ES)
Air Force Institute of Technology
Graduate School of Engineering and Management (AFIT/ENY)
2950 Hobson Way
WPAFB OH 45433-7765

8. PERFORMING ORGANIZATION REPORT NUMBER
AFIT/GAE/ENY/09-M10

9. SPONSORING / MONITORING AGENCY NAME(S) AND ADDRESS(ES)
Dr. Richard Rivir, Air Force Research Laboratory/Propulsion Directorate
1950 Fifth Street, Building 18 Room D120
Wright-Patterson AFB, OH 45433-7251
785-2744

10. SPONSOR/MONITOR'S ACRONYM(S)
AFMC AFRL/RZ

11. SPONSOR/MONITOR'S REPORT NUMBER(S)

12. DISTRIBUTION / AVAILABILITY STATEMENT
APPROVED FOR PUBLIC RELEASE; DISTRIBUTION UNLIMITED

13. SUPPLEMENTARY NOTES

14. ABSTRACT

An investigation was conducted to examine the effect of a row of cylindrical surface dimples in reducing the heat load on a turbine blade leading edge model. The models consisted of a foam cylindrical leading edge with a flat afterbody fabricated from Plexiglass. A single coolant hole was located 21.5° from the leading edge, angled 20° to the surface and 90° from the streamwise direction. The leading edge diameter to hole diameter ratio was D/d = 18.7. A row of seven dimples was placed upstream of one of the coolant holes. Infrared thermography techniques were used to determine the adiabatic effectiveness, η, and heat transfer coefficient, h, distributions so that the net heat flux reduction could be calculated. Freestream conditions consisted of Reynolds numbers of 60,000 and 30,000 at both low turbulence and high turbulence. At Re = 60k, the dimples proved to increase the area averaged η by an average of 0.007, while the dimpled cases performed equally, if not slightly poorer, than a smooth surface at the lower Reynolds number. The heat transfer coefficient was not greatly affected by the presence of the dimples beyond an x/d location of 0.5. Because the heat transfer coefficient remained relatively unchanged while η increased at Re = 60k, the area averaged net heat flux reduction was increased slightly, by an average of 0.02, for the cases with dimples at those freestream conditions. Although, the dimpled cases provided slight improvement to the adiabatic effectiveness for some cases, any advantage was generally less than the uncertainty, indicating that the dimples' effect was negligible.

15. SUBJECT TERMS
Turbine, Film, Cooling, Dimple, Adiabatic Effectiveness, Leading Edge

16. SECURITY CLASSIFICATION OF:			17. LIMITATION OF ABSTRACT	18. NUMBER OF PAGES	19a. NAME OF RESPONSIBLE PERSON
a. REPORT	b. ABSTRACT	c. THIS PAGE			Dr. Paul King
U	U	U	UU	171	19b. TELEPHONE NUMBER (Include Area Code) (937) 255-6565, ext 4559 (Paul.King@afit.edu)